Barley Husk as a Multifunctional Biomass Precursor for Silica/Carbon Composite Anodes in Rechargeable Lithium-ion and Sodium-ion Batteries

Alireza Fereydoonisefiddashti

School of Chemistry, Pharmacy and Pharmacology
University of East Anglia
Norwich
U.K.
2026

A thesis submitted in fulfillment of the requirements for the degree of Doctor of Philosophy of University of East Anglia.

Declaration

I declare that the work contained in this thesis submitted for the degree of Doctor of Philosophy is my work, except where due reference is made to other authors, and has not previously been submitted by me for a degree at this or any other universities.

Alireza Fereydoonisefiddashti

Acknowledgments

First of all, sincere thanks are extended to the supervisory team: Dr Yimin Chao, for the opportunity to undertake this PhD and for his guidance throughout the project; Professor Joseph Wright, for his generous support, encouragement, and valuable advice; and Professor Konstantinos Chalvatzis, for his guidance and support.

Gratitude is extended to all members of the Yimin Chao research group, past and present, particularly Dr Chenghao Yue and Dr Jayshree Ahire, for their kindness, collegiality, and support during the PhD.

Sincere thanks are also expressed to my parents for their unwavering encouragement and support.

Finally, financial support is gratefully acknowledged from the University of East Anglia's Critical Decade for Climate Change Doctoral Training Programme, funded by the Leverhulme Trust under its Doctoral Scholarship Scheme.

Abstract

This thesis evaluates barley husk as a sustainable, multifunctional precursor for silica/carbon and silicon/carbon composite anodes for rechargeable lithium-ion and sodium-ion batteries. Barley husk, combining carbonaceous and silica-rich fractions within a single biomass feedstock, is converted using scalable thermal processing and low-complexity post-treatment. Processing-structure relationships are established using complementary characterisation, including X-ray diffraction, Raman spectroscopy, electron microscopy with elemental mapping, X-ray photoelectron spectroscopy, thermogravimetric analysis, and nitrogen sorption.

In lithium half-cells, an optimised barley-husk-derived silica/carbon composite delivers ~380 mAh g^{-1} at C/5 and retains 87.9% of its capacity after 400 cycles, with coulombic efficiency rising above 98% after the initial formation period. The initial Coulombic efficiency (~60%) is limited by irreversible lithium consumption associated with solid-electrolyte interphase (SEI) formation and partial SiO_2 conversion. Kinetic analysis indicates mixed storage with a predominantly surface-controlled contribution, consistent with fast charge transfer within a porous hard-carbon-like framework. Building on this platform, silicon nanoparticles are incorporated into the biomass-derived matrix to access alloying-driven capacity while retaining the mechanical buffering and interfacial stabilisation provided by the carbon network; a composition window is identified in which reversible capacity increases without compromising cycle stability. Feasibility is further demonstrated in a lithium-ion full cell paired with a layered oxide cathode, highlighting a route towards device-relevant architectures.

For sodium-ion batteries, barley-husk-derived hard carbon is tuned through carbonisation to control disorder, interlayer spacing, and nanopore population, enabling the characteristic sloping and low-voltage plateau contributions to sodium storage and providing practical guidance on balancing capacity, first-cycle irreversibility, and rate performance. Overall, the thesis provides an integrated processing-structure-electrochemistry framework and supports barley husk as a low-cost precursor for composite anodes across lithium-ion and sodium-ion chemistries.

Contents

List of figures

List of tables

Abbreviations

A	Ampere
AC	Alternating current
BET	Brunauer-Emmett-Teller (specific surface area method)
BH	Barley husk
BJH	Barrett-Joyner-Halenda (pore size distribution method)
BM	Ball milling
C-rate	Charge/discharge rate normalised to capacity
CB	Conductive carbon black
CC	Constant current
CD	Current density
CE	Coulombic efficiency
CV	Cyclic voltammetry
dQ/dV	Differential capacity (derivative of capacity with respect to voltage)
DMC	Dimethyl carbonate
EC	Ethylene carbonate
EDX / EDS	Energy-dispersive X-ray spectroscopy
EIS	Electrochemical impedance spectroscopy
FEC	Fluoroethylene carbonate
FESEM	Field-emission scanning electron microscopy
FWHM	Full width at half maximum
g	gram
GCD	Galvanostatic charge-discharge
HRTEM	High-resolution transmission electron microscopy
ICE	Initial Coulombic efficiency
kg	kilogram
LIB	Lithium-ion battery
mA	milliampere
mAh g^{-1}	Unit for specific capacity

mg cm⁻²	Unit for areal loading
mV	millivolt
N/P	Negative-to-positive capacity ratio
NMC	Nickel manganese cobalt oxide
NMC622	$LiNi_{0.6}Mn_{0.2}Co_{0.2}O_2$ cathode
OCP / OCV	Open-circuit potential / open-circuit voltage
PDF	Powder diffraction file (XRD reference database)
PE	Polyethylene
PVDF	Poly(vinylidene fluoride)
PAA	Poly(acrylic acid) (if used)
PSD	Particle size distribution
R_{ct}	Charge-transfer resistance in EIS fitting
R_s	Solution/series resistance in EIS fitting
R_{SEI}	SEI resistance in EIS fitting
SIB	Sodium-ion battery
SEI	Solid electrolyte interphase
SEM	Scanning electron microscopy
TEM	Transmission electron microscopy
TGA	Thermogravimetric analysis
V	Volt
vs.	versus
W	Watt
Wh kg⁻¹	Unit for specific energy
XPS	X-ray photoelectron spectroscopy
XRD	X-ray diffraction
Z′, Z″	Real and imaginary impedance components in EIS

1. General introduction

1.1. Background and motivation

Efficient and affordable electrochemical energy storage is a central requirement for global decarbonisation efforts and for the ongoing electrification of transport and stationary energy systems. Electricity generation from renewable sources such as solar photovoltaics and wind power is expanding rapidly, yet their inherently variable output creates mismatches between supply and demand, which must be addressed by storage technologies capable of supporting stable and flexible grid operation.[1, 2] Rechargeable batteries are central to this transition, underpinning portable electronics, electric vehicles and an emerging class of grid-scale storage installations.[2, 3]

Lithium-ion batteries (LIBs) currently dominate the rechargeable battery market owing to their high energy density, good cycle life and steadily decreasing cost per kilowatt-hour.[4] Despite these advantages, increasing attention has been directed toward issues of resource availability, environmental impact and the long-term cost of key battery materials such as lithium, cobalt and nickel have stimulated interest in complementary chemistries based on more abundant metals.[5] Sodium-ion batteries (SIBs), in particular, are attracting attention as promising candidates for medium- and large-scale storage due to the wide availability and low cost of sodium salts, despite their somewhat lower energy density compared with LIBs.[5, 6] At the same time, the sustainability and cost structure of electrode materials have become increasingly important considerations in battery development.[7]

1.2. Rechargeable lithium- and sodium-ion batteries

LIBs and SIBs share a common “rocking-chair” architecture, in which alkali ions shuttle between a positive electrode (cathode) and a negative electrode (anode) through an ion-conducting electrolyte while electrons flow through an external circuit.[8] The choice of electrode materials and electrolyte determines the cell voltage, energy density, rate capability and lifetime. Conventional LIBs employ layered transition-metal oxides, spinels or polyanionic compounds as cathodes and graphite as the anode, whereas SIBs typically use analogous Na-containing cathodes

paired with hard carbon anodes because graphite does not intercalate Na^+ to a sufficient extent under standard electrolytes.[9]

A more detailed discussion of battery components, operating principles and representative cell chemistries is provided in Chapter 2. The present chapter focuses on the motivation for developing alternative anode materials within this broader framework.

1.3. Anode materials and the role of silicon and hard carbon

The anode plays a crucial role in determining the specific capacity, rate performance and safety of both LIBs and SIBs. Graphite, the state-of-the-art anode in commercial LIBs, delivers a reversible capacity of 372 mAh g^{-1} through the formation of LiC_6,[1] but its theoretical capacity and relatively low operating potential impose limitations on further energy-density improvements.[10] In SIBs, graphite is largely inactive because the energetics and size of Na^+ do not favour stable Na-graphite intercalation under conventional electrolytes.[8]

Hard carbon has emerged as the leading anode candidate for SIBs and as an attractive alternative anode for certain LIB applications. It is a non-graphitising carbon characterised by turbostratic stacking, enlarged interlayer spacing and a combination of micropores (< 2 nm), mesopores (2 to 50 nm), and macropores (> 50 nm).[10] These features enable Na^+ and Li^+ storage via a combination of adsorption at defects, interlayer insertion and filling of closed nanopores, resulting in capacities typically in the range 250 to 350 mAh g^{-1} for Na-ion cells.[6]

Silicon offers a much higher theoretical capacity (~3579 mAh g^{-1} for $Li_{15}Si_4$) and has therefore been widely investigated as an anode material for LIBs.[8] However, the large volumetric expansion associated with alloying, the instability of the solid-electrolyte interphase (SEI) and the loss of electrical contact during cycling lead to rapid capacity fading and poor Coulombic efficiency if Si is used in isolation. Embedding silicon or silicon oxides within a conductive carbon matrix is a widely adopted strategy to mitigate these issues, but many reported architectures relying on

[1] The theoretical specific capacity of graphite can be obtained from the stoichiometric reaction forming LiC_6 using Faraday's law, $Q=nF/(3.6M)$, where n=1 mol e^- per mol C_6 and M is the molar mass of C_6.

complex syntheses or low mass loadings that are difficult to scale.[8, 11] Together, these factors highlight the potential of composite anodes that integrate the high capacity of silicon with the structural stability and favourable kinetics associated with hard carbon.

1.4. Biomass-derived anodes and rationale for barley husk

In recent years, biomass-derived carbons and silica/carbon composites have been increasingly explored as anode materials because they allow low-value agricultural or forestry residues to be transformed into functional electrode components.[12] Many biomasses are rich in carbon and, in some cases, contain significant amounts of silica or other inorganic species that can act as in situ templates or precursors for composite structures. By appropriate thermal treatment and, where necessary, activation or milling, these resources can yield hard carbons with hierarchical porosity or SiO_2/C materials that buffer silicon-related volume changes and enhance SEI stability.[13]

Barley husk is an abundant by-product of the brewing and malting industries, generated in large quantities worldwide and currently used mainly as low-value animal feed or burnt for process heat.[14] Its composition is dominated by lignocellulosic carbon with a substantial silica content, making it an intrinsically suitable dual-source precursor for both hard carbon and silica-based phases. Prior work on related cereal husks has demonstrated the feasibility of producing porous carbons, SiO_2/C and SiC from such feedstocks, but systematic investigations of barley husk as a multifunctional precursor for lithium- and sodium-ion battery anodes are scarce.[14]

In this work, the combined carbon and silica content of barley husk is used to develop a family of hard carbon and silica/carbon composite anodes, and it investigates how thermal processing, ball milling, silicon incorporation and cell chemistry influence their electrochemical behaviour.

1.5. Research aims and questions

The overall aim of this thesis is to develop and understand barley husk-derived silica/carbon composite anodes for rechargeable lithium- and sodium-ion batteries, with particular emphasis on the relationships between processing, structure and electrochemical performance.

The work addresses the following research questions:

1. How do carbonisation temperature and ball-milling duration influence the structure and texture of barley husk-derived silica/carbon composites? How do interlayer spacing, crystallite size, defect density and pore-size distribution evolve with processing?
2. How do these structural and textural changes affect Li-ion storage behaviour in half-cells? What are the impacts on capacity, initial Coulombic efficiency, rate capability, impedance response and apparent Li^+ diffusion coefficient?
3. How does an optimised barley husk-derived anode compare with commercial graphite under identical cell conditions? What advantages and trade-offs emerge in terms of capacity, voltage profile, ICE and long-term stability?
4. Can the barley husk-derived host be used as a scaffold for silicon to create high-capacity hybrid anodes? What is the practical Si loading window in BH/Si composites that balances capacity, ICE and cycling stability in half- and full-cell configurations?
5. How does the optimised barley husk-derived hard carbon perform in sodium-ion cells compared with its Li-ion behaviour? What similarities and differences arise in Na^+ versus Li^+ storage mechanisms, and how do these relate to structural descriptors such as d_{002} and porosity?

1.6. Scope and limitations of the study

The scope of the thesis is limited to anode materials derived from barley husk and their hybrids with commercial silicon powder. Commercial NMC622 is used as a representative high-energy cathode for full-cell testing. Electrochemical performance is primarily evaluated in half-cells

against Li metal (for LIB anodes) and Na metal (for SIB anodes), with selected full-cell experiments to demonstrate device-level relevance.

The study focuses on the influence of thermal processing, ball milling and silicon content on structure and performance. Other variables such as binder chemistry, electrolyte composition and electrode calendering are kept constant once a suitable baseline has been established, in order to isolate the effects of the barley husk-derived active materials. Long-term cycling tests extend to several hundred cycles for selected systems, but lifetime extrapolation beyond this range and large-format cell behaviour are outside the scope of the present work.

1.7. Thesis structure

The thesis is organised as follows.

Chapter 1 provides the general introduction, background, and overall context for the thesis.

Chapter 2 reviews anode materials for lithium- and sodium-ion batteries, with emphasis on silicon, silicon oxides and biomass-derived carbons, and introduces the conceptual role of silica/carbon composites in enhancing anode stability.

Chapter 3 summarises the materials characterisation and electrochemical techniques used throughout the work, including structural probes (XRD, Raman), textural analysis (N_2 physisorption), surface analysis (XPS) and electrochemical diagnostics (GCD, CV, EIS, differential capacity analysis).

Chapter 4 describes the processing of barley husk into silica/carbon composites via carbonisation and ball milling, and establishes the resulting processing-structure relationships using Raman spectroscopy, XRD and N_2 adsorption.

Chapter 5 investigates Li-ion storage in this family of composites, quantifying the impact of carbonisation temperature and milling duration on capacity, ICE, rate capability and kinetic parameters in Li half-cells.

Chapter 6 benchmarks the optimised barley husk-derived anode against a commercial graphite anode under identical cell conditions and positions its performance within the wider landscape of biomass-derived silicon-based anodes.

Chapter 7 explores the incorporation of commercial silicon into the barley husk-derived host to create high-capacity BH/Si hybrid anodes, including full-cell tests with NMC622 cathodes.

Chapter 8 extends the study to sodium-ion batteries, examining Na-ion storage in barley husk-derived hard carbon and comparing Na^+ and Li^+ storage mechanisms for the same structural platform.

Chapter 9 synthesises the main findings, highlights the original contributions of the thesis, discusses limitations and outlines directions for future research.

1.8. References

[1] A. Aghahosseini, A.A. Solomon, C. Breyer, T. Pregger, S. Simon, P. Strachan, A. Jäger-Waldau. *Appl Energy* 2023,331,120401.

[2] S. Teske, T. Pregger, S. Simon, T. Naegler. *Current Opinion in Environmental Sustainability* 2018,30,89–102.

[3] C. Xu, Y. Gao. *Energy* 2025,316,134453.

[4] M. Winter, B. Barnett, K. Xu. *Chem Rev* 2018,118,11433–11456.

[5] T.M. Gür. *MRS Bulletin* 2021,46,1153–1163.

[6] W. Luo, F. Shen, C. Bommier, H. Zhu, X. Ji, L. Hu. *Acc Chem Res* 2016,49,231–240.

[7] W. Wu, M. Wang, J. Wang, C. Wang, Y. Deng. *ACS Appl Energy Mater* 2020,3,3884–3892.

[8] A. Fereydooni, C. Yue, Y. Chao. *Small* 2024,20,2307275.

[9] H. Zhang, I. Hasa, S. Passerini. *Adv Energy Mater* 2018,8,1702582.

[10] V.L. Chevrier, G. Ceder. *J Electrochem Soc* 2011,158,A1011.

[11] L. Sun, Y. Liu, R. Shao, J. Wu, R. Jiang, Z. Jin. *Energy Storage Mater* 2022,46,482–502.

[12] A. V. Baskar, G. Singh, A.M. Ruban, J.M. Davidraj, R. Bahadur, P. Sooriyakumar, P. Kumar, A. Karakoti, J. Yi, A. Vinu. *Adv Funct Mater* 2023,33,2208349.

[13] Z. Gao, Y. Zhang, N. Song, X. Li. *Mater Res Lett* 2017,5,69–88.

[14] C. Yue, A. Fereydooni, P. Nakhanivej, M.B. Murria, M. Liu, Y. Zeng, Z. Wei, Q. Fu, X. Zhao, M.J. Loveridge, Y. Chao. *RSC Sustainability* 2025,3,2915.

2. Background: anodes for Li- and Na-ion batteries

2.1. Energy storage and role of rechargeable batteries

Global electricity generation increased from approximately 6,100 TWh in 1971 to over 26,000 TWh in 2018 and continues to rise. Projections suggest that demand could roughly triple by 2050, driven by population growth, electrification of transport and increased deployment of renewable power sources.[1–5] Historically, this demand has been met predominantly by fossil fuels (coal, oil and natural gas), but concerns over resource depletion and environmental impact are accelerating the transition towards sustainable and renewable energy sources.[2, 3, 5]

Renewable energy technologies such as solar photovoltaics and wind power are central to global decarbonisation pathways. However, their intermittency, driven by weather and seasonal variability, poses challenges for reliable grid integration.[6] The mismatch between when energy is generated and when it is actually needed has renewed attention on storage technologies that can buffer these fluctuations and support stable operation of the system. The shifting composition of global electricity storage is illustrated in Fig. 2.1, which shows the relative contributions of pumped hydro storage (PSH), batteries, thermal storage, and compressed-air energy storage (CAES) between 2020 and 2024.[7–10] While PSH continues to dominate total storage capacity, the contribution of grid-scale batteries has expanded dramatically since 2020, reflecting their increasing role in energy storage systems.

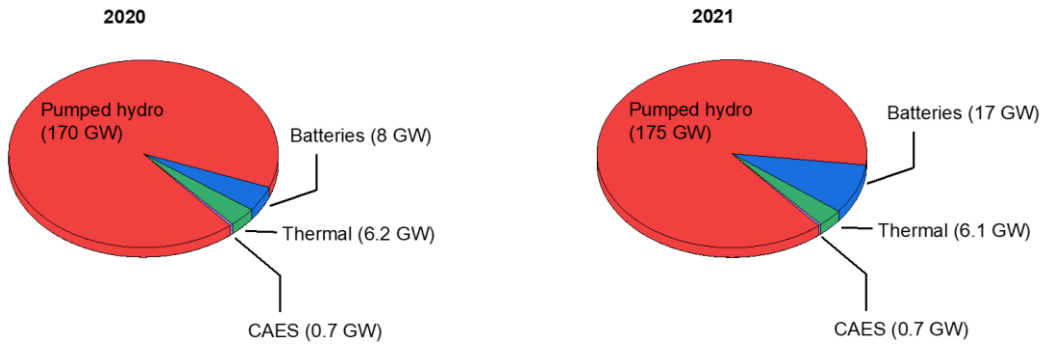

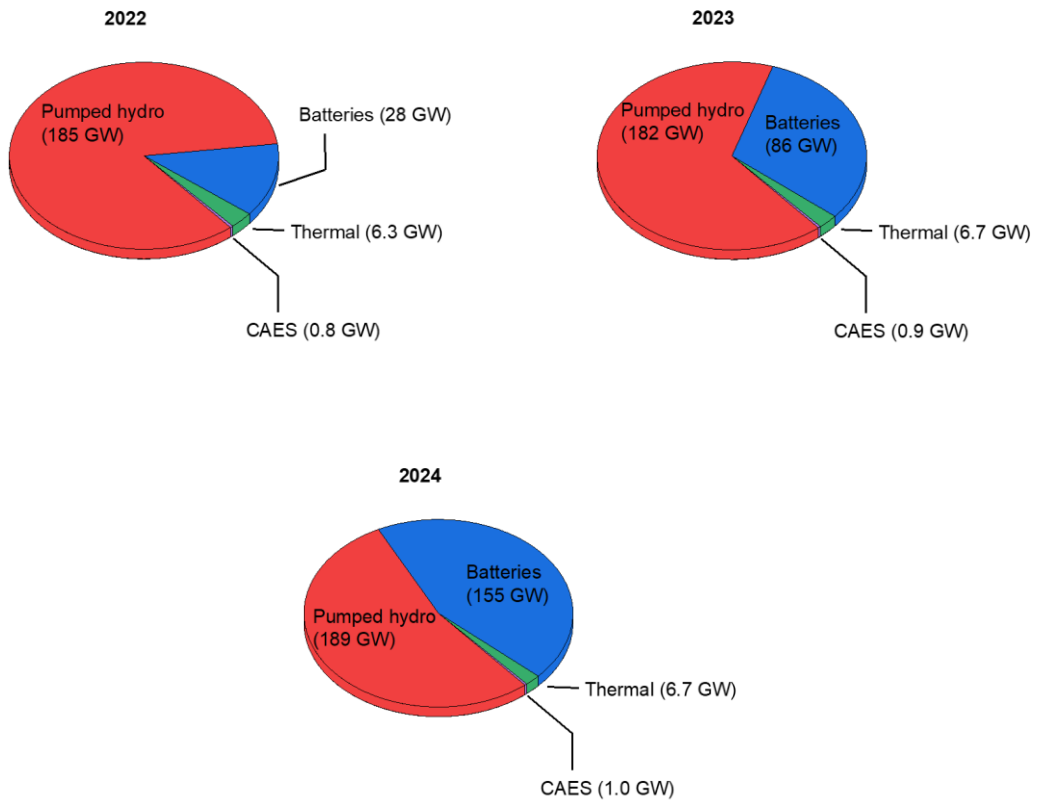

Figure 2.1. Global energy storage mix by technology (2020 to 2024).

Among various storage technologies, including pumped hydro, compressed air, flywheels and supercapacitors, electrochemical energy storage systems, and in particular rechargeable batteries, are especially versatile due to their high round-trip efficiency, modularity and applicability across scales. Recent deployment data show that global annual battery storage additions grew rapidly after 2015 and have accelerated sharply since 2020.[4, 11, 12] Cumulative installed grid-scale battery capacity followed the same trend, rising from less than 1 GW in 2010 to approximately 200 GW in 2024 (Fig. 2.2a), illustrating how rapidly batteries are becoming central to renewable integration.[11, 12]

Among the available battery technologies, lithium-ion batteries (LIBs) currently dominate commercial applications. Comparative analyses of energy densities across storage systems (Table 2.1) further show that LIBs provide favourable gravimetric and volumetric energy densities relative to most electrochemical and mechanical systems. These advantages, together with the

substantial reduction in LIB pack prices in recent years, have driven their commercial success in portable electronics, electric vehicles (EVs) and, increasingly, stationary grid-scale storage.

Table 2.1. Comparative energy densities of storage systems.

Storage Type	Material/Chemical	Energy Density		Ref.
		Gravimetric (Wh kg^{-1})	Volumetric (Wh L^{-1})	
Chemical	Liq. H_2	33,570	2,200	[13]
	Ammonia	5,710	3,750	[14]
	Ethanol	7,490	5,890	[15]
	Methanol	5,620	4,470	[16]
	Gasoline	12,330	9,060	[17]
Thermal	Cast iron (sensible*)	0.14	1.08	[18]
	Aluminium (sensible)	0.26	0.69	[18]
	Molten salt (sensible)	<0.45	<0.7	[18]
	Water (sensible)	1.2	1.2	[18]
	Water (latent)	93	—	[18]
	NaCl (latent)	139	300	[18]
	$LiNO_3$ (latent)	103	245	[18]
Mechanical	Steel flywheel	50	403	[9]
	Carbon comp. flywheel	300-350	465-543	[9]
	Compressed air	2-12	7	[9]
Electrochemical	Lithium-ion battery	150-250	400-700	[19]
	Sodium-ion battery	90-160	200-400	[20]
	Lead-acid battery	30-50	60-110	[21]
	Sodium-sulphur battery	150-240	150-300	[22]
	Na-$NiCl_2$ battery	100-160	140-250	[9]
	Vanadium redox flow	15-35	25-35	[9]
	EDLC/supercapacitor	5-10	7-10	[23]

* Latent heat refers to energy stored or released during a phase change, while sensible heat refers to energy stored or released through a temperature change without phase transition.

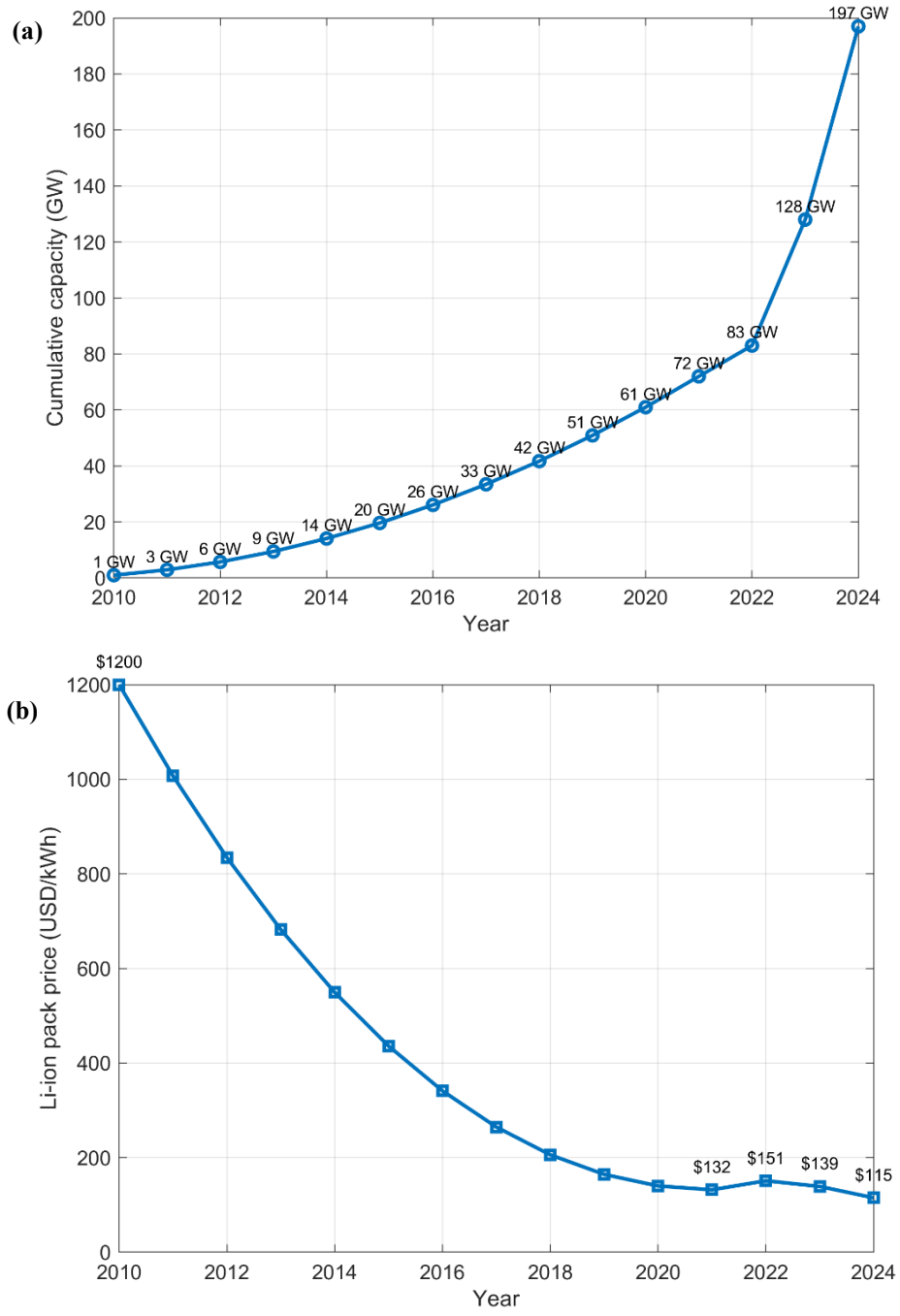

Figure 2.2. (a) Cumulative global grid-scale battery storage (2010 to 2024), and (b) lithium-ion battery pack prices (2010 to 2024).

The manufacturing cost reduction of LIBs in the past decade follows a noteworthy trend. The average LIB pack price has fallen by more than 85% since 2010, reaching near the \$140 kWh^{-1} threshold in 2024, a key driver of their competitiveness in both EVs and grid applications (Fig.

2.2b).[24] This trend highlights the effect of economies of scale, advances in manufacturing, and improvements in electrode and electrolyte materials.

Despite these advances, LIBs face several challenges. Raw material constraints, particularly relating to lithium and cobalt resources and their geographically concentrated supply chains, together with the environmental impacts of mining, processing and end-of-life disposal, raise concerns about long-term sustainability and cost. In parallel, further improvements in gravimetric and volumetric energy density (relative to existing LIB chemistries and, ultimately, to the energy content of chemical fuels), cycling stability and safety are required to meet the demands of large-scale electrification in EVs, portable electronics and stationary storage.

Taken together, these issues have prompted a move toward exploring alternative rechargeable battery chemistries that may alleviate some of the limitations of current systems. Among these, sodium-ion batteries (SIBs) are particularly attractive because sodium is far more abundant and widely distributed than lithium and can be sourced from lower-cost feedstocks. Although SIBs typically operate at somewhat lower cell voltages and energy densities than LIBs, their potential advantages in terms of raw material availability, sustainability and projected cost make them promising candidates for medium- and large-scale stationary storage and, in some cases, low- to mid-range mobility applications. Exploiting the full potential of both LIBs and SIBs hinges critically on the development of suitable electrode materials, especially high-capacity, structurally stable anodes. The following sections therefore outline the operating principles of these systems and examine the role of anode materials in determining their energy density, rate capability and lifetime.

2.2. Lithium-ion and sodium-ion batteries

LIBs and SIBs share a common “rocking-chair” architecture, in which alkali ions shuttle reversibly between two host electrodes through an ion-conducting electrolyte while electrons flow through an external circuit. A schematic representation of a typical cell configuration is shown in Fig. 2.3. The cell comprises a negative electrode (anode) and a positive electrode (cathode), each made of porous composite layers containing the active material, conductive additive and polymer binder,

cast onto metallic current collectors. The electrodes are separated by a porous polymer membrane, which is impregnated with a liquid electrolyte and prevents electrical short-circuiting while permitting ion transport between the electrodes.

For clarity throughout this thesis, electrode naming follows the convention based on their roles during discharge, which keeps the terminology consistent across the different cell configurations discussed. The anode denotes the electrode that is negative during discharge and supplies electrons to the external circuit, whereas the cathode is positive during discharge and accepts electrons. In half-cell measurements versus Li/Li^+ or Na/Na^+, the working electrode is still referred to according to its function as an anode or cathode in a full cell, unless specified otherwise.

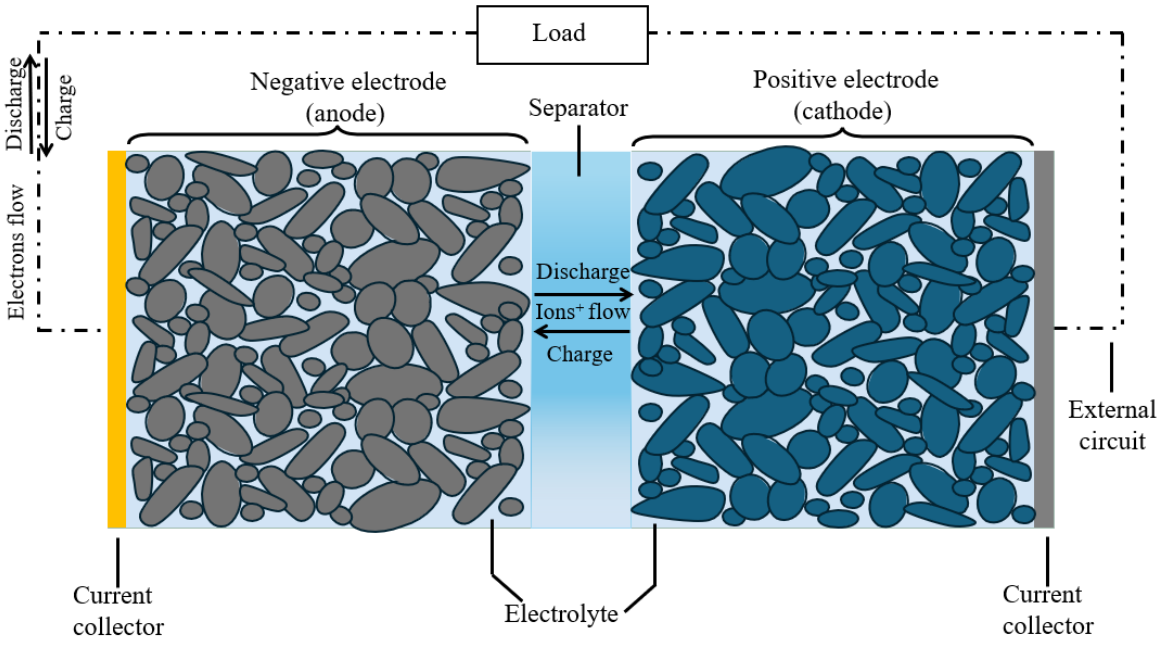

Figure 2.3. Schematic illustration of a rechargeable alkali-ion battery during discharge, showing the negative electrode (anode), positive electrode (cathode), porous separator filled with electrolyte, current collectors and external circuit.

In conventional LIBs, the cathode is commonly a lithium transition-metal oxide (e.g. $LiCoO_2$, $LiNi_xMn_yCo_zO_2$ or related layered oxides), and the anode is typically graphite.[25] The electrolyte usually consists of a lithium salt such as $LiPF_6$ dissolved in a mixture of organic carbonate solvents, providing high ionic conductivity within a wide electrochemical stability window. A microporous polyolefin separator (e.g. polypropylene or polyethylene) physically isolates the electrodes while

allowing Li^+ transport. During charge, lithium is deintercalated from the cathode and inserted into the anode; during discharge, the reverse process occurs. The half-reactions during discharge for a layered oxide cathode and graphite anode can be expressed via the reduction and the oxidation reaction shown in Eqs. (2.1) and (2.2),[25] respectively

$$Li_{1-x}M_yO_z + xLi^+ + xe^- \rightarrow LiM_yO_z \quad (2.1)$$

$$Li_xC_6 \rightarrow 6C + xLi^+ + xe^- \quad (2.2)$$

where $x < 1$, M represents one or more transition metals (e.g. Ni, Co, Mn), and O denotes oxygen. The overall cell reaction is obtained by combining Eqs. (2.1) and (2.2), with Li^+ ions shuttling through the electrolyte and electrons flowing through the external circuit to power the load. The difference in electrochemical potential between the lithiated and delithiated states of the electrodes gives rise to the cell voltage, typically in the range of 3.0 to 4.2 V for commercial LIBs.

SIBs adopt an analogous cell configuration, replacing Li^+ with Na^+ as the charge carrier while maintaining similar composite electrode, separator and electrolyte architectures. Cathode materials include layered transition-metal oxides ($Na_xM_yO_z$), polyanionic compounds (e.g. $Na_3V_2(PO_4)_3$) and Prussian blue analogues, whereas hard carbon is the most widely investigated anode material because graphite does not accommodate Na^+ to a sufficient extent under practical conditions. The electrolyte typically comprises sodium salts such as $NaPF_6$ or $NaClO_4$ dissolved in organic carbonates. During operation, Na^+ ions shuttle between the cathode and anode in a manner directly analogous to Li^+ in LIBs, and the cathode half-reaction for a layered oxide can be written in discharge direction as Eq. (2.3)[25, 26]

$$Na_{1-x}M_yO_z + xNa^+ + xe^- \rightarrow NaM_yO_z \quad (2.3)$$

while the corresponding anode reaction involves Na^+ storage within hard carbon or alloying-type hosts. Typical SIBs operate at somewhat lower average cell voltages and energy densities than LIBs. This mainly reflects the smaller electrochemical potential difference between practical Na-based cathode/anode couples, which is rooted in the more positive Na/Na^+ redox potential relative to Li/Li^+ and in the different host chemistries available for Na storage. The larger ionic radius of Na^+ further restricts the range of suitable insertion hosts and often shifts electrode operating potentials, while its greater atomic mass contributes to the lower gravimetric energy density of

SIBs; nevertheless, SIBs reliance on earth-abundant sodium and potentially lower costs makes them attractive for large-scale stationary storage and selected mobility applications.[26]

In both LIBs and SIBs, the choice and design of electrode materials strongly influence energy density, rate capability, round-trip efficiency and cycle life. In the following section we will see that the anode, in particular, plays a central role because it often limits the achievable specific capacity and can introduce safety issues such as dendrite growth or excessive volume change. The following section therefore focuses on anode materials and their ion-storage mechanisms, laying the groundwork for the subsequent discussion of alternative anode materials and their role in boosting the battery capacity.

2.3. Anode materials: key to enhancing battery performance

The literature has well established that electrode materials, especially anodes, hold significant promise for enhancing battery energy density when compared to cathode materials in both LIBs and SIBs.[27–30] From a general perspective, anode materials can be classified into three main categories according to their ion storage mechanisms: (1) intercalation (or insertion), [31, 32] (2) alloying, [33–36] and (3) conversion.[35–38]

Commercial LIB anodes are mainly composed of intercalating graphite, offering a theoretical capacity of approximately 370 mAh g^{-1} for LiC_6.[39] However, graphite is regarded as a thermodynamically unfavorable intercalation medium for SIBs, specifically for compounds like NaC_6 or NaC_8.[40] Theoretical studies have also indicated a reversible capacity of approximately 35 mAh g^{-1} for NaC_{64}.[41] This limited capacity is attributed to specific factors, notably the larger ionic radius of Na^+ (1.06 Å) compared to Li^+ (0.76 Å), which hinders the ion intercalation process.[42–45] As an alternative, various carbonaceous materials with larger interlayer spacings have been proposed for intercalation-type SIB anodes, with hard carbon gaining significant attention in this field.[46] Numerous efforts have been undertaken to enhance the Na storage capacity of hard carbon, including selecting appropriate precursors[47–49] and optimizing operating conditions;[50–55] however, its capacity remains inadequate for large-scale use. Additionally, carbon-based anodes exhibit relatively low reaction potentials with Li and Na, leading to dendritic deposition during charge/discharge cycles, which poses safety risks such as short circuits.[56]

Conversion-type anode materials store Li^+ or Na^+ through chemical conversion of the active phase into new products, rather than by simple ion insertion into an existing host lattice. This mechanism can provide significantly higher capacities than carbon-based anodes, although it is often accompanied by poor conductivity and limited cycling stability. Numerous studies have explored the use of these conversion-based materials as anodes.[57–62] However, despite their exceptionally high capacity, their practical application is greatly limited by low electrical conductivity and poor cycling stability.[37, 63]

Recently, alloying materials in LIBs and SIBs have attracted significant attention, largely because they can accommodate higher charge densities and are generally more cost-effective and safer than many intercalation-based alternatives. These alloy-type anodes operate through the following electrochemical reactions $M + xN \rightleftharpoons N_xM$ where N is the host alkaline element (i.e., Li or Na) and M is the alloying agent. The most widely used metals and metalloids for alloy-type anodes include silicon (Si), germanium (Ge), antimony (Sb), tin (Sn), and bismuth (Bi).[20, 64] Table 2.2 presents a summary of the main characteristics of these elements. A visual comparison of their evaluated properties in SIBs is shown in Fig. 2.4a, where a scale from 1 (least favorable) to 5 (most favorable) is used. These values are normalized according to the maximum and minimum results listed in Table 1. Additionally, theoretical capacities and volume expansions during alloying in LIBs and SIBs are compared separately in Fig. 2.4b and 2.4c, respectively.

Table 2.2. Electrochemical properties of common alloying anode materials.

Element	Alloying Compound	Theoretical Capacity (mAh g^{-1}) [65–69]	Volume Expansion (%) [65–68, 70]	Volumetric Capacity (mAh cm^{-3}) [20, 64, 66]	Electrical Conductivity (S cm^{-1}) [20, 65]	Density (g cm^{-3}) [20, 66]	Terrestrial Abundance (%) [71]	Annual Extraction (ton) [72]
Si	$Li_{22}Si_5$	4200	400	--	2.52×10^{-6}	2.33	28.2	7.20×10^6
	NaSi	954	114	2190				
Ge	$Li_{22}Ge_5$	1624	370	--	1.45×10^{-2}	5.32	1.5×10^{-4}	3.65×10^4
	NaGe	369	300	1624				
Sb	Li_3Sb	660	200	--	2.88×10^4	6.68	2×10^{-5}	1.30×10^5
	Na_3Sb	660	390	660				
Sn	$Li_{22}Sn_5$	994	340	--	9.50×10^4	7.31	2.3×10^{-4}	2.80×10^5
	$Na_{15}Sn_4$	847	423	994				
Bi	Li_3Bi	385	200	--	8.67×10^3	9.75	8.5×10^{-7}	1.02×10^4
	Na_3Bi	385	250	3800				

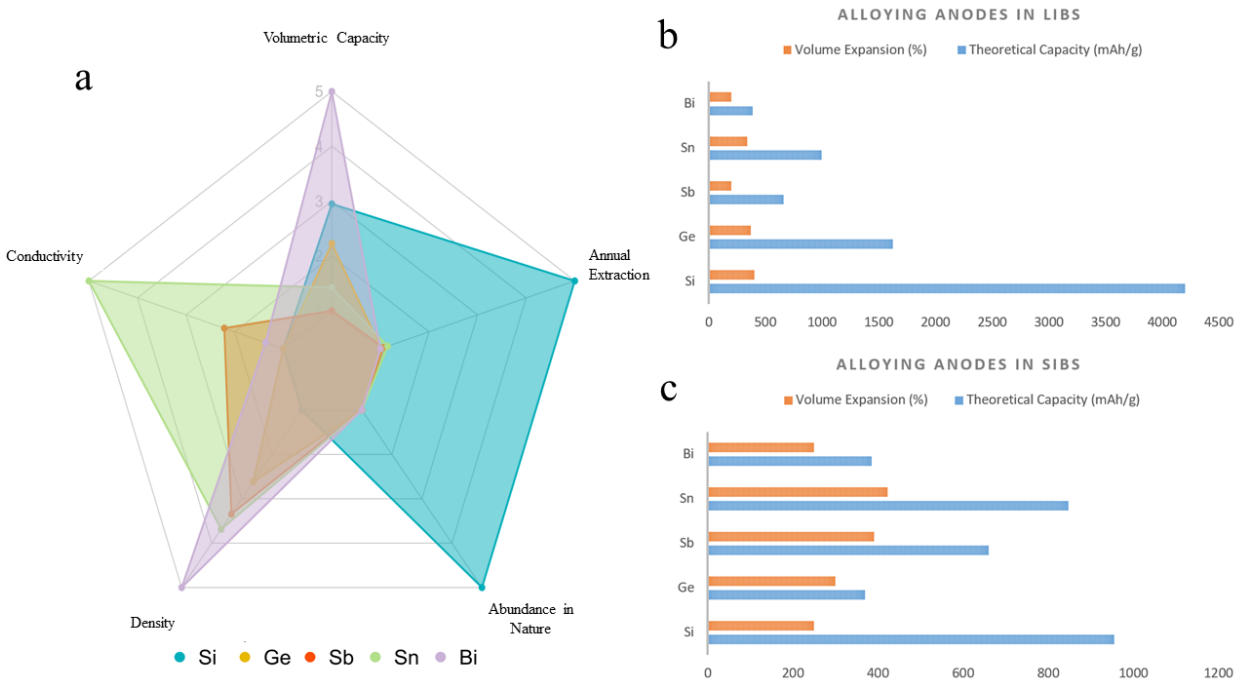

Figure 2.4. (a) Comparison of common alloying-type elements used as anode materials in SIBs, (b) and (c) theoretical capacity and volume expansion of alloying-type anodes in LIBs and SIBs.

Within this broader group, silicon is notable for its exceptionally high theoretical capacity in both lithium and sodium systems, which continues to make it a focal point of research. In addition, due to its abundance, ease of extraction, low operating potential, and environmental compatibility, Si has long been regarded as one of the most promising anode materials for LIBs, with many studies successfully demonstrating its use in high-performance LIB systems.[73–77] Although Si offers the highest theoretical capacity and the lowest volume expansion among alloy-type SIB anode materials, its use in high-performance SIBs has received limited attention. This may be due in part to the recent resurgence of interest in SIBs. Additionally, Si anodes experience significant volume changes during charge/discharge cycles, leading to severe pulverization of the material, which in turn results in capacity loss and poor cycling performance.[78, 79] Looking back at the development of Si as an anode material for LIBs, it becomes evident that nanoengineering has played a crucial role in addressing these challenges. Designing nano-structured alloys has led to improved gravimetric capacities and rate performance, enhanced resistance to fracture, reduced ion diffusion distances, and controlled volume expansion.[79–82] The review in this chapter aims to provide a

concise overview of the use of Si nanoparticles in LIBs, highlighting the strategies developed to overcome associated challenges, with the goal of offering insights and inspiration for their application in SIBs and potentially other battery systems.

2.4. Silicon in lithium-ion batteries

It is well established that Si-based anodes in LIBs face major drawbacks, including low electrical conductivity (~10^{-5} S cm^{-1}), slow ion diffusion kinetics (~10^{-14} cm^2 s^{-1}), and significant volume changes during the lithiation-delithiation process (~400%), all of which contribute to reduced overall performance.[76–78]

To address these limitations, researchers have designed advanced nanostructures. For instance, Pang et al.[83] synthesized a hollow Si@C nanostructure (Fig. 2.5a) by carbonising an emulsified precursor at 1000 °C for 2 hours with a heating rate of 10 °C min^{-1}, in which polyacrylonitrile served as the carbon source and the silicon phase was introduced separately as the templated core, followed by HF etching to generate the hollow architecture. This nanocomposite maintained a specific capacity of 700 mAh g^{-1} at 0.25 A g^{-1} after 100 cycles. More recently, Ma et al.[84] developed a yolk-shell Si@void@C nanoparticle structure embedded within a 3D carbon network (Fig. 2.5b to 2.5d). Their synthesis involved UV illumination of a water-oil microemulsion, followed by freeze-drying and hydrothermal treatment. This yolk-shell design achieved a high capacity of 1160 mAh g^{-1} at 0.3 A g^{-1} after 300 cycles. The strong performance of these hollow structures highlights their effectiveness in accommodating the volume expansion of pure silicon. In a more recent study, Zhang et al.[85] employed titanium nitride (TiN) as a coating layer (Fig. 2.6a) to construct a yolk-shell-like Si@TiN nanocomposite (Fig. 2.5e and 2.5f). This composite demonstrated a reversible capacity of 2047 mAh g^{-1} at 1 A g^{-1} after 180 cycles and a discharge capacity of 903 mAh g^{-1} at a high current density of 12 A g^{-1} (Fig. 2.6b to 2.6d). The unique yolk-shell structure effectively buffers the volume expansion of Si nanoparticles during repeated cycling, while the conductive TiN shell enhances electronic conductivity, contributing to the material's outstanding cycling stability.

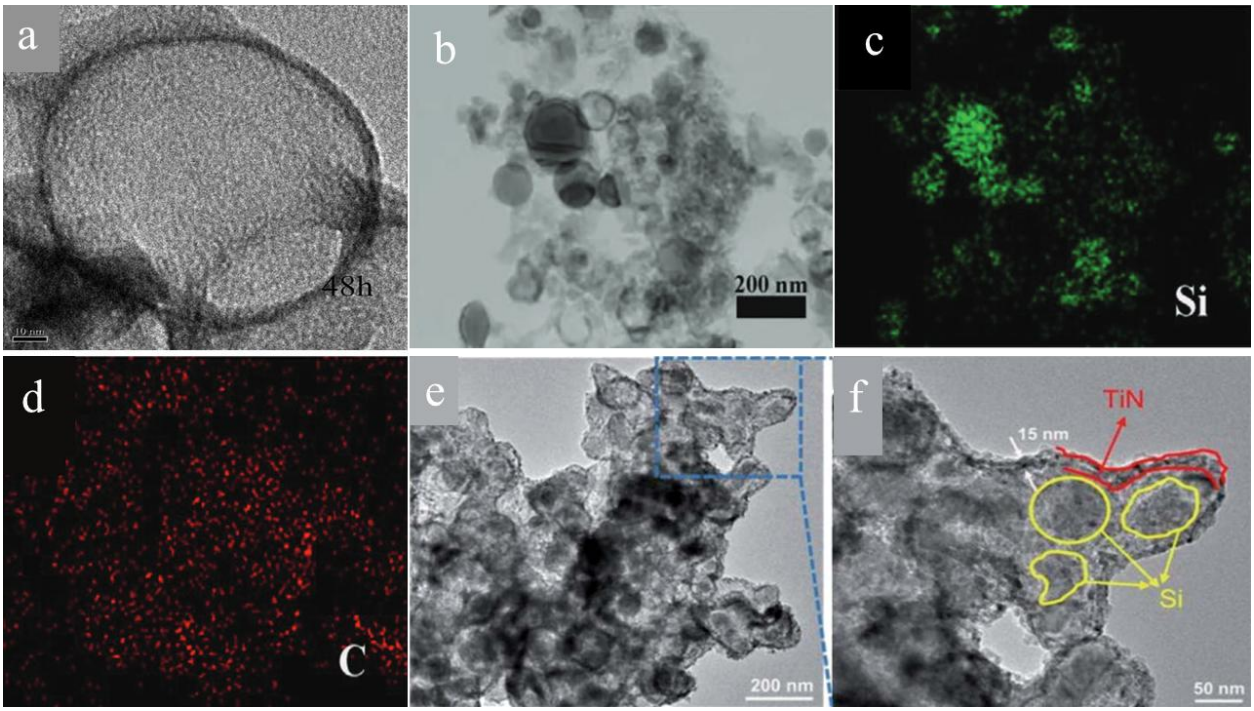

Figure 2.5. (a) TEM image of hollow Si@C after 48h of HF etching. Reprinted with permission.[83] Copyright 2015, Royal Society of Chemistry. (b)-(d) STEM image of Si@void@C/C and corresponding elemental mapping of Si and C. Reprinted with permission.[84] Copyright 2021, John Wiley and Sons. (e) and (f) STEM image of Si@TiN. Reprinted under terms of the CC-BY-NC 3.0 license.[85] Copyright 2022, Royal Society of Chemistry.

It is important to emphasize, however, that despite the success of these nanocomposites in reducing anode volume expansion, their large-scale production remains challenging. This is mainly due to high manufacturing costs and low initial Coulombic efficiency (ICE), the latter being attributed to the high surface area of nanomaterials, which increases their reactivity with electrolytes.[86–90]

In recent years, various strategies have been developed to reduce manufacturing costs, primarily by replacing pure silicon with more affordable alternatives. The upcoming sections outline these approaches and the materials involved.

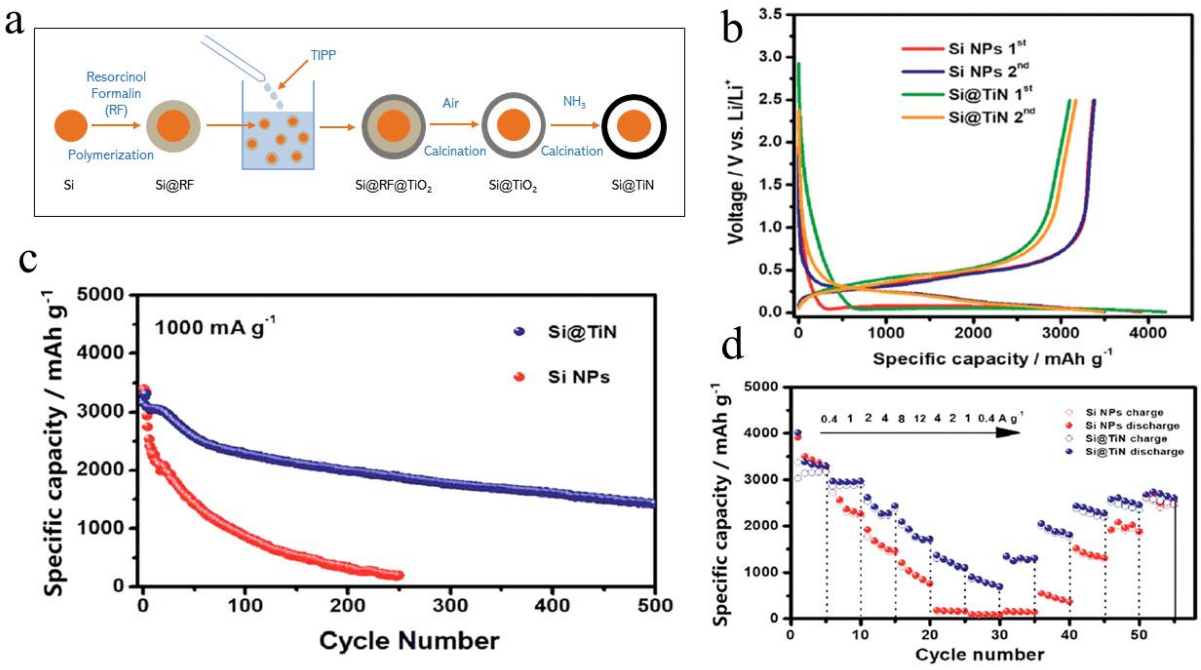

Figure 2.6. (a) Graphical depiction of the synthesis of the yolk-shell Si@TiN composite. Reproduced under terms of the CC-BY-NC 3.0 license.[85] Copyright 2022, Royal Society of Chemistry. (b) The first and second galvanostatic charge/discharge profile, (c) cycling performance at a current density of 1 Ag^{-1}, and (d) rate performance of the Si-NPs and Si@TiN samples. Reprinted under terms of the CC-BY-NC 3.0 license.[85] Copyright 2022, Royal Society of Chemistry.

2.4.1. Silicon monoxide

Silicon oxides have emerged as promising alternatives to elemental Si, owing to their high abundance, low cost, simple synthesis process, and relatively reduced volume expansion.[90] Silicon monoxide (SiO), in particular, has attracted significant interest as an anode material for LIBs. Incorporating carbon as a matrix or scaffold to reinforce the SiO structure can help buffer volume changes and enhance the electrical conductivity of the anode. Ohzuku et al.[91] developed a SiO/C composite (Fig. 2.7a) containing 50 wt% SiO combined with carbon fiber (9 wt%), deposited carbon (20 wt%), and graphite (21 wt%). This composite delivered a discharge capacity of 700 mAh g^{-1} after 100 cycles at 0.5 C. When used as the anode in a 14500 full cell paired with a $LiCo_{1/3}Ni_{1/3}Mn_{1/3}O_2/LiCoO_2$ cathode, the group reported a capacity of 200 mAh g^{-1} at a current

density of 1 A g^{-1} after 300 cycles.[92] Liu et al.[93] employed a chemical vapor deposition (CVD) method to fabricate SiO coated with graphene (Fig. 2.7b). This composite achieved an impressive capacity of 1600 mAh g^{-1} and an initial Coulombic efficiency of 95% after 100 cycles at 0.32 A g^{-1}. The high capacity was credited to the composite's unique structure, which ensured stable electrical contact, enhanced ion diffusion, and effectively buffered volume expansion.

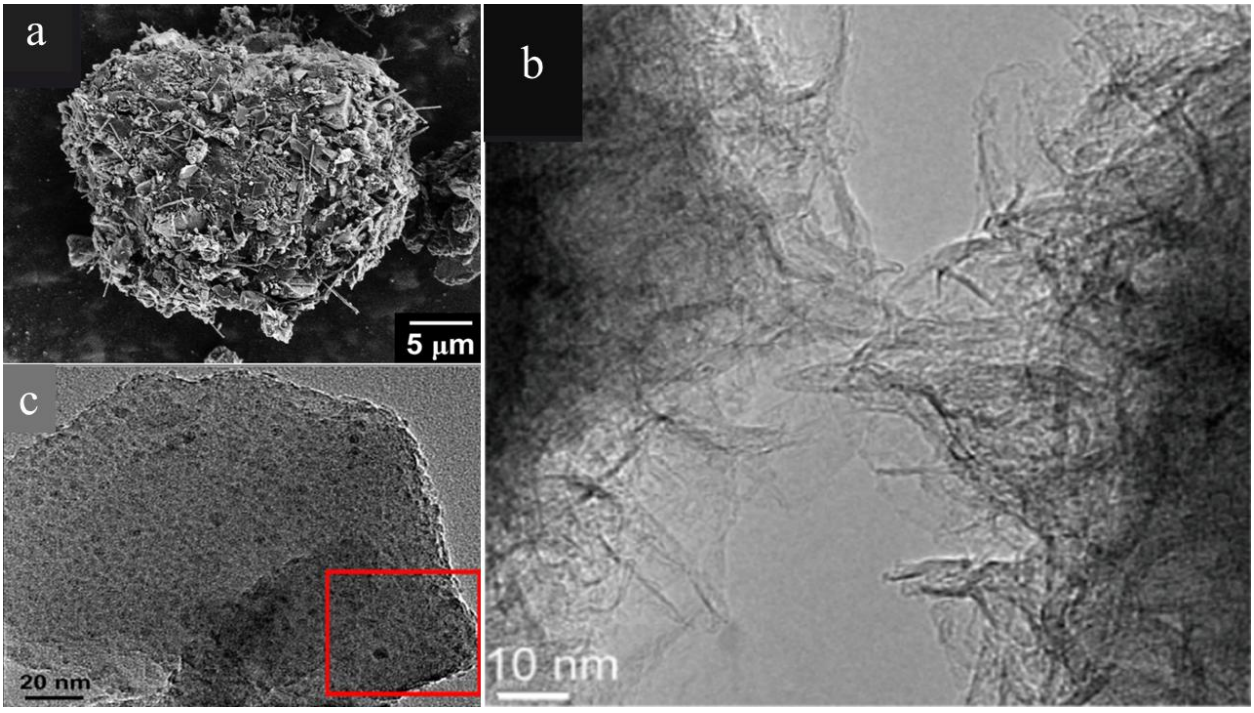

Figure 2.7. (a) SEM image of SiO/C composite. Reprinted with permission.[91] Copyright 2011, IOPscience. (b) TEM image of connected particles of graphene coated on SiO. Reprinted with permission.[93] Copyright 2017, American Chemical Society. (c) HRTEM image of SiO/Fe_2O_3 composite. Reprinted with permission[94]. Copyright 2013, Elsevier.

Various metals and metal oxides have also been incorporated into SiO anodes to improve lithium storage performance. Wang et al.[94] used mechanical milling to synthesize a SiO/Fe_2O_3 composite (Fig. 2.7c), which achieved a capacity of 600 mAh g^{-1} at a current density of 4.8 A g^{-1}, retaining 71% of its capacity after 50 cycles. Amine et al.[95] applied ultrahigh energy ball milling to create an advanced SiO/$Sn_xCo_yC_z$ anode composite. A blend of 50 wt% $Sn_{30}Co_{30}C_{40}$ with 50 wt% SiO exhibited a stable capacity of 900 mAh g^{-1} at 0.3 A g^{-1}. By replacing Co with Fe, they later

developed a series of SiO/$Sn_xFe_yC_z$ composites. Among them, the SiO/$Sn_{30}Fe_{30}C_{40}$ composition also delivered a capacity of 900 mAh g^{-1} at the same current density (0.3 A g^{-1}).[96] Miyachi et al.[97] investigated the effects of Ti, Ni, and Fe doping on SiO. Their findings revealed an 84% ICE for SiO doped with 25 wt% Ni, and an impressive 100% ICE for Ni-doped SiO with added lithium. In a study conducted by Yamamura and coworkers[98], SiO was uniformly coated with Fe_2SiO_4 by heating at 800 °C for 3 hours under an Ar atmosphere, resulting in an anode with an ICE of 89.3%.

2.4.2. Silicon dioxide

Silicon dioxide (SiO_2), primarily found in the Earth's crust as a crystalline polymorph, requires nanoparticle engineering to fully achieve its theoretical capacity of 1965 mAh g^{-1} as an anode material.[99–101] To reduce the particle size of bulk SiO_2, Liang et al.[102] applied ball milling over different durations. The anode prepared from SiO_2 milled for 24 hours (Fig. 2.8a) achieved a capacity of 602 mAh g^{-1} at 0.1 A g^{-1} over 150 cycles, with an ICE of approximately 55% and a capacity retention of 99.8% relative to the second cycle. SiO_2 has also actively been incorporated into more complex nanostructures. For example, Favors and coworkers[103] employed a hard-template growth method to synthesize SiO_2 nanotubes (Fig. 2.8b), which delivered a discharge capacity of 1247 mAh g^{-1} after 100 cycles at a 0.5 C-rate. However, the ICE of 43.3% highlights the need for significant improvement. More recently, Ma et al.[104] synthesized a hierarchically porous multi-shell hollow SiO_2 structure (Fig. 2.8c) using a sacrificial template approach with Na_2SiO_3 as the precursor. When applied as an anode material, the resulting hollow spheres delivered a capacity of 750 mAh g^{-1} after 500 cycles at a current density of 0.1 A g^{-1}.

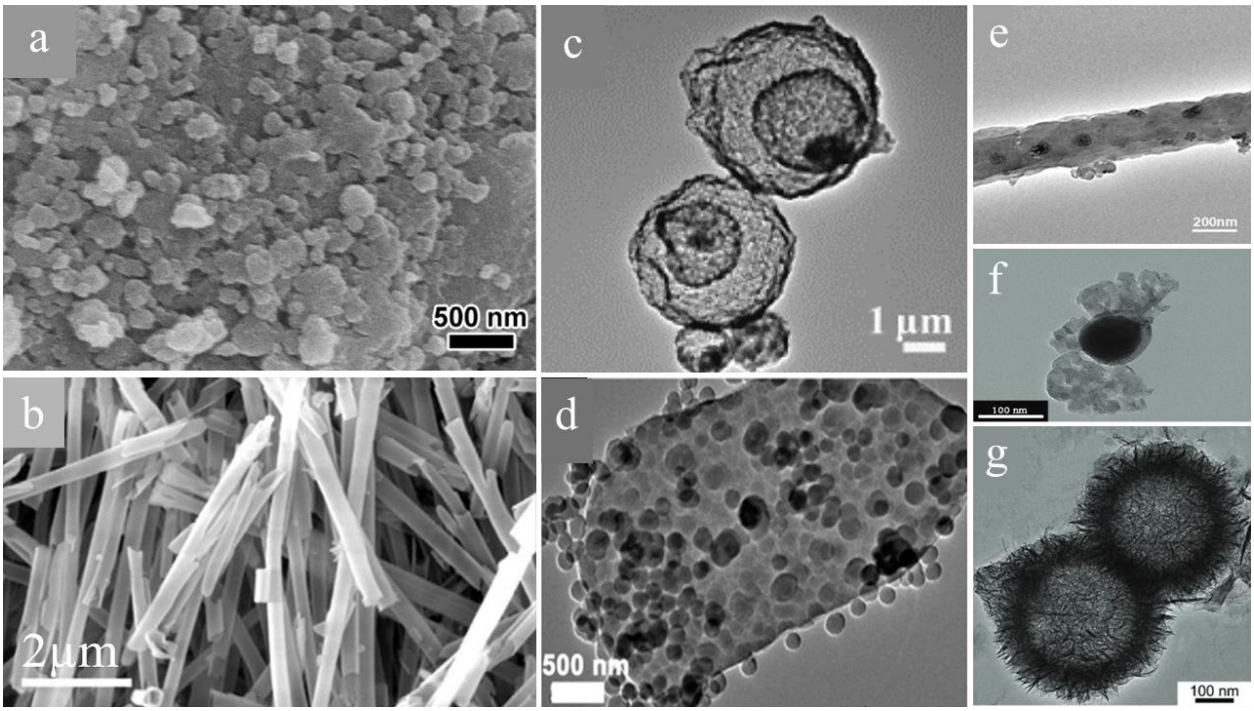

Figure 2.8. (a) FESEM image of the SiO_2 samples with 24h ball milling. Reprinted with permission.[102] Copyright 2017, Elsevier. (b) SEM image of SiO_2 nano tubes. Reprinted under terms of the CC license.[103] Copyright 2014, Springer Nature. (c) TEM image of multi-shell hollow SiO_2 spheres. Reprinted with permission.[104] Copyright 2017, Elsevier. (d) SEM image of plum-pudding like SiO_2/graphite. Reprinted with permission.[105] Copyright 2015, Royal Society of Chemistry. (e) TEM image of SiO_2/C nanofibers. Reprinted with permission.[106] Copyright 2015, Elsevier. (f) TEM image of SiO_2@CYB. Reprinted with permission.[107] Copyright 2021, John Wiley and Sons. (g) TEM image of Ni/SiO_2 hollow spheres. Reprinted with permission[108]. Copyright 2018, John Wiley and Sons.

Given that SiO_2 possesses the lowest electrical conductivity among silicon oxides, substantial efforts have been devoted to combining it with carbon to enhance its electrochemical performance.[105–112] Zhang et al.[105] fabricated a plum-pudding nanostructure consisting of SiO_2 nanospheres embedded in flake graphite using a hydrothermal method (Fig. 2.8d). The resulting composite demonstrated a discharge capacity of 702 mAh g^{-1} after 100 cycles at a current density of 0.1 A g^{-1}, along with an impressive Coulombic efficiency of 99%. Wu et al.[106] synthesized SiO_2/C nanofibers (Fig. 2.8e) by incorporating ~30 nm SiO_2 nanoparticles into polyacrylonitrile (PAN) via electrospinning, followed by carbonization at 800 °C for 2 hours with a heating rate of 2 °C min^{-1}. Anodes fabricated from nanofibers containing 15% silica exhibited a reversible capacity of 658 mAh g^{-1} after 100 cycles at a current density of 0.05 A g^{-1}. To enhance the

reversible capacity of SiO_2 anodes, Wang et al.[107] developed a yarn-ball-like structure composed of nanoscale SiO_2 entangled with carbon wires (Fig. 2.8f) through a polycondensation reaction between citric acid and ethylene glycol. The resulting composite, SiO_2@CYB, effectively mitigated volume expansion and improved electrical conductivity, achieving a first discharge capacity of 1297 mAh g^{-1} at 0.1 A g^{-1} with an initial Coulombic efficiency of 94%. However, the exact mechanisms behind the formation of the carbon-yarn-ball structure remain unclear. Yan et al.[113] synthesized hollow porous SiO_2 nanocubes using a two-step hard-template method (Fig. 2.9.a and 2.9.b). This nanocomposite achieved a reversible capacity of 919 mAh g^{-1} over 30 cycles (Fig. 2.9c to 2.9e), showing stable performance beyond the 12th cycle. The favorable electrochemical behavior is attributed to the unique hollow structure, which includes a spacious interior and multiple shell pockets that buffer volume changes and minimize structural stress during Li^+ insertion and extraction. These features also enhance Li^+ transport during charge and discharge. The study suggests that the formation of either permanent or reversible lithium silicates within the anode is key to sustaining long-cycle capacity, with rapid Li^+ movement facilitating the generation of Li_2O and Si, contributing to the reversibility.

It has been shown that combining SiO_2 with conductive metals can significantly improve both electrochemical activity and electrical conductivity. Zhou et al.[108] synthesized a novel SiO_2/Ni nanocomposite by reducing nickel silicate under an inert atmosphere (Fig. 2.8g). Owing to its unique structural characteristics, the composite delivered a capacity of 672 mAh g^{-1} at 0.1 A g^{-1} after 50 cycles. This approach may also be extended to fabricate other SiO_2/metal nanocomposites.

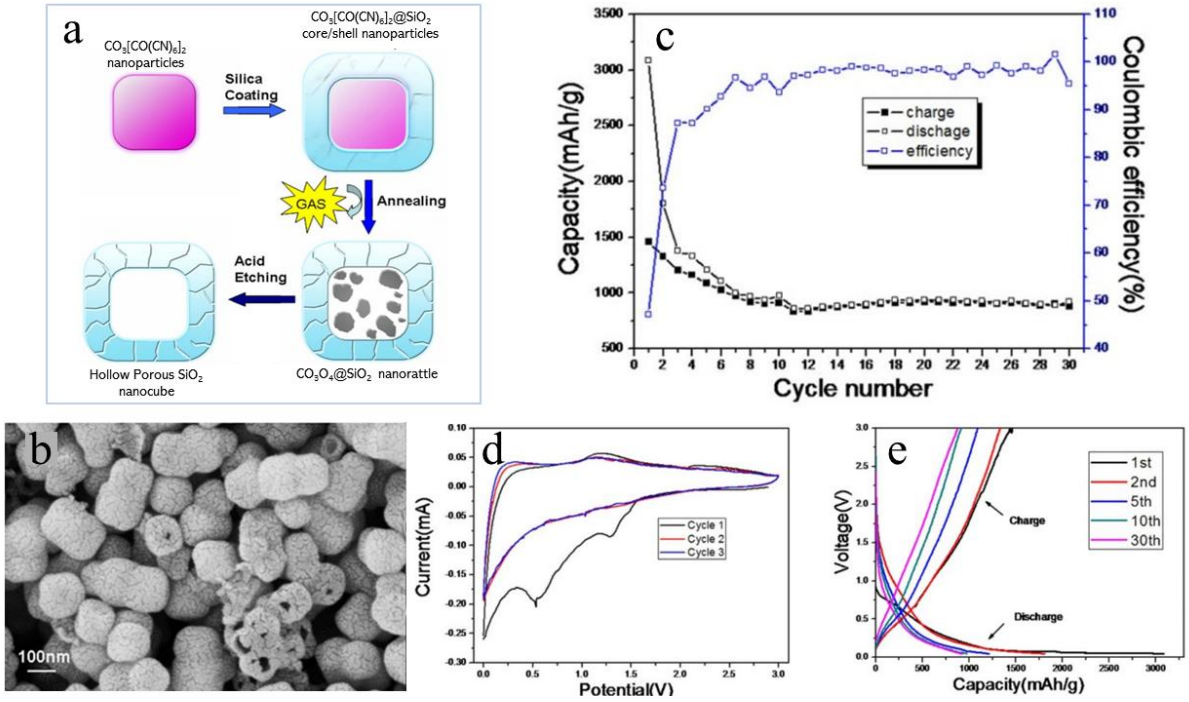

Figure 2.9. (a) Graphical depiction of the synthesis of hollow porous SiO_2 nanocube, and their (b) SEM image, (c) cycling performance at a current density of 0.1 Ag^{-1}, (d) cyclic voltammetry between 3 and 0 V at a scan rate of 0.1 mVs^{-1}, and (e) galvanostatic discharge/charge profiles. reprinted under terms of the CC-BY license.[113]

To lower costs and promote sustainability, utilizing biomass as a precursor presents several advantages. Li and colleagues[114] employed rice husks (RHs), a Si-rich biomass, to synthesize a core-shell C@SiO_2 composite. With a carbon content of 38.27 wt%, the composite delivered a capacity of 534 mAh g^{-1} after 1000 cycles at a current density of 1 A g^{-1}, equivalent to 93% of the capacity achieved using its commercial raw material counterpart. In a separate study, Li et al.[115] applied magnesiothermic reduction and additive modification to lignin-SiO_2 extracted from rice husks. The resulting composite achieved an initial discharge capacity of 2560 mAh g^{-1} at 0.1 A g^{-1}, attributed to its highly porous structure. However, the material exhibited a low ICE of 44%, likely due to its large specific surface area. Ma et al.[116] extracted sugar residues from rice husk biomass using acid hydrolysis, followed by a two-step carbonization and 12 hours of ball milling to produce a C/SiO_2 composite. When used as an anode material, the composite initially delivered a discharge capacity of 1185 mAh g^{-1} at 0.1 A g^{-1} with an initial Coulombic efficiency of 56%. Due to the

simplicity and eco-friendliness of this method, it holds potential for large-scale biomass processing, though further improvement in ICE is still needed.

2.4.3. Nonstoichiometric Silicon suboxides (SiO_x)

Nonstoichiometric silicon suboxides (SiO_x) have emerged as promising anode materials for next-generation LIBs. Specifically, Si-rich silicon suboxides (SiO_x with $x < 1$) offer high capacity but suffer from poor cycling stability, while O-rich silicon suboxides exhibit lower capacity but superior cyclic performance.[117] Yan et al.[118] integrated both Si-rich and O-rich silicon suboxides into rolled-up bilayer nanosheets (Fig. 2.10a and 2.10b). During 100 cycles of battery testing, these nanosheets delivered a specific capacity of approximately 1300 mAh g^{-1} at 0.1 A g^{-1}. The reported combination of capacity retention and cycling stability was ascribed to the Si-rich layer providing the dominant storage contribution, while the O-rich layer mitigated volume-change-induced degradation.

Sohn et al.[119] produced nanosized Si embedded within a SiO_x matrix (Fig. 2.10c) through high-energy mechanical milling (HEMM) combined with a disproportionation reaction of SiO. Their findings demonstrated that microstructural engineering of SiO can enhance lithium storage, with a 10-hour HEMM-treated sample achieving a reversible capacity of approximately 1000 mAh g^{-1}. However, the material exhibited low capacity retention over 50 cycles.

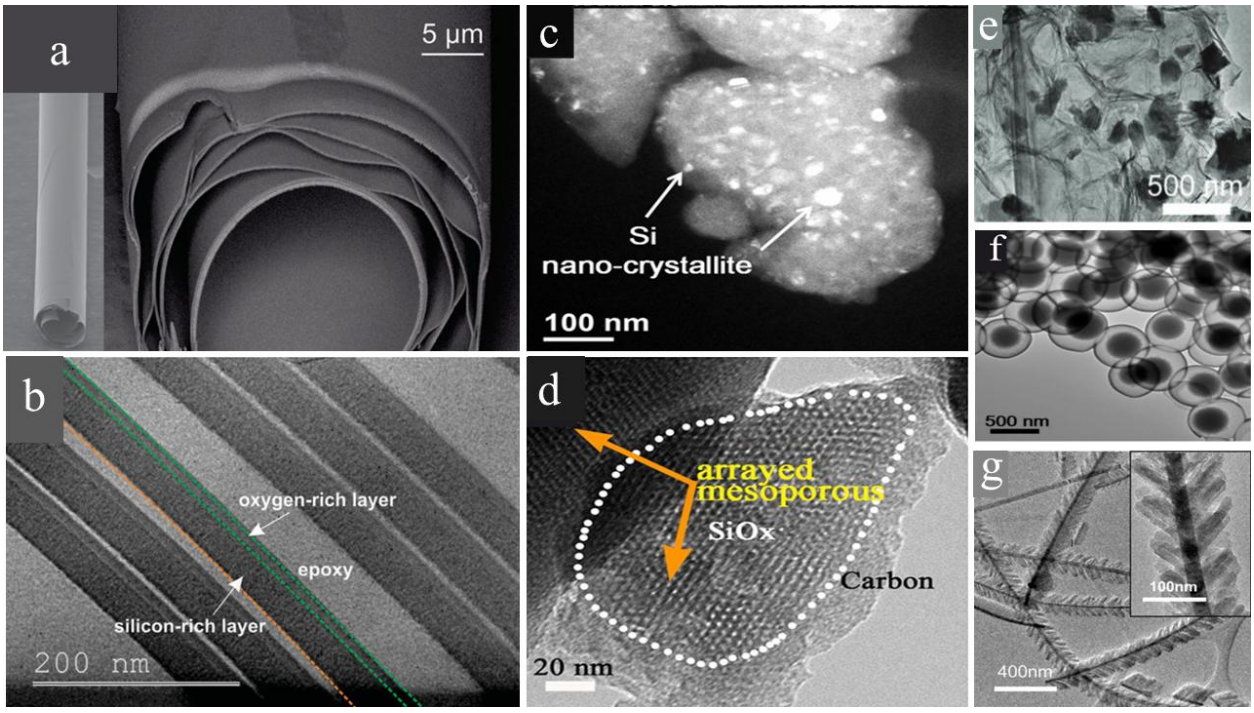

Figure 2.10. (a), (b) SEM and TEM bright-field images of rolled-up SiO_x/SiO_y bilayer nanomembrane. Reprinted with permission.[118] Copyright 2014, John Wiley and Sons. (c) dark field TEM image of 10h-HEMM $Si@SiO_x$. Reprinted with permission.[119] Copyright 2013, Elsevier. (d) TEM image of mesoporous SiO_x/C composite. Reprinted with permission.[120] Copyright 2014, IOPscience. (e) $SiO_x@G$ composite. Reprinted with permission.[121] Copyright 2018, John Wiley and Sons. (f) TEM image of SiO_x/C-CVD. Reprinted with permission.[122] Copyright 2018, Elsevier. (g) TEM image of $SiO_x/NiSi_x$ nanowires. Reprinted with permission.[123] Copyright 2012, Elsevier.

SiO_x/C composites have shown superior cyclability and rate capability compared to unmodified SiO_x, primarily due to carbon's excellent electrical conductivity and its effectiveness in buffering volume changes during cycling. Zhao et al.[120] fabricated a SiO_x/C composite with an arrayed mesoporous structure (Fig. 2.10d), where the oxygen content was set at $x = 1.2$. The designed achieved a capacity of 780 mAh g^{-1} after 350 cycles at a current density of 0.1 A g^{-1}, with a minimal capacity decay rate of 0.02% per cycle. Xu et al.[121] engineered a $SiO_x@G$ composite (Fig. 2.10e) by encapsulating SiO_x nanoparticles within a self-assembled graphene bubble sheet. After 1000 cycles at a current density of 1 A g^{-1}, the composite maintained a capacity of 780 mAh g^{-1}, corresponding to 80% of its initial capacity. Liu et al.[122] employed a combination of sol-gel processing, selective etching, and chemical vapor deposition (CVD) to coat semi-graphitic

carbon on both the inner and outer surfaces of SiO_x, forming a yolk@shell-like SiO_x/C structure (Fig. 2.10f). This engineered nanostructure delivered a capacity of 972 mAh g^{-1} after 500 cycles at 1 A g^{-1}. When paired with a $LiCoO_2$ cathode, the full cell achieved an impressive energy density of 428 Wh kg^{-1}.

Similar to the integration of metals with SiO and SiO_2, SiO_x has also been combined with metals to enhance performance and cycling stability. Jo and coworkers[123] utilized SiH_4 CVD and thermal evaporation to grow SiO_x/$NiSi_x$ nanowires (Fig. 2.10g). These nanowires showed an impressive initial discharge capacity of 4058 mAh g^{-1} at 0.15 A g^{-1} with an initial Coulombic efficiency of 43%, eventually stabilizing at 800 mAh g^{-1} after 100 cycle. Table 2.3 offers additional insights into the electrochemical performance of various Si-based anodes employed in LIBs. It should be noted that the electrochemical performance values reported in the literature are not always directly comparable, as they are strongly influenced by differences in electrode formulation, active-material loading, electrolyte composition, voltage window, current density, cell design, and testing protocol. As a result, the reported capacities and cycle-life data should be interpreted primarily as indicative of the potential of each material design rather than as strictly reproducible benchmark values across different studies.

Table 2.3. Electrochemical performance of some of Si-based anodes used in LIBs.

Composite - Reference	Composite microscopic view	Reversible cap ($mAhg^{-1}$) / cycle num	Discharge rate/ current	Cap retention (%)	ICE (%)
porous SiO_x - Image reprinted with permission.[124] Copy right 2014, Elsevier.	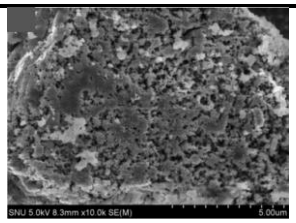	1242 / 100	0.1 C for 1st cycle & 0.2 C for following cycles	46.8	64.4
Li/SiO - Image reprinted with permission.[125] Copyright 2016, Elsevier.	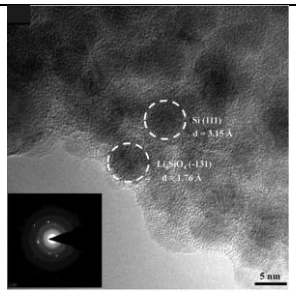	750 / 15	0.02 C	61.4	82.12

Hollow Porous SiO_2 - nanocubes Image reprinted under terms of the CC-BY license.[113] Copyright 2013, Springer Nature.	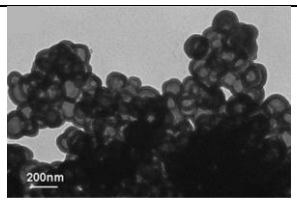	919 / 30	0.1 Ag^{-1}	29.7	47
hollow SiO_2/C nanospheres - Image reprinted with permission.[126] Copyright 2017, Elsevier.	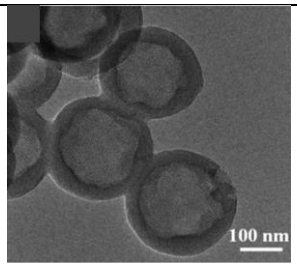	441 / 500	0.5 Ag^{-1}	50	68
C/SiO_2/C - Image reprinted under terms of the CC-BY license.[127] Copyright 2015, Royal Society of Chemistry.	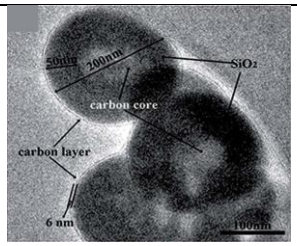	1055 / 150	0.5 Ag^{-1}	41.4	56.5
SiO_2/C-N - Image reprinted with permission.[128] Copyright 2015, Royal Society of Chemistry.	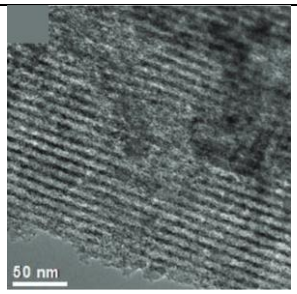	800 / 100	0.2 Ag^{-1}	27.5	42
porous SiO_2/C - Image reprinted with permission.[129] Copyright 2014, Elsevier.	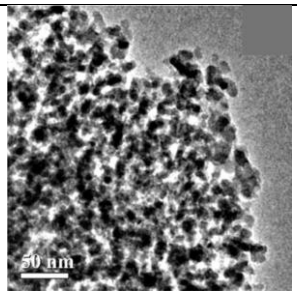	210 / 30	1 Ag^{-1}	78.6	59
SiO_2 nanospheres - Image reprinted with permission.[130] Copyright 2014, American Chemical Society.	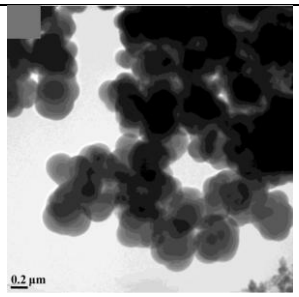	876.7 / 500	1 C	50.8	54.8

SiO_2 - Image reprinted with permission.[131] Copyright 2012, Royal Society of Chemistry.	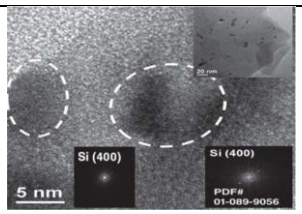	800 / 200	0.1 Ag^{-1}	35.6	37
FeSi@Si/SiO_x - Image reprinted with permission.[132] Copyright 2017, Elsevier.	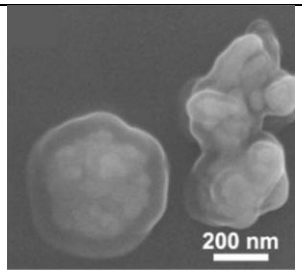	727 / 600	0.2 Ag^{-1}	46.9	51.8
3D SiO_x/C@RGO - Image reprinted with permission.[133] Copyright 2014, Royal Society of Chemistry.	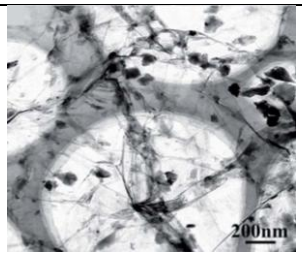	1284 / 100	0.1 Ag^{-1}	53.4	51
Si/SiO_x/C - Image reprinted with permission.[134] Copyright 2014, American Chemical Society.	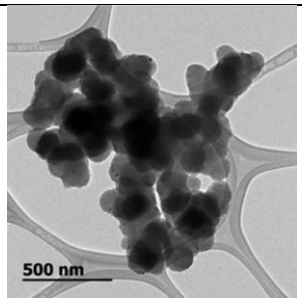	740 / 100	0.2 Ag^{-1}	45.4	58.4

2.5. Silicon in sodium-ion batteries

Similar to LIBs, alloy-type materials have been shown to offer the highest specific capacities among anode candidates for high-energy SIBs.[135–137] Among alloy-type materials for SIB anodes, phosphorus offers the highest theoretical specific capacity of 2560 mAh g^{-1} by forming the Na_3P alloy phase. However, its extremely low electrical conductivity (~10^{-14} S cm^{-1}), significant volume expansion (>300%), and notable safety concerns hinder its practical application in commercial batteries.[136–138] In comparison, silicon provides a theoretical capacity of 954 mAh g^{-1} in SIBs by

forming the binary phase NaSi, while exhibiting a relatively low volume expansion of just 114%, which is the smallest among all alloy-type anode materials for SIBs.[139–141] Given its distinctive properties, silicon stands out as a highly promising candidate for next-generation SIBs, warranting further in-depth investigation into its application. A review of its use in LIB anodes reveals that earlier studies offer valuable guidance for designing Si-based anodes and addressing key challenges such as limited electrical conductivity. With slight modifications, these design strategies could be effectively adapted for Si-based anodes in SIB systems.

To begin with, it is important to note that first-principles calculations have shown crystalline silicon (c-Si) to be electrochemically inactive with elemental sodium, primarily due to its high sodiation energy barrier.[142, 143] In contrast, amorphous silicon (a-Si) exhibits a significantly lower sodiation energy barrier than crystalline Si (c-Si),[144] making it a more favorable candidate and the focus of several research studies. For example, Xu et al.[145] investigated the reversible Na-ion storage behavior of Si nanoparticles containing both crystalline (c-Si) and amorphous (a-Si) phases (Fig. 2.11a). When cycled at 0.02 A g^{-1}, the resulting SIB demonstrated a reversible capacity of 248 mAh g^{-1} after 100 cycles. More recently, Jangid et al.[146] fabricated Si nanowires (Fig. 2.11b) featuring a crystalline Si (c-Si) core and an amorphous Si (a-Si) shell. These nanowires delivered a capacity of 125 mAh g^{-1} after 100 cycles at a current rate of C/10.

Several studies have explored the development of buffering structures for SIB anodes. For example, Han et al.[147] synthesized sponge-like amorphous silicon (a-Si) (Fig. 2.11c) by reacting magnesium powder with silicon tetrachloride. When used as an anode in SIBs and cycled at 0.1 A g^{-1}, the material achieved a reversible capacity of 176 mAh g^{-1} after 100 cycles. Huang et al.[148] reported a capacity of 152 mAh g^{-1} at 0.5 A g^{-1} for their rolled-up amorphous silicon (a-Si) nanomembranes (Fig. 2.11d), maintaining 85% of the capacity after extended cycling over 2000 cycles.

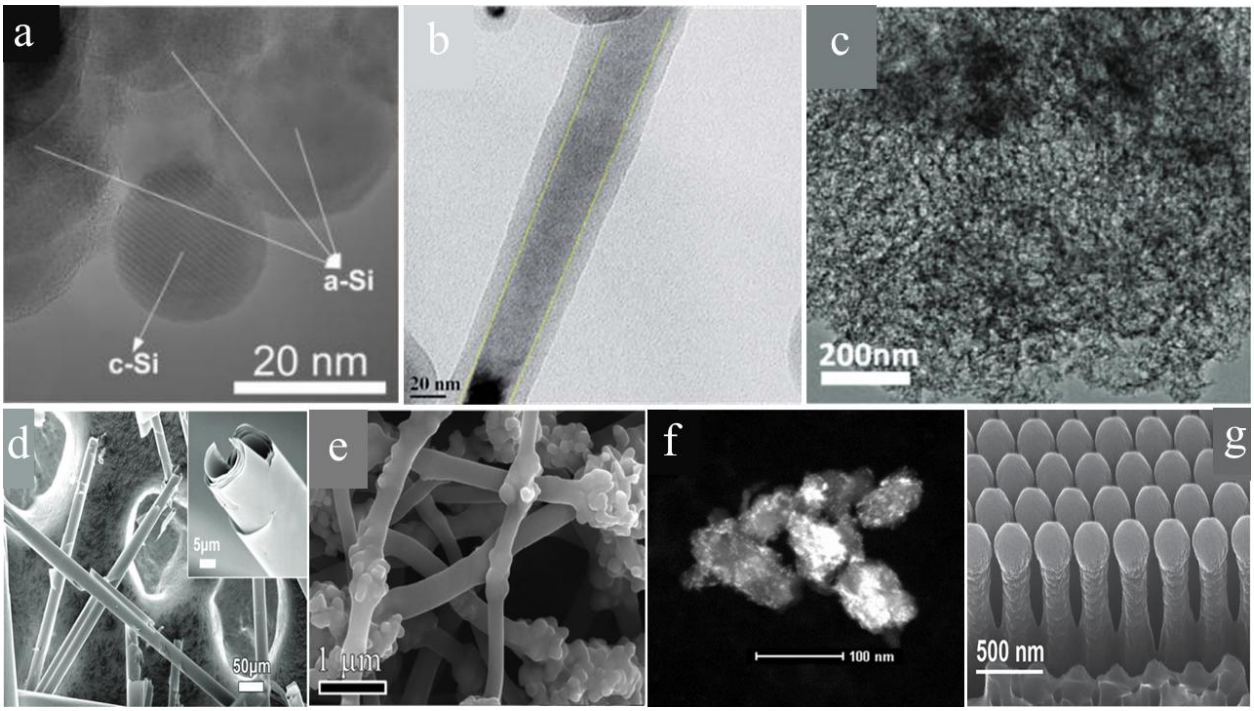

Figure 2.11. (a) High-resolution TEM image of as-prepared Si nanoparticles. Reprinted with permission.[145] Copyright 2016, John Wiley and Sons. (b) TEM image of a-Si shell/ c-Si core nanowires. Reprinted with permission.[146] Copyright 2018, Royal Society of Chemistry. (c) TEM image of the prepared a-Si. Reprinted with permission.[147] Copyright 2018, Royal Society of Chemistry. (d) SEM image of rolled-up a-Si. Reprinted with permission.[148] Copyright 2018, John Wiley and Sons. (e) fabricated bamboo-rattle-like structure of Si/C. Reprinted with permission.[139] Copyright 2017, John Wiley and Sons. (f) dark-field SEM image of Sn coated a-Si. Reprinted with permission.[149] Copyright 2016, Elsevier. (g) SEM image of the Si/TiN/Ti/Ge nanorods. Reprinted with permission.[150] Copyright 2015, John Wiley and Sons.

Rather than using bare a-Si, some studies have incorporated silicon oxides into their synthesis methods. Zhang et al.[139] employed electrospinning, carbonization, and HF treatment to create a bamboo-rattle-like structure composed of yolk-shell C/Si nanobeads embedded within carbon nanofibers (Fig. 2.11e). This composite demonstrated a reversible capacity of 454 mAh g^{-1} at 0.05 A g^{-1} after 200 cycles. Chandra et al.[151] successfully enhanced the capacity of a silicon oxycarbide (SiOC) anode to 287 mAh g^{-1} by employing an ether-based electrolyte, with testing conducted at a current density of 0.025 A g^{-1}.

Several studies have investigated the combination of amorphous silicon (a-Si) with other alloying metals. A notable example is the work by Lim et al.,[149] who fabricated a Sn-coated a-Si composite (Fig. 2.11f) that delivered a capacity of 140 mAh g^{-1} at a C/20 rate after 5 cycles. Yue et al.[150]

Also, Yue et al.[150] fabricated hexagonal match-like Si/Ge nanorods buffered by TiN/Ti interlayering medium (Fig. 2.11g) via a cost-effective approach. After 200 cycles at 0.4 Ag^{-1}, a reversible capacity of 390 $mAhg^{-1}$ and an ICE of 50% was recorded for their composite.

As can be seen, the body of research on Si-based anodes for SIBs is comparatively limited. Several factors contribute to this disparity, as outlined below:

- **Technology maturity**: Since their commercialization in the 1990s, LIBs have become the leading energy storage solution for portable electronics, electric vehicles, and various other applications.[152] This widespread adoption has driven extensive research focused on performance enhancement, including the development of high-capacity materials like silicon. In contrast, SIBs are still emerging and have not yet reached a comparable level of technological maturity or commercial deployment. As a result, research into advanced anode materials such as Si for SIBs remains relatively limited.
- **Electrochemical behavior of Si in SIBs**: In LIBs, the alloying of silicon with lithium enables high theoretical specific capacities, making Si-based anodes highly attractive. However, in SIBs, the alloying reaction between silicon and sodium is significantly less favorable and, as previously discussed, is largely restricted to amorphous silicon (a-Si).[144] This limited reactivity reduces the potential performance gains, which may discourage researchers from pursuing Si-based anode development for SIBs.
- **Initial focus of SIBs**: A primary driver behind the development of SIBs has been the goal of offering a more cost-effective alternative to LIBs by utilizing the abundance and wide availability of sodium.[153] As a result, both early and ongoing research in the field has largely prioritized the use of inexpensive, readily available materials, particularly for cathodes, such as layered oxide compounds.[154–158] This focus has limited the exploration of more advanced and costly materials like silicon for anode development.
- **Research funding and commercial interests**: The commercial success and widespread use of LIBs have attracted significant research funding aimed at enhancing their performance. In contrast, SIBs are still in the early stages of development and have yet to achieve the same level of market adoption.[159, 160] Consequently, there are fewer financial and industrial resources dedicated to the advancement of SIB technologies, including the investigation of high-performance materials such as Si-based anodes.

- **Infrastructure and expertise**: Due to the commercial dominance of LIBs, research infrastructure, technical expertise, and academic focus have largely been aligned with LIB-related advancements. This established momentum naturally supports continued exploration of materials such as Si nanoparticles. In contrast, newer technologies like SIBs require time to develop dedicated resources and expertise, which can delay progress and limit the investigation of advanced materials like Si for their anodes.

While the current gap in Si-focused research between LIBs and SIBs can be attributed to the factors outlined above, it is important to recognize that as SIB technology advances and gains commercial relevance, interest in exploring high-performance anode materials such as silicon is expected to grow, driving further innovation and performance improvements in SIBs.

Given the growing interest in utilizing Si-based anodes for SIBs and drawing on insights from their application in LIBs, we identify several key factors that must be addressed to enhance the practical sodium storage capacity of Si-NP anodes and support their scalability.

2.5.1. Volume fluctuations

The volume expansion of the anode leads to particle fragmentation, triggering repeated formation of the SEI layer. This process consumes Na^+ ions, thereby reducing the available capacity. Incorporating hollow porous structures can improve the anode's mechanical resilience during sodiation/desodiation by providing internal void space to accommodate silicon's expansion. These voids act as buffers, minimizing particle fracture and helping preserve structural integrity. However, while such structures support electrical connectivity and long-term cycling stability, the presence of void space may lower the active material density, potentially decreasing overall energy storage. Thus, a careful balance between mechanical durability and energy density is essential when designing hollow structures.

Another approach to addressing volume expansion is embedding Si nanoparticles (Si-NPs) within a flexible carbonaceous matrix. This matrix can serve as both a structural scaffold and a protective coating, limiting direct contact between Si-NPs and the electrolyte, thereby reducing excessive SEI formation. Given hard carbon's excellent sodium storage properties,[54, 161–164] incorporating

Si-NPs into such a medium could offer added advantages. Although hard carbon is increasingly favored as a SIB anode material, its use for hosting Si-NPs has not yet been reported as of this review. The limited progress in this area may stem from factors such as conductivity mismatches, electrolyte compatibility issues, incomplete understanding of Na storage mechanisms in hard carbon, manufacturing challenges, cost considerations, and scalability concerns.

Utilizing Si nanoparticles in the form of suboxides, rather than as pure Si, presents several advantages; most notably reduced volume expansion. As previously noted in LIB studies, Si suboxides experience less expansion than pure silicon, which helps lower mechanical stress and improve anode durability. Their cost-effectiveness also supports more financially feasible production and scaling of SIBs, potentially aiding broader adoption. While Si suboxides have a lower theoretical capacity, their oxygen content can be adjusted through various reduction techniques. This tunability allows for a balanced compromise between minimizing volume change and maintaining capacity, enabling optimized anode performance.

2.5.2. Electrolyte compatibility

Side reactions between the electrolyte and silicon lead to undesirable SEI formation, which in turn reduces the effective sodium storage capacity of the anode.[165] Exploring and applying electrolytes with tailored additives that remain stable over a wide potential range can help suppress side reactions and promote the formation of a stable, thin SEI layer. Broadly, to enable high capacity, long-term stability, and structural adaptability in SIBs, the electrolyte must exhibit these critical characteristics:[166–168]

- Ionic conductivity exceeding 0.1 mS cm^{-1}at room temperature and higher,
- High Na^{+} transference number with minimal electronic transference,
- Wide electrochemical stability range,
- Robust mechanical and thermal resilience,
- Long-term durability to maintain performance under operational conditions,
- Environmental safety and sustainability, and
- Cost- effectiveness for practical large-scale applications.

Furthermore, the development of durable solid-state electrolytes offers additional benefits, particularly in addressing safety issues associated with conventional liquid electrolytes.[169]

2.5.3. Sodium related kinetic limitations

The larger ionic radius of Na^+ compared to Li^+ can lead to slower diffusion within the anode structure.[43] To address this, engineered Si architectures with high specific surface areas (such as porous Si, Si nanowires, nanotubes, or hollow spheres) can be employed to shorten Na^+ diffusion paths, thereby improving the kinetics of sodium insertion and extraction.

2.5.4. Incomplete alloying

During standard battery operation, the conversion to NaSi may remain incomplete, leading to partial alloying and reduced capacity. As in LIBs, improving the extent of alloying in SIBs can be achieved by optimizing electrode fabrication parameters and employing binders specifically suited to withstand the alloying and dealloying processes.[159, 170]

2.5.5. Silicon from biomass-based materials

One of the main drivers for developing SIBs is to create a cost-effective energy storage alternative. In this context, incorporating high-cost materials (such as certain Si nanocomposites) may at times contradict the goal of affordability. A promising strategy to reduce Si production costs involves using biomass as a precursor for Si-based materials. Depending on the processing method and biomass source, this approach can yield a substantial amount of silicon. Rice husks, in particular, are a well-established example due to their high silica content and successful application as a Si precursor in LIBs.[114–116]

The production of biomass-derived silicon typically begins with acid washing to eliminate impurities, followed by a reduction process to convert silica into silicon. Depending on the specific

preparation method, the resulting silicon may appear as amorphous silicon (a-Si) or silicon nanoparticles (Si-NPs), often embedded within a carbonaceous matrix.[116] Since this silicon originates from an abundant, low-cost source, it aligns well with the cost-efficiency goals driving SIB development. It also should be noted that although the biomass precursor is abundant and low-cost, the overall cost of biomass-derived silicon depends on the specific processing route, as reduction and purification can introduce additional expense and complexity. Its main advantage therefore lies in the use of an inexpensive and widely available starting material, rather than in guaranteeing a low-cost final process.

2.5.6. Silicon-based alloys and heteroatom doping

Alloying silicon with metals that possess higher electrical conductivity can enhance electrochemical stability, leading to more consistent and prolonged charge/discharge cycling. This approach helps mitigate the rapid capacity degradation commonly observed with pure silicon anodes. Examples of such hybrid nanocomposites are porous Si/silver nanostructures used in high-performance photovoltaic devices[171] , SiO_2/Ni nanocomposite used in LIBs anodes,[108] and Si/Ge nanorods in SIBs anodes.[150] Furthermore, heteroatom doping has been employed to enhance the electrical conductivity of anode composites and to adjust the interlayer spacing of hard carbon, thereby improving ion transport and overall electrochemical performance.[49, 172–175] These alloying and doping strategies present promising opportunities for further investigation and application in the development of high-performance Si-based anodes.

2.6. Biomass-derived anodes: a sustainable alternative

2.6.1. Sustainability and cost motivation

The rapid expansion of lithium-ion and sodium-ion battery technologies has sharpened the focus on the sustainability and cost of electrode materials. Conventional anode materials are typically synthesised from high-purity petrochemical precursors or mined minerals using energy-intensive

processing routes, which contribute significantly to the overall environmental footprint and cost of batteries.[176] At the same time, the agricultural and forestry sectors generate large volumes of lignocellulosic residues that are often underutilised or disposed of by combustion, leading to greenhouse-gas and particulate emissions.[177]

Biomass-derived anodes offer a route to mitigate these issues by turning low-value waste streams into functional carbonaceous or silica/carbon materials. Many types of biomass are rich in carbon and, in some cases, contain significant amounts of inorganic components such as silica or alkali salts, which can be exploited as in situ templates or precursors for composite anodes.[177] The use of such resources aligns with circular-economy principles, reduces dependence on fossil-derived precursors and can lower the energy and cost associated with electrode production. These advantages are particularly relevant for large-scale stationary storage, where cost per kilowatt-hour is a primary driver, and for emerging sodium-ion technologies that aim to leverage earth-abundant elements.

2.6.2. Biomass-derived hard carbon anodes

Hard carbon is a non-graphitising form of carbon characterised by a highly disordered structure, turbostratic stacking, relatively large interlayer spacing and a combination of micro-, meso- and macroporosity. These features make hard carbon a promising anode material for both LIBs and SIBs, enabling ion storage through a combination of adsorption at defect sites, filling of nanopores and limited interlayer insertion.[176] Biomass precursors are particularly attractive for hard carbon production because they are renewable, widely available and, after appropriate heat treatment, can yield carbons with tailored porosity and structural disorder.

A broad range of biomass sources has been investigated, including nut shells, fruit peels, wood, straw, seaweed and pitch-based residues.[177, 178] For LIBs, biomass-derived hard carbons typically deliver reversible capacities in the range of 300 to 400 mAh g^{-1} at moderate current densities, often with sloping voltage profiles extending down to 0.01 to 0.05 V vs Li/Li^+. In SIBs, they have emerged as the leading anode class, with typical reversible capacities of 250 to 350 mAh g^{-1} and good cycling stability at average potentials of 0.1 to 0.2 V vs Na/Na^+.[176] The electrochemical

performance is strongly influenced by the precursor composition and the carbonisation temperature, which together determine the extent of graphitic ordering, defect density, pore size distribution and surface area.

From a mechanistic perspective, biomass-derived hard carbons often exhibit a characteristic combination of a sloping region at higher potentials and a low-potential plateau in Na-ion cells. The former is attributed to adsorption of Na^+ at defects, edges and heteroatom sites, while the latter is associated with Na^+ filling of closed nanopores or interlayer spaces in the disordered carbon matrix. Careful control of porosity and surface area is required: excessive microporosity can lead to high irreversible capacity and unstable solid-electrolyte interphase (SEI) formation, whereas too little closed porosity suppresses the plateau capacity that is desirable for high energy density.[176]

Biomass-derived hard carbons therefore provide a versatile platform for tuning structure and performance through selection of the precursor and optimisation of thermal treatment. However, most reported systems rely purely on the carbon component of the biomass, without exploiting any intrinsic inorganic phases, such as silica, that could enable multifunctional composite anodes.

2.6.3. Biomass-derived SiO_2/C and Si-containing composites

Silica-rich biomasses, such as rice husks, horsetail plants and certain grasses, offer an additional opportunity: they can serve simultaneously as carbon sources and as precursors for silicon- or silica-containing phases.[160] Controlled thermal treatment and selective etching of these precursors can yield SiO_2/C or Si/C composites in which the inorganic phase is finely dispersed within a conductive carbon matrix. In the context of LIBs, such composites have attracted attention as alternatives to pure silicon because the silica or sub-stoichiometric silicon oxides can buffer volume changes and form stable Li_2O or Li_4SiO_4 matrices during cycling, while the carbon provides electronic conductivity and additional storage sites.

Reported biomass-derived SiO_2/C anodes for LIBs typically deliver reversible capacities in the range of 400 to 800 mAh g^{-1}, with improved capacity retention compared with nanostructured silicon alone.[179] The enhanced stability is commonly attributed to the rigid yet ion-conductive silica framework and the intimate contact between the oxide phase and carbon, which together

accommodate the strain associated with alloying reactions and help stabilise the SEI. In some systems, partial reduction of SiO_2 during carbonisation or post-treatment introduces active silicon domains that further increase capacity while remaining mechanically supported by the surrounding matrix.[176]

For SIBs, the exploration of biomass-derived Si or SiO_2-containing anodes is still at an early stage. A few recent works have demonstrated that dispersing Si or SiO_2 nanoparticles derived from biomass within a hard carbon matrix can promote more homogeneous Na^+ storage and mitigate pulverisation, but the range of precursors and processing strategies remains limited.[180] Overall, existing reports indicate that silica-rich biomass can be transformed into multifunctional composite anodes that combine the advantageous features of hard carbon and SiO_2-based phases, yet systematic investigations of structure-property relationships and cross-chemistry comparisons between LIBs and SIBs are scarce.

2.6.4. Barley husks as a multifunctional biomass precursor

Barley husk is an abundant agricultural by-product generated in large quantities by the brewing and malting industries. Global barley production exceeds 140 million tonnes per year, and the associated husk fraction represents a substantial, low-cost residue with limited high-value applications.[181] Chemically, barley husk consists primarily of lignocellulosic components (cellulose, hemicellulose and lignin) together with a significant fraction of silica and minor inorganic species, making it inherently suitable as a dual-source precursor for both carbon and SiO_2.[181]

Systematic exploitation of barley husk as a multifunctional precursor for battery anodes remains limited in this field. In particular, there is a lack of comprehensive work on: (i) the relationship between carbonisation conditions, resultant hard carbon structure and Li/Na storage behaviour; (ii) the role of the naturally embedded silica in forming SiO_2/C frameworks; and (iii) the comparative performance of barley-husk-derived anodes in LIB and SIB half-cells and full cells.

Given its combined carbon and silica content, barley husk presents a promising platform for designing anodes that integrate hard carbon domains with SiO_2-based phases in a single, low-cost

precursor. Tailoring the thermal treatment and post-processing routes offers the possibility to adjust the balance between graphitic ordering, porosity and silica distribution, thereby tuning specific capacity, rate capability and cycling stability. Addressing the above-mentioned gaps through detailed structural and electrochemical characterisation is central to the experimental work presented in the following chapters, which investigates barley husk-derived hard carbons and SiO_2/C composites as anode materials for both lithium-ion and sodium-ion batteries.

2.7. Conclusion

This chapter has reviewed the role of rechargeable lithium-ion and sodium-ion batteries in modern energy storage, with particular emphasis on how anode materials govern energy density, rate capability and cycle life. Conventional graphite anodes perform well in LIBs but are unsuitable for most SIB systems, which has stimulated the exploration of alternative intercalation, alloying and conversion-type materials. Silicon and silicon oxides offer very high theoretical capacities and have been intensively studied in LIBs, while more recent work has evaluated their potential in SIBs, revealing substantial challenges related to volume change, reaction kinetics and electrolyte compatibility. In parallel, biomass-derived hard carbons and silica/carbon composites have emerged as promising low-cost, sustainable anodes, especially when obtained from silica-rich precursors.

Despite this progress, several important gaps remain. The coupled structural and electrochemical roles of carbon and silica in biomass-derived anodes are not yet fully understood, particularly with regard to how precursor composition and processing conditions influence pore structure, SEI formation and Li^+/Na^+ storage mechanisms. Comparative studies of lithium- and sodium-ion storage in anodes derived from the same biomass are scarce, and very few investigations provide a comprehensive analysis combining galvanostatic cycling with cyclic voltammetry, rate capability tests, impedance spectroscopy and differential capacity analysis. Moreover, barley husk, although abundant and intrinsically rich in both carbon and silica, has received limited attention as a multifunctional precursor for SiO_2/C-based anodes in either LIBs or SIBs.

The subsequent chapters address these gaps by (i) developing synthesis routes to obtain hard carbon and SiO_2/C composites from barley husk, (ii) systematically characterising their structural, textural and chemical properties, and (iii) evaluating their performance and storage mechanisms as anodes in lithium-ion and sodium-ion cells. Together, these studies aim to establish barley husk as a sustainable, high-value feedstock for next-generation anode materials and to clarify the interplay between biomass-derived carbon matrices and silica-based phases in dual-chemistry battery systems.

2.8. References

[1] C. Xu, Y. Gao. *Energy* 2025,316,134453.

[2] T. Kober, H.W. Schiffer, M. Densing, E. Panos. *Energy Strategy Reviews* 2020,31,100523.

[3] J.L. Holechek, H.M.E. Geli, M.N. Sawalhah, R. Valdez. *Sustainability* 2022,14,4792.

[4] D.D. Gvozdenac, B.D. Gvozdenac-Urošević, Z.K. Morvaj. *Thermal Science* 2025,29,713–730.

[5] A. Aghahosseini, A.A. Solomon, C. Breyer, T. Pregger, S. Simon, P. Strachan, A. Jäger-Waldau. *Appl Energy* 2023,331,120401.

[6] N.A. Sepulveda, J.D. Jenkins, A. Edington, D.S. Mallapragada, R.K. Lester. *Nat Energy* 2021,6,506–516.

[7] M.I. Khan, F. Asfand, S.G. Al-Ghamdi. *J Energy Storage* 2022,55,105860.

[8] A. Blakers, M. Stocks, B. Lu, C. Cheng. *Progress in Energy* 2021,3,022003.

[9] T.M. Gür. *MRS Bulletin* 2021,46,1153–1163.

[10] G. Smdani, M.R. Islam, A.N. Ahmad Yahaya, S.I. Bin Safie. *Energy and Environment* 2023,34,1094–1141.

[11] A.A. Kebede, T. Kalogiannis, J. Van Mierlo, M. Berecibar. *Renewable and Sustainable Energy Reviews* 2022,159,112213.

[12] International Energy Agency. *IEA publication*.

[13] D.G. Madden, D. O'Nolan, et al. *J Am Chem Soc* 2022,144,13729–13739.

[14] Y. Kojima. *Int J Hydrogen Energy* 2019,44,18179–18192.

[15] A.B. Bocarsly, E. Niangar. *ECS Trans* 2008,16,1285–1291.

[16] K. Charoen, C. Prapainainar, P. Sureeyatanapas, T. Suwannaphisit, K. Wongamornpitak, P. Kongkachuichay, S.M. Holmes, P. Prapainainar. *J Clean Prod* 2017,142,1309–1320.

[17] L.E. Caceres-Martinez, J. Saavedra Lopez, R.A. Dagle, R. Gillespie, H.I. Kenttämaa, G. Kilaz. *Fuel* 2024,358,129986.

[18] J.A. Otero, R.D. Santiago-Acosta, R. Pérez-Álvarez, E.M. Hernández-Cooper. *Appl Therm Eng* 2025,274,126448.

[19] D. Stampatori, P.P. Raimondi, M. Noussan. *Energies (Basel)* 2020,13,2638.

[20] G. Li, S. Guo, B. Xiang, S. Mei, Y. Zheng, X. Zhang, B. Gao, P.K. Chu, K. Huo. *Energy Materials* 2022,2,200020.

[21] F. Mohammadi, M. Saif. *e-Prime - Advances in Electrical Engineering, Electronics and Energy* 2023,3,100127.

[22] A.G. Olabi, C. Onumaegbu, T. Wilberforce, M. Ramadan, M.A. Abdelkareem, A.H. Al – Alami. *Energy* 2021,214,118987.

[23] M. Yao, Y. Chen, Z. Wang, C. Shao, J. Dong, Q. Zhang, L. Zhang, X. Zhao. *Chemical Engineering Journal* 2020,395,124057.

[24] S. Orangi, N. Manjong, D.P. Clos, L. Usai, O.S. Burheim, A.H. Strømman. *J Energy Storage* 2024,76,109800.

[25] G. Pistoia, B. Liaw Editors, 'Behaviour of Lithium-Ion Batteries in Electric Vehicles: Battery Health Performance Safety and Cost'. 2018.

[26] Y. Tian, G. Zeng, A. Rutt, T. Shi, H. Kim, J. Wang, J. Koettgen, Y. Sun, B. Ouyang, T. Chen, Z. Lun, Z. Rong, K. Persson, G. Ceder. *Chemical Reviews* 2021,121,1623–1669.

[27] L. Zhai, G. Li, X. Yang, S. Park, D. Han, L. Mi, Y. Wang, Z. Li, S.Y. Lee. *Adv Funct Mater* 2022,32,2108798.

[28] K. Mishra, N. Yadav, S.A. Hashmi. *J Mater Chem A Mater* 2020,8,22507–22543.

[29] J.U. Choi, N. Voronina, Y.K. Sun, S.T. Myung. *Adv Energy Mater* 2020,10,2002027.

[30] X. Pu, H. Wang, D. Zhao, H. Yang, X. Ai, S. Cao, Z. Chen, Y. Cao. *Small* 2019,15,1805427.

[31] B. Xiao, T. Rojo, X. Li. *ChemSusChem* 2019,12,133–144.

[32] T. Perveen, M. Siddiq, N. Shahzad, R. Ihsan, A. Ahmad, M.I. Shahzad. *Renewable and Sustainable Energy Reviews* 2020,119,109549.

[33] S. Liang, Y.J. Cheng, J. Zhu, Y. Xia, P. Müller-Buschbaum. *Small Methods* 2020,4,2000218.

[34] H. Tan, D. Chen, X. Rui, Y. Yu. *Adv Funct Mater* 2019,29,1808745.

[35] L. Wang, J. Świątowska, S. Dai, M. Cao, Z. Zhong, Y. Shen, M. Wang. *Mater Today Energy* 2019,11,46–60.

[36] H. Zhang, I. Hasa, S. Passerini. *Adv Energy Mater* 2018,8,1702582.

[37] C. Wu, S.X. Dou, Y. Yu. *Small* 2018,14,1703671.

[38] Y. Lu, L. Yu, X.W. (David) Lou. *Chem* 2018,4,972–996.

[39] X. Li, Y. Wang, L. Lv, G. Zhu, Q. Qu, H. Zheng. *Energy Materials* 2022,2,200014.

[40] P.C. Tsai, S.C. Chung, S.K. Lin, A. Yamada. *J Mater Chem A Mater* 2015,3,9763–9768.

[41] P. Ge, M. Fouletier. *Solid State Ion* 1988,28–30,1172–1175.

[42] P.C. Tsai, S.C. Chung, S.K. Lin, A. Yamada. *J Mater Chem A Mater* 2015,3,9763–9768.

[43] L.F. Zhao, Z. Hu, W.H. Lai, Y. Tao, J. Peng, Z.C. Miao, Y.X. Wang, S.L. Chou, H.K. Liu, S.X. Dou. *Adv Energy Mater* 2021,11,2002704.

[44] Q.-H. Zhang, Jun and Wang, Da-Wei and Lv, Wei and Qin, Lei and Niu, Shuzhang and Zhang, Siwei and Cao, Tengfei and Kang, Feiyu and Yang. *Adv Energy Mater* 2018,8,1801361.

[45] G. Li, K. Chen, Y. Wang, Z. Wang, X. Chen, S. Cui, Z. Wu, C. Soutis, W. Chen, L. Mi. *Nanoscale* 2020,12,8493–8501.

[46] Y. Kim, Yongil and Kim, Jae-Kwang and Vaalma, Christoph and Bae, Geun Hyeong and Kim, Guk-Tae and Passerini, Stefano and Kim. *Carbon N Y* 2018,129,564–571.

[47] M. Saavedra, L. Simonin, C. Matei, C. Vaulot, S. Perez, C. Dupont. *Fuel Processing Technology* 2022,231,107223.

[48] X. Li, Yunming and Xu, Shuyin and Wu, Xiaoyan and Yu, Juezhi and Wang, Yuesheng and Hu, Yong-Sheng and Li, Hong and Chen, Liquan and Huang. *J Mater Chem A Mater* 2015,3,71–77.

[49] C. Wu, Feng and Liu, Lu and Yuan, Yifei and Li, Yu and Bai, Ying and Li, Tao and Lu, Jun and Wu. *ACS Appl Mater Interfaces* 2018,10,27030–27038.

[50] D. Chen, W. Zhang, K. Luo, Y. Song, Y. Zhong, Y. Liu, G. Wang, B. Zhong, Z. Wu, X. Guo. *Energy Environ Sci* 2021,14,2244–2262.

[51] Y. Sun, Fei and Wang, Hua and Qu, Zhibin and Wang, Kunfang and Wang, Lijie and Gao, Jihui and Gao, Jianmin and Liu, Shaoqin and Lu. *Adv Energy Mater* 2021,11,2002981.

[52] C. Wu, Feng and Zhang, Minghao and Bai, Ying and Wang, Xinran and Dong, Ruiqi and Wu. *ACS Appl Mater Interfaces* 2019,11,12554–12561.

[53] T.-P. Mehmood, Asad and Ali, Ghulam and Koyutuerk, Burak and Pampel, Jonas and Chung, Kyung Yoon and Fellinger. *Energy Storage Materials2* 2020,28,101–111.

[54] B. Sun, Ning and Guan, Zhaoruxin and Liu, Yuwen and Cao, Yuliang and Zhu, Qizhen and Liu, Huan and Wang, Zhaoxiang and Zhang, Peng and Xu. *Adv Energy Mater* 2019,9,1901351.

[55] J. Xiao, Lifen and Lu, Haiyan and Fang, Yongjin and Sushko, Maria L and Cao, Yuliang and Ai, Xinping and Yang, Hanxi and Liu. *Adv Energy Mater* 2018,8,1703238.

[56] H. Hou, X. Qiu, W. Wei, Y. Zhang, X. Ji. *Adv Energy Mater* 2017,7,1602898.

[57] H. Chang, Y.-R. Wu, X. Han, T.-F. Yi. *Energy Materials* 2022,1,100003.

[58] K. Chen, G. Li, Z. Hu, Y. Wang, Z. Wang, N. Qin, X. Chen, W. Chen, Z. Wu, C. Soutis, L. Mi. *Energy and Fuels* 2021,35,6265–6271.

[59] X. Xiong, C. Yang, G. Wang, Y. Lin, X. Ou, J.H. Wang, B. Zhao, M. Liu, Z. Lin, K. Huang. *Energy Environ Sci* 2017,10,1757–1763.

[60] X. Ou, L. Cao, X. Liang, F. Zheng, H.S. Zheng, X. Yang, J.H. Wang, C. Yang, M. Liu. *ACS Nano* 2019,13,3666–3676.

[61] C. Yang, X. Liang, X. Ou, Q. Zhang, H.S. Zheng, F. Zheng, J.H. Wang, K. Huang, M. Liu. *Adv Funct Mater* 2019,29,1807971.

[62] L. Cao, X. Liang, X. Ou, X. Yang, Y. Li, C. Yang, Z. Lin, M. Liu. *Adv Funct Mater* 2020,30,1910732.

[63] T.L. Kulova, A.M. Skundin. *Energies (Basel)* 2022,15,8615.

[64] M. Lao, Y. Zhang, W. Luo, Q. Yan, W. Sun, S.X. Dou. *Advanced Materials* 2017,29,1700622.

[65] H. Gao, W. Ma, W. Yang, J. Wang, J. Niu, F. Luo, Z. Peng, Z. Zhang. *J Power Sources* 2018,379,1–9.

[66] J. Sottmann, M. Herrmann, P. Vajeeston, Y. Hu, A. Ruud, C. Drathen, H. Emerich, H. Fjellvåšg, D.S. Wragg. *Chemistry of Materials* 2016,28,2750–2756.

[67] D. Su, S. Dou, G. Wang. *Nano Energy* 2015,12,88–95.

[68] W. Devina, H. Setiadi Cahyadi, I. Albertina, C. Chandra, J.H. Park, K. Yoon Chung, W. Chang, S. Kyu Kwak, J. Kim. *Chemical Engineering Journal* 2022,432,134276.

[69] P. Li, H. Kim, S. Myung, Y. Sun. *Energy Storage Mater* 2021,35,550–576.

[70] S.C. Jung, D.S. Jung, J.W. Choi, Y.K. Han. *Journal of Physical Chemistry Letters* 2014,5,1283–1288.

[71] D. R. Lide, ed., *CRC Handbook of Chemistry and Physics*, 97th ed., CRC Press, Boca Raton, FL, 2016–2017, section "Abundance of Elements in the Earth's Crust and in the Sea".

[72] U.S. Geological Survey, Mineral Resources Program, *Commodity Statistics and Information*, U.S. Geological Survey, 2016.

[73] A.R. Kamali, D. J. Fray. *New Mat for Electrochem Systems* 2010,13,147–160.

[74] H.K. Liu, Z.P. Guo, J.Z. Wang, K. Konstantinov. *J Mater Chem* 2010,20,10055–10057.

[75] H. Kim, E.J. Lee, Y.K. Sun. *Materials Today* 2014,17,285–297.

[76] P. Li, G. Zhao, X. Zheng, X. Xu, C. Yao, W. Sun. *Energy Storage Mater* 2018,15,422–446.

[77] L. Sun, Y. Liu, R. Shao, J. Wu, R. Jiang, Z. Jin. *Energy Storage Mater* 2022,46,482–502.

[78] C.K. Chan, H. Peng, G. Liu, K. McIlwrath, X.F. Zhang, R.A. Huggins, Y. Cui. *Nat Nanotechnol* 2008,3,31–35.

[79] Y. Liu, L. Qin, F. Liu, Y. Fan, J. Ruan, S. Zhang. *J Power Sources* 2018,406,167–175.

[80] J. Liu, Y. Yang, P. Lyu, P. Nachtigall, Y. Xu. *Advanced Materials* 2018,30,1800838.

[81] T. Xu, D. Wang, P. Qiu, J. Zhang, Q. Wang, B. Xia, X. Xie. *Nanoscale* 2018,10,16638–16644.

[82] B. Wang, X. Li, B. Luo, L. Hao, M. Zhou, X. Zhang, Z. Fan, L. Zhi. *Advanced Materials* 2015,27,1526–1532.

[83] C. Pang, H. Song, N. Li, C. Wang. *RSC Adv* 2015,5,6782–6789.

[84] J. Ma, H. Tan, H. Liu, Y. Chao. *Particle and Particle Systems Characterization* 2021,38,1–9.

[85] T. Zhang, C. Chen, X. Bian, B. Jin, Z. Li, H. Xu, Y. Xu, Y. Ju. *RSC Adv* 2022,12,19678–19685.

[86] D. Lin, Z. Lu, P.C. Hsu, H.R. Lee, N. Liu, J. Zhao, H. Wang, C. Liu, Y. Cui. *Energy Environ Sci* 2015,8,2371–2376.

[87] C. Wang, H. Wu, Z. Chen, M.T. Mcdowell, Y. Cui, Z. Bao. *Nat Chem* 2013,5,1042–1048.

[88] S.W. Lee, M.T. McDowell, J.W. Choi, Y. Cui. *Nano Lett* 2011,11,3034–3039.

[89] M. Pasta, C.D. Wessells, R.A. Huggins, Y. Cui. *Nat Commun* 2012,3,1149.

[90] H. Kim, M. Seo, M.H. Park, J. Cho. *Angew Chem Int Ed* 2010,49,2146–2149.

[91] M. Yamada, A. Ueda, K. Matsumoto, T. Ohzuku. *J Electrochem Soc* 2011,158,A417.

[92] M. Yamada, K. Uchitomi, A. Ueda, K. Matsumoto, T. Ohzuku. *J Power Sources* 2013,225,221–225.

[93] L. Shi, C. Pang, S. Chen, M. Wang, K. Wang, Z. Tan, P. Gao, J. Ren, Y. Huang, H. Peng, Z. Liu. *Nano Lett* 2017,17,3681–3687.

[94] M. Zhou, M.L. Gordin, S. Chen, T. Xu, J. Song, D. Lv, D. Wang. *Electrochem commun* 2013,28,79–82.

[95] B. Liu, A. Abouimrane, Y. Ren, M. Balasubramanian, D. Wang, Z.Z. Fang, K. Amine. *Chemistry of Materials* 2012,24,4653–4661.

[96] B. Liu, A. Abouimrane, D.E. Brown, X. Zhang, Y. Ren, Z.Z. Fang, K. Amine. *J Mater Chem A Mater* 2013,1,4376–4382.

[97] M. Miyachi, H. Yamamoto, H. Kawai. *J Electrochem Soc* 2007,154,A376.

[98] H. Yamamura, S. Nakanishi, H. Iba. *J Power Sources* 2013,232,264–269.

[99] Y. Zhong, M. Yang, X. Zhou, Z. Zhou. *Mater Horiz* 2015,2,553–566.

[100] P.G. Bruce, B. Scrosati, J.M. Tarascon. *Angew Chem Int Ed* 2008,47,2930–2946.

[101] Y. Sun, N. Liu, Y. Cui. *Nat Energy* 2016,1,1–12.

[102] C. Liang, L. Zhou, C. Zhou, H. Huang, S. Liang, Y. Xia, Y. Gan, X. Tao, J. Zhang, W. Zhang. *Mater Res Bull* 2017,96,347–353.

[103] Z. Favors, W. Wang, H.H. Bay, A. George, M. Ozkan, C.S. Ozkan. *Sci Rep* 2014,4,4605.

[104] X. Ma, Z. Wei, H. Han, X. Wang, K. Cui, L. Yang. *Chemical Engineering Journal* 2017,323,252–259.

[105] H.H. Li, L.L. Zhang, C.Y. Fan, K. Wang, X.L. Wu, H.Z. Sun, J.P. Zhang. *Physical Chemistry Chemical Physics* 2015,17,22893–22899.

[106] X. Wu, Z.Q. Shi, C.Y. Wang, J. Jin. *Journal of Electroanalytical Chemistry* 2015,746,62–67.

[107] D. Wang, T. Wang, M. He, T. Wang, H. Wang. *Nano, Macro, Small* 2021,17,2103878.

[108] C. Tang, Y. Liu, C. Xu, J. Zhu, X. Wei, L. Zhou, L. He, W. Yang, L. Mai. *Adv Funct Mater* 2018,28,1704561.

[109] Y. Yao, J. Zhang, L. Xue, T. Huang, A. Yu. *J Power Sources* 2011,196,10240–10243.

[110] M. Li, Y. Yu, J. Li, B. Chen, X. Wu, Y. Tian, P. Chen. *J Mater Chem A Mater* 2015,3,1476–1482.

[111] J. Meng, Y. Cao, Y. Suo, Y. Liu, J. Zhang, X. Zheng. *Electrochim Acta* 2015,176,1001–1009.

[112] Z. Xiang, Y. Chen, J. Li, X. Xia, Y. He, H. Liu. *Journal of Solid State Electrochemistry* 2017,21,2425–2432.

[113] N. Yan, F. Wang, H. Zhong, Y. Li, Y. Wang, L. Hu, Q. Chen. *Sci Rep* 2013,3,1568.

[114] Y. Li, L. Liu, X. Liu, Y. Feng, L. Yu, Z. He, X. Cui, M. Zhang, Y. Zhu. *Ionics (Kiel)* 2022,151–160.

[115] Y. Li, L. Liu, X. Liu, Y. Feng, B. Xue, L. Yu, L. Ma, Y. Zhu, Y. Chao, X. Wang. *Mater Chem Phys* 2021,262,124331.

[116] L. Ma, L. Liu, X. Liu, Y. Li, Y. Feng, Y. Tian, Y. Chao, Y. Zhu, X. Wang. *J Electron Mater* 2021,50,4426–4432.

[117] C.Y. Chou, G.S. Hwang. *Chemistry of Materials* 2013,25,3435–3440.

[118] L. Zhang, J. Deng, L. Liu, W. Si, S. Oswald, L. Xi, M. Kundu, G. Ma, T. Gemming, S. Baunack, F. Ding, C. Yan, O.G. Schmidt. *Advanced Materials* 2014,26,4527–4532.

[119] Y. Hwa, C.M. Park, H.J. Sohn. *J Power Sources* 2013,222,129–134.

[120] C. Gao, H. Zhao, P. Lv, C. Wang, J. Wang, T. Zhang, Q. Xia. *J Electrochem Soc* 2014,161,A2216–A2221.

[121] Q. Xu, J.K. Sun, Z.L. Yu, Y.X. Yin, S. Xin, S.H. Yu, Y.G. Guo. *Advanced Materials* 2018,30,1707430.

[122] Z. Liu, Y. Zhao, R. He, W. Luo, J. Meng, Q. Yu, D. Zhao, L. Zhou, L. Mai. *Energy Storage Mater* 2019,19,299–305.

[123] K. Song, S. Yoo, K. Kang, H. Heo, Y.M. Kang, M.H. Jo. *J Power Sources* 2013,229,229–233.

[124] B.C. Yu, Y. Hwa, J.H. Kim, H.J. Sohn. *Electrochim Acta* 2014,117,426–430.

[125] J.H. Yom, S.W. Hwang, S.M. Cho, W.Y. Yoon. *J Power Sources* 2016,311,159–166.

[126] W. An, J. Fu, J. Su, L. Wang, X. Peng, K. Wu, Q. Chen, Y. Bi, B. Gao, X. Zhang. *J Power Sources* 2017,345,227–236.

[127] X. Cao, X. Chuan, R.C. Massé, D. Huang, S. Li, G. Cao. *J Mater Chem A Mater* 2015,3,22739–22749.

[128] Y. Liang, L. Cai, L. Chen, X. Lin, R. Fu, M. Zhang, D. Wu. *Nanoscale* 2015,7,3971–3975.

[129] X. Yang, H. Huang, Z. Li, M. Zhong, G. Zhang, D. Wu. *Carbon N Y* 2014,77,275–280.

[130] J. Tu, Y. Yuan, P. Zhan, H. Jiao, X. Wang, H. Zhu, S. Jiao. *Journal of Physical Chemistry C* 2014,118,7357–7362.

[131] W.S. Chang, C.M. Park, J.H. Kim, Y.U. Kim, G. Jeong, H.J. Sohn. *Energy Environ Sci* 2012,5,6895–6899.

[132] W. He, Y. Liang, H. Tian, S. Zhang, Z. Meng, W.Q. Han. *Energy Storage Mater* 2017,8,119–126.

[133] C. Guo, D. Wang, T. Liu, J. Zhu, X. Lang. *J Mater Chem A Mater* 2014,2,3521–3527.

[134] M.S. Park, E. Park, J. Lee, G. Jeong, K.J. Kim, J.H. Kim, Y.J. Kim, H. Kim. *ACS Appl Mater Interfaces* 2014,6,9608–9613.

[135] J. Qian, Y. Chen, L. Wu, Y. Cao, X. Ai, H. Yang. *Chemical Communications* 2012,48,7070–7072.

[136] W. Li, S.L. Chou, J.Z. Wang, J.H. Kim, H.K. Liu, S.X. Dou. *Advanced Materials* 2014,26,4037–4042.

[137] C. Chen, K. Fu, Y. Lu, J. Zhu, L. Xue, Y. Hu, X. Zhang. *RSC Adv* 2015,5,30793–30800.

[138] Y. Kim, Y. Park, A. Choi, N.S. Choi, J. Kim, J. Lee, J.H. Ryu, S.M. Oh, K.T. Lee. *Advanced Materials* 2013,25,3045–3049.

[139] L. Zhang, X. Hu, C. Chen, H. Guo, X. Liu, G. Xu, H. Zhong, S. Cheng, P. Wu, J. Meng, Y. Huang, S. Dou, H. Liu. *Advanced Materials* 2017,29,1604708.

[140] D.H. Nam, T.H. Kim, K.S. Hong, H.S. Kwon. *ACS Nano* 2014,8,11824–11835.

[141] S.C. Jung, H.J. Kim, Y.J. Kang, Y.K. Han. *J Alloys Compd* 2016,688,158–163.

[142] V. V. Kulish, O.I. Malyi, M.F. Ng, Z. Chen, S. Manzhos, P. Wu. *Physical Chemistry Chemical Physics* 2014,16,4260–4267.

[143] S.M. Zheng, Y.R. Tian, Y.X. Liu, S. Wang, C.Q. Hu, B. Wang, K.M. Wang. *Rare Metals* 2021,40,272–289.

[144] M.K. Jangid, A. Vemulapally, F.J. Sonia, M. Aslam, A. Mukhopadhyay. *J Electrochem Soc* 2017,164,A2559–A2565.

[145] Y. Xu, E. Swaans, S. Basak, H.W. Zandbergen, D.M. Borsa, F.M. Mulder. *Adv Energy Mater* 2016,6,1501436.

[146] M.K. Jangid, A.S. Lakhnot, A. Vemulapally, F.J. Sonia, S. Sinha, R.O. Dusane, A. Mukhopadhyay. *J Mater Chem A Mater* 2018,6,3422–3434.

[147] Y. Han, N. Lin, T. Xu, T. Li, J. Tian, Y. Zhu, Y. Qian. *Nanoscale* 2018,10,3153–3158.

[148] S. Huang, L. Liu, Y. Zheng, Y. Wang, D. Kong, Y. Zhang, Y. Shi, L. Zhang, O.G. Schmidt, H.Y. Yang. *Advanced Materials* 2018,30,1706637.

[149] C.H. Lim, T.Y. Huang, P.S. Shao, J.H. Chien, Y.T. Weng, H.F. Huang, B.J. Hwang, N.L. Wu. *Electrochim Acta* 2016,211,265–272.

[150] C. Yue, Y. Yu, S. Sun, X. He, B. Chen, W. Lin, B. Xu, M. Zheng, S. Wu, J. Li, J. Kang, L. Lin. *Adv Funct Mater* 2015,25,1386–1392.

[151] C. Chandra, W. Devina, A.D.M. Sarofil, J. Kim. *Chemical Engineering Journal* 2022,438,135411.

[152] M. Winter, B. Barnett, K. Xu. *Chem Rev* 2018,118,11433–11456.

[153] W. Zhang, F. Zhang, F. Ming, H.N. Alshareef. *EnergyChem* 2019,1,100012.

[154] C. Wang, L. Liu, S. Zhao, Y. Liu, Y. Yang, H. Yu, S. Lee, G.H. Lee, Y.M. Kang, R. Liu, F. Li, J. Chen. *Nat Commun* 2021,12,2256.

[155] W. Zuo, X. Liu, J. Qiu, D. Zhang, Z. Xiao, J. Xie, F. Ren, J. Wang, Y. Li, G.F. Ortiz, W. Wen, S. Wu, M.S. Wang, R. Fu, Y. Yang. *Nat Commun* 2021,12,4903.

[156] E.A. Wu, S. Banerjee, et al. *Nat Commun* 2021,12,1256.

[157] X. Shen, Q. Zhou, M. Han, X. Qi, B. Li, Q. Zhang, J. Zhao, C. Yang, H. Liu, Y.S. Hu. *Nat Commun* 2021,12,2848.

[158] Q. Shi, R. Qi, X. Feng, J. Wang, Y. Li, Z. Yao, X. Wang, Q. Li, X. Lu, J. Zhang, Y. Zhao. *Nat Commun* 2022,13,3205.

[159] H. Kim, H. Kim, Z. Ding, M.H. Lee, K. Lim, G. Yoon, K. Kang. *Adv Energy Mater* 2016,6,1600943.

[160] A. V. Baskar, G. Singh, A.M. Ruban, J.M. Davidraj, R. Bahadur, P. Sooriyakumar, P. Kumar, A. Karakoti, J. Yi, A. Vinu. *Adv Funct Mater* 2023,33,2208349.

[161] M.-M. Xie, Fei and Xu, Zhen and Guo, Zhenyu and Titirici. *Progress in Energy* 2020,2,042002.

[162] S. Dou, Xinwei and Hasa, Ivana and Saurel, Damien and Vaalma, Christoph and Wu, Liming and Buchholz, Daniel and Bresser, Dominic and Komaba, Shinichi and Passerini. *Materials Today* 2019,23,87–104.

[163] S. Wahid, Malik and Puthusseri, Dhanya and Gawli, Yogesh and Sharma, Neha and Ogale. *ChemSusChem* 2018,11,506–526.

[164] J.R. Fitzpatrick, S.I.R. Costa, N. Tapia-Rui. *Johnson Matthey Technology Review* 2022,66,44–60.

[165] Z. Liang, F. Tian, G. Yang, C. Wang. *Nat Commun* 2023,14,3591.

[166] Y. Jin, P.M.L. Le, P. Gao, Y. Xu, B. Xiao, M.H. Engelhard, X. Cao, T.D. Vo, J. Hu, L. Zhong, B.E. Matthews, R. Yi, C. Wang, X. Li, J. Liu, J.G. Zhang. *Nat Energy* 2022,7,718–725.

[167] Z. Deng, T.P. Mishra, E. Mahayoni, Q. Ma, A.J.K. Tieu, O. Guillon, J.N. Chotard, V. Seznec, A.K. Cheetham, C. Masquelier, G.S. Gautam, P. Canepa. *Nat Commun* 2022,13,4470.

[168] D.A. Rakov, F. Chen, S.A. Ferdousi, H. Li, T. Pathirana, A.N. Simonov, P.C. Howlett, R. Atkin, M. Forsyth. *Nat Mater* 2020,19,1096–1101.

[169] X. Wang, C. Zhang, M. Sawczyk, J. Sun, Q. Yuan, F. Chen, T.C. Mendes, P.C. Howlett, C. Fu, Y. Wang, X. Tan, D.J. Searles, P. Král, C.J. Hawker, A.K. Whittaker, M. Forsyth. *Nat Mater* 2022,1057–1065.

[170] H.-Q. Gong, X.-Y. Wang, L. Ye, B. Zhang, X. Ou. *Tungsten* 2023,3,574–584.

[171] R. Ramadan, M. Manso-Silván, R.J. Martín-Palma. *J Mater Sci* 2020,55,5458–5470.

[172] Z. Li, L. Ma, T.W. Surta, C. Bommier, Z. Jian, Z. Xing, W.F. Stickle, M. Dolgos, K. Amine, J. Lu, T. Wu, X. Ji. *ACS Energy Lett* 2016,1,395–401.

[173] X. Han, Liang and Li, Zhimin and Yang, Fei and Xiao, Zhihua and Yu, Yintao and Ning, Guoqing and Jia. *Powder Technol* 2021,382,541–549.

[174] A. Agrawal, K. Biswas, S.K. Srivastava, S. Ghosh. *Journal of Solid State Electrochemistry* 2018,22,3443–3455.

[175] Y. Feng, L. Liu, X. Liu, Y. Teng, Y. Li, Y. Guo, Y. Zhu, X. Wang, Y. Chao. *Electrochim Acta* 2020,359,136933.

[176] A. Fereydooni, C. Yue, Y. Chao. *Small* 2024,20,2307275.

[177] C. del M. Saavedra Rios, V. Simone, L. Simonin, S. Martinet, C. Dupont. *Biomass Bioenergy* 2018,117,32–37.

[178] H. Parsimehr, A. Ehsani, S. Ahmadreza. *Biomass Convers Biorefin* 2021,14,12413–12429.

[179] M.K. Rybarczyk, Y. Li, M. Qiao, Y. Hu, M. Titirici, M. Lieder. *Journal of Energy Chemistry* 2019,29,17–22.

[180] S. Guo, Y. Chen, L. Tong, Y. Cao, H. Jiao, Z. long, X. Qiu. *Electrochim Acta* 2022,410,140017.

[181] C. Yue, A. Fereydooni, P. Nakhanivej, M.B. Murria, M. Liu, Y. Zeng, Z. Wei, Q. Fu, X. Zhao, M.J. Loveridge, Y. Chao. *RSC Sustainability* 2025,3,2915.

3. Characterisations and methods

3.1. Introduction

A rigorous assessment of electrode performance requires linking physical and structural characteristics to electrochemical behaviour. In this chapter, the characterisation techniques used to analyse the barley husk-derived anodes and their composites are described in detail. The chosen methods probe morphology, crystallinity, composition, surface chemistry and thermal stability, each of which influences electrochemical response.

In addition, the electrochemical methods employed to assess the performance of lithium-ion and sodium-ion half-cells are presented. Electrochemical testing includes galvanostatic cycling, cyclic voltammetry and electrochemical impedance spectroscopy, which together inform capacity retention, reaction pathways and kinetic limitations.

The methods described in this chapter are applied in the subsequent Chapters to elucidate the structure-property-performance relationships of the barley husk-derived carbon and silica/carbon samples and anodes.

3.2. Material characterisations

3.2.1. Scanning electron microscopy

Scanning electron microscopy (SEM) was employed to investigate the morphology, surface texture, and microstructural features of the barley husk-derived carbon and silica/carbon composites. SEM provides high-resolution images that enable visual inspection of particle size, porosity, structural uniformity, and the distribution of embedded silicon or silica within the carbon matrix.

A schematic overview of the SEM setup is presented in Fig. 3.1. It shows the main components involved in the beam generation, focusing, scanning, and detection processes. As it can be seen, a focused electron beam is rastered across the specimen surface. The interaction between the beam and the sample generates secondary electrons, originating from the near-surface region and providing topographical contrast, and backscattered electrons, which are sensitive to atomic

number and reveal compositional contrast.[1] These signals are collected by appropriate detectors and converted into high-resolution images of the surface morphology. These morphological features influence ion-transport length scales, electrolyte access and mechanical integrity during cycling.[2]

Since the synthesised carbonaceous and composite materials are not inherently conductive, a thin gold layer (approximately 5 nm) was deposited on their surfaces using a Polaron SC7640 sputter coater (Quorum technologies, UK) prior to imaging. This prevents surface charging and enhances image resolution.

All SEM analyses in this work were conducted using a Zeiss Gemini 300 FE field-emission scanning electron microscope. Imaging was performed under high-vacuum conditions with accelerating voltages between 5 and 20 kV, adjusted based on the conductivity and resolution requirements of each sample. Unless otherwise specified, all micrographs presented in this thesis were obtained using the secondary electron imaging mode.

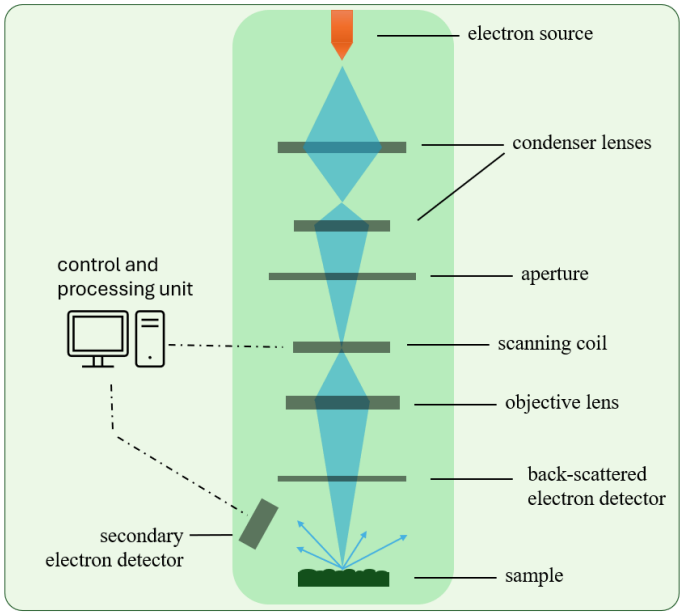

Figure 3.1. Schematic diagram of a Scanning Electron Microscope (SEM), showing the main components.

3.2.2. Energy dispersive X-ray spectroscopy

Energy dispersive X-ray spectroscopy (EDS) was employed alongside SEM to identify and map the elemental composition of the synthesised anode materials. In particular, it was used to confirm the presence and spatial distribution of silicon, carbon, oxygen, and other elements within the barley husk-derived carbon matrix and the silica/carbon composites. This information is vital for verifying the uniformity of silicon integration, the effectiveness of purification steps, and the compositional consistency of the prepared materials.

EDS operates on the principle of X-ray emission following inelastic interactions between the primary electron beam and the atoms in the sample. When the incident electrons from the SEM column strike the specimen, they can dislodge inner-shell (core) electrons from the atoms. As a result, electrons from higher energy levels fall into the vacant lower energy states, releasing energy in the form of characteristic X-ray photons. The energy of these emitted X-rays is specific to the atomic structure of each element, enabling elemental identification.[1]

Although the technique is fundamentally distinct from SEM imaging, it is typically integrated into the same instrument. As shown schematically in Fig. 3.1, the interaction volume where the electron beam meets the sample generates not only secondary and backscattered electrons but also X-rays. These are collected by an EDS detector positioned at an oblique angle relative to the sample surface.

In this work, EDS analysis was conducted using an integrated Oxford Instruments Ultim Max 170. Spectral and elemental mapping modes were both used to analyse the local chemical environment of selected regions. Operating conditions included an accelerating voltage of 15 to 20 kV and a working distance of approximately 8.5 mm to optimise spatial resolution and X-ray signal intensity.

3.2.3. X-ray diffraction

X-ray diffraction (XRD) is a fundamental characterisation technique used to determine the crystal structure, phase composition, and degree of crystallinity of solid-state materials. In this study, XRD was employed to analyse the structural nature of the synthesised barley husk-derived materials and their silica/carbon composites. The diffraction patterns provide insights into whether

the resulting products contain amorphous, semi-crystalline, or well-ordered crystalline domains, which are critical parameters influencing their electrochemical performance.

The basic working principle of XRD involves directing monochromatic X-rays onto a material and detecting the angles at which the rays are diffracted due to interaction with the periodic atomic planes within the sample. This diffraction occurs when the conditions of Bragg's law are satisfied, which relates the X-ray wavelength (λ), the interplanar spacing in the crystal (d), and the angle of incidence (θ). Constructive interference occurs at discrete angles, yielding a diffraction pattern that can be used for phase identification and qualitative assessment of ordering.[1]

Fig. 3.2a illustrates the core elements of a conventional θ to 2θ XRD measurement configuration. The system consists of a primary optics section, where X-rays are generated from a sealed X-ray tube, typically with a Cu anode providing Cu Kα radiation (λ = 1.5406 Å). The incident beam is shaped and conditioned using divergence slits and Soller slits to ensure beam collimation. The sample is mounted on a central stage and rotated to vary the angle θ during the scan. The secondary optics section, located on the diffracted beam path, contains anti-scatter and receiving slits, an optional monochromator for wavelength refinement, and a detector that records the intensity of the diffracted X-rays at varying 2θ angles.

To support the conceptual understanding of how diffraction arises, Fig. 3.2b presents a schematic representation of X-ray diffraction from parallel atomic planes. In this illustration, an incident X-ray beam interacts with atoms in adjacent crystal planes. The path difference between X-rays reflected from successive planes must be an integer multiple of the wavelength in order to produce constructive interference. This condition is defined by Bragg's law in Eq (3.1)

$$n\lambda = 2dsin(\theta) \tag{3.1}$$

where n is the order of reflection, λ is the X-ray wavelength, d is the spacing between planes, and θ is the angle of incidence.[1] The angle between the incident and diffracted beam is denoted as 2θ, and this is the quantity scanned during measurement.

All XRD measurements in this work were performed using a Rigaku Smartlab SE diffractometer operating at 40 kV and 30 mA, equipped with a Cu X-ray source and a high-resolution 1D detector. Samples were scanned in the 2θ range of 5° to 80°, with a step size of 0.02° and a scan speed optimised for both resolution and signal-to-noise ratio. Identification of crystalline phases was

carried out by comparing measured patterns with entries from the ICDD PDF-4+ database. For carbonaceous samples, broad humps centred near $2\theta \approx 22$ to 26° were interpreted as signatures of amorphous or turbostratic carbon. Sharper peaks were associated with retained crystalline silica phases such as quartz or cristobalite, if present. The relative sharpness and intensity of the diffraction peaks were also used qualitatively to evaluate the degree of crystallinity among different samples.

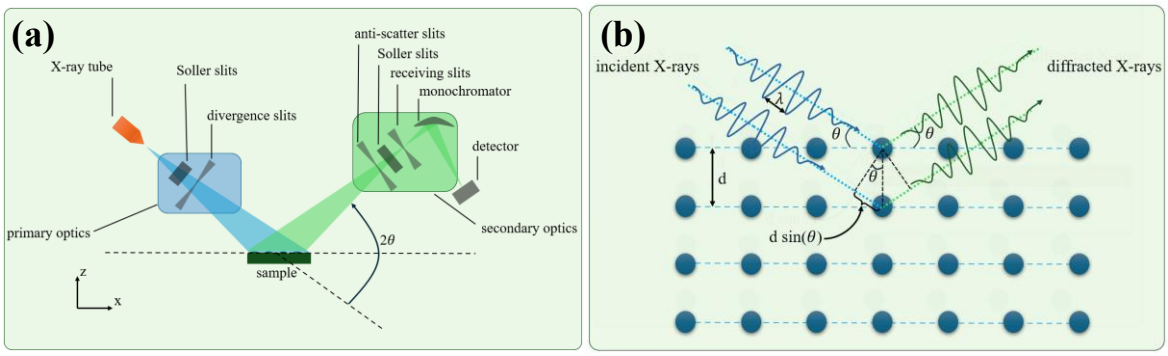

Figure 3.2. (a) Schematic diagram of a typical X-ray diffraction setup in θ to 2θ geometry, highlighting the main components of primary and secondary optics, and (b) Bragg diffraction from crystalline atomic planes, illustrating the origin of constructive interference and the basis of Bragg's law.

3.2.4. Raman spectroscopy

Raman spectroscopy was used to assess bonding or ordering in the carbon phase and to verify silica-related signatures in the composites. This is especially valuable when analysing carbonaceous and silica-containing materials derived from biomass, where subtle structural variations directly influence electrochemical performance.

Fig. 3.3 illustrates the Raman spectroscopy setup and its underlying physical principles. In Fig. 3.3a, a schematic diagram of a Raman spectrometer is presented, showing the full optical pathway from the laser excitation source to data acquisition. A laser beam is directed through a series of optical components, including neutral density (ND), interference, and notch filters, to modulate the intensity and spectral purity of the laser line. A dichroic mirror reflects the incoming laser towards the sample positioned on a motorised stage. The laser light is focused onto the sample surface through a microscope objective, exciting molecular vibrations. Scattered light from the sample is collected by the same objective and directed back through the dichroic mirror.[1]

Only a small fraction of the scattered photons undergo a shift in energy due to inelastic scattering; this is the Raman effect. The collected light passes through further filtering elements before entering the spectrometer, where it is dispersed by a grating and detected by a CCD (Charge-Coupled Device) array. The resulting spectrum reveals peaks corresponding to specific vibrational modes of the sample material, which are plotted as intensity versus Raman shift (typically in cm^{-1}). In this work, Raman measurements were performed using a HORIBA Scientific LabRAM Odyssey Raman spectrometer, providing high-resolution spectral data essential for identifying the degree of graphitisation and silica structure in the barley husk-derived materials.

The fundamental mechanism of Raman scattering is summarised in Fig. 3.3b, which depicts the interaction between incident laser light and the vibrational energy levels of a molecule. When a photon of energy $h\nu$ interacts with a molecule, most scattering events are elastic (Rayleigh scattering), in which the scattered light retains the same energy as the incident photon. However, a small proportion undergoes inelastic scattering, resulting in a change in photon energy. If the scattered photon has lower energy than the incident photon, it corresponds to Stokes Raman scattering; if it has higher energy, it corresponds to anti-Stokes Raman scattering.[1] These processes reflect transitions between vibrational energy levels mediated by a virtual state, as depicted in the diagram.

In this study, Raman spectroscopy serves to evaluate the structural quality and composition of the silica/carbon composite anodes. In particular, this technique enables differentiation between ordered and amorphous carbon domains, assessment of graphitisation levels, and confirmation of silica incorporation, all of which are pivotal in understanding the charge transport mechanisms and stability of the anode material. For the carbonaceous components, particular attention was given to the D (~1350 cm^{-1}) and G (~1580 cm^{-1}) bands; the intensity ratio I_D/I_G was used as an indicator of structural disorder and degree of graphitization.

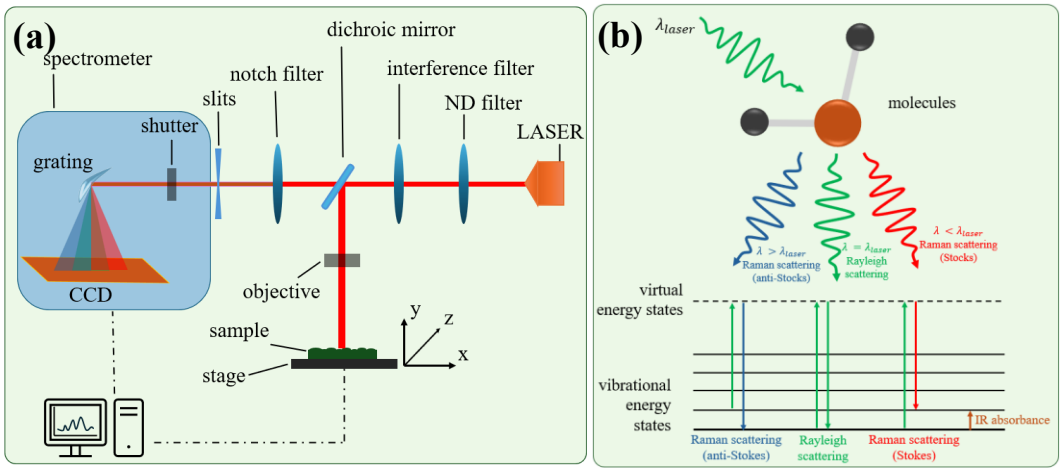

Figure 3.3. (a) Schematic layout of a Raman spectroscopy system, showing the main optical and electronic components used for excitation, filtering, and spectral detection. (b) Representation of the Raman scattering process based on molecular vibrational transitions, highlighting Stokes, anti-Stokes, and Rayleigh scattering pathways, along with corresponding energy level shifts.

3.2.5. X-ray photoelectron spectroscopy

X-ray photoelectron spectroscopy (XPS) is a powerful surface-sensitive technique used to determine the elemental composition, oxidation states, and chemical bonding environments of materials. It is particularly valuable in the analysis of electrode materials where surface phenomena, such as solid-electrolyte interphase (SEI) formation and surface functional groups, significantly influence electrochemical performance.

The working principle of XPS is based on the photoelectric effect. When a material is irradiated with monochromatic X-rays, typically Al K_α (1486.6 eV) or Mg K_α (1253.6 eV), core-level electrons from atoms near the surface absorb the photon energy and are ejected from the material if the photon energy exceeds their binding energy.[1] The kinetic energy (E_k) of the emitted photoelectrons is measured, and the binding energy (E_b) is then calculated using Eq. (3.2)

$$E_b = h\nu - E_k - \phi \tag{3.2}$$

where $h\nu$ is the energy of the incident X-ray photons, and ϕ is the spectrometer work function. This relation enables the identification of elements and their chemical states.[1]

As depicted in Fig. 3.4, the X-ray source directs a beam of photons onto the sample surface, resulting in the emission of photoelectrons. These electrons are collected by a transfer lens system, which focuses them through a series of mesh electrodes and slits into a hemispherical energy analyzer. Inside the analyzer, electrons are separated based on their kinetic energy as they follow a curved electrostatic path. The energy-dispersed electrons then reach a multichannel detector, which records the number of electrons at each energy level. The resulting energy distribution was processed to obtain binding-energy spectra for chemical-state assignment.

XPS offers a probing depth of approximately 5 to 10 nm, making it highly sensitive to surface chemistry.[1] This is particularly relevant in the context of electrode materials for lithium- and sodium-ion batteries, where surface modifications, carbon coatings, and native oxides can influence the charge transfer and cycling stability.[3] Furthermore, XPS can distinguish between different oxidation states, enabling detailed analysis of transition metals, silicon oxides, or surface carbon functionalities, which are often present in biomass-derived carbon-silica composite systems.

In this study, XPS was employed to characterize the surface elemental composition and bonding configurations of the barley husk-derived composite materials. All XPS measurements in this work were performed using a Thermo Fisher ESCALAB Xi+ spectrometer. All spectra were calibrated using the C 1s peak at 284.8 eV as a reference. This technique provided essential insights into the nature of carbon, silicon, and oxygen species, as well as the presence of dopants or residual impurities. These findings helped correlate surface chemistry with the observed electrochemical behavior, particularly in terms of capacity retention and SEI formation.

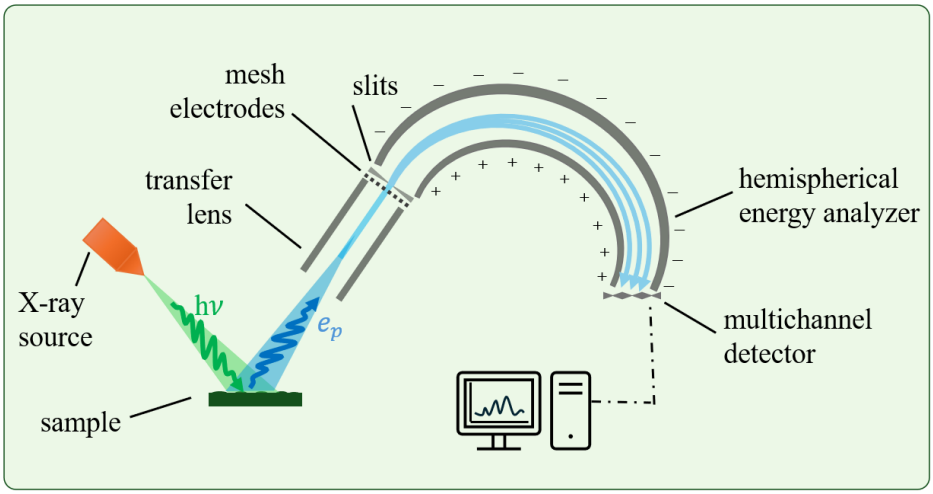

Figure 3.4. Schematic diagram of an X-ray Photoelectron Spectroscopy (XPS) system, illustrating the emission of photoelectrons (e_p) from the sample surface upon irradiation with X-rays (hν).

3.2.6. Dynamic light scattering

Dynamic light scattering (DLS), also known as photon correlation spectroscopy (PCS), is a non-destructive and highly sensitive technique used to determine the size distribution of particles suspended in a fluid. It is especially suited for analyzing nanoparticles, colloids, and polymers with dimensions in the range of 1 to 1000 nm.[4]

DLS determines particle-size distributions from intensity-fluctuation autocorrelation functions arising from Brownian motion. When a monochromatic laser beam passes through colloidal dispersion, particles in motion scatter the light. Due to their constant motion, caused by thermal energy in the liquid, the intensity of the scattered light fluctuates over time. These fluctuations are detected at a defined angle (usually 90° or lower, e.g., 12° or 173° depending on the instrument configuration) and converted into an autocorrelation function, which reflects how the scattered intensity varies with delay time.[4]

As shown in Fig. 3.5, the DLS setup involves a laser source whose coherent beam is collimated and directed through a transparent sample cuvette containing the dispersed particles. Scattered light at an angle θ is collected by an optical system and guided to a photodetector. A portion of the incident beam is also routed as a reference light via beam splitters and mirrors. The resulting interference pattern provides a beat frequency corresponding to the motion of particles, which is recorded over time.

The analysis of these intensity fluctuations is used to calculate the diffusion coefficient (D) of the particles via the Siegert relation. From this, the hydrodynamic diameter (d_H) can be derived using the Stokes-Einstein equation in Eq. (3.3)

$$d_H = \frac{k_B T}{3\pi\eta D} \tag{3.3}$$

where k_B is Boltzmann's constant, T is the absolute temperature, and η is the solvent viscosity.[4] The hydrodynamic diameter includes not only the core particle size but also any surface-attached molecules or solvated layers, making DLS a particularly useful tool for evaluating agglomeration, dispersion stability, or surface functionalisation.

In this work, DLS measurements were carried out to estimate the size distribution of suspended silicon particles used in some of the anodes. This analysis provided insights into the uniformity of dispersion and the degree of aggregation, both of which are critical for ensuring consistent electrode performance. Furthermore, DLS complements solid-state techniques like XRD and SEM by offering information on the particle size in the fluid state, relevant during slurry preparation or surface functionalization stages.

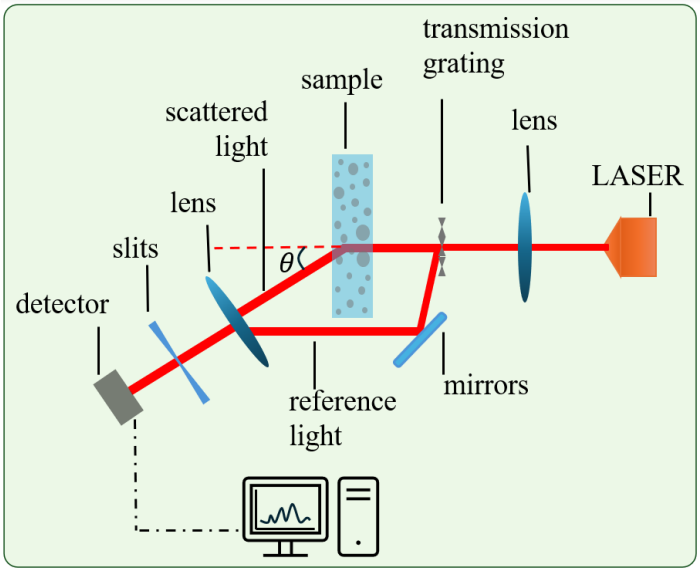

Figure 3.5. Schematic representation of a Dynamic Light Scattering (DLS) system.

3.2.7. Thermogravimetric analysis

Thermogravimetric analysis (TGA) is a thermal analysis technique used to measure the change in mass of a material as a function of temperature or time under a controlled atmosphere. It provides critical information about the thermal stability, composition, and decomposition behavior of materials.[1] In battery-related materials research, TGA is commonly employed to evaluate the content and thermal behavior of carbon, silica, binders, or other organic/inorganic constituents in composite electrodes.

The basic principle of TGA involves heating a small mass of the sample (typically 5 to 20 mg) in a high-precision balance located within a furnace. The temperature is increased linearly over time, usually at a rate of 5 to 20 °C min^{-1}, while the system is purged with a specific gas such as nitrogen, air, or argon depending on the analysis objectives. As the temperature rises, the sample undergoes physical or chemical transformations (e.g. dehydration, decomposition, oxidation), and any associated mass change is continuously recorded.[1]

In this work, TGA was used to evaluate the thermal decomposition behavior and composition of the barley husk-derived silica/carbon composites. By analyzing the weight loss in an oxidative atmosphere (air), the carbon content within the composite could be estimated based on the combustion of the carbonaceous phase. At the same time, the residue remaining at elevated temperatures corresponds primarily to the thermally stable inorganic phase, such as silica (SiO_2).

This analysis not only confirmed the successful incorporation of carbon into the silica matrix but also enabled the quantification of each phase, which is essential for understanding the electrochemical contributions of each component. Additionally, the thermal stability profile provided insights into the processing conditions and potential performance limitations of the materials under elevated temperatures, which may be encountered during electrode fabrication or operation.

TGA thus serves as a complementary technique to structural and morphological characterisations, enabling a more complete understanding of the hybrid composite's composition and its suitability for lithium- and sodium-ion battery applications.

3.3. Electrochemical tests

3.3.1. Galvanostatic charge-discharge

Galvanostatic charge-discharge (GCD) testing is a fundamental electrochemical method used to assess the specific capacity, cycling stability, coulombic efficiency, and rate capability of electrode materials under practical operating conditions. This technique involves charging and discharging a battery electrode at a constant current while recording the corresponding voltage response over time. In this study, GCD tests were performed to evaluate the performance of barley husk-derived silica-carbon composite anodes in both lithium-ion and sodium-ion half-cells.

The measurements were carried out using a LAND CT2001A battery testing system under ambient conditions. The cells were assembled in CR2016 coin cell configuration, using lithium or sodium metal as counter and reference electrodes, a glass fibre separator, and a suitable electrolyte (as described in Chapter 2). The electrodes were cycled between predetermined voltage limits, typically 0.01 to 3.0 V vs. Li/Li^+ or 0.01 to 2.5 V vs. Na/Na^+, at various current densities (e.g., 100 mA g^{-1} for initial cycling, and increasing values for rate performance assessment).

The voltage profiles obtained from GCD testing provide critical insights into the lithiation/sodiation mechanisms and the reversibility of the reactions. Plateau regions in the discharge-charge curves often indicate specific phase transitions or alloying reactions, whereas sloping regions are commonly associated with intercalation or capacitive behaviour. The initial charge-discharge cycles are especially important, as they capture irreversible phenomena such as SEI formation, electrolyte decomposition, and structural rearrangement within the active material. GCD data were used as the primary basis for reporting capacity, Coulombic efficiency and voltage-profile evolution. The results serve as a critical link between the structural properties established in previous characterisation sections and the practical performance metrics relevant to energy storage systems.

3.3.2. Cyclic voltammetry

Cyclic voltammetry (CV) is a versatile electrochemical technique used to investigate redox activity, reversibility, and the underlying charge storage mechanisms of electrode materials. In this

study, CV measurements were employed to examine the lithiation/delithiation and sodiation-desodiation processes occurring within the barley husk-derived silica/carbon composite anodes.

All CV experiments were conducted using a CHI 660E electrochemical workstation, with CR2016-type half-cells assembled in an argon-filled glovebox. The measurements were performed within a potential window of 0.01 to 3.0 V vs. Li/Li^+ or 0.01 to 2.5 V vs. Na/Na^+, under ambient conditions.

The resulting voltammograms display characteristic cathodic and anodic peaks that reflect the electrochemical reactions of active material with lithium or sodium ions. In the initial cycle, broad and less defined cathodic peaks often appear due to irreversible processes such as electrolyte decomposition and SEI formation. These features are commonly observed in carbonaceous and silicon-containing systems. In subsequent cycles, the emergence of sharper and more defined peaks indicates the stabilisation of electrochemical reactions and improved reversibility.

The position, symmetry, and intensity of the redox peaks offer insights into the kinetic and thermodynamic properties of the electrode reactions. Peak shifts or changes in intensity over multiple cycles can signify structural evolution, polarisation effects, or changes in electronic conductivity. Cycle-to-cycle overlap in CV was taken as an indicator of reaction stabilisation and improved reversibility.

Moreover, CV is valuable for probing the nature of the charge storage process. Depending on the material, the current response may arise from surface-controlled capacitive behaviour, bulk intercalation, or alloying mechanisms. These different processes can be qualitatively inferred from the shape of the voltammograms; capacitive responses typically result in nearly rectangular or sloped profiles, while diffusion-limited processes produce pronounced redox peaks.[5]

In this study, CV was particularly useful for distinguishing between the electrochemical contributions of the carbon matrix and the embedded silica or silicon-rich domains. The analysis provided complementary information to galvanostatic cycling data, offering mechanistic insights into how the structural features of the biomass-derived composites influence their electrochemical behaviour.

3.3.3. Electrochemical impedance spectroscopy

Electrochemical impedance spectroscopy (EIS) is a powerful diagnostic tool used to analyse the charge transfer, ionic diffusion, and interfacial characteristics of electrochemical systems. In this study, EIS was performed to evaluate the resistive and capacitive behaviour of the barley husk-derived silica/carbon composite anodes, providing insights into both kinetic limitations and electrode-electrolyte interface stability.

All impedance measurements were conducted using a CHI 660E electrochemical workstation. The tests were carried out on CR2016-type half-cells after selected cycles, at open circuit potential (OCP) and over a frequency range typically from 100 kHz to 0.01 Hz, with a small amplitude sinusoidal excitation voltage (commonly 5 or 10 mV). These conditions were selected to ensure that the system remained within the linear response regime.[6]

The resulting Nyquist plots typically consist of a depressed semicircle in the high-to-mid frequency region, followed by a sloped line at lower frequencies. The high-frequency intercept with the real axis represents the uncompensated solution resistance (R_s), which includes the resistance of the electrolyte and internal cell components. The diameter of the semicircle corresponds to the charge transfer resistance (R_{ct}) at the electrode-electrolyte interface, a critical parameter for evaluating reaction kinetics and SEI characteristics. The inclined low-frequency region is attributed to the Warburg impedance, associated with the diffusion of lithium or sodium ions within the bulk electrode material.[6]

Fitting the impedance data to an appropriate equivalent circuit model enables quantitative extraction of these electrochemical parameters. In systems involving complex hybrid structures, such as carbon/silica composites, multiple resistive and capacitive elements may be involved, reflecting contributions from the conductive carbon matrix, insulating silica domains, and interfacial film formation.

EIS was used to track resistance evolution with cycling, particularly changes associated with interfacial films and charge-transfer kinetics. A decrease in R_{ct} after initial cycles may indicate activation of the electrode material, while a gradual increase over extended cycling is often associated with electrode passivation, mechanical stress accumulation, or breakdown of the conductive network.

3.3.4. Rate performance testing

Rate performance testing is an essential electrochemical evaluation for assessing the capability of electrode materials to deliver stable capacity at varying current densities, which simulates different charge/discharge rates in practical applications. In this study, the rate performance of the fabricated electrodes was systematically evaluated using GCD measurements at a series of current densities. This test allows direct comparison of the electrodes' behaviour under slow and fast cycling conditions.

The test protocol typically involves charging and discharging the cell at gradually increasing current densities (e.g., 0.05, 0.1, 0.2, 0.5, 1, 2 C-rates), followed by a return to the initial current density to evaluate the reversibility and structural integrity of the electrode material. A well-performing anode should retain a significant portion of its capacity at high rates and recover its original capacity when cycled back at low current density, indicating good reaction kinetics, ionic/electronic conductivity, and structural stability.

For biomass-derived carbon and silica/carbon composite anodes, rate capability is particularly important due to their potential porous microstructure, which can facilitate electrolyte penetration and short diffusion pathways for Li^+ or Na^+ ions.[7] Furthermore, the presence of carbon helps improve electronic conductivity, which is crucial for fast charge transfer under high-rate cycling.

In this work, rate performance testing was conducted using the same galvanostatic mode as described in Section 3.3.1, employing the coin half-cell configuration and a fixed voltage window. The resulting rate capability plots provide insight into the electrode's tolerance to dynamic electrochemical conditions and serve as a basis for comparing the performance of barley husk-derived anodes with commercial graphite or other biomass-based systems.

3.3.5. Differential capacity analysis

Differential capacity analysis (dQ/dV) is a powerful diagnostic tool used to reveal subtle electrochemical features that may not be evident in conventional voltage-capacity curves. By plotting dQ/dV against cell voltage (V), this method enables a more detailed interpretation of redox processes, phase transitions, and surface reactions such as SEI formation during cycling.

In this study, dQ/dV analysis was performed using the charge-discharge data collected from galvanostatic cycling experiments (Section 3.3.1). The derivative was numerically calculated as

the change in capacity with respect to the change in voltage, using appropriate smoothing to minimise noise without distorting key features.

For anode materials such as those derived from barley husk, which may involve both alloying (Si-related) and intercalation or pseudocapacitive (C-related) mechanisms, dQ/dV plots can help identify the electrochemical signatures of each contribution. For example, characteristic peaks near 0.1 to 0.2 V (vs. Li^+/Li) or 0.3 to 0.5 V (vs. Na^+/Na) may correspond to alloying/dealloying of silicon, while broad features at higher voltages can be indicative of capacitive charge storage in disordered carbon.[6, 8]

Additionally, the evolution of dQ/dV curves over multiple cycles provides insights into the stability of the electrode material and the reversibility of electrochemical reactions. Shifts in peak positions, suppression of certain features, or appearance of new peaks can signal irreversible structural changes, loss of active material, or growth of resistive SEI layers.

The dQ/dV analysis therefore serves as a complementary method to cyclic voltammetry (Section 3.3.2), offering higher resolution in detecting electrochemical events during constant current cycling. It is especially valuable for complex composite systems like silica/carbon anodes, where multiple reaction mechanisms may coexist.

3.3.6. Long-term stability

Long-term cycling stability is one of the most critical indicators of an electrode material's practical applicability in rechargeable battery systems. While initial capacity and rate performance provide insight into the short-term behaviour of a material, extended cycling tests are required to evaluate the structural integrity, reversibility of electrochemical reactions, and persistence of interfacial stability over time.[5, 9]

In this study, long-term galvanostatic charge-discharge cycling was conducted over several hundred cycles under a constant current density, typically at a moderate rate such as 0.05 or 0.2 C-rate, depending on the specific test conditions. These measurements were designed to assess both capacity retention and Coulombic efficiency over extended periods.

Particularly for the silica/carbon anode composites derived from barley husk, long-term performance testing is crucial for understanding the synergistic effects between the active silicon oxide domains and the carbon matrix. The carbonaceous phase, typically disordered or turbostratic,

serves to buffer the volume expansion of SiO_x during cycling and to maintain electrical connectivity. A gradual capacity decay or a sharp drop-off in performance may indicate mechanical pulverisation, SEI thickening, or loss of electrical contact, all of which are common degradation pathways in high-capacity anode materials.[2, 10]

The evolution of Coulombic efficiency throughout cycling also provides valuable information on parasitic reactions such as electrolyte decomposition and continued SEI formation. Stable values above 99% typically reflect minimal side reactions and high reversibility, whereas persistently low efficiencies may suggest instability at the electrode-electrolyte interface.[5]

To support these observations, post-mortem analysis such as SEM imaging, XPS, or EIS can be employed to investigate electrode morphology, surface composition, and interfacial resistance after long-term cycling. However, the primary electrochemical metric (capacity retention as a function of cycle number) remains the most direct indicator of anode robustness and cycle life.[9]

Overall, the long-term stability tests in this study serve to benchmark the electrochemical durability of the barley husk-derived anode system in both lithium- and sodium-ion configurations, providing critical insight into its suitability for real-world energy storage applications.

3.4. Summary of characterisation methods

A comprehensive suite of material characterisation and electrochemical testing methods was employed in this study to investigate the physicochemical properties and electrochemical performance of the synthesised anode materials. Each technique serves a distinct purpose, providing complementary information essential for understanding structure-property-performance relationships in both lithium-ion and sodium-ion storage systems.

Structural and morphological features were primarily assessed using scanning electron microscopy (SEM), and dynamic light scattering (DLS), providing insight into surface texture, particle morphology, pore architecture, and particle size distribution. Crystallographic and structural phase analyses were conducted via X-ray diffraction (XRD), while Raman spectroscopy provided molecular-level information regarding the degree of graphitisation and structural disorder.

Elemental and compositional analyses were carried out using energy-dispersive X-ray spectroscopy (EDS), X-ray photoelectron spectroscopy (XPS), and thermogravimetric analysis

(TGA), enabling assessment of surface chemistry, elemental distribution, and thermal stability. These characterisation techniques collectively form the basis for understanding the material's fundamental composition and structure.

In parallel, electrochemical characterisation was performed to evaluate the performance of the fabricated electrodes. GCD testing provided direct measurements of specific capacity and cycling behaviour, while cyclic voltammetry (CV) offered insights into redox reactions and capacitive contributions. Electrochemical impedance spectroscopy (EIS) further elucidated the charge transfer and interfacial resistances, especially those related to solid-electrolyte interphase (SEI) formation. Rate performance tests and long-term cycling studies assessed the electrode behaviour under various current loads and extended cycling conditions. Finally, differential capacity analysis (dQ/dV) enabled a deeper understanding of the reaction mechanisms and phase evolution processes during cycling.

Table 3.1 summarises the primary function, classification, key information obtained, and instruments employed for each characterisation technique. This integrative approach ensures that both structural and electrochemical dimensions of the material system are thoroughly addressed, forming a robust foundation for subsequent performance interpretation and mechanism analysis.

Table 3.1. Comparative summary of characterisation techniques used in this study.

Technique	Purpose	Type	Information Gained	Instrument Used
SEM (Scanning Electron Microscopy)	Examine surface morphology and microstructure	Structural	Particle size, porosity, structure, and surface texture	Zeiss Gemini 300 FE
EDS (Energy Dispersive X-ray Spectroscopy)	Elemental composition mapping	Compositional	Qualitative/semi-quantitative elemental distribution	Zeiss Gemini 300 FE (attached EDS)
XRD (X-ray Diffraction)	Identify crystalline phases and structure	Structural	Crystal structure, phase identification, and interlayer spacing	Rigaku Smartlab SE
Raman Spectroscopy	Analyse molecular vibrations and bonding	Compositional	Degree of graphitisation, structural disorder, D/G band ratio	Renishaw inVia Raman Microscope
XPS (X-ray Photoelectron Spectroscopy)	Surface chemical composition and bonding	Compositional	Elemental states, surface chemistry, functional groups	Kratos Axis Ultra DLD
DLS (Dynamic Light Scattering)	Determine particle size distribution in suspension	Structural	Hydrodynamic diameter and particle size distribution	Malvern Zetasizer Nano ZS
TGA (Thermogravimetric Analysis)	Assess thermal stability and composition	Compositional	Organic/inorganic content, water content, decomposition temperature	Mettler Toledo TGA/DSC 3+
GCD (Galvanostatic Charge-Discharge)	Evaluate charge/discharge behaviour	Electrochemical	Specific capacity, coulombic efficiency, voltage profiles	LAND CT2001A
CV (Cyclic Voltammetry)	Study redox activity and kinetic behaviour	Electrochemical	Reversible reactions, peak currents, pseudocapacitive contributions	CHI 660E
EIS (Electrochemical Impedance Spectroscopy)	Probe internal resistances and interface properties	Electrochemical	SEI resistance, charge transfer resistance, Warburg impedance	CHI 660E
Rate Performance Testing	Evaluate capacity retention at different current densities	Electrochemical	Rate capability, power performance, diffusion kinetics	LAND CT2001A

Differential Capacity Analysis	Examine redox behaviour and detect reaction processes	Electrochemical	Phase transitions, SEI evolution, plateau shifts	MATLAB/Origin (processed from GCD data)
Long-Term Stability Tests	Assess extended cycling behaviour	Electrochemical	Capacity retention, degradation rate, performance fade	LAND CT2001A

3.5. References

[1] Y. Leng, *Materials Characterization: Introduction to Microscopic and Spectroscopic Methods*, 2nd ed., Wiley-VCH, Weinheim, 2013.

[2] Y. Feng, L. Liu, X. Liu, Y. Teng, Y. Li, Y. Guo, Y. Zhu, X. Wang, Y. Chao. *Electrochim Acta* 2020,359,136933.

[3] Y. Yao, J. Zhang, L. Xue, T. Huang, A. Yu. *J Power Sources* 2011,196,10240–10243.

[4] D. Langevin, O. Lozano, et al. *NanoImpact* 2018,10,97–107.

[5] T. B. Reddy, ed.; D. Linden, Editor Emeritus, *Linden's Handbook of Batteries*, 4th ed., McGraw-Hill, New York, 2011.

[6] A. J. Bard, L. R. Faulkner, *Electrochemical Methods: Fundamentals and Applications*, 2nd ed., Wiley, New York, 2000.

[7] Y. Zhu, M. Chen, Q. Li, C. Yuan, C. Wang. *Carbon N Y* 2018,129,695–701.

[8] J. Qian, Y. Chen, L. Wu, Y. Cao, X. Ai, H. Yang. *Chemical Communications* 2012,48,7070–7072.

[9] D. McNulty, E. Carroll, C. O'Dwyer. *Adv Energy Mater* 2017,7,1602291.

[10] L. Ma, L. Liu, X. Liu, Y. Li, Y. Feng, Y. Tian, Y. Chao, Y. Zhu, X. Wang. *J Electron Mater* 2021,50,4426–4432.

4. Barley-husk-derived silica/carbon composites

4.1. Introduction

This chapter establishes the processing-structure relationships of barley-husk-derived silica/carbon (BH-SiO_2/C) composites that are later used as anodes. The central premise is that the structural state of the carbon matrix and the dispersion of the embedded biogenic silica are governed by two controllable processing variables: carbonisation temperature (T) and ball-milling time (BM). The work therefore proceeds in two parts. First, a temperature series (450 to 1150 °C) under N_2 is used to map how bonding-scale order and turbostratic stacking evolve in the unmilled materials. Secondly, at a fixed high-temperature state, ball milling is applied as an orthogonal lever to tune texture without changing bulk chemistry.

This chapter begins with the materials route from raw husks to powders and electrodes, including a single post-milling HCl wash that removes soluble inorganics while retaining SiO_2. Structural characterisation then focuses on Raman spectroscopy and X-ray diffraction for the temperature series, from which quantitative descriptors are extracted: Raman area-ratio indices and XRD stacking metrics. The ball-milling section employs N_2 physisorption (BET, t-plot, BJH) to quantify accessible surface and pore structure at BM000 to BM120. Throughout, sample identifiers follow BH-T####-BM###, and a quality-control protocol links synthesis batches to characterisation datasets to ensure that comparisons isolate tuning variables rather than uncontrolled variance. The electrochemical consequences of the processing-structure states established here are evaluated in Chapter 5.

4.2. Material preparation

Barley husks (BH) were processed to obtain a silica/carbon composite suitable for LIB anodes. The route comprised washing, drying and grinding of the raw biomass, carbonisation under an inert atmosphere, short-duration ball milling, an acid wash to remove residual inorganics, and electrode fabrication by slurry casting on copper, followed by coin-cell assembly. The workflow is summarised in Fig. 4.1 and the sample identifiers follow BH-T####-BM###, where T#### is

the carbonisation temperature (°C) and BM### is the ball-milling time (minutes). Slurry formulation, coating and coin-cell assembly procedure will be discussed in detail in chapter 5.

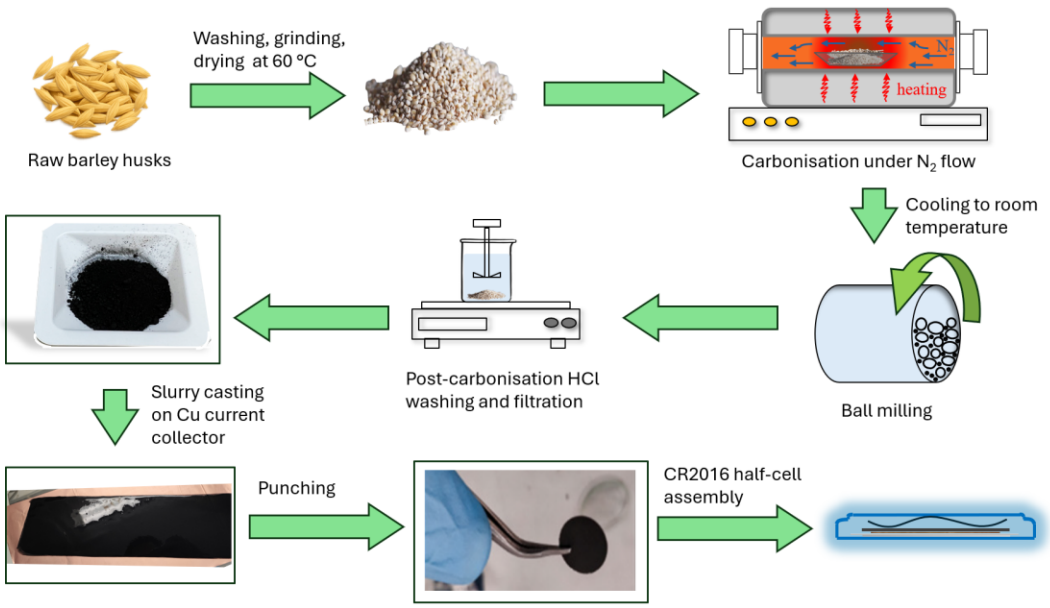

Figure 4.1. Preparation of barley-husk-derived silica/carbon anodes and electrode fabrication.

4.2.1. Biomass pre-processing

Raw BH were obtained from a local brewery near Norwich City, United Kingdom. As the first step, BH were thoroughly rinsed with deionised water to remove dust, soluble salts and residual surface debris, then oven-dried at 60 °C to a constant mass (Memmert UFB 400 universal oven). Dried material was mechanically ground to yield a flowable powder with a narrow particle-size distribution, improving thermal homogeneity during carbonisation and reproducibility across batches. The washing and grinding step also reduces alkali/alkaline-earth impurities that otherwise catalyse uncontrolled carbon burn-off at high temperature. SEM/EDS in Section 4.2.4 confirms the progressive removal of such species and the presence of intrinsic Si-rich domains within the organic matrix.

4.2.2. Carbonisation under nitrogen

Ground BH powder was placed in ceramic crucibles and heated in a three-zone tube furnace (Carbolite TZF 12/65/550) under flowing nitrogen gas. A temperature series was carried out over 450 to 1150 °C in 100 °C increments (ΔT = 100 °C). For each set-point, the furnace was ramped at 5 °C min^{-1} to the target, held for 2 hours, and then cooled to room temperature under nitrogen. Products are denoted BH-T####-BM000 (e.g., BH-T0750-BM000). Carbonisation temperature, T, is treated as a manipulated variable in this chapter, and its influence on structure and electrochemical behaviour is examined in Section 4.3. The inert environment suppresses oxidative loss of carbon and inhibits conversion of biogenic silica into high-temperature crystalline polymorphs.

The SEM images in Fig. 4.2 clearly show how strongly the morphology depends on the carbonisation temperature. At 750 °C, the original honeycomb-like lumen structure of the barley husk is still largely preserved, with open, rounded pores and thin cell walls. When the temperature increases to 1150 °C, the surface becomes noticeably smoother and decorated with small nodular features. The cross-sections also reveal significant densification of the walls, partial narrowing or even closure of the hollow defects, and the development of a thicker, more compact carbon skin.

The clear contrast between the two temperatures highlights the strong structural evolution of the material with increasing carbonisation temperature and encourages a more quantitative analysis in Section 4.3, where parameters such as interlayer spacing (d_{002}), crystallite thickness (L_c), and defect-related features are discussed in detail.

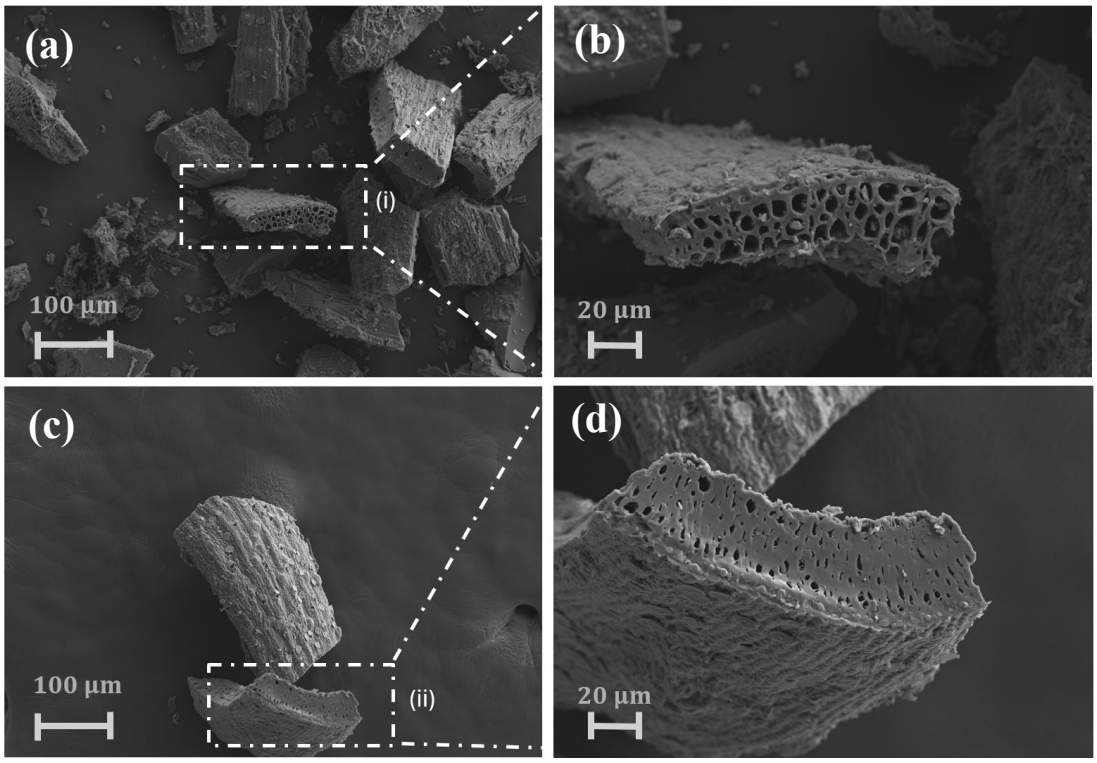

Figure 4.2. SEM cross-sections of BH samples with no milling; (a) BH-T0750-BM000 overview, (b) detail of region (i) in (a), (c) BH-T1150-BM000 overview, and (d) detail of region (ii) in (c).

4.2.3. Ball milling

Carbonised powders were subjected to short ball-milling with 1/2-inch (12.7 mm) stainless steel balls for various durations up to 120 minutes (from BM000 to BM120) using a dual-clamp high-energy ball mill (Spex Industries Digital Mixer Mill Model 8000D) at a rotating speed of 1400 RPM. Unless stated otherwise, other parameters (ball-to-powder ratio, jar volume and fill) were held constant across the series. After milling, powders underwent the single HCl wash described in Section 4.2.4 to remove soluble inorganics and any wear debris.

Fig. 4.3a and 4.3b show the SEM images of the BH-T1150-BM000 and BH-T1150-BM020 powders, respectively. The SEM image in Fig. 4.3a depicts the sample with no ball milling, showing a relatively uneven and coarse morphology. In contrast, the SEM image in Fig. 4.3b illustrates the sample from the same temperature series with 20 minutes of ball milling, which

displays a more fine-grained structure. The ball-milling step is necessary for particle-size reduction and for improving the physical homogeneity of the silica/carbon composite. Mechanical comminution facilitates a more uniform dispersion of SiO_2 within the carbon matrix and increases the specific surface area, which shortens ionic diffusion pathways and improves charge-transfer kinetics during charge-discharge. Overall, milling promotes more effective electrolyte contact with the active material, shortens ion-transport pathways and can improve charge-transfer kinetics and rate performance.[1–3] Electrochemical implications are assessed in Chapter 5.

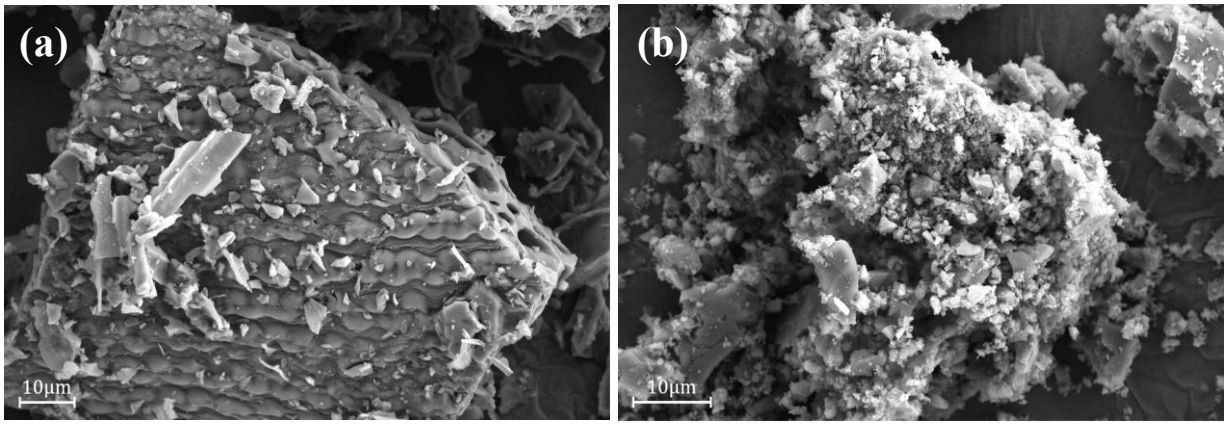

Figure 4.3. SEM images of (a) BH-T1150-BM000 and (b) BH-T1150-BM020, showing the milling effect on BH samples.

Cross-sectional SEM in Fig. 4.4a shows a carbonaceous wall with embedded silica spots. Point EDS at Site 1 detects Si and O (silica-rich domain) together with trace K, Mg and Ca, consistent with natural origin of the sample. Site 2 is mainly C with minor O from surface functionalities. A weak Au signal in both sites arises from sputter coating. These observations confirm a carbon matrix with embedded SiO_2 domains and residual alkali/alkaline-earth species, motivating ball milling to homogenise and expose silica-rich regions and also a post-milling acid wash to remove soluble impurities before electrode fabrication.

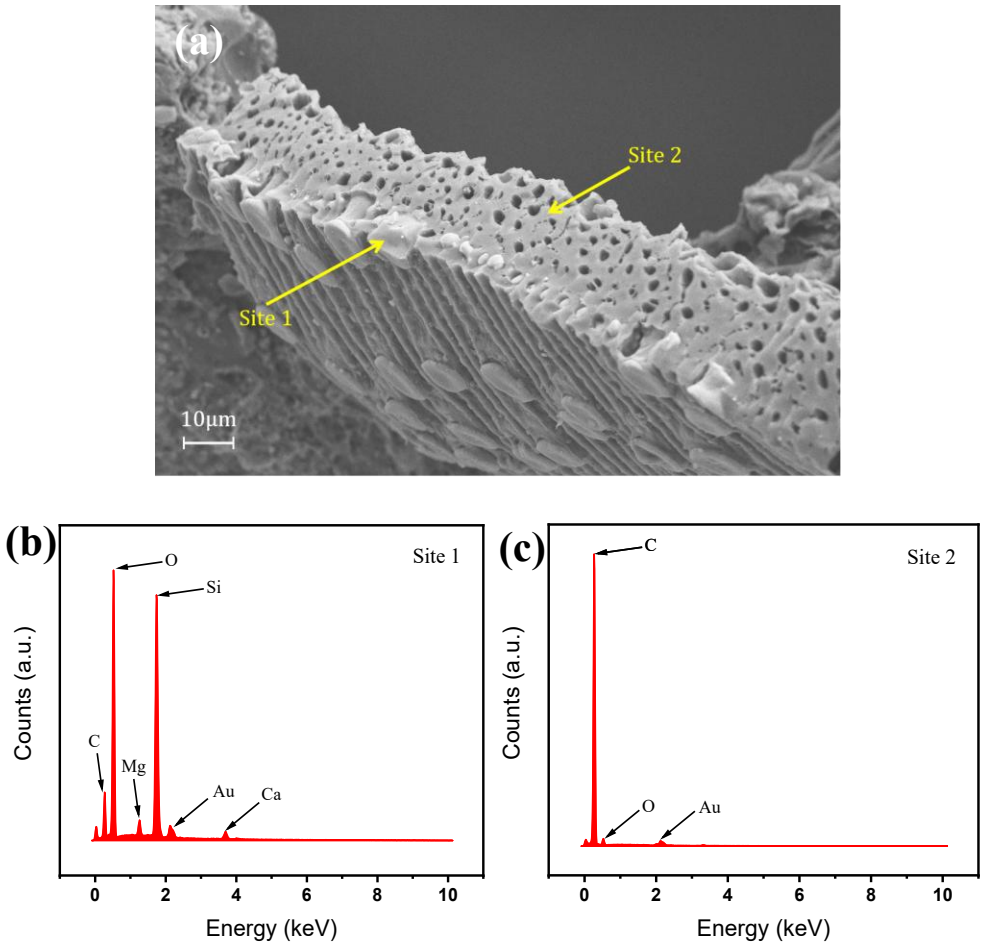

Figure 4.4. (a) SEM image of BH-T1150-BM000 sample, (b) and (c) EDX analysis of selected sites.

4.2.4. Acid washing and filtration

To remove residual soluble metal salts and trace ash without dissolving silica, powders were then immersed in 1M HCl (purchased from Merck) with a 1 g : 50 mL of solid:liquid ratio at room temperature for 8 hours. This was followed by vacuum filtration and washing with deionized water until neutralized. Finally, the product was dried at 50 °C overnight. This treatment dissolves alkali/alkaline-earth carbonates/oxides and chlorides while leaving SiO_2 largely intact. As an example, post-wash SEM with EDS elemental mapping of a BH-T1150-BM000 is reported in Fig. 4.5 which shows the distribution of C, O, and Si in the sample. The elemental mapping confirms

effective purification as the K, Mg and Ca signals are not detected after acid washing, and the same result was obtained across multiple scan areas as well as other samples, indicating uniform cleaning of the samples.

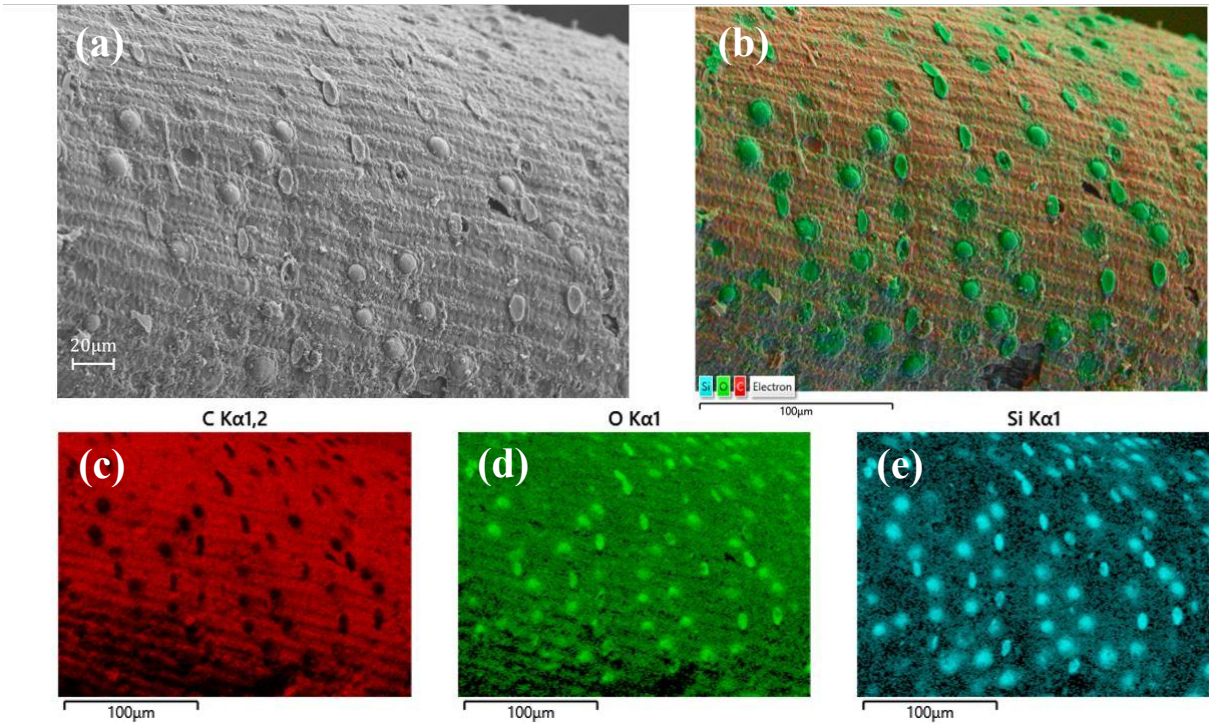

Figure 4.5. (a) SEM image of BH-T1150-BM000 powder sample after acid wash, (b) Corresponding EDX elemental mapping including Carbon, Silicon, and Oxygen, (c) Carbon mapping, (d) Oxygen mapping, and (e) Silicon mapping.

To complement the elemental mappings with chemical-state information and to probe the surface composition and oxidation states, XPS was employed on BH-T1150-BM020 sample, and the results are reported in Fig. 4.6. The XPS survey in Fig. 4.6a shows C, O and Si as the major elements. Using Gaussian functions, high-resolution spectra of C1s, O1s and Si2p were deconvoluted and presented in Fig. 4.6b to 4.6d. A primary Si2p peak is observable around 103.2 eV, which is attributable to SiO_2. The C1s spectrum includes peaks at 284.8 eV, indicative of graphite-like sp^2 hybridised C, as well as peaks at 283.65 eV and 286.4 eV, corresponding to C-Si and C-O bonds, respectively.[4] These XPS results

confirm that Si is mainly in the form of SiO_2, which is embedded in a carbon matrix. This finding aligns with our SEM/EDX observations.

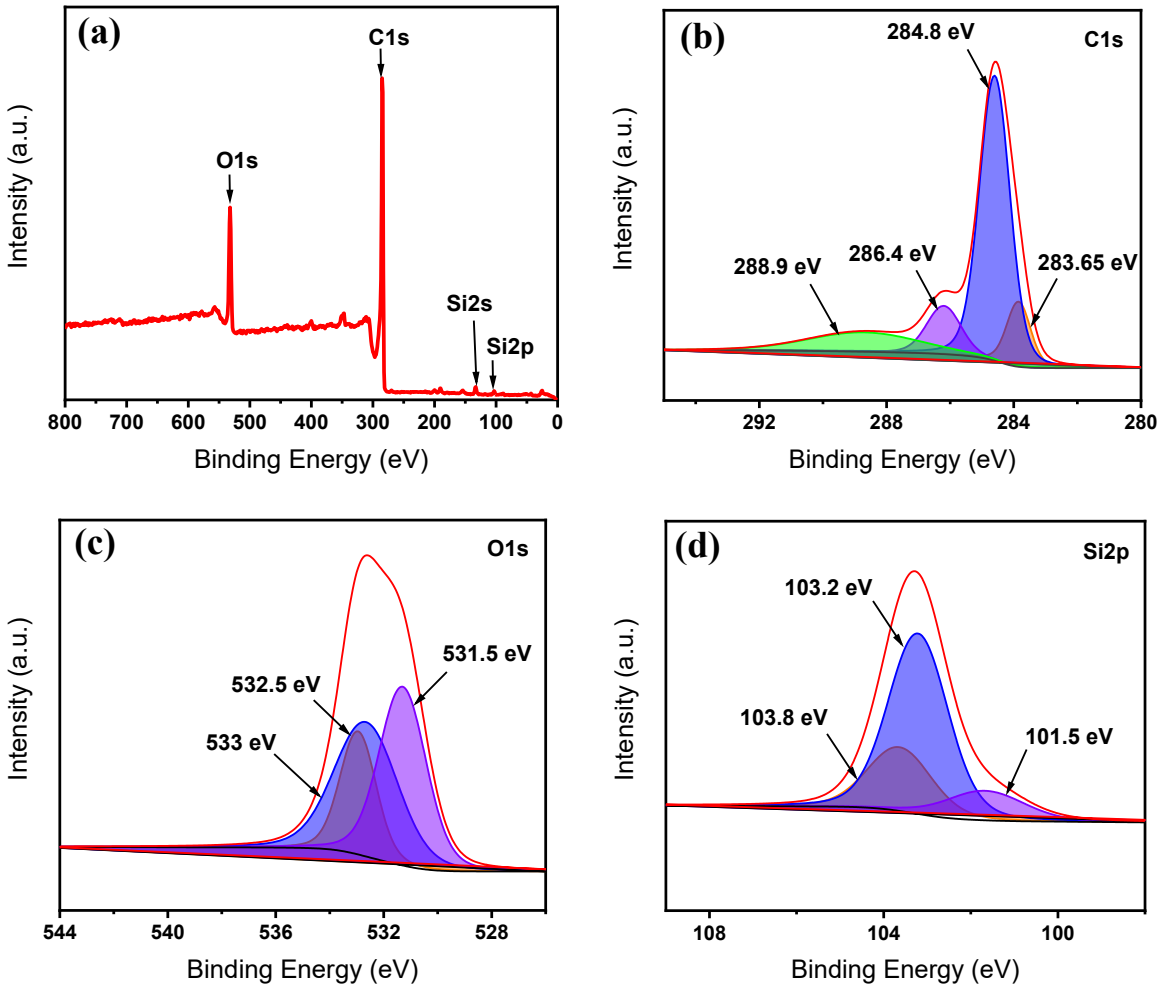

Figure 4.6. (a) XPS survey spectra of BH-T1150-BM020 and high-resolution spectra and deconvoluted peaks of (b) C1s, (c) O1s, and (d) Si2p.

The acid-washed BH-derived powder was further examined using TGA and DSC analysis to determine the silica content in the samples and the results for BH-T1150-BM000 are illustrated in Fig. 4.7. To perform this test, the sample was placed in a 40 µL platinum pan and heated to 1100 °C in synthetic air flow. The TGA profile is Fig. 4.7a shows an initial mass loss below ~200 °C from adsorbed moisture/volatiles, followed by the principal, continuous loss between ~200 and ~700 °C due to oxidation of the carbon matrix to CO

and CO_2. Beyond ~400 °C, the main mass loss is associated with oxidation of the carbon matrix, including more thermally stable carbonaceous domains.[5, 6]

The DSC profile in Fig. 4.7b shows an initial endothermic peak at approximately 100 °C, corresponding to the loss of adsorbed water in the sample. A sharp endothermic transition between 500 °C and 600 °C represents the energy required for the decomposition reactions. Beyond 700 °C, an accelerated weight decrease suggests further decomposition, potentially related to the oxidation of more resilient carbon structures or volatilization of additional carbonaceous material.[7, 8] The final residual weight (~14% at 1100 °C) indicates the presence of inorganic residue, likely SiO_2, as supported by XPS analysis. Additionally, the broad exothermic peak starting at ~700 °C is attributed to the oxidation of residual carbon.

Although the TGA/DSC data shown were obtained for BH-T1150-BM000, the absolute silica mass is expected to be the same for all samples derived from the same BH batch, irrespective of carbonisation temperature. Under flowing N_2, SiO_2 is retained during heat treatment and is not removed by the subsequent HCl wash; temperature mainly affects the carbon yield. Accordingly, the apparent SiO_2 weight fraction of the product may vary slightly with yield, but replicate measurements across the series fell within analytical scatter (≈ ±1 to 2 wt%), indicating batch consistency. The mass of biogenic silica is therefore set by the precursor batch, and TGA/DSC serves primarily to establish the silica content when changing BH source batches or comparing different precursors.

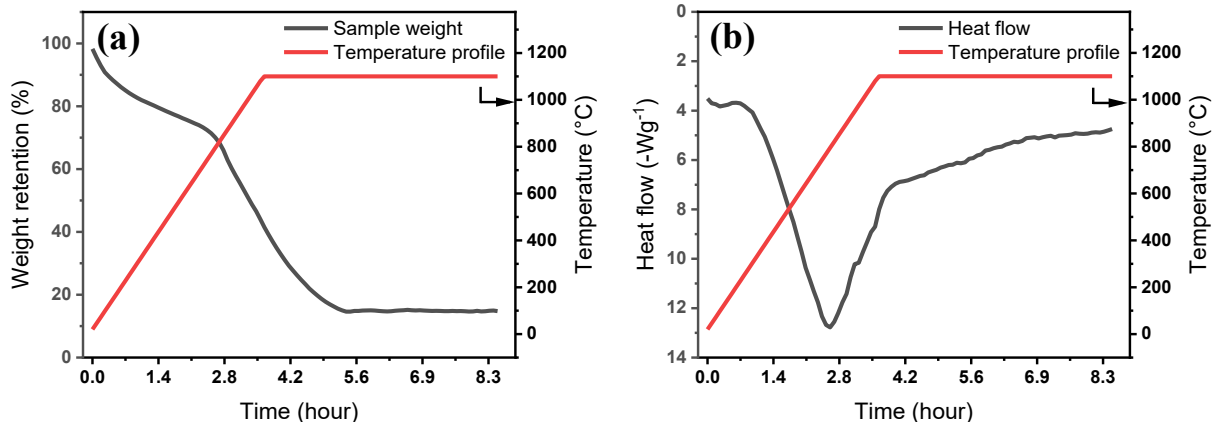

Figure 4.7. (a) TGA and (b) DSC profiles of BH-T1150-BM000 powder.

4.3. Temperature effect

4.3.1. Motivation and diagnostic tools

The carbonisation temperature is expected to greatly influence the structure of BH-derived SiO_2/C composites, yet the nature and extent of these changes are not *a priori* obvious for this specific precursor. In particular, it is necessary to determine how varying temperature would alter the arrangement and disorder of the sp^2 carbon network, as well as the stacking characteristics of turbostratic domains. To interrogate temperature as a tuning parameter, a series of BH powders was carbonised at discrete set-points from 450 to 1150 °C in 100 °C increments under N_2. To isolate temperature as the sole processing variable, the ball-milling time was fixed at 20 min for the entire series in this section. Accordingly, all temperature-varied samples discussed in this section are denoted BH-T####-BM020. After carbonisation at each set-point (450 to 1150 °C), powders were milled for 20 min under identical conditions and subjected to the single post-milling HCl wash described in Section 4.2.4. Structural characterisation (Raman and XRD) was performed on these samples so that any differences can be attributed to temperature, not milling history. The influence of milling duration itself is treated as a separate manipulated variable in Section 4.4. The corresponding electrochemical evaluation is presented in Chapter 5.

4.3.2. Raman spectroscopy across the temperature series

Raman scattering was used to probe the vibrational modes of the carbon framework and are shown in Fig. 4.8a to 4.8h for different temperatures. These Raman spectra were baseline-corrected with a Shirley background and deconvoluted into T, D, D′ and G components in CasaXPS using pseudo-Voigt line shapes (LA≈1.6) and non-linear least-squares (Levenberg-Marquardt) method. Peak positions and FWHM were lightly constrained to physically reasonable windows and the same fitting model was applied to all samples; band areas from these fits were used to compute the reported ratios. As it can be seen in Fig. 4.8, all the spectra show two main peaks at approximately 1590 cm^{-1} and 1356 cm^{-1}, corresponding to the graphitic band (G-band) and the disorder band (D-band) of carbon, respectively. The G-band can be attributed to the in-plane stretching vibration of sp^2 carbon atoms in a graphitic structure, designated to the regions of ordered graphitic carbon.

The D-band, however, is associated with the breathing modes of sp^2 atoms in rings and shows defects and disorder in the carbon structure, suggesting a significant amount of amorphous carbon or structural defects. Two auxiliary peaks were also used in the fitting. Firstly, D′ band (~1620 cm^{-1}), which is a *second* defect-activated mode arising from intra-valley scattering near Γ (longitudinal optical branch). Secondly, a low-wavenumber T band (~1000 to 1200 cm^{-1}) which is a disorder-related envelope observed in hard/disordered carbons, commonly attributed to vibrations of non-aromatic motifs and very small aromatic clusters.[9–11]

Hard carbons from biomass exhibit both defect-activated modes (D, D′) and a low-wavenumber disorder envelope (T) in addition to G. Using only D and G forces the T and D′ contributions into the baseline and inflates band areas/widths, whereas a four-component fit (with a common background and consistent constraints) can capture the physically distinct motifs, yield stable residuals, and provide interpretable metrics for comparing temperature-driven structural changes.

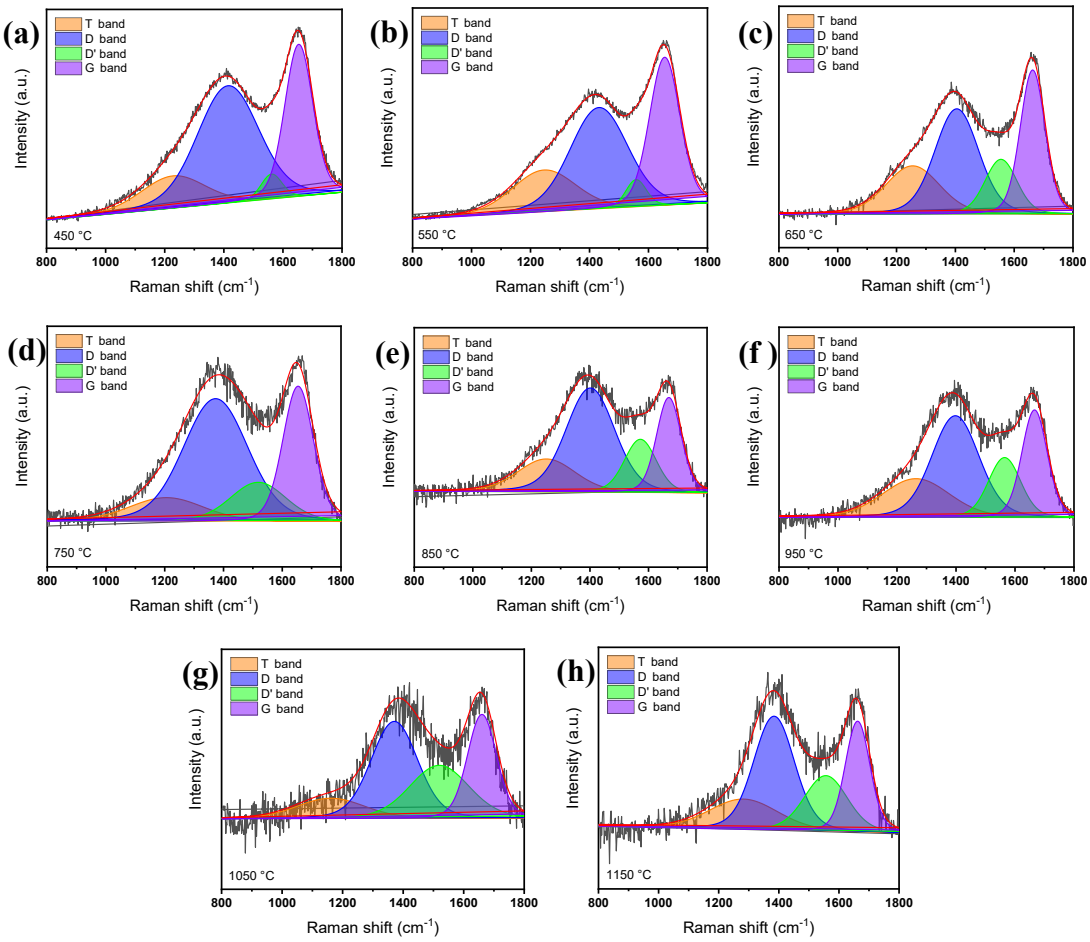

Figure 4.8. Raman spectra of BH-T###-BM020 samples with different carbonisation temperature from (a) 450 to (h) 1150 °C.

After fitting, the integrated band areas were converted into compact indices that track bonding-scale order/disorder as a function of carbonisation temperature. Let A_T, A_D, $A_{D'}$ and A_G denote the fitted areas of the T, D, D′ and G components, and define the total area as Eq. (4.1).

$$A_{tot} = A_T + A_D + A_{D'} + A_G \tag{4.1}$$

Then the graphitisation index γ can be formulated in Eq. (4.2) which captures the fraction of ordered sp² response.

$$\gamma = \frac{A_G}{A_{tot}} \tag{4.2}$$

Furthermore, the complementary total disorder index, denoted as δ in Eq. (4.3), collects the non-aromatic/sp³ contribution (T) together with defect-activated modes (D, D′).

$$\delta = \frac{A_T + A_D + A_{D'}}{A_{tot}} \tag{4.3}$$

To isolate the low-wavenumber envelope associated with small aromatic clusters and heteroatom/sp³ motifs, a non-aromatic proxy is defined as α in Eq. (4.4).

$$\alpha = \frac{A_T}{A_{tot}} \tag{4.4}$$

Finally, a γ/δ ratio as formulated in Eq. (4.5) can illustrate a crystallite/defect balance which summarises the growth of ordered sp² domains relative to the total disorder background.

$$\frac{\gamma}{\delta} = \frac{A_G}{A_T + A_D + A_{D'}} \tag{4.5}$$

Using Eqs. (4.2) to (4.5) for the sample series in this section results in the temperature trends shown in Fig. 4.9. The stacked spectra in Fig. 4.9a evolve systematically with increasing temperature, and the corresponding area-ratio indices in Fig. 4.9b confirm progressive aromatisation and ordering. Specifically, γ increases from 0.06 (450 °C) to 0.23 (1150 °C), while δ decreases from 0.945 to 0.769. The T-band fraction α falls from 0.73 to 0.57, consistent with the removal of non-aromatic/heteroatom-rich motifs. Consequently, γ/δ rises from 0.19 to 0.30, indicating that ordered sp² character grows faster than the residual disorder. These area-based metrics (derived using a common Shirley background and identical peak constraints at all temperatures) provide a quantitative bridge to the XRD stacking parameters discussed later in section 4.3.3 of this chapter.

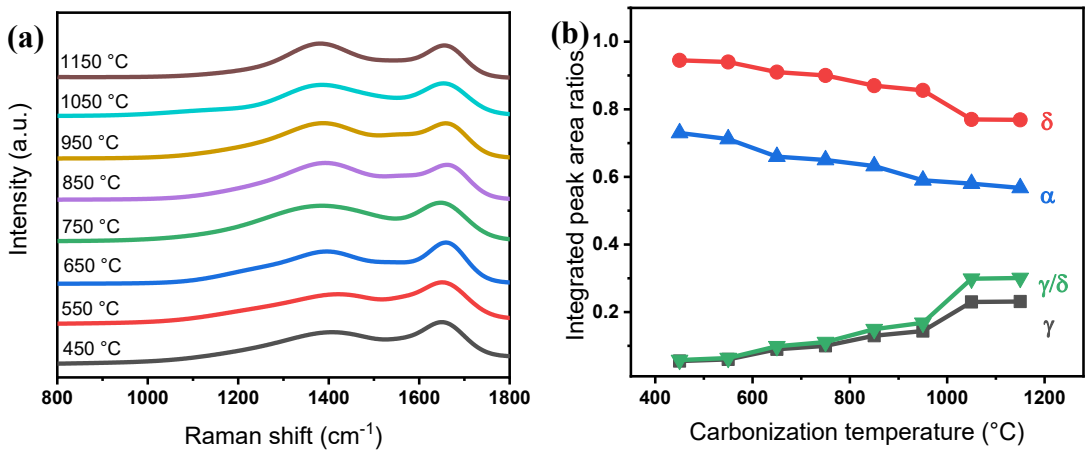

Figure 4.9. (a) stacked Raman spectra of BH-T###-BM020 samples with different carbonisation temperature from 450 to 1150 °C, and (b) variation of integrated-area indices γ, δ, α and γ/δ with respect to carbonisation temperature.

4.3.3. X-ray diffraction: stacking evolution and derived metrics

XRD measurements have been also conducted to study phase structure and crystalline properties of BH-T###-BM020 samples prepared at different carbonisation temperature and the XRD results are reported in Fig. 4.10a. The XRD analysis of each samples shows a broad peak around 23° of 2θ, which can be attributed to the overlapping peaks of the (002) plane of amorphous carbon and silica. This broad peak correlates with the interlayer spacing along the c-axis, which is effective for ion insertion if used as the negative electrode in battery. Furthermore, a characteristic peak observed at approximately 43° of 2θ corresponds to the (100) crystal plane of carbon, marking the hexagonal lattice structure typically formed by the interaction of sp^2 hybridised atoms in the carbon material. This peak is associated with the disordered turbostratic carbon structure.[12, 13] The broad nature of the peaks in these samples confirms the absence of long-range order and the presence of an amorphous carbon framework.[14, 15]

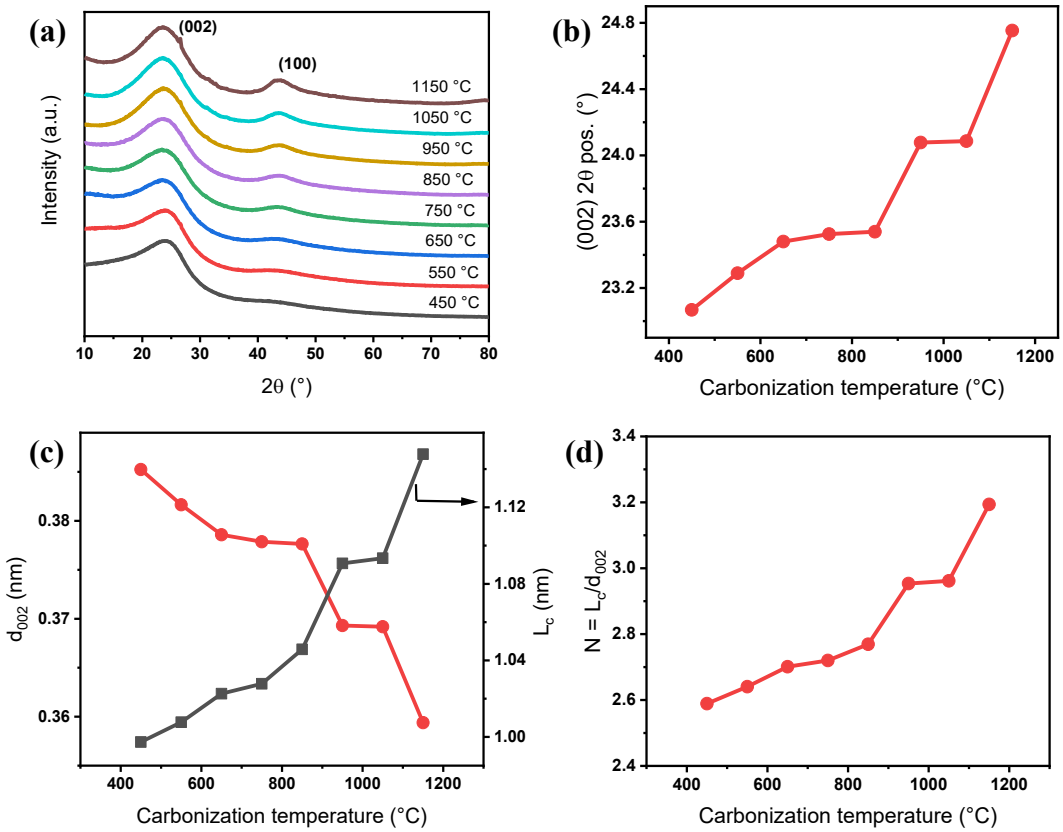

Figure 4.10. XRD variations of BH-T####-BM020 samples with respect to carbonisation temperature. (a) Stacked XRD patterns, (b) (002) peak position (2θ) shifts with temperature, (c) interlayer spacing d_{002} (left axis) and crystallite thickness L_c (right axis) with temperature, and (d) estimated layer number $N = L_c/d_{002}$.

To move beyond the qualitative identification of the (002) and (100) peaks, the structural change with temperature was quantified using the XRD results. Firstly, the interlayer spacing directly reflects turbostratic contraction or expansion and is relevant to ion insertion pathways. This parameter is calculated using Bragg's diffraction equation in Eq. (4.6)

$$d_{002} = \frac{\lambda}{2\,sin(\theta)} \tag{4.6}$$

where d_{002} is interlayer spacing, λ is the X-ray wavelength (1.54 Å for Cu Kα radiation), and θ is half of the 2θ angle for the (002) peak. The results for the (002) peak position and the interlayer spacing d_{002} are reported in Table 4.1, and their variations with carbonisation temperature can be seen in Fig. 4.10b and the left axis in Fig. 4.10c, respectively. The (002) maximum shifts from

23.06° at 450 °C to 24.75° at 1150 °C. The increase is gradual up to ~850 to 950 °C, followed by a sharper rise to 24.75° at 1150 °C, consistent with temperature-driven contraction of the average interlayer spacing reported in the literature.[11, 16] Calculated d_{002} decreases in steps from 0.38 nm (450 to 550 °C) to 0.37 nm (650 to 850 °C), 0.36 nm (950 to 1050 °C) and 0.35 nm at 1150 °C, showing an overall of 7.9% contraction. Even at the highest temperature, d_{002} is still larger than that of ideal graphite (0.335 nm),[17] confirming a turbostratic rather than a fully graphitic structure.

The other quantitative parameters used in this section are crystallite thickness and the corresponding layer count describe the size of stacked domains along the c-axis and are often correlated with electronic transport and SEI stability. Crystallite size along the c-axis (L_C) is calculated using Scherrer equation as formulated in Eq. (4.7)

$$L_C = \frac{K\lambda}{\beta_c \cos(\theta)} \tag{4.7}$$

where K is the Scherrer constant (0.89 for carbon materials), and β_c is the full width at half maximum (FWHM) of the (002) peak in radians and it is corrected for instrumental broadening. To calculate β_c, The (002) peak was first fitted with a pseudo-Voigt function after linear background subtraction (same 2θ window for all samples). The measured FWHM, β_{meas}, was taken from the fit and corrected for instrumental broadening using a silicon standard as formulated in Eq. (4.8)

$$\beta_c = \sqrt{\beta_{meas}^2 - \beta_{inst}^2} \tag{4.8}$$

where β_{inst} is the FWHM of the standard measured under identical optics and scan settings. The corrected β_c was then used in Eq. (4.7) to compute L_C. Using the calculated L_C and d_{002}, number of carbon Layers along the c-axis (N) can be calculated using Eq. (4.9) formulation.

$$N = \frac{L_C}{d_{002}} \tag{4.9}$$

Results for L_C and N are listed in Table 4.1 and their variations with carbonisation temperature are plotted in Fig. 4.10c and 4.10d, respectively. The crystallite thickness along the c-axis L_c increases from 0.997 nm to 1.147 nm, showing a 15.1% increase. Furthermore, the estimated number of layers per stack rises from 2.59 (450 °C) to 3.19 (1150 °C) which

indicates 23.4% increase. The steepest increase occurs beyond ~950 °C, where simultaneous d_{002} contraction and L_C growth compound.

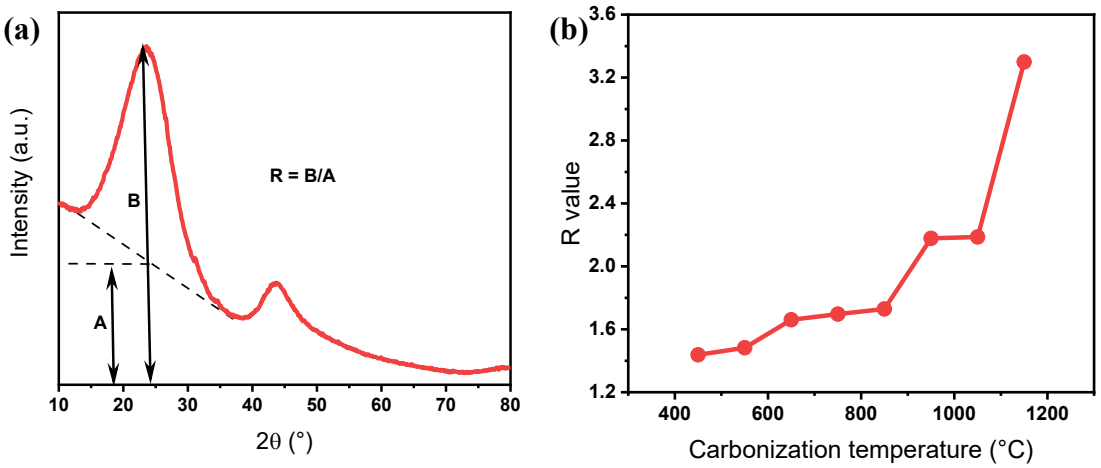

Figure 4.11. (a) Visual representation of A and B values from XRD spectrum used in Eq. (4.10), and (b) variations of R value with carbonisation temperature.

Additionally, an empirical sharpening factor R is used to further distinguish structural differences induced by carbonisation temperature. This empirical factor captures the progressive definition of the (002) peak and provides a sensitive probe of ordering when peak decomposition is broad. This parameter follows Eq. (4.10)

$$R = \frac{B}{A} \tag{4.10}$$

where B is the peak intensity and A is the local baseline intensity, which are illustrated in Fig. 4.11a and can be also found in Table 4.1. The variation of R value with temperature is also reported in Table 4.1, as well as its illustration Fig. 4.11b. Although R has no absolute physical meaning, it provides a sensitive internal descriptor of peak definition when used consistently across the series. The baseline under (002) decreases from A = 1568 to 900, which translated to a 42.6% change, while the peak height increases from B = 2254 to 2969, which is a 31.7% increase. These opposing trends yield progressively cleaner patterns with a more defined (002) feature, resulting in R to be increased strongly from 1.44 to 3.30 (≈+130%). As R combines peak intensification with baseline suppression, it serves as a sensitive single-number descriptor of ordering; its sharp rise beyond

~950 to 1150 °C aligns with the inflection seen in d_{002}, FWHM and N, and with the Raman indices (γ, δ, α) for the same temperature window.

In general, the tabulated values extracted from the diffraction series show the same monotonic behaviour: (002) 2θ increases with temperature, d_{002} decreases, L_C and N increase, and R improves. Taken together, the XRD analysis confirms a move towards more ordered turbostratic stacks at higher carbonisation temperatures while retaining the amorphous/turbostratic character expected for hard carbons.

Table 4.1. The detailed XRD results of the BH-T###-BM020 samples.

Temperature (°C)	(002) 2θ pos. (°)	FWHM	d_{002} (nm)	L_c (nm)	N	A	B	R
450	23.06	8.13	0.38	0.997	2.588	1568	2254	1.437
550	23.28	8.05	0.38	1.007	2.640	1529	2267	1.482
650	23.48	7.93	0.37	1.022	2.701	1520	2524	1.660
750	23.52	7.89	0.37	1.027	2.720	1509	2560	1.696
850	23.53	7.76	0.37	1.045	2.769	1498	2590	1.728
950	24.07	7.44	0.36	1.090	2.953	1333	2903	2.177
1050	24.08	7.43	0.36	1.093	2.961	1329	2906	2.186
1150	24.75	7.08	0.35	1.147	3.193	900	2969	3.298

4.4. Ball milling effect

4.4.1. Motivation and diagnostic tools

Ball milling is treated here as the second manipulated variable, orthogonal to carbonisation temperature. Its primary role is expected to be textural, affecting particle size, interparticle packing and the development of accessible porosity, rather than altering the bulk chemistry or phase of the BH-derived SiO_2/C. To isolate milling effects, the carbonisation temperature is fixed at T = 1150 °C, and powders are processed at defined durations (BM000, BM010, BM020, BM060, BM120) under identical conditions and post-treated by the same HCl wash. The objective is to quantify how milling time controls accessible surface area, pore-size distribution (particularly in the

mesopore regime), and pore volume/connectivity, as these attributes govern slurry dispersion, electrolyte infiltration and kinetic response in electrodes.

Nitrogen physisorption at 77 K is adopted as the principal tool because it provides reproducible, model-agnostic metrics of texture for disordered carbons. The BET specific surface area (SSA) is determined from the adsorption isotherm using the Rouquerol criteria to select the linear region (positive C constant; $V(1-P/P_0)$ increasing with P/P_0). From the same dataset, the external/micropore split can be estimated by t-plot analysis, and the mesopore size distribution extracted from the desorption branch via BJH (2 to 50 nm) together with the cumulative pore volume near $P/P_0 \approx 0.98$. Nitrogen is adequate here because milling predominantly generates mesopores and external surface; CO_2 (273 to 298 K) would be reserved for sub-nanometre micropores if required. All samples are degassed under vacuum (e.g., 120 °C until a stable outgassing rate) to a common protocol, and the same mass, equilibration and analysis settings are applied across the series to ensure comparability.

The section proceeds by reporting the adsorption-desorption isotherms, BET SSA, BJH distributions and cumulative pore volumes for BH-T1150-BM### samples. These textural descriptors are used in upcoming chapters to interpret electrolyte access, charge-transfer kinetics and rate performance, with milling time serving as a practical processing lever.

4.4.2. N_2 adsorption-desorption analysis

After degassing each BH-T1150-BM### powder to a constant outgassing rate, N_2 adsorption-desorption isotherms at 77 K were recorded under identical instrument settings. The specific surface area and pore metrics were derived from the adsorption branch using the Brunauer-Emmett-Teller (BET) formalism with the Rouquerol selection to ensure a physically valid linear region.

The BET formalism is written as Eq. (4.11)

$$\frac{P}{V(P_0 - P)} = \frac{1}{V_m C} + \frac{(C-1)}{V_m C}\frac{P}{P_0} \tag{4.11}$$

where P is the equilibrium pressure, P_0 the saturation pressure, V the adsorbed volume at P, V_m the monolayer capacity, and C the BET constant related to the adsorbent-adsorbate interaction. To avoid over- or under-estimating V_m, the linear fitting range was chosen according to Rouquerol criteria: (i) the calculated $V(1 - P/P_0)$ increases monotonically with P/P_0; (ii) the intercept and slope of Eq. (4.11) are positive (therefore $V_m > 0$ and $C > 0$); and (iii) the resulting surface coverage lies within the classical BET regime (typically $P/P_0 \approx 0.05$ to $P/P_0 \approx 0.30$) for these carbons. With the best-fit slope s and intercept i as described in Eq. (4.12) and (4.13).

$$V_m = \frac{1}{s + i} \tag{4.12}$$

$$C = 1 + \frac{s}{i} \tag{4.13}$$

The BET specific surface area was then obtained from V_m via Eq. (4.14)

$$S_{BET} = \frac{V_m N_A s_{N_2}}{m} \tag{4.14}$$

where N_A is Avogadro's number, $s_{N_2} = 0.162\ nm^2\ molecule^{-1}$ is the N_2 molecular cross-section at 77 K, and m is the sample mass (converted to the same molar volume basis as V_m).

To probe micropore/external area partitioning, a t-plot was constructed using a standard statistical thickness equation for N_2 at 77 K; the linear region of V vs film thickness t results an external surface area from the slope and a micropore volume V_μ from the intercept in Eq (4.15)

$$V = S_{ext} t + V_\mu \tag{4.15}$$

For mesopore size distribution (2 to 50 nm), the BJH method was applied to the desorption branch, using the Kelvin relation in Eq. (4.16) and with an adsorbed-film thickness correction as formulated in Eq. (4.17)

$$\ln\left(\frac{P}{P_0}\right) = -\frac{2\gamma V_\ell}{r_k RT} \tag{4.16}$$

$$r_p = r_k + t \tag{4.17}$$

where γ is the surface tension of liquid N_2, V_ℓ its molar volume, r_k the Kelvin radius, r_p the pore radius and t the statistical film thickness.

Isotherms and BJH outputs are presented in Fig. 4.12a and 4.12b, and the derived parameters are summarised in Table 4.2.

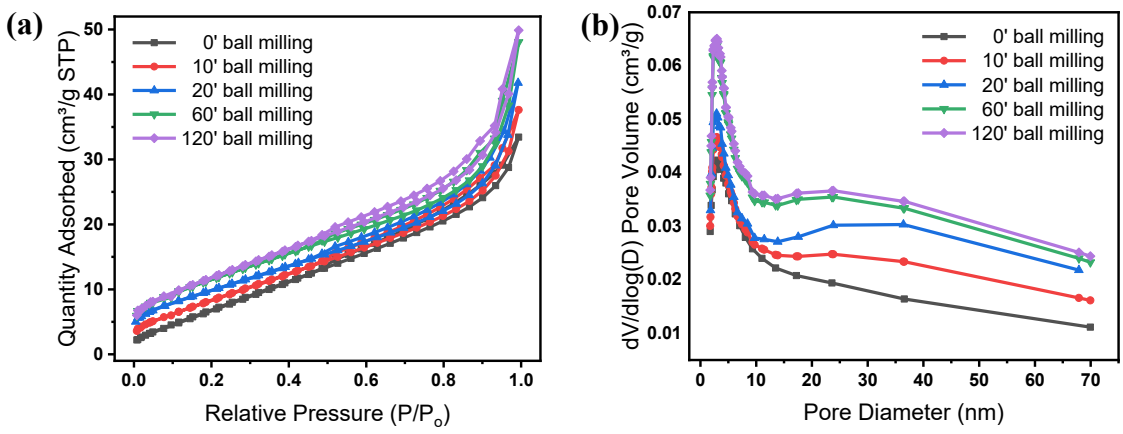

Figure 4.12. N_2 physisorption of BH-T1150-BM### at 77 K. (a) Adsorption-desorption isotherms, and (b) BJH mesopore size distributions from the desorption branch.

Table 4.2. Textural parameters from N_2 physisorption (77 K) for BH-T1150-BM###.

	0' ball milling	10' ball milling	20' ball milling	60' ball milling	120' ball milling
$\mathbf{V_m (cm^3/g)}$	7.59	8.03	8.71	10.05	10.42
$\mathbf{S_{BET} (m^2/g)}$	33.03	34.93	37.93	43.72	45.34

As shown in Fig. 4.12a, the adsorption-desorption isotherms for BH-T1150-BM### samples are Type IV with an H3/H4-like hysteresis loop opening from $P/P_0 \approx 0.4$ to 1.0, consistent with slit-type mesoporosity generated by fracture and de-agglomeration during milling. The BJH desorption distributions in Fig. 4.12b exhibit a dominant mesopore band centred in the 2 to 5 nm range with a broad tail extending to tens of nanometres, indicating mesopores with some macropore access.

Quantitatively, BET analysis using Eqs. (4.11) to (4.14) results in a monotonic rise in monolayer capacity V_m and surface area S_{BET} with milling time (Table 4.2). Relative to BM000 (no milling), V_m increases from 7.59 to 8.03, 8.71, 10.05 and 10.42 cm³ g⁻¹ for 10, 20, 60 and 120 minutes, corresponding to gains of 5.8%, 14.7%, 32.4% and 37.3%, respectively. The associated S_{BET} rises from 33.03 to 34.93, 37.93, 43.72 and 45.34 m² g⁻¹, i.e., +5.8%, +14.8%, +32.4% and +37.3%, mirroring the V_m trend as expected from Eq. (4.14). The largest increment occurs between BM000

and BM060 showing a net increase of 10.7 $m^2\ g^{-1}$, after which the gain from BM060 to BM120 shows a modest increase of 1.62 $m^2\ g^{-1}$.

The BJH analysis in Eq. (4.16) supports this interpretation: the mesopore band strengthens markedly from BM000 to BM020, grows further at BM060, and changes only slightly at BM120; the distributions for BM060 and BM120 are nearly superimposed over 2 to 50 nm. Together with the isotherm opening in Fig. 4.12a, this indicates that accessible mesopore volume and external surface are largely established by short-to-moderate milling (≤ 60 min). Prolonged milling to 120 minutes offers only incremental surface growth and may promote limited re-agglomeration or pore coalescence, which counteracts further activation.

In summary, the five-point series demonstrates that ball milling at T = 1150 °C mainly modulates texture; V_m and S_{BET} increase by ~15% at 20 minutes, by ~32% at 60 minutes, and approach a plateau by 120 minutes, while the BJH mesopore envelope retains its position and broad shape. These observations, derived from Eqs. (4.11) to (4.16) and reported in Fig. 4.12 and Table 4.2, provide a quantitative basis for selecting milling time as a practical lever for electrolyte access and kinetics; the electrochemical implications are evaluated in Chapter 5.

4.5. Conclusion

This chapter defined a robust route to BH-derived SiO_2/C powders and established how carbonisation temperature and ball-milling time set their structural state. Carbonisation under N_2 from 450 to 1150 °C produced a progressive transition from defect-rich amorphous carbon to more ordered turbostratic stacks. Raman spectra fitted with a four-band model (T, D, D′, G) were converted into area-ratio indices that increased the information content beyond the conventional I_D/I_G ratio. With rising temperature, γ increased while δ and α decreased, evidencing aromatisation and the attenuation of non-aromatic/heteroatom motifs. XRD corroborated this evolution quantitatively: the (002) peak shifted to higher 2θ with a contraction of d_{002} from 0.38 to 0.35 nm, while L_c and the layer count N increased and the empirical sharpening factor R more than doubled. The structure remains turbostratic at all temperatures ($d_{002} > 0.335$), consistent with hard-carbon behaviour rather than graphitisation.

At fixed T = 1150 °C, ball milling acted primarily on texture. N_2 physisorption showed Type-IV isotherms with H3/H4-type hysteresis for all samples; V_m and S_{BET} rose from 7.59 $cm^3\ g^{-1}$ and 33.0 $m^2\ g^{-1}$ (BM000) to 10.42 $cm^3\ g^{-1}$ and 45.3 $m^2\ g^{-1}$ (BM120), respectively, with the largest gains achieved by BM060 and only modest change thereafter. BJH analysis revealed a stable mesopore band (≈2 to 5 nm) whose intensity increased with milling, indicating that accessible mesopore volume and external surface are largely established by short-to-moderate milling. Microscopy confirmed the associated fragmentation and improved dispersion of silica-rich domains.

Together these results show that temperature controls bonding and stacking, whereas milling controls accessible texture. The processing windows identified here as T ≳ 950 °C for tightened turbostratic stacking and BM ≈ 20 to 60 min for efficient textural activation. These processing windows provide practical levers for electrode design. The impact of these structural states on initial coulombic efficiency, rate capability, SEI formation and long-term cycling is analysed in Chapter 5, where the structure descriptors developed here are used directly to interpret electrochemical behaviour such as initial Coulombic efficiency, rate capability and ageing signatures.

4.6. References

[1] C. Li, Wenbin and Huang, Jianfeng and Feng, Liangliang and Cao, Liyun and Ren, Yijie and Li, Ruizi and Xu, Zhanwei and Li, Jiayin and Yao. *J Alloys Compd* 2017,716,210–219.

[2] D. Alvira, D. Antorán, J.J. Manyà. *Chemical Engineering Journal* 2022,447,137468.

[3] Y. Feng, L. Liu, X. Liu, Y. Teng, Y. Li, Y. Guo, Y. Zhu, X. Wang, Y. Chao. *Electrochim Acta* 2020,359,136933.

[4] Y. Li, L. Liu, X. Liu, Y. Feng, L. Yu, Z. He, X. Cui, M. Zhang, Y. Zhu. *Ionics (Kiel)* 2022,151–160.

[5] R.F. Susanti, S. Alvin, J. Kim. *Journal of Industrial and Engineering Chemistry* 2020,91,317–329.

[6] A. Jo, B. Lee, B. Guk, H. Lim, J. Tark, S. Yol, J. Kim, S. Hee, H. Jin, G. Lee, K. Baeg, B. Jeong, J. Hwan. *Carbon N Y* 2023,201,549–560.

[7] M. Jiao, J. Qi, Z. Shi, C. Wang. *J Mater Sci* 2018,53,2149–2160.

[8] H. Cheng, N. Garcia-Araez, A.L. Hector. *Mater Adv* 2021,2,7956–7966.

[9] Y. Feng, X. Liu, L. Liu, Z. Zhang, Y. Teng, D. Yu, J. Sui, X. Wang. *ChemistrySelect* 2018,3,10338–10344.

[10] H.D. Asfaw, R. Gond, A. Kotronia, C.W. Tai, R. Younesi. *Sustainable Materials and Technologies* 2022,32,e00407.

[11] L. Sbrascini, A. Staffolani, L. Bottoni, H. Darjazi, L. Minnetti, M. Minicucci, F. Nobili. *ACS Appl Mater Interfaces* 2022,14,33257–33273.

[12] W. Lee, H. Jang, M. Kim, H. Kim, J. Oh, S. Paek. *J Alloys Compd* 2019,778,382–390.

[13] D. Bhattacharjya, H.Y. Park, M.S. Kim, H.S. Choi, S.N. Inamdar, J.S. Yu. *Langmuir* 2014,30,318–324.

[14] M.K. Rybarczyk, Y. Li, M. Qiao, Y. Hu, M. Titirici, M. Lieder. *Journal of Energy Chemistry* 2019,29,17–22.

[15] Y. Li, X. Liu, L. Liu, W. Liu, Y. Feng, Y. Guo, Y. Zhu, J. Wang, X. Wang. *J Electrochem Soc* 2019,166,A2425.

[16] H. Parsimehr, A. Ehsani, S. Ahmadreza. *Biomass Convers Biorefin* 2021,14,12413–12429.

[17] S.H. Huh. *Carbon N Y* 2014,78,617–621.

5. Electrochemical performance of barley-husk-derived SiO_2/C anodes in Li-ion batteries

5.1. Introduction

This chapter evaluates the electrochemical behaviour of barley-husk-derived silica/carbon composites (BH-T####-BM###) in Li-ion half-cells and establishes how processing governs performance. Chapter 4 showed that carbonisation temperature sets bonding-scale order and turbostratic stacking, while ball-milling modulates texture (surface area and mesoporosity). Here, those two variables are mapped to cell-level responses under a single, standardised electrode formulation and electrolyte. The study proceeds in two stages: first, the effect of carbonisation temperature is examined at fixed milling time (BM020); second, the effect of milling duration is assessed at fixed temperature (1150 °C). For each subset, galvanostatic voltage profiles, cycling and rate metrics, and EIS-derived kinetic parameters (including the apparent Li^+ diffusivity) are reported. The goal is to identify a processing window that maximises reversible capacity, rate capability and kinetic efficiency under practical loadings, while maintaining acceptable initial coulombic efficiency. The optimised condition derived here is then carried forward as a baseline for the head-to-head graphite benchmark in Chapter 6.

5.2. Scope, test protocol, and performance metrics

All measurements were carried out on CR2016 half-cells prepared with identical electrode architecture, electrolyte and testing schedule to isolate the contribution of the active material only. Slurry composition, coating and cell assembly are given in Sections 5.2.1 and 5.2.2.

5.2.1. Slurry formulation and coating

Slurries containing the respective active material (BH-T####-BM###), conductive agent (carbon black, C65) and binder (22.5 g L^{-1} polyacrylic acid in water) in a mass ratio of 7:2:1 were prepared using deionised water as the solvent. This choice of binder, conductive agent, and the mass ratio has been widely adopted for SiO_x/C and hard-carbon anodes due to its

mechanical robustness and favourable interaction with SEI components.[1–4] The working anodes were fabricated by casting the prepared slurries with an applicator gap of 200 µm onto copper-foil current collectors, followed by drying in a vacuum oven (Fistreem M Oven VAC1600) at 80 °C for 12 hours. The prepared electrodes were then punched into circular disks with a diameter of 14 mm (1.54 cm^2) area and a mass loading of 1.0 to 1.5 mg cm^{-2} (typically ~1.0 mg cm^{-2} for the datasets reported here).

5.2.2. Coin-cell assembly

The punched electrodes were subsequently transferred to an argon-filled glovebox (MBRAUN UNIlab plus ECO with <0.5 ppm of O_2 and H_2O atmospheric conditions) to be used as anodes in CR2016 coin cells. Li metal chips and microporous membranes (Celgard 2500) were used as the counter electrode and separator, respectively. The overall half-cell configuration is illustrated schematically in Fig. 5.1. Additionally, 1.2 M $LiPF_6$ in ethylene carbonate/ethyl methyl carbonate (EC:EMC = 1:3 v/v) with 15 wt% fluoroethylene carbonate (FEC) and 3 wt% vinylene carbonate (VC) was used as the electrolyte (purchased from Shenzhen Laborxing Technology Ltd). This electrolyte formulation is widely used for SiO_x and hard-carbon anodes, as the high-EMC solvent blend offers low viscosity and good ionic conductivity, while the FEC/VC co-additives promote the formation of a stable, inorganic-rich SEI on high-surface-area electrodes and suppress continuous electrolyte decomposition.[1] After assembly, the cells were rested for 24 h before testing. After resting, the coin cells were removed from the glove box for testing. Electrochemical performance was evaluated using several methods. Galvanostatic cycling, rate testing, cyclic voltammetry (CV) and electrochemical impedance spectroscopy (EIS) were performed as detailed in Section 5.2.3.

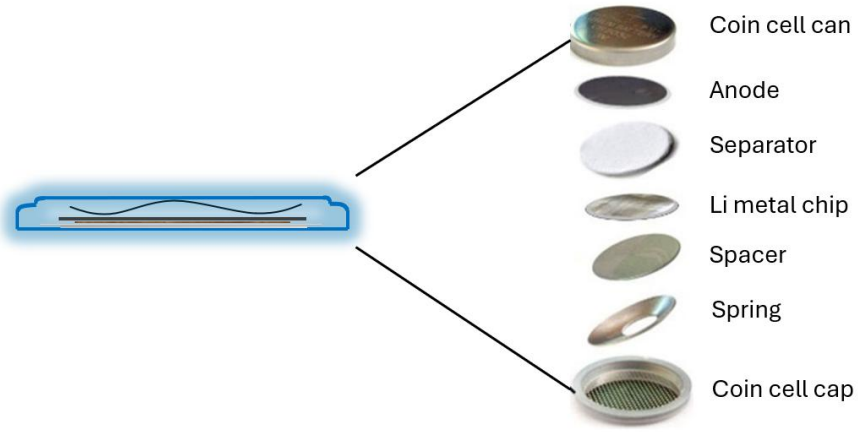

Figure 5.1. Schematic illustration of a coin-cell half-cell configuration used in this work, showing the sequence of components (not to scale).

5.2.3. Testing protocol

Before describing the testing protocols, three performance metrics frequently used in the following analysis are briefly defined: C-rate, initial coulombic efficiency (ICE) and capacity retention. The C-rate denotes the current that would charge or discharge the active material in 1 h (1C); C/5 and C/20 correspond to currents five- and twenty-fold lower, respectively. The ICE is the percentage of charge recovered during the first charge step relative to the charge inserted during the first discharge step. It indicates how much of the active transporting ion (in this case Li^+) inserted in the first cycle participates in reversible storage, with lower ICE values reflecting larger irreversible losses associated with solid-electrolyte interphase (SEI) formation, electrolyte decomposition and structural rearrangements. Capacity retention at a given cycle is expressed as the reversible capacity at that cycle relative to the capacity in a chosen reference cycle (typically the first cycle after formation), reported as a percentage; it therefore quantifies how well the electrode maintains its capacity during prolonged cycling.

All cells underwent two initial formation cycles at C/20 between 0.01 and 3.0 V, followed by galvanostatic cycling at C/5 within the same voltage window for up to 50 cycles, with 1 min rest periods prior to each discharge step. The overall formation and cycling schedule is summarised in the flowchart in Fig. 5.2. Unless otherwise stated, capacities are quoted from the 5^{th} cycle onwards to avoid the formation transient. An analogous protocol was used for long-term cycling, in which the number of discharge-charge cycles was extended at the same current and voltage limits to assess the long-term stability of the cells.

Additionally, rate performance used a stepped sequence C/10 (5 cycles) → C/5 (5) → C/3 (5) → 1C (5) → C/10 (5). CV was performed at 0.2 mV s^{-1} within 0.01 to 3.0 V to identify redox features associated with the carbon and silica components. EIS used a 5 to 10 mV perturbation over 100 to 0.01 Hz at open circuit, immediately after the 1st and 50th galvanostatic cycles. Spectra were fitted by non-linear least squares using the equivalent circuit in Fig. 5.5. The Warburg coefficient σ was obtained from the low-frequency linear relation in Eq. (5.1); the apparent diffusion coefficient D_{Li^+} was then calculated from Eq. (5.2) using a common set of geometric-thermodynamic parameters for all cells to ensure comparability.

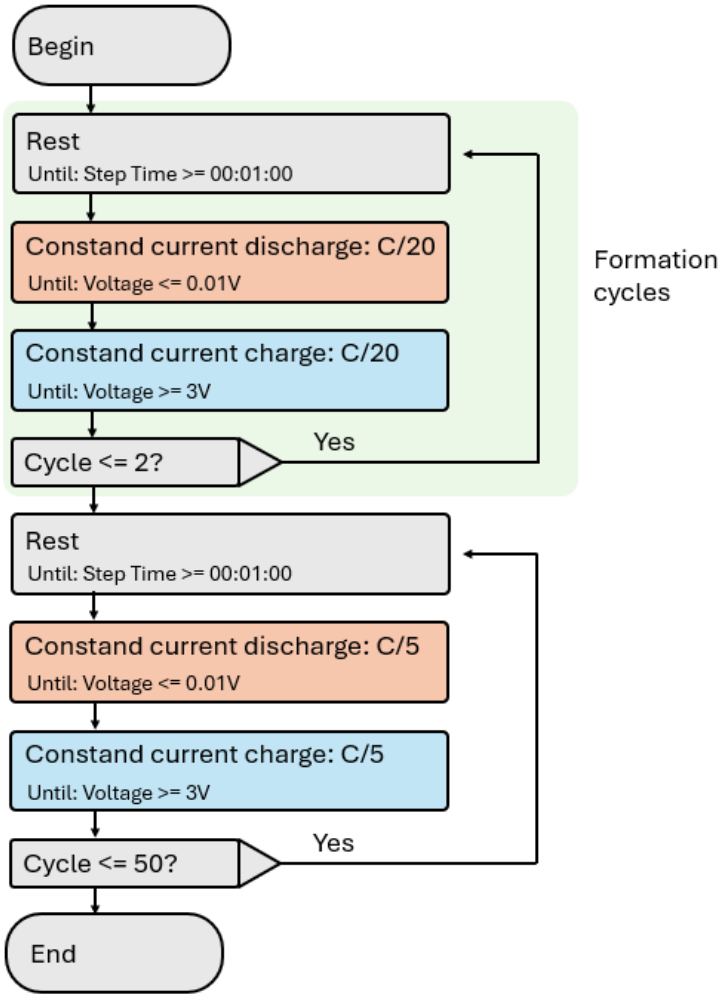

Figure 5.2. Flowchart of the 50-cycle galvanostatic testing protocol consist of formation and cycling steps used for the Li-ion half-cells for the datasets shown in this chapter.

5.2.4. Quality control and traceability

Slurry preparation and coating were standardised to stabilise electrode architecture. Solids content was maintained in the 35 to 40 wt% range, with viscosity at room temperature constrained to ~600 to 1200 mPa·s to ensure reproducible casting. Finished electrodes were required to meet a target loading of 1.0 to 1.5 mg cm^{-2} on Cu with an intra-sheet variation ≤ ±0.05 mg cm^{-2}; thickness and areal density were cross-checked to keep porosity within ~30 to 45%, avoiding densification differences that could mask the effects of T or BM.

Finally, a light electrochemical screen of the sentinel cell (same electrolyte and loading as the study set) provided an operational check: third-cycle capacity at C/10 ≥ 300 mAh g^{-1} within ±5%, and charge-transfer resistance from fresh-cell EIS within ±20% of the sentinel mean, with solution resistance stable to ±10%. Instrument calibrations (XRD 2θ using a Si standard; Raman wavenumber at 520.7 cm^{-1}; mass balances; gas-flow meters) were verified on a monthly schedule and logged alongside sample IDs. Furthermore, for each condition, multiple coin cells were assembled and tested to confirm reproducibility. Reported electrochemical values, including ICE, were based on consistent behaviour across replicate cells and averaged where appropriate. Collectively, these measures underpin the comparisons made in Sections 5.3 and 5.4, ensuring that observed trends are attributable to the carbonisation temperature and ball-milling time rather than uncontrolled processing variance.

5.3. Effect of carbonisation temperature

Chapter 4 established that carbonisation temperature governs bonding-scale order and turbostratic stacking, with 550 °C to 1150 °C spanning the transition from highly defective char to more ordered hard carbon. To isolate this variable electrochemically, ball-milling time was fixed at 20 min (BM020), and all electrodes were prepared, formed and tested under the same conditions (electrolyte, binder, loading and protocol defined in Section 5.2). The four temperatures selected were 550, 750, 950 and 1150 °C, so sample distinct structural follow the same texture and cell chemistry.

Fig. 5.3 shows the galvanostatic charge-discharge (lithiation-delithiation) profiles of the first five cycles for each temperature. From these voltage profiles, it can be seen that all samples show an initial slope in their discharge direction from 1.0 V to ~0.2 V vs Li^+/Li. This slope is

associated with adsorption-defect and surface-controlled storage, and it is followed by a low-voltage segment (≲0.2 V) attributed to interlayer nanopore filling. Such voltage profiles showcase the characteristics behaviour hard carbon anodes.[5, 6]

Across the temperature series, the first-cycle irreversibility decreases systematically with the carbonisation temperature. As summarised in Fig. 5.4b, the ICE rises from 48.6 % at 550 °C to 50.2 % (750 °C) and 51.4 % (950 °C), and finally reaching 59.2 % at 1150 °C. This trend aligns with the higher graphitization degree of the samples at higher carbonisation temperatures reported in Chapter 4, which diminishes irreversible uptake during formation; therefore, the 1150 °C sample shows the smallest first-cycle capacity loss.

The <0.2 V segment of the voltage profiles in Fig.5.3 grows progressively with temperature. In the BH-T1150-BM020 anode, the low-voltage contribution is visibly longer and flatter by cycles 2 to 5 than in the anodes with 550 to 750 °C samples, consistent with tighter stacking (smaller d_{002}) and thicker turbostratic domains providing more efficient interlayer storage (as shown in Section 4.3). Conversely, the BH-T550-BM020 anode is dominated by the higher-voltage slope with only a short low-voltage segment.

Another notable trend is that the separation between charge and discharge traces (hysteresis) narrows with temperature, and the profiles stabilise within the first 3 to 5 cycles for all samples. Lower-temperature anodes show a larger early-cycle drift, consistent with more extensive SEI growth and surface reactions.

Overall, these voltage profiles link the temperature-set structure to the storage mechanism. Increasing temperature suppresses defect-to-surface-dominated uptake (reducing irreversible loss) while enhancing the low-voltage, interlayer contribution that carries useful reversible capacity.

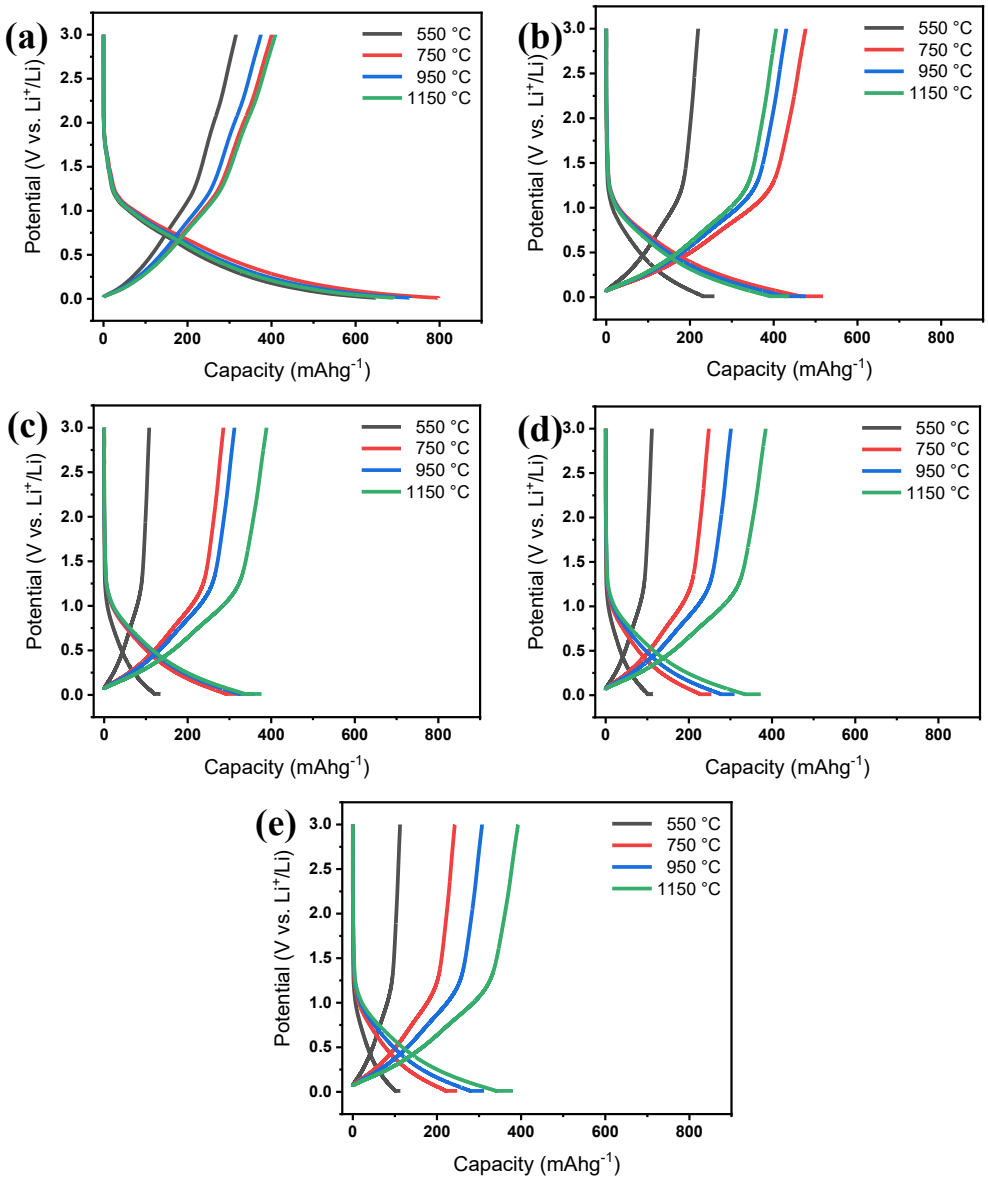

Figure 5.3. Charge-discharge voltage profiles of BH-T####-BM020 anodes with active materials prepared at different carbonisation temperatures at their (a) 1st, (b) 2nd, (c) 3rd, (d) 4th, and (e) 5th cycle under a C/5 current.

The cycling performance and CE of the BH-T####-BM020 anodes over their first 50 cycles at a current of C/5 are shown in Fig. 5.4a. All anodes exhibit a rapid capacity drop during the first formation cycle, followed by stabilization and consistent performance. As also shown in Fig. 5.4b, the calculated ICE values are 48.6%, 50.2%, 51.4%, and 59.2% for BH-T550-BM020, BH-T750-BM020, BH-T950-BM020, BH-T1150-BM020, respectively. This increasing trend in ICE matches the trend in first-cycle overlap seen in the voltage profiles and reinforcing the link between higher temperature and reduced first-cycle loss. After formation cycles, the approximate fifth-cycle specific capacities reach 380 mAh g^{-1} (BH-T1150-BM020), 310 mAh

g^{-1} (BH-T950-BM020), 250 mAh g^{-1} (BH-T750-BM020) and 110 mAh g^{-1} (BH-T550-BM020).

The rate performance of the BH-T####-BM020 anodes under varying C-rates is illustrate in Fig. 5.4c and shows distinct trends in specific capacity retention at different current densities for different anodes. The BH-T1150-BM020 anode maintains ~360 mAh g^{-1} at C/5, ~350 mAh g^{-1} at C/3, and ~320 mAh g^{-1} at 1C, recovering to ~380 mAh g^{-1} upon returning to the initial C/10 rate. The BH-T950-BM020 anode follows with ~280 mAh g^{-1} (C/5), ~260 mAh g^{-1} (C/3) and ~210 mAh g^{-1} (1C), also showing near-full recovery. The BH-T750-BM020 and BH-T550-BM020 anodes deliver correspondingly lower values across all rates and do not recover to their initial C/10 plateaus on the final step. The relative ranking 1150 °C ≥ 950 °C > 750 °C > 550 °C persists at every rate, indicating that the structural state set by temperature governs both reversible capacity and kinetic response. The stronger rate retention at higher temperature can be attributed to the sharper (002) peak in the powder XRD discussed in Chapter 4, which translated to reduced d_{002}, increased L_c and N, as well as higher R. It can be seen that such structural properties favour improved electronic transport and more efficient low-voltage storage.

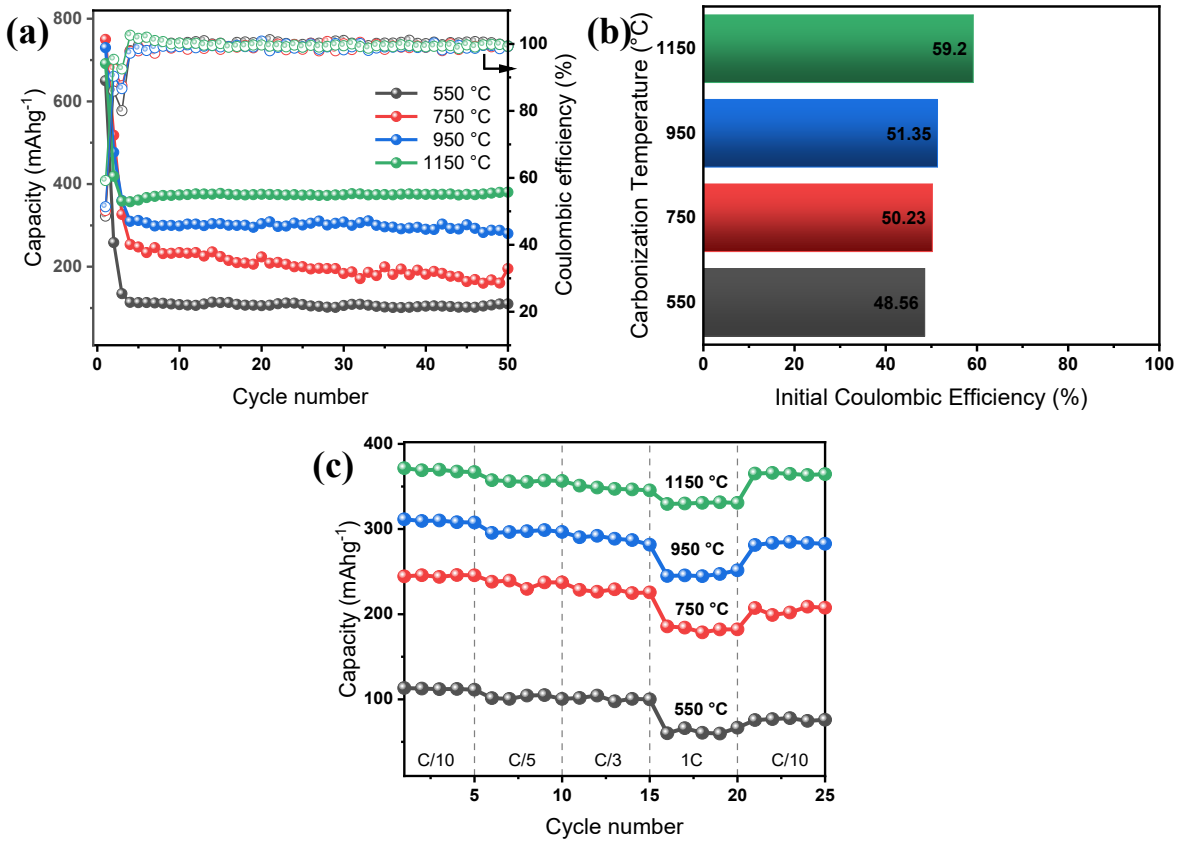

Figure 5.4. Electrochemical performance of BH-T####-BM020 anodes with active materials prepared at different carbonisation temperatures; (a) cycling performance and CE of the anodes over the first 50 cycles at a current of C/5, (b) corresponding ICE of the anodes, and (c) rate capability of the anodes.

To complement the galvanostatic results above, electrochemical impedance spectroscopy (EIS) was used to separate ohmic, interfacial and diffusion contributions to cell resistance for the BH-T####-BM020 anode series. It is used here to compare kinetic/transport characteristics of BH-T####-BM020 anodes prepared at different carbonisation temperatures under otherwise identical conditions. All the EIS spectra were collected at open circuit after a rest period following the 1st and 50th cycles, using a voltage amplitude of 5 mV over a frequency range from 100 kHz to 0.01 Hz. EIS data fitting was performed by non-linear least squares in ZView software, with identical bounds for all anodes to enable direct comparison.

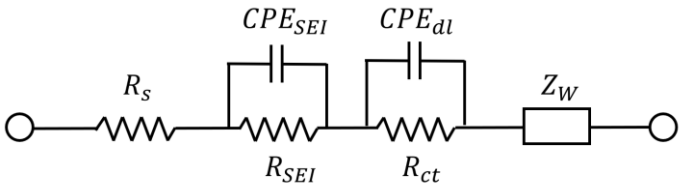

Figure 5.5. Equivalent circuit model used for EIS fitting.

All spectra are well described by the Randles-type circuit model as depicted in Fig. 5.5. During model selection, the spectra were trial-fitted with several candidate circuits such as single-arc Randles, two-arc models with(out) explicit SEI, and variants with finite-length Warburg. The topology in Fig. 5.5 consistently gave the lowest residuals and Kramers-Kronig-consistent parameter sets across all anode series and both cycle states, while more complex circuits did not reduce the error meaningfully. So, it was adopted for all datasets to ensure comparability.

As it can be seen in Fig. 5.5, this model comprises a ohmic resistance R_s, an SEI arc with R_{SEI} and CPE_{SEI}, a charge-transfer arc with R_{ct} and CPE_{dl}, and a low-frequency Warburg element Z_W. The constant-phase elements (CPE) account for non-ideal capacitive behaviour of rough, porous electrodes; their exponents were constrained to physically reasonable windows (0.6 to 1.0). The Warburg response was also analysed by the standard linear relation as formulated in Eq. (5.1) to obtain the Warburg coefficient.

$$Z' = R_s + \sigma\omega^{-0.5} \tag{5.1}$$

where σ is Warburg coefficient ($\Omega\ s^{0.5}$).[7] The apparent Li^+ diffusion coefficient D_{Li^+} was then calculated from σ using Eq. (5.2)

$$D_{Li^+} = \frac{R^2T^2}{2A^2n^4F^4C^2\sigma^2} \tag{5.2}$$

where R is the universal gas constant ($8.314\ J\ mol^{-1}K^{-1}$), T is the temperature (K), A is anode surface area (cm^{-2}), n is the number of electrons per ion insertion (equal to 1 for Li^+), F is the Faraday constant ($96485\ C\ mol^{-1}$), and C is concentration of Li^+ in the active material ($mol\ cm^{-3}$).[7]

The fitted parameters are listed in Table 5.1 and show a clear and monotonic dependence on carbonisation temperature of the anodes. On the 1st cycle, the ohmic term R_s decreases from 5.86 Ω for BH-T550-BM020 to 2.28 Ω for BH-T1150-BM020, and further relaxes to 3.98 and 2.16 Ω by the 50th cycle for the same anodes, respectively. This drop in R_s reflects improved wettability and stabilisation of the cell components after formation. The charge-transfer resistance R_{ct} follows a similar trend, falling from 78.83 Ω (for BH-T550-BM020) through 64.09 Ω (for BH-T750-BM020) and 59.09 Ω (for BH-T950-BM020) to 35.48 Ω (for BH-T1150-BM020) on the 1st cycle. After 50 cycles, R_{ct} fitted values are 53.34, 42.57, 37.63, 24.63 Ω, for the same anode series order. Relative to 550 °C, the 1150 °C anode exhibits approximately 55% lower R_{ct} after formation and after ageing. This decrease in the charge transfer resistance of the anodes can be related the material characterisations of BH-T###-BM020 powder samples described in Chapter 4. Increasing the carbonisation temperature produces tighter turbostratic stacking, meaning smaller d_{002}, larger L_C/N, higher sharpening factor R, which supports faster interfacial charge transfer.

Diffusion coefficients derived from the low-frequency tail further confirm the carbonisation temperature effect on the electrochemical performance of the anodes. As it can be seen in Table 5.1, the Warburg coefficient decreases with temperature. On the 1st cycle $\sigma = 1.29, 1.04, 0.95,$ and $0.57\ \Omega\ s^{0.5}$ for 550, 750, 950, and 1150 °C, respectively, and falls further by the 50th cycle to 0.87, 0.70, 0.62, and $0.41\ \Omega\ s^{0.5}$. Using Eq. (5.2), the corresponding D_{Li^+} during the 1st cycle increases from 2.13×10^{-8} for BH-T550-BM020 to 1.09×10^{-7} cm² s⁻¹ for BH-T1150-BM020, showing a five-fold improvement from 550 to 1150 °C. During the 50th cycle thought, the corresponding D_{Li^+} varies from 4.67×10^{-8} to 2.10×10^{-7} cm² s⁻¹ for BH-T550-BM020 and BH-T1150-BM020, respectively. Each anode shows an improvement in D_{Li^+} of roughly a factor of two between cycles 1 and 50.

A larger D_{Li^+} signifies faster Li^+ transport within the composite electrode, which means a more rapid migration through the SEI and penetration into the active carbon domains, which reduces concentration polarisation and supports higher reversible capacities at elevated rates.[7, 8] The temperature dependence of D_{Li^+} is consistent with the structural evolution established in Chapter 4. Anodes with more graphitized structure show more efficient low-voltage interlayer pathways for Li storage while maintaining sufficient spacing for insertion. Consequently, anodes carbonised at 1150 °C combine the lowest interfacial resistances with the highest

diffusion coefficients, explaining their superior ICE, rate retention and cycling stability observed throughout this section.

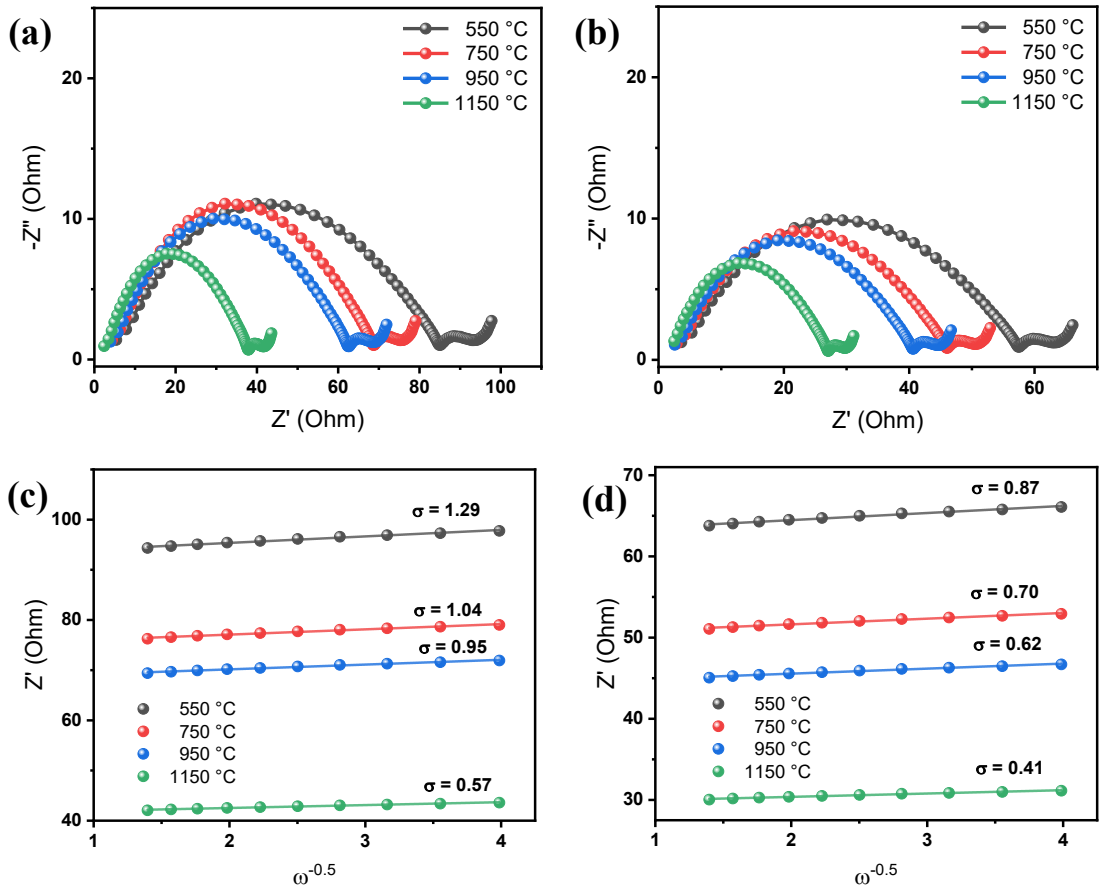

Figure 5.6. Nyquist plots of BH-T####-BM020 anodes after (a) the 1st cycle and (b) the 50th cycle. Corresponding Z' vs $\omega^{-1/2}$ plots with linear fits after (c) the 1st cycle and (d) the 50th cycle used to obtain the Warburg coefficient σ.

Table 5.1. Fitted EIS parameters and derived D_{Li^+} for BH-T####-BM020 anodes for the 1st and 50th cycles.

Temp. (°C)	1st cycle				50th cycle			
	$R_s(\Omega)$	$R_{ct}(\Omega)$	$\sigma(\Omega\, s^{-0.5})$	$D_{Li^+}(cm^2s^{-1})$	$R_s(\Omega)$	$R_{ct}(\Omega)$	$\sigma(\Omega\, s^{-0.5})$	$D_{Li^+}(cm^2s^{-1})$
550	5.86	78.83	1.29	2.13×10^{-8}	3.98	53.34	0.87	4.67×10^{-8}
750	4.72	64.09	1.04	3.27×10^{-8}	3.29	42.57	0.70	7.22×10^{-8}

950	3.14	59.09	0.95	3.92×10^{-8}	2.86	37.63	0.62	9.21×10^{-8}
1150	2.28	35.48	0.57	1.09×10^{-7}	2.16	24.63	0.41	2.10×10^{-7}

5.4. Effect of ball-milling duration

In Chapter 4 it was shown that at fixed carbonisation temperature, short ball-milling up to 20 to 60 min chiefly increases the surface area and mesopore volume with diminishing returns thereafter. It was also shown that very long milling can trigger re-agglomeration or partial pore collapse. To translate these structural changes into electrochemical behaviour of the anodes, the carbonisation temperature of the active material used in the anode formulation was fixed at 1150 °C and the milling duration was varied across BM000, BM010, BM020, BM060 and BM120. All anodes were formulated and tested identically as explain previously in Section 5.2, so differences reflect the milling variable alone.

The first five charge-discharge profiles for BH-T1150-BM### anodes are shown in Fig. 5.7. All samples exhibit the typical hard-carbon response. Similar to the cyclic performance of BH-T####-BM020 anodes series in Fig. 5.4a, the charge-discharge profiles consist of a sloping lithiation above 0.2 V followed by a low-voltage segment approximately below 0.2 V. With moderate milling, from BM010 to BM060, the low-voltage portion lengthens and the profiles become slightly flatter by cycles 2 to 5, indicating a larger contribution from efficient low-voltage storage and reduced polarisation. The active material no ball milling (BM000), retains a shorter <0.2 V region and greater hysteresis. BM120 shows no further gain relative to BM060, and a small increase in hysteresis appears, consistent with the structural over-milling effects inferred in Chapter 4.

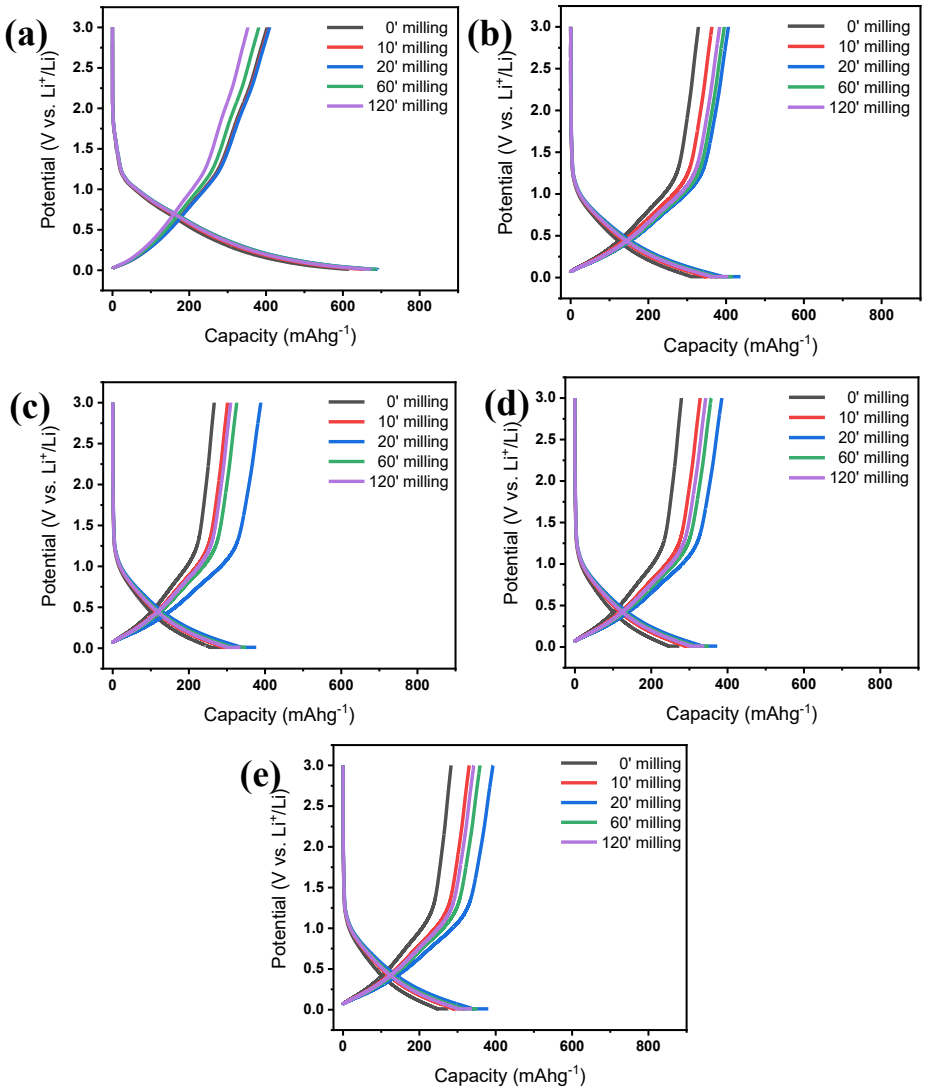

Figure 5.7. Charge-discharge voltage profiles of BH-T1150-BM### anodes with active materials prepared at different ball milling duration at their (a) 1st, (b) 2nd, (c) 3rd, (d) 4th, and (e) 5th cycle under a C/5 current.

The cycling performance and CE of the BH-T1150-BM### anodes over their first 50 cycles at a current of C/5 are shown in Fig. 5.8a. All anodes stabilise after the first few cycles, but the reversible capacity clearly peaks at BM020. Over 50 cycles, capacity retention remains high for BM020 and BM060, fade by only ~5 to 8 %, with CE ≥ 98 % after formation, while BM010 and BM120 show moderate decay of ~10 to 15%, and BM000 exhibits the strongest drift of ~30 to 40%. The differences in capacity retention across milling times can be ascribed to the effect of ball milling on surface area and mesopore connectivity of the active materials. Short-to-moderate milling increases external surface and mesopore connectivity, which means better

electrolyte access and shorter ion paths. In contrast, zero milling leaves the particles under-activated and very long milling offers no further porosity gain and may partially degrade it.

Ball milling duration also affects the ICE of the anodes, as illustrated in Fig. 5.8b. The ICE decreases monotonically with milling time. BH-T1150-BM000 shows the highest ICE of 65.23%, and then BM010 and BM020 possess the next ICE values with 62.12% and 59.20%, respectively. Eventually, the lowest ICE can be seen in BM060 and BM120 with only 55.49% and 52.36%, respectively. This trend is consistent with the BET/t-plot results in Chapter 4, where the greater accessible surface area and mesoporosity produce a larger interfacial area for SEI formation during the first lithiation and expose more active sites, both of which consume charge irreversibly. In addition, milling exposes silica-rich domains more uniformly, which increases the wetted interface in the composite during formation. The net effect is a controlled trade-off. Milling improves reversible capacity and rate performance up to 20 to 60 min, at the cost of progressively lower ICE. Among the series, BM020 provides the best balance, with the highest reversible capacity and only a moderate ICE.

Rate capability of the anodes was tested under the same stepped protocol used in the temperature study, and results are plotted in Fig. 5.8c. The capacity ranking established at C/5 carries through the entire series, with BM020 consistently highest, BM060 close behind, BM120 and BM010 intermediate, and BM000 lowest. Quantitatively, BM020 delivers approximately 380 mAh g^{-1} at C/10, 360 mAh g^{-1} at C/5, 350 mAh g^{-1} at C/3 and 320 mAh g^{-1} at 1C, then recovers to 380 mAh g^{-1} on returning to C/10 again. Among the other anodes, BM060 shows the highest capacity across all C-rates as well as an acceptable recovery in its capacity while returning the C/10. Nevertheless, BM000 remains the least capable across all rates.

It can be seen that short-to-moderate milling (BM020 to BM060) increases surface area and mesopore connectivity, leading to better electrolyte wettability and shorter ion-transport paths. However, over-milling (BM120) may introduce re-agglomeration or partial pore collapse, reducing rate performance despite comparable CE after formation. Overall, BM020 offers the best balance of high absolute capacity and strong rate retention under identical cell chemistry and loading.

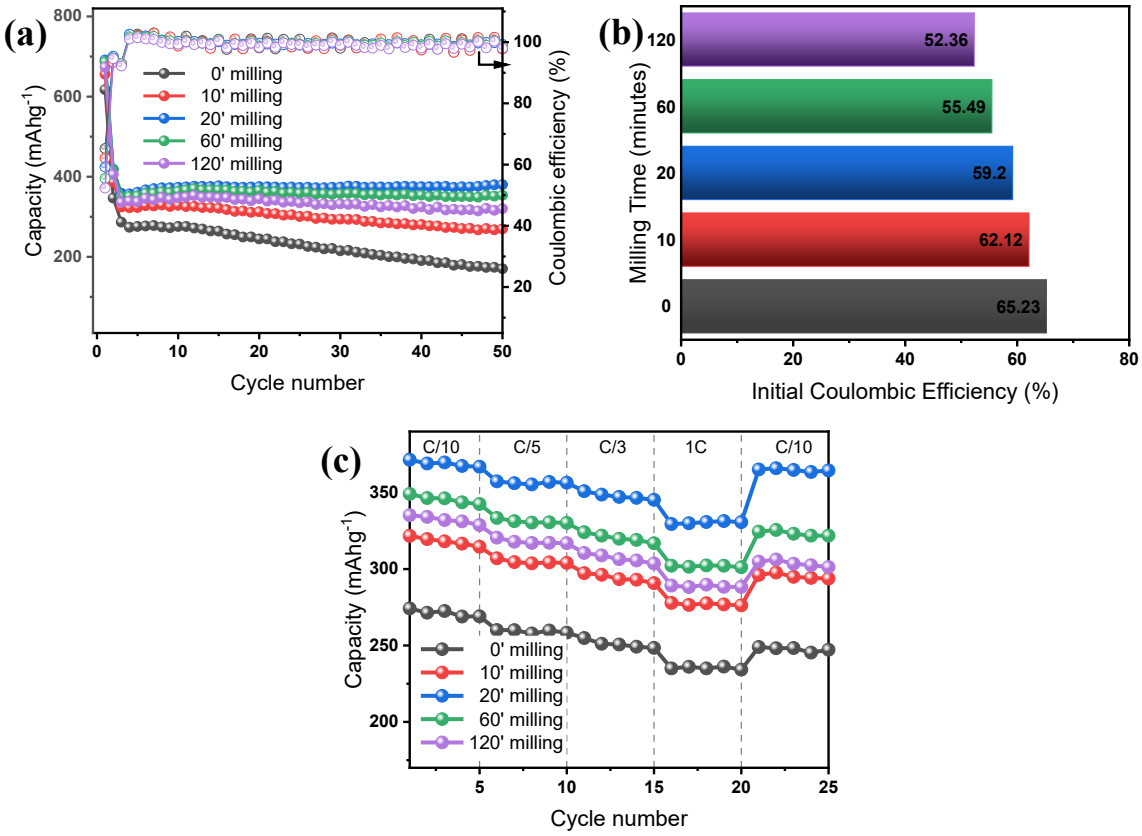

Figure 5.8. Electrochemical performance of BH-T1150-BM### anodes with active materials prepared at different ball-milling durations; (a) cycling performance and coulombic efficiency of the anodes over the first 50 cycles at a current of C/5, (b) corresponding ICE of the anodes, and (c) Rate capability of the anodes.

EIS was also applied to the BH-T1150-BM### series to isolate the kinetic consequences of milling at fixed carbonisation temperature. Spectra were acquired and fitted under the same conditions and with the same circuit as in Fig. 5.5 and the Warburg slopes were obtained from linear fits of Z' versus $\omega^{-0.5}$. The full parameter set for the 1st and 50th cycles is reported in Fig. 5.9 and Table 5.2.

On the 1st cycle, R_s increases with milling time from 1.42 Ω (BM000) to 4.27 Ω (BM120), likely reflecting the looser packing and higher porosity of heavily milled powders before complete wetting and SEI consolidation. A similar monotonic rise is observed for R_{ct}, from 28.88 Ω (BM000) through 33.29 Ω (BM010) and 35.48 Ω (BM020) to 43.53 Ω (BM060) and 64.12 Ω (BM120). In parallel, the Warburg coefficient σ grows from 0.46 to 1.04 Ω $s^{-0.5}$, and the derived diffusion coefficient D_{Li^+} falls from 1.67×10^{-7} to 3.27×10^{-8} $cm^2\ s^{-1}$. These first-cycle trends are consistent with the larger fresh surface area generated by milling; more

area demands more SEI to be formed, which transiently increases interfacial and diffusive impedances despite the ultimately beneficial structural changes.

After 50 cycles, the ranking reverses and clearly identifies an optimum milling window. R_s converges to low values for BM020 and BM060 (2.16 and 2.29 Ω) and remains higher for BM000 and BM120 (3.06 and 4.30 Ω). The charge-transfer resistance decreases sharply to 24.63 Ω (BM020) and 30.89 Ω (BM060), while remaining substantially larger for BM010 (47.53 Ω), BM120 (45.80 Ω) and BM000 (59.00 Ω). The Warburg slopes show the same ordering, with a minimum at BM020, starting from $\sigma = 0.41$ for BM020, and then varying to 0.51 (BM060), 0.74 (BM120), 0.78 (BM010) and 0.96 Ω $s^{0.5}$ (BM000). Using Eq. (5.2), this yields the highest D_{Li^+} for BM020 (2.10×10^{-7} cm² s⁻¹) and BM060 (1.36×10^{-7} cm² s⁻¹), intermediate values for BM010 and BM120 (5.82×10^{-8} and 6.46×10^{-8} cm² s⁻¹, respectively), and the lowest for BM000 (3.84×10^{-8} cm² s⁻¹). The evolution from the 1st to the 50th cycle therefore tracks the galvanostatic results; once the SEI stabilises and the electrode is fully wetted, moderate milling delivers lower R_{ct}, smaller σ and larger D_{Li^+}, consistent with improved access to the mesoporous network and shorter diffusion paths; no milling leaves pathways under-developed, and over-milling (120 min) offers no kinetic advantage and may re-agglomerate or partially collapse pores.

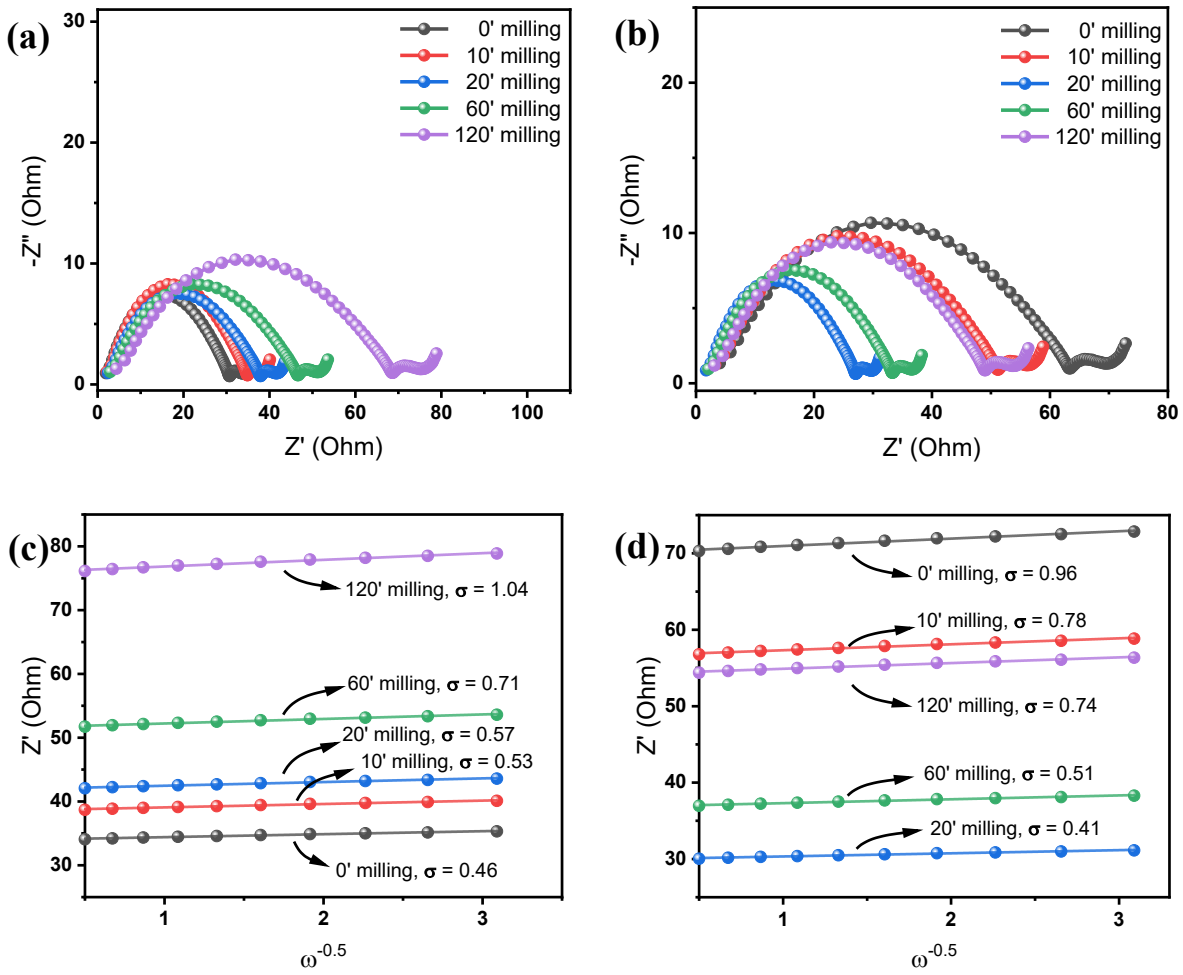

Figure 5.9. Nyquist plots of BH-T1150-BM### anodes after (a) the 1st cycle and (b) the 50th cycle. Corresponding Z' vs $\omega^{-0.5}$ plots with linear fits after (c) the 1st cycle and (d) the 50th cycle used to obtain the Warburg coefficient σ.

Table 5.2. Fitted EIS parameters and derived D_{Li^+} for BH-T1150-BM### anodes for the 1st and 50th cycles.

Time (min)	1st cycle				50th cycle			
	$R_s(\Omega)$	$R_{ct}(\Omega)$	$\sigma(\Omega\, s^{-0.5})$	$D_{Li^+}(cm^2s^{-1})$	$R_s(\Omega)$	$R_{ct}(\Omega)$	$\sigma(\Omega\, s^{-0.5})$	$D_{Li^+}(cm^2s^{-1})$
0	1.42	28.88	0.46	1.67×10^{-7}	4.30	59.0	0.96	3.84×10^{-8}
10	1.55	33.29	0.53	1.26×10^{-7}	3.34	47.53	0.78	5.82×10^{-8}
20	2.28	35.48	0.57	1.09×10^{-7}	2.16	24.63	0.41	2.10×10^{-7}
60	2.97	43.53	0.71	7.02×10^{-8}	2.29	30.89	0.51	1.36×10^{-7}
120	4.27	64.12	1.04	3.27×10^{-8}	3.06	45.80	0.74	6.46×10^{-8}

Overall, the impedance analysis confirms the kinetic origin of the performance ranking established in Fig. 5.8. BH-T1150-BM020 achieves the best compromise with the lowest impedances and the highest apparent diffusion coefficient after conditioning which explains its superior reversible capacity and rate retention under otherwise identical conditions. The processing window for carbonisation temperature and ball milling duration tuned here (T ≈ 1150 °C, BM ≈ 20 min) is used as the baseline formulation in the next chapter. A direct benchmark against a standard graphite anode appears in Chapter 6, where it frames the performance gains from silica/carbon composites.

5.5. Conclusion

Electrochemical testing under a single, controlled protocol establishes clear processing-performance links for BH-derived SiO_2/C anodes:

1. Carbonisation temperature governs storage mechanism and kinetics. Raising temperature from 550 → 1150 °C increases ICE (48.6 → 59.2%), boosts reversible capacity and rate retention, and reduces both R_{ct} and the Warburg slope. The apparent diffusivity rises by approximately five-fold between 550 and 1150 °C after formation, and by the 50th cycle reaches ~2.1×10^{-7} cm^2 s^{-1} for BH-T1150-BM020, consistent with tighter turbostratic stacking (smaller d_{002}, larger L_C, higher R) enabling more efficient low-voltage interlayer/nanopore storage.

2. Ball-milling duration introduces a controlled trade-off between texture and first-cycle efficiency. Short-to-moderate milling (~20 to 60 min) opens external/mesopore networks, improving electrolyte access and shortening ion paths; this manifests as higher reversible capacity, stronger rate performance, lower R_{ct} and smaller σ after conditioning. Prolonged milling (120 min) provides no additional porosity benefit and can slightly degrade kinetics, while no milling leaves the texture under-activated. ICE decreases monotonically with milling time owing to larger interfacial area for SEI formation. Across the series, BH-T1150-BM020 offers the best balance.

The processing window T ≈ 1150 °C and BM ≈ 20 min therefore defines a robust baseline for the BH platform, combining competitive capacity with good rate capability and stable cycling.

The optimised BH-T1150-BM020 anode identified here is therefore used in Chapter 6 for a like-for-like comparison with a commercial graphite anode under identical cell conditions.

5.6. References

[1] H. Zhao, J. Li, Q. Zhao, X. Huang, S. Jia, J. Ma, Y. Ren. *Electrochemical Energy Reviews* 2024,1,11.

[2] J. Liu, Y. Yang, P. Lyu, P. Nachtigall, Y. Xu. *Advanced Materials* 2018,30,1800838.

[3] K. Wang, Y. Xu, H. Wu, R. Yuan, M. Zong, Y. Li, V. Dravid, W. Ai, J. Wu. *Carbon N Y* 2021,178,443–450.

[4] J. Kim, K. Kim, S. Lee. *Energies (Basel)* 2021,2104.

[5] L.F. Zhao, Z. Hu, W.H. Lai, Y. Tao, J. Peng, Z.C. Miao, Y.X. Wang, S.L. Chou, H.K. Liu, S.X. Dou. *Adv Energy Mater* 2021,11,2002704.

[6] L. Sbrascini, A. Staffolani, L. Bottoni, H. Darjazi, L. Minnetti, M. Minicucci, F. Nobili. *ACS Appl Mater Interfaces* 2022,14,33257–33273.

[7] Y. He, G. Xu, C. Wang, L. Xu, K. Zhang. *Electrochim Acta* 2018,264,173–182.

[8] J.K. Dora, D. Nayak, S. Ghosh, V. Adyam, N. Yedla, T.K. Kundu. *Sustain Energy Fuels* 2020,4,6054–6065.

6. Benchmarking barley husk-derived SiO_2/C anodes against graphite in lithium-ion batteries

6.1. Introduction

Chapter 5 identified BH-T1150-BM020 as an optimised barley husk-derived silica/carbon composite anode, combining high reversible capacity, good rate capability and robust cycling stability in Li half-cells. However, the practical relevance of any alternative anode material ultimately depends on how it compares with commercial graphite, which remains the industrial benchmark for lithium-ion batteries.

This chapter benchmarks BH-T1150-BM020 directly against a standard graphite anode (Gr-Ref) under identical electrode formulation, cell architecture, electrolyte and testing protocol. The comparison focuses on galvanostatic voltage profiles, cycling stability, rate performance, electrochemical impedance, cyclic voltammetry, kinetic analysis and post-mortem morphology. These results are then positioned within the broader landscape of biomass-derived Si- and SiO_2-based anodes using literature data.

The objectives are to quantify the advantages and trade-offs associated with replacing graphite by a barley husk-derived SiO_2/C composite, to clarify the mechanistic origins of any differences in performance, and to assess whether the BH-based anode can be considered a viable, sustainable alternative for Li-ion battery applications.

6.2. Scope, test protocol, and performance metrics

All measurements in this chapter were carried out on CR2016 Li half-cells assembled with either the optimised barley husk-derived composite (labelled BH-T1150-BM020) or a commercial graphite (powder purchased from Acros Organics) anode (labelled Gr-Ref) as the working electrode. In both cases, the electrode formulation, coating conditions and cell hardware were kept identical to isolate the influence of the active material. Slurries containing active material, carbon black (C65) and polyacrylic acid binder in a mass ratio of 7:2:1 were

cast onto Cu foil and processed as described in Sections 5.2.1 and 5.2.2, with areal loadings in the range 1.0 to 1.5 mg cm^{-2}.

The electrolyte and testing schedule were also consistent with Chapter 5. Cells were cycled between 0.01 and 3.0 V vs Li^+/Li using a Li-metal counter electrode and a 1.2 M $LiPF_6$ EC/EMC (1:3 v/v) electrolyte containing 15 wt% FEC and 3 wt% VC. Formation comprised low-current cycles to stabilise the solid-electrolyte interphase (SEI), followed by cycling at C/5 and rate tests between C/10 and 2C, as detailed in Section 5.2.3. CV was recorded at 0.2 mV s^{-1} and EIS was performed using a 5 mV perturbation over 100 to 0.01 Hz at open circuit after selected cycles.

Performance metrics were defined as in Chapter 5. The C-rate denotes the current that would charge or discharge the active material in 1 h (1C); C/5 and C/10 correspond to currents five- and ten-fold lower, respectively. The initial coulombic efficiency (ICE) expresses the percentage of charge recovered during the first charge step relative to the charge inserted during the first discharge step, and capacity retention at a given cycle is reported relative to a chosen reference cycle (typically the first cycle after formation).

For post-mortem analysis, selected cells were disassembled in an argon-filled glovebox after 10 and 100 cycles at C/5. The anodes were carefully removed, and residual electrolyte was gently rinsed off using anhydrous dimethyl carbonate (DMC, Sigma-Aldrich). The electrodes were then dried under inert conditions within the glovebox for 12 to 24 h. No thermal treatment was applied to the samples in order to preserve their surface morphology for subsequent post-mortem SEM imaging.

6.3. Benchmark against a standard graphite anode

This section benchmarks the optimised barley husk-derived silica/carbon composite anode (BH-T1150-BM020) against a commercial graphite reference anode (labelled Gr-Ref) under identical electrode formulation, cell architecture and cycling protocol. The objective is to place the BH-derived anode system on a familiar performance scale, identify mechanistic differences in lithiation-delithiation behaviour, and clarify where the BH-based anode outperforms or falls short relative to mainstream graphite.

6.3.1. Voltage profiles and cyclic performance

The galvanostatic charge-discharge profiles of BH-T1150-BM020 and the graphite reference anode (Gr-Ref) for the first five cycles at C/5 are shown in Fig. 6.1a and 6.1b, respectively. Gr-Ref exhibits the characteristic flat lithiation plateau near 0.1 V, associated with Li^+ intercalation into a well-ordered graphitic layered structure. The profile stabilises rapidly after the first cycle, with a narrow voltage hysteresis window and nearly overlapping charge-discharge curves, which is consistent with effective solid-electrolyte interphase (SEI) formation and highly reversible intercalation behaviour.

In contrast, BH-T1150-BM020 displays a predominantly sloping voltage profile without a pronounced low-potential plateau, as shown in Fig. 6.1a. This response is typical of disordered hard carbon-like materials, where Li storage proceeds through a combination of adsorption on defect sites, filling of nanopores and insertion into turbostratic or amorphous domains.[1] Over the first five cycles, the BH-T1150-BM020 profile gradually stabilises; the discharge capacity experiences a modest increase while the hysteresis between charge and discharge is slightly reduced by the third cycle, indicating progressive stabilisation of the SEI and equilibration of surface and pore-filling processes.

BH-T1150-BM020 delivers a higher specific capacity than Gr-Ref under these conditions, which is attributed to its hierarchical porosity and the additional storage contribution from the embedded silica phase, in line with the structural analysis presented in Chapters 4 and 5. The composite anode, however, exhibits a larger voltage hysteresis than graphite, reflecting the more complex combination of storage mechanisms and possible local interactions at the silica-carbon interface. From the first formation cycle, the initial Coulombic efficiency (ICE) of BH-T1150-BM020 is approximately 60 %, consistent with hard carbon systems containing SiO_2, whereas Gr-Ref achieves an ICE of around 89 %. The higher irreversible capacity of BH-T1150-BM020 is associated with its higher specific surface area, extensive porosity and the presence of oxygen-containing functionalities, all of which promote electrolyte decomposition and SEI growth during the initial cycles.

The cycling behaviour and Coulombic efficiency of BH-T1150-BM020 and Gr-Ref at C/5 over 50 cycles are presented in Fig. 6.1c. Both anodes show an initial capacity drop between the first and second cycles, followed by rapid stabilisation and highly consistent capacity retention. After the formation period, BH-T1150-BM020 maintains a higher reversible capacity of approximately 380 mAh g^{-1} over most of the cycling window, compared with Gr-Ref, which

stabilises at around 350 mAh g^{-1}. This moderate yet persistent capacity advantage is consistent with the porous composite architecture and the contribution of the silica component to additional Li storage and mechanical buffering of volume changes.

The Coulombic efficiency of both anodes increases sharply after the first few cycles, reaching values above 98 %, which indicates that parasitic reactions are strongly suppressed once a passivating SEI has formed. The combination of enhanced specific capacity, stable Coulombic efficiency and comparable cycling stability positions BH-T1150-BM020 as a credible sustainable alternative to conventional graphite.

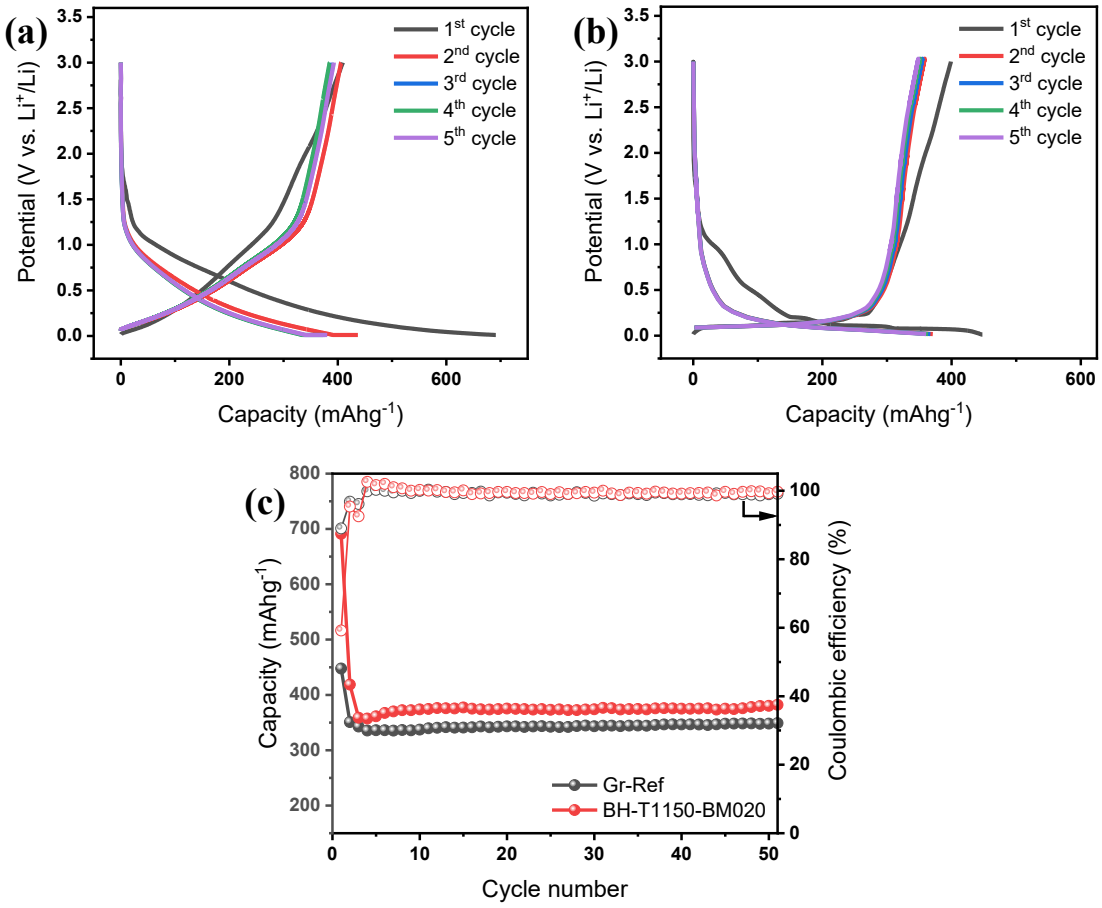

Figure 6.1. Charge-discharge voltage profiles of (a) BH-T1150-BM020 and (b) Gr-Ref anodes for the first five consecutive cycles at a C/5 current, and (c) Cycling performance and Coulombic efficiency of the same anodes over the first 50 cycles at a current of C/5.

6.3.2. Rate capability and long-term performance

The rate performance of BH-T1150-BM020 and Gr-Ref is presented in Fig. 6.2a. At low C-rates (C/10 and C/5), both electrodes deliver relatively stable specific capacities, with BH-T1150-BM020 maintaining values close to 400 mAh g^{-1} and Gr-Ref stabilising around 350 mAh g^{-1}. On increasing the C-rate to C/3, 1C and 2C, the capacity of both anodes decreases, reflecting kinetic limitations associated with Li^+ transport and charge transfer at higher current densities. Across the entire rate window, BH-T1150-BM020 consistently delivers higher capacity than Gr-Ref, indicating that the porous composite architecture accommodates faster Li^+ insertion-extraction without severe polarisation. When the current density is returned to C/10, both electrodes recover capacities close to their initial values, which points to good structural integrity and reversible Li storage under dynamic operating conditions.

Fig. 6.2b compares the extended cycling stability of BH-T1150-BM020 and Gr-Ref at C/5 over 400 cycles. After the initial formation period, both electrodes exhibit gradual capacity fading with no abrupt degradation events. BH-T1150-BM020 retains approximately 97.9 %, 96.4 %, 93.9 % and 87.9 % of its capacity after 100, 200, 300 and 400 cycles, respectively, while Gr-Ref retains 96.6 %, 94.4 %, 90.9 % and 87.7 % at the same checkpoints. The BH-derived composite therefore maintains both a higher absolute capacity and slightly better retention than graphite over prolonged cycling. This behaviour is consistent with the robust porous morphology and mechanically reinforcing silica framework identified in Chapters 4 and 5, which together accommodate repeated Li insertion-extraction and mitigate structural fatigue in comparison with the purely graphitic reference.

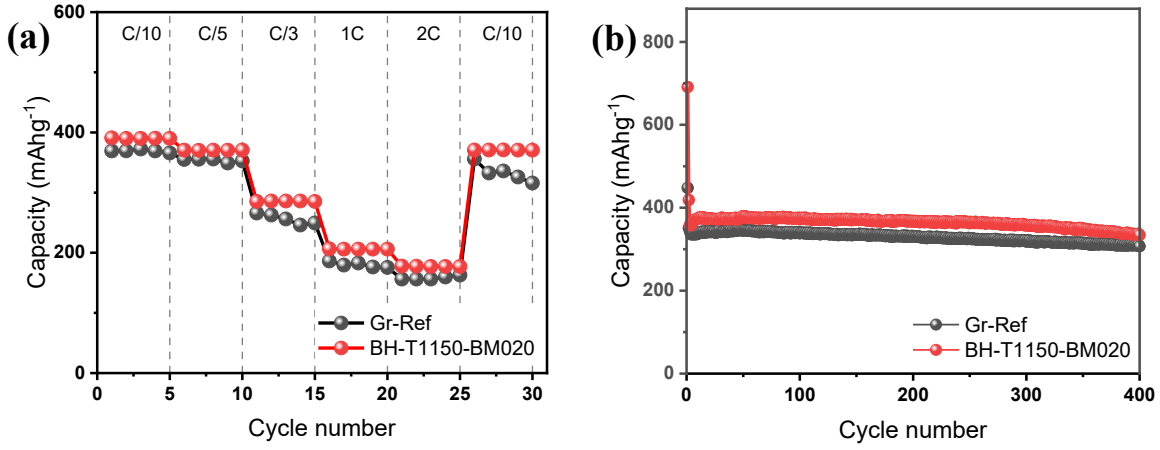

Figure 6.2. (a) Rate capability of BH-T1150-BM020 and Gr-Ref anodes at current densities between C/10 and 2C and back to C/10. (b) Long-term cycling performance of BH-T1150-BM020 and Gr-Ref anodes over 400 cycles at C/5.

6.3.3. Electrochemical impedance

To be Electrochemical impedance spectroscopy (EIS) was used to compare the evolution of interfacial and transport resistances for BH-T1150-BM020 and Gr-Ref. Spectra were recorded at open circuit after the 1st and 50th galvanostatic cycles over the 100 to 0.01 Hz frequency range, and were fitted with the same Randles-type equivalent circuit employed in Chapter 5, comprising an ohmic resistance R_s, an SEI arc, a charge-transfer resistance R_{ct} with a double-layer constant-phase element, and a low-frequency Warburg element.

The Nyquist plots in Fig. 6.3a and 6.3b show that both anodes exhibit a depressed semicircle at intermediate frequencies followed by a Warburg-type tail at low frequencies, characteristic of Li^+ transfer across the electrode-electrolyte interface and subsequent diffusion within the active material. After the first cycle, R_s is slightly higher for BH-T1150-BM020 (2.28 Ω) than for Gr-Ref (1.75 Ω), which may reflect the somewhat higher porosity and lower packing density of the composite electrode. The corresponding R_{ct} values are comparable (35.48 Ω for BH-T1150-BM020 and 33.59 Ω for Gr-Ref), indicating similar initial charge-transfer kinetics at the lithiated SEI-covered interfaces (Table 6.1).

By the 50th cycle, both electrodes show reduced semicircle diameters and lower fitted R_{ct}, consistent with activation of the electrode surfaces and stabilisation of the SEI. For BH-T1150-BM020, R_{ct} decreases to 24.63 Ω, which is slightly lower than the 26.86 Ω measured for Gr-Ref, while R_s decreases for both anodes. This trend indicates that, once formed, the silica/carbon composite supports charge transfer at least as efficiently as the graphitic reference, despite its more complex heterogeneous microstructure.

The low-frequency region was further analysed using the linear relation to extract the Warburg coefficient σ and, via the approach outlined in Section 5.2.3, the apparent Li^+ diffusion coefficient D_{Li^+}. For both anodes, σ decreases between the 1st and 50th cycles, corresponding to an increase in D_{Li^+}. BH-T1150-BM020 shows D_{Li^+} increasing from 1.09×10^{-7} to 2.10×10^{-7} cm^2s^{-1}, which is slightly higher than the increase from 1.17×10^{-7} to 1.83×10^{-7} cm^2s^{-1} observed for Gr-Ref (Table 6.1). These impedance results corroborate the rate-capability data in Fig. 6.2a. The BH-derived composite achieves comparable or lower interfacial resistance and slightly higher apparent Li^+ diffusivity after formation, which together help explain its ability to retain more of its low-rate capacity at elevated C-rates relative to the graphite anode.

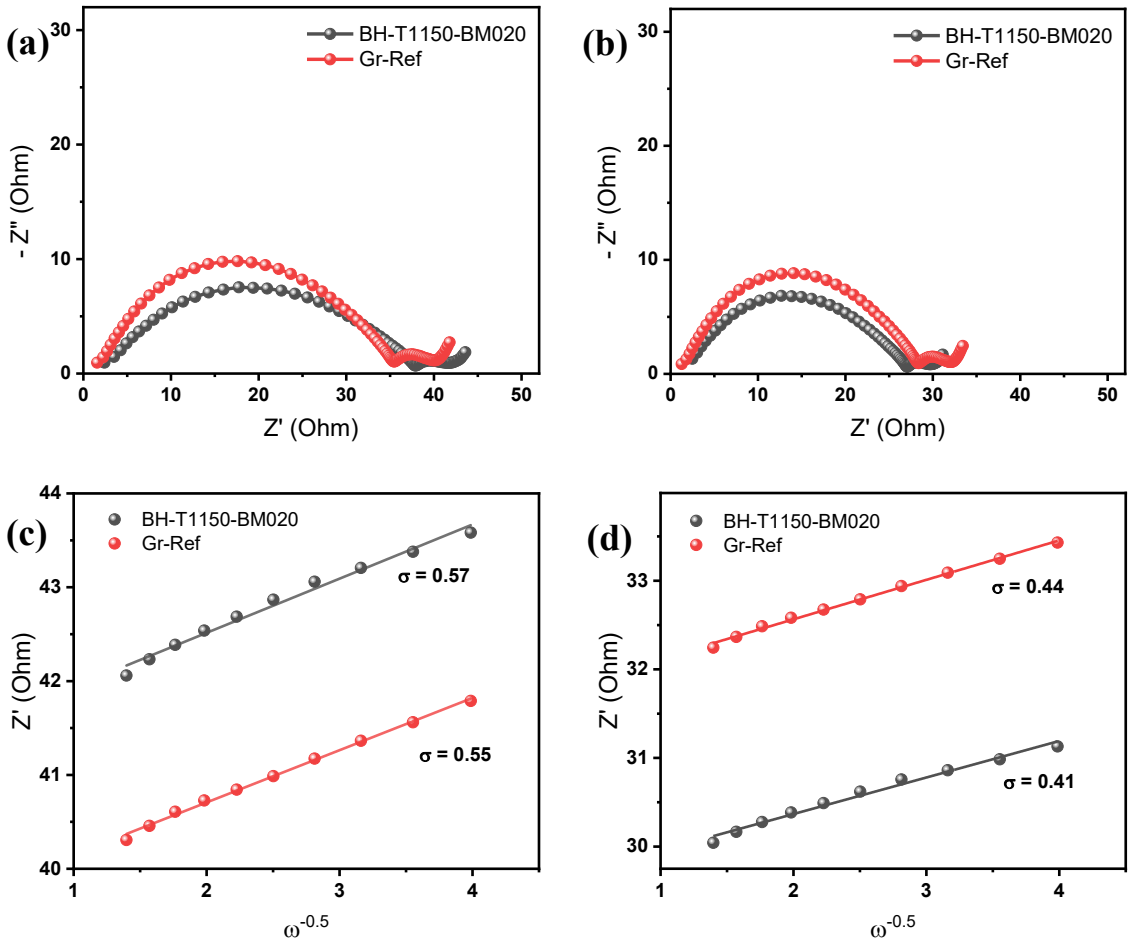

Figure 6.3. Nyquist plots of BH-T1150-BM020 and Gr-Ref anodes after (a) the 1st cycle and (b) the 50th cycle. Corresponding Z' vs $\omega^{-0.5}$ plots with linear fits after (c) the 1st cycle and (d) the 50th cycle used to obtain the Warburg coefficient σ.

Table 6.1. Fitted EIS parameters and derived D_{Li^+} for BH-T1150-BM020 and Gr-Ref anodes for the 1st and 50th cycles.

anode	1st cycle				50th cycle			
	$R_s(\Omega)$	$R_{ct}(\Omega)$	$\sigma(\Omega\, s^{-0.5})$	$D_{Li^+}(cm^2s^{-1})$	$R_s(\Omega)$	$R_{ct}(\Omega)$	$\sigma(\Omega\, s^{-0.5})$	$D_{Li^+}(cm^2s^{-1})$
Gr-Ref	1.75	33.59	0.55	1.17×10^{-7}	1.40	26.86	0.44	1.83×10^{-7}
BH-T1150-BM020	2.28	35.48	0.57	1.09×10^{-7}	2.16	24.63	0.41	2.10×10^{-7}

6.3.4. Cyclic voltammetry

The cyclic voltammograms of BH-T1150-BM020 and Gr-Ref, recorded between 0.01 and 3.0 V at 0.2 mV s^{-1}, are shown in Fig. 6.4a and 6.4b, respectively. For BH-T1150-BM020 in Fig. 6.4a the first cathodic sweep exhibits several distinct reduction features at approximately 1.85, 1.17 and 0.76 V. The peak at around 0.76 V is associated with the formation of the SEI, which is predominantly established during the initial cycle and contributes to the irreversible capacity loss. The broader reduction features at higher potentials, centred at approximately 1.85 and 1.17 V, are attributed to the initial conversion of the embedded SiO_2 phase. These features are assigned collectively to the irreversible reactions described by Eqs. (6.1), (6.3) and (6.4), namely the formation of lithium silicates (such as $Li_2Si_2O_5$ and Li_4SiO_4) together with Li_2O and electrically conductive Si.[2, 3] These peaks are largely absent in subsequent cycles, confirming the irreversible character of the initial SiO_2 conversion reactions. Because these first-cycle cathodic processes overlap in potential, a strict one-to-one assignment of each individual peak to a single equation is not intended; rather, the two broad peaks represent the combined electrochemical signature of the SiO_2 conversion reactions.

On the anodic sweep, a pronounced oxidation peak centred near 0.9 V is observed. This peak is assigned to the delithiation/dealloying of Li_xSi formed during the cathodic scan, consistent with Eq. (6.2). A much smaller anodic signal at around 0.16 V is attributed to the reversible insertion and extraction of Li^+ within the disordered carbon matrix. By the second and third cycles, the voltammograms of BH-T1150-BM020 largely overlap, with disappearance of the high-potential cathodic conversion features and stabilisation of the low-potential redox response.[4] This behaviour indicates that SEI formation and SiO_2 conversion are mostly confined to the first cycle, while subsequent cycles are dominated by reversible Li storage in the carbon framework and in the silicon generated from SiO_2 reduction. These observations are consistent with the sloping voltage profiles and relatively low initial Coulombic efficiency discussed earlier for BH-T1150-BM020.

The CV response of Gr-Ref shown in Fig. 6.4b contrasts with that of the BH-derived composite. Graphite displays the well-known pair of sharp redox peaks located at low potential, associated with the stepwise formation and decomposition of staged Li/graphite intercalation compounds. The peak positions and intensities stabilise rapidly after the first cycle, with only minor changes between the second and third scans, indicating highly reversible intercalation with limited side reactions. Compared with BH-T1150-BM020, the graphite voltammograms show fewer faradaic features and a narrower potential range of pronounced current, reflecting the simpler

intercalation mechanism and the absence of conversion reactions involving SiO_2. Together, these CV results support the earlier galvanostatic analysis; BH-T1150-BM020 accommodates additional Li-storage processes linked to SiO_2 conversion and silicon alloying, at the expense of higher first-cycle irreversibility, whereas Gr-Ref behaves as a highly reversible, purely intercalation-type anode.

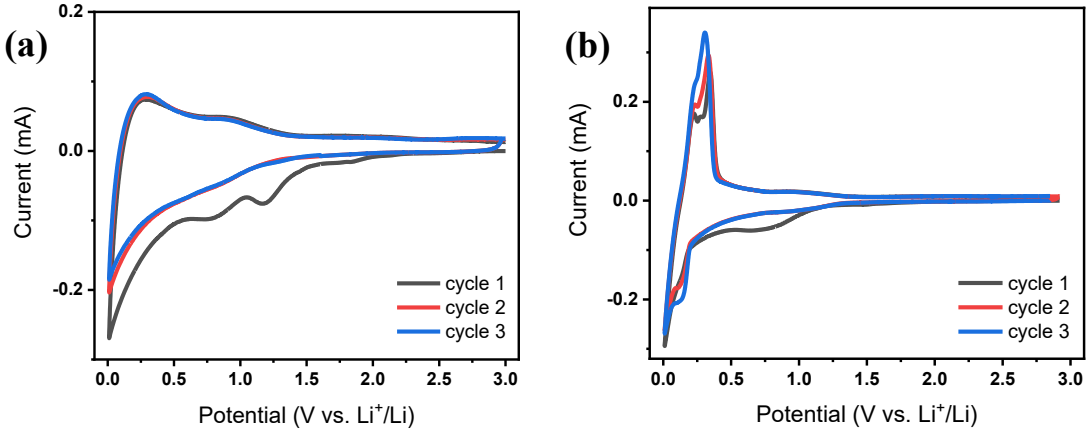

Figure 6.4. CV curves at different cycles at a scan rate of 0.2 mVs^{-1} for (a) BH-T1150-BM020 and (b) Gr-Ref anodes.

$$5SiO_2 + 4Li^+ + 4e^- \rightleftharpoons 2Li_2Si_2O_5 + Si \quad (6.1)$$

$$Si + xLi^+ + xe^- \rightleftharpoons Li_xSi \quad (6.2)$$

$$SiO_2 + 4Li^+ + 4e^- \rightarrow 2LiO_2 + Si \quad (6.3)$$

$$2SiO_2 + 4Li^+ + 4e^- \rightarrow Li_4SiO_4 + Si \quad (6.4)$$

6.3.5. Post-mortem SEM

Post-mortem SEM was employed to examine morphological changes in BH-T1150-BM020 and Gr-Ref after cycling at C/5, with images acquired before cycling and after 10 and 100 cycles, as shown in Fig. 6.5 and 6.6. For BH-T1150-BM020, the pristine anode exhibits a highly textured, porous surface consistent with the morphology described in Chapter 4 and as shown in Fig. 6.5a and 6.6a. After 10 cycles and in Fig. 6.5b and 6.6b, the overall architecture remains largely unchanged and a thin, conformal layer is observed on the particle surfaces, attributed to SEI formation. Even after 100 cycles and in Fig. 6.5c and 6.6c, the composite preserves its interconnected porous network without obvious signs of particle cracking, collapse or delamination. The maintenance of this open framework is consistent with the stable

capacity and high Coulombic efficiency observed during long-term cycling reported in Fig. 6.1 and 6.2, and indicates that the silica/carbon framework provides effective mechanical support during repeated lithiation-delithiation.

In contrast, the Gr-Ref electrode initially displays the expected relatively smooth, flake-like morphology of graphite particles, as shown in Fig. 6.5d and 6.6d. After 10 cycles, the surface appears more covered by a continuous SEI layer, with partial smoothing of the flake features, as can be seen from Fig. 6.5e and 6.6e. By 100 cycles in Fig. 6.5f and 6.6f, the graphite surface shows further passivation; flake edges become less distinct and particle boundaries appear more rounded, suggesting progressive SEI growth and mild surface reconstruction due to electrolyte side reactions. However, no severe degradation features such as large-scale cracking, exfoliation or particle detachment are observed, which aligns with the gradual, rather than catastrophic, capacity fading recorded electrochemically.

Overall, the post-mortem SEM comparison indicates that both anodes maintain their structural integrity over 100 cycles at C/5, but the BH-T1150-BM020 composite preserves its porous architecture more clearly, with a finely distributed SEI and no discernible mechanical damage. This morphological robustness supports the slightly superior capacity retention of BH-T1150-BM020 relative to graphite and underpins its suitability as a durable, biomass-derived alternative to conventional graphitic anodes.

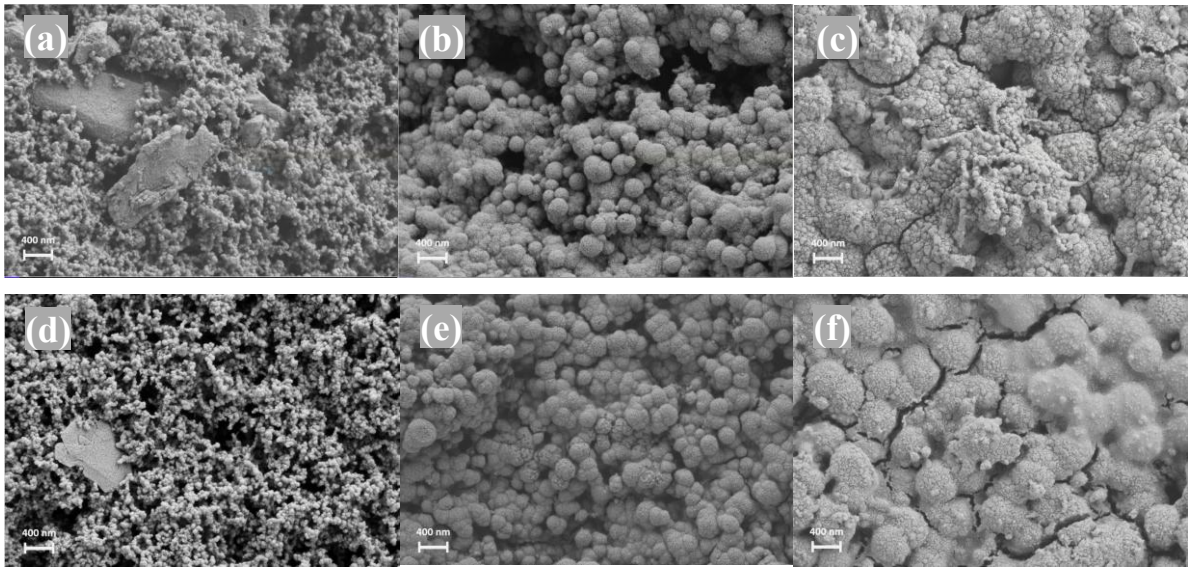

Figure 6.5. Post-mortem SEM images of BH-T1150-BM020 and Gr-Ref anodes at different cycling stages under a C/5 current. (a-c) BH-T1150-BM020 before cycling, after 10 cycles and after 100 cycles, respectively. (d-f) Gr-Ref before cycling, after 10 cycles and after 100 cycles, respectively.

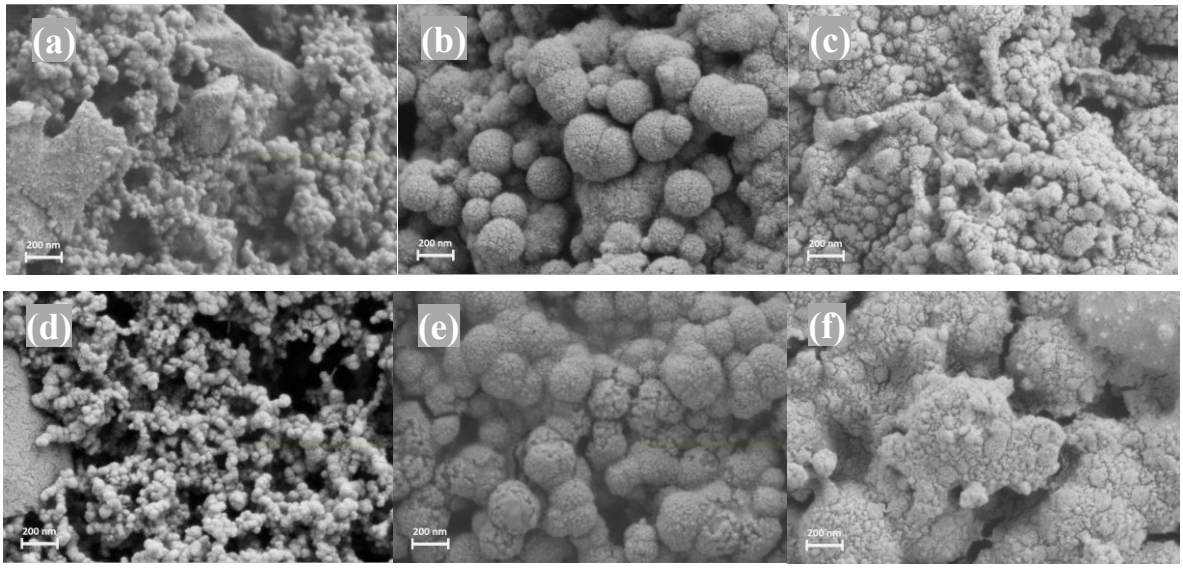

Figure 6.6. Higher-magnification post-mortem SEM images of BH-T1150-BM020 and Gr-Ref anodes at the same cycling stages as in Fig. 6.5 under a C/5 current. (a-c) BH-T1150-BM020 before cycling, after 10 cycles and after 100 cycles, respectively. (d-f) Gr-Ref before cycling, after 10 cycles and after 100 cycles, respectively.

6.3.6. Kinetic analysis

To further probe the charge-storage kinetics of BH-T1150-BM020 relative to Gr-Ref, CV measurements were performed at scan rates between 0.2 and 1.0 mV s^{-1} and the results are depicted in Fig. 6.7a and 6.7b. For both anodes, the peak currents increase systematically with scan rate while retaining similar shapes, indicating stable redox behaviour over the investigated range. The scan-rate dependence of the peak current, i, was analysed using Eq. (6.5).[5, 6]

$$i = av^b \tag{6.5}$$

where v is the scan rate and a and b are adjustable parameters. Rearranging to the logarithmic form as formulated in Eq. (6.6).

$$\log(i) = b\ log(v) + log\ (a) \tag{6.6}$$

allows the parameter b to be extracted from the slope of the $log(i) - log(v)$ plots for the anodic and cathodic peaks, as shown in Fig. 6.7c and 6.7d. A b-value of 0.5 corresponds to a semi-infinite diffusion-controlled process, whereas $b \approx 1$ indicates a surface-controlled, capacitive response.[7]

For BH-T1150-BM020, the fitted b-values are approximately 0.70 for the anodic peak and 0.71 for the cathodic peak, indicating a mixed but predominantly pseudocapacitive contribution to charge storage. In contrast, Gr-Ref exhibits lower b-values, closer to 0.55 for the anodic peak and 0.65 for the cathodic peak, which are characteristic of diffusion-limited Li^+ intercalation in graphite. The higher b-values of BH-T1150-BM020 are consistent with a greater fraction of fast, surface-controlled processes associated with its disordered carbon domains, accessible porosity and silica-derived interfacial regions identified in Chapter 4.

These kinetic signatures align with the rate-capability data in Fig. 6.2a, where BH-T1150-BM020 maintains a larger fraction of its low-rate capacity at elevated C-rates compared with graphite. The porous silica/carbon framework facilitates rapid Li^+ transport and accommodates pseudocapacitive storage, whereas the more ordered Gr-Ref relies predominantly on diffusion-controlled intercalation. This difference in charge-storage mechanism underpins the dynamic advantage of the BH-derived composite in high-rate operation.

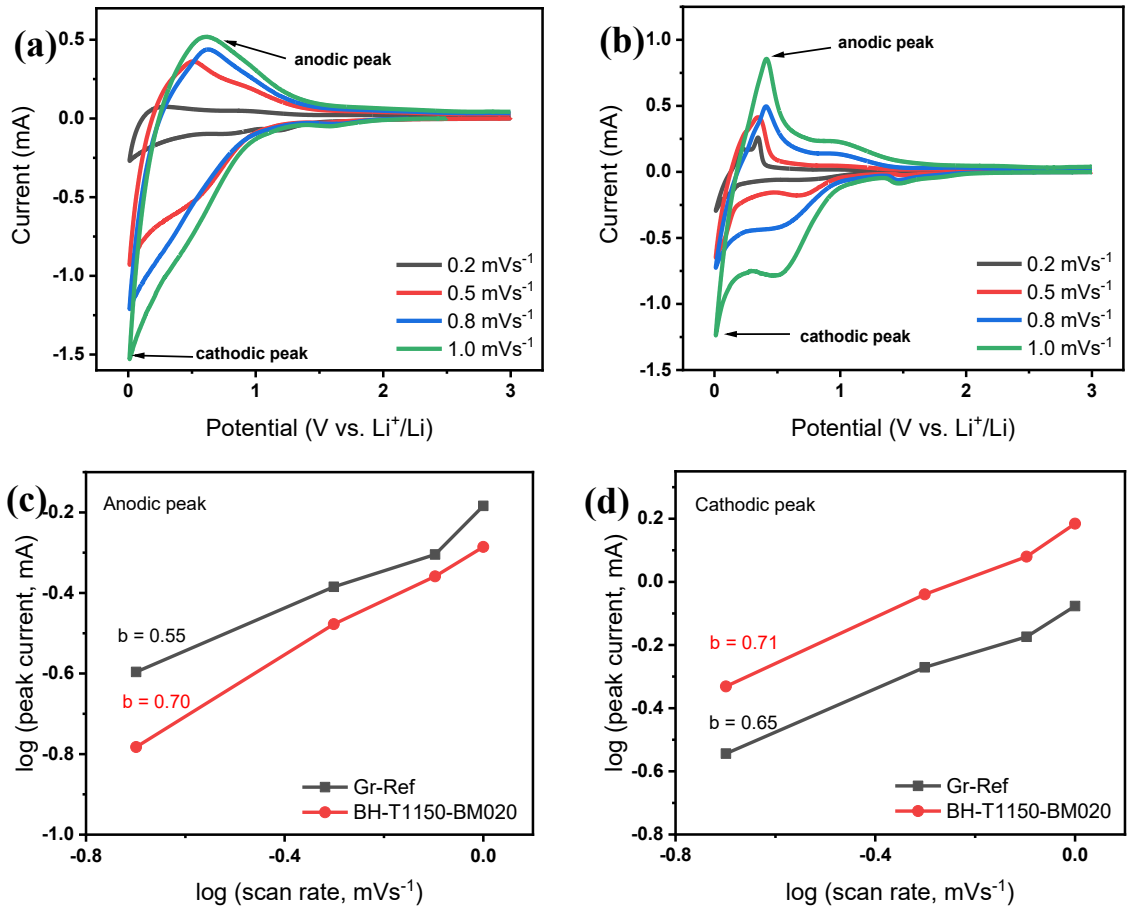

Figure 6.7. CV curves at varying scan rates ($v = 0.2, 0.5, 0.8, and\ 1.0\ mVs^{-1}$) for (a) BH-T1150-BM020 and (b) Gr-Ref anodes, (c) $log(i) - log(v)$ plot for anodic peak currents to determine the b-value, and (d) $log(i) - log(v)$ plot for cathodic peak currents to determine the b-value.

6.4. Positioning biomass-derived Si-based anodes

Table 6.2 summarises representative reports of Si- and SiO_2-based composite anodes derived from silica-rich agricultural by-products, including rice husks and corn cobs, processed by various chemical and thermal routes into Si/C or SiO_2/C materials. The majority of studies focus on rice-husk-derived feedstocks. In contrast, the present work employs barley husk as a comparatively unexplored biomass precursor and converts it into a SiO_2/C composite via direct pyrolysis followed by a scalable, template-free ball-milling step. The synthesis does not rely on corrosive etchants or complex solvent systems, which aligns more closely with industrial constraints on cost, safety and environmental impact.

When benchmarked against the literature, BH-T1150-BM020 delivers competitive specific capacity together with high Coulombic efficiency and excellent capacity retention over 400 cycles (Table 6.2). Although more elaborate protocols such as multi-step chemical activation, templating or Mg reduction can further tailor porosity or silicon content, they frequently increase process complexity, cost and waste generation. The processing route adopted here therefore represents a deliberate balance between performance and practical manufacturability. Within this landscape, BH-T1150-BM020 delivers a moderate specific capacity (~380 mAh g^{-1}) but stands out for combining extended cycling to 400 cycles with a simple, scalable synthesis that avoids multi-step chemical activation or high-temperature magnesiothermic reduction. Building on this baseline, subsequent chapters examine strategies such as controlled silicon incorporation and tailored thermal/ball-milling conditions to further enhance the electrochemical response of barley-husk-derived anodes and improve their suitability for large-scale LIBs applications.

Table 6.2. Comparison of reported Si-based anode materials derived from biomass waste and their electrochemical performance in lithium-ion batteries.

Biomass source	**Composite type and synthesis method**	**Electrode composition (wt%)**	**Specific capacity (mAh g^{-1})**	**Capacity retention**	**reference**
Rice husks	Si/C, deep eutectic solvent treatment followed by carbonization	80:10:10	372.5	~ 86% after 80 cycles	[8]
Rice husks	Si/C, acid-leaching followed by high-temperature carbonization	80:10:10	345.4	~ 89% after 80 cycles	[8]
Corn cobs	Si/CCDHC, carbonization and ball milling	80:5:15	~690	87% after 100 cycles	[9]
Rice husks	Si/C, alkali extraction, acid precipitation, followed by carbonization, ball milling, Mg reduction, and additive modification	80:10:10	~600	95% after 1000 cycles	[10]
Barley husks	SiO_2/C, direct pyrolysis and ball milling	70:20:10	~380	87.9% after 400 cycles	This work

6.5. Conclusion

This chapter has benchmarked an optimised barley husk-derived silica/carbon composite anode (BH-T1150-BM020) against a commercial graphite reference under identical cell configuration, electrolyte and testing conditions. Galvanostatic voltage profiles and cycling

data show that BH-T1150-BM020 delivers a higher reversible capacity (~380 mA h g^{-1} at C/5) than graphite (~350 mA h g^{-1}), albeit with a lower initial coulombic efficiency (~60 % vs ~89 %) and a more sloping voltage response characteristic of hard-carbon-like materials containing SiO_2. After formation, both anodes exhibit stable capacity retention and Coulombic efficiencies above 98 % over 50 to 400 cycles, with BH-T1150-BM020 maintaining slightly higher absolute capacity and marginally better long-term retention.

Complementary electrochemical diagnostics reveal mechanistic differences between the two systems. CV and kinetic analysis indicate that BH-T1150-BM020 accommodates additional Li-storage processes linked to SiO_2 conversion and silicon alloying, alongside pseudocapacitive contributions associated with its disordered carbon domains and accessible porosity, whereas the graphite reference behaves as a purely intercalation-type anode with diffusion-limited kinetics. EIS measurements show that, following SEI maturation, the BH-derived composite achieves charge-transfer resistance and apparent Li^+ diffusivity that are comparable to or better than those of graphite, consistent with its superior rate capability. Post-mortem SEM confirms that both electrodes retain their structural integrity during cycling, but the BH-T1150-BM020 anode preserves its porous architecture and exhibits a finely distributed SEI without obvious mechanical damage, supporting its favourable long-term stability.

When positioned against other biomass-derived Si- and SiO_2-based anodes reported in the literature, BH-T1150-BM020 offers competitive capacity and retention while relying on a relatively simple processing route based on direct pyrolysis and ball milling. The comparison with graphite demonstrates that a barley husk-derived SiO_2/C composite can match or exceed the performance of conventional graphitic anodes in Li half-cells, at the cost of lower ICE and increased voltage hysteresis but with clear sustainability advantages. These findings establish BH-T1150-BM020 as a robust baseline for further optimisation; subsequent chapters explore strategies such as controlled silicon incorporation and broader cell chemistries to further enhance the electrochemical response and expand the application space of barley husk-based anodes.

6.6. References

[1] G. Wang, M. Yu, X. Feng. *Chemical Society Reviews* 2021,50,2388–2443.

[2] W. Wu, M. Wang, J. Wang, C. Wang, Y. Deng. *ACS Appl Energy Mater* 2020,3,3884–3892.

[3] Z. Yang, Y. Du, G. Hou, Y. Ouyang, F. Ding, F. Yuan. *Electrochim Acta* 2020,329,135141.

[4] J. Tu, Y. Yuan, P. Zhan, H. Jiao, X. Wang, H. Zhu, S. Jiao. *Journal of Physical Chemistry C* 2014,118,7357–7362.

[5] V. Augustyn, P. Simon, B. Dunn. *Energy Environ Sci* 2014,7,1597–1614.

[6] P. Simon, Y. Gogotsi, B. Dunn. *Science (1979)* 2014,343,1210–1211.

[7] H. Yang, R. Xu, Y. Yao, S. Ye, X. Zhou, Y. Yu. *Adv Funct Mater* 2019,29,1809195.

[8] C. Padwal, H.D. Pham, L.T.M. Hoang, S. Mundree, D. Dubal. *Sustainable Materials and Technologies* 2023,35,e00547.

[9] L. Sbrascini, A. Staffolani, L. Bottoni, H. Darjazi, L. Minnetti, M. Minicucci, F. Nobili. *ACS Appl Mater Interfaces* 2022,14,33257–33273.

[10] Y. Li, L. Liu, X. Liu, Y. Feng, B. Xue, L. Yu, L. Ma, Y. Zhu, Y. Chao, X. Wang. *Mater Chem Phys* 2021,262,124331.

.

7. Silicon-enriched barley-husk composites as high-capacity anodes in Li-ion batteries

7.1. Introduction

The previous chapters demonstrated that barley husk (BH) can be converted into a high-performance hard-carbon anode, with the optimised BH-T1150-BM020 formulation delivering capacities above commercial graphite while maintaining excellent rate capability and cycling stability. Nevertheless, the gravimetric capacity of hard carbon remains fundamentally limited by its adsorption-intercalation storage mechanism, which constrains the achievable energy density in practical Li-ion cells. Silicon, by contrast, and as outlined in Chapter 2, offers an exceptionally high theoretical capacity of ~3579 mAh g^{-1} through the formation of Li–Si alloys, but suffers from large volumetric expansion, unstable solid-electrolyte interphase (SEI) layers and rapid mechanical degradation during cycling.[1]

A widely explored strategy to mitigate these drawbacks is to embed Si within a conductive carbon matrix, producing Si/C or Si/SiO_2/C composites that buffer the volume change, enhance electrical connectivity and help to stabilise the SEI. Approaches include nano-structuring of Si, encapsulation within porous carbons, and the use of elastic binders and SEI-modifying electrolyte additives. Many of these systems, however, rely on complex synthetic routes, high-cost precursors or low mass loadings that are not easily transferable to large-scale electrode manufacture. There remains a need for simpler, scalable architectures where a structurally robust carbon host can accommodate substantial Si fractions without sacrificing interfacial stability or rate performance.[1]

Biomass-derived carbons provide an attractive platform in this context. Their intrinsic porosity, heteroatom doping and embedded inorganic phases can be tailored through thermal processing, offering built-in free volume and chemically active interfaces that are beneficial for hosting alloying-type additives.[1–3] The BH-derived SiO_2/C composite developed in Chapters 4 to 6 is particularly promising: it combines a disordered hard-carbon framework with finely dispersed biogenic silica and a hierarchical micro/mesoporous network. This structure not only stores Li efficiently but also offers mechanical compliance and silica-rich interfaces that could help to anchor and stabilise exogenous Si.

Building on this foundation, the present chapter investigates silicon-enriched BH composites as high-capacity anodes for Li-ion batteries. Commercial Si powder is incorporated into the optimised BH-T1150-BM020 host (and, for comparison, into a graphite matrix) over a controlled composition range, yielding BH/Si hybrids that span BH-dominated to Si-rich regimes. By keeping the electrode architecture, electrolyte and test protocol identical to those in Chapter 5, the influence of Si content and host type on electrochemical behaviour can be isolated. The study combines structural and morphological analysis of the hybrids with half-cell cycling, rate capability tests, differential capacity analysis and post-mortem SEM, and extends the most promising composition to full-cell testing against an NMC622 cathode.

The central aim is to define a practical design window for Si incorporation in BH-derived anodes, in which the alloying capacity of Si is leveraged while preserving the favourable kinetics and stability of the BH host. Particular attention is paid to the trade-offs between Si loading, initial Coulombic efficiency (ICE), long-term capacity retention and rate performance, and to how BH/Si hybrids position themselves relative to pure BH and commercial graphite. The insights gained here inform the broader objective of this thesis: the development of biomass-derived Si/SiO_2/C architectures that deliver high energy density without sacrificing durability or sustainability.

7.2. Scope, test protocol, and performance metrics

All silicon-containing anodes in this chapter were evaluated in Li half-cells under a common electrode architecture, electrolyte and testing schedule to ensure that differences in performance could be attributed directly to active-material composition. The formulations, slurry preparation and coin-cell protocol follow the procedures established in Chapter 5, with the only additional variable being the partitioning of the active mass between BH, graphite and silicon.

7.2.1. Anode formulations and nomenclature

The anodes investigated in this chapter were designed to probe how exogenous silicon interacts with the optimised BH-T1150-BM020 host and with commercial graphite. The formulations are summarised schematically in Fig. 7.1 and numerically in Table 7.1. In all cases, the anode composition follows the same overall architecture as in Chapter 5, with 20 wt% carbon black (C65) as the conductive agent and 10 wt% polyacrylic acid (PAA) as the aqueous binder.

The control anodes consist of a graphite electrode (Gr) and a barley-husk electrode (BH), where the active phase is either commercial battery-grade graphite or BH-T1150-BM020, respectively, each occupying 70 wt% of the electrode mass (70:20:10, active:C65:PAA). The BH material corresponds to the optimised carbonisation-milling condition identified in Chapters 4 and 5; it provides a disordered hard-carbon matrix with embedded biogenic silica and well-developed micro- and mesoporosity.

To introduce silicon, the active 70 wt% fraction was repartitioned between BH and Si or between graphite and Si while keeping the C65 and PAA contents unchanged. It is noteworthy that the numbers above each bar in Fig. 7.1 indicate the nominal composite capacities calculated via a simple mass-weighted sum of the individual component capacities, assuming 372 mAh g^{-1} for graphite and the high theoretical capacity of crystalline Si. These values represent ideal upper bounds and are consistently higher than the reversible capacities measured electrochemically in Section 7.4, where practical penalties from SEI formation, kinetic limitations and mechanical degradation reduce the accessible capacity, especially at high Si fractions.

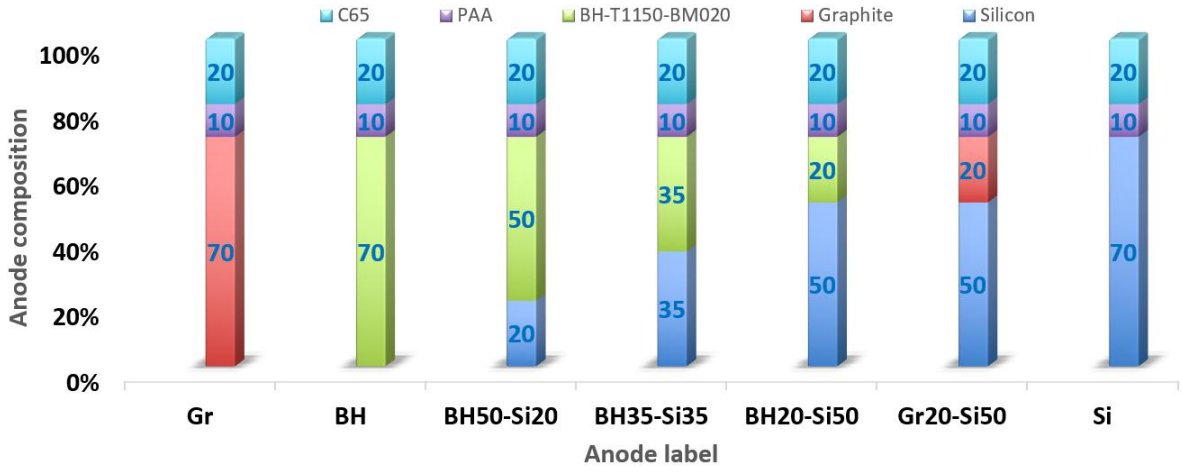

Figure 7.1. Electrode compositions and labeling of the silicon-containing anodes investigated in this chapter.

Table 7.1. Composition and labels of prepared anode series in this chapter.

Anode	Anode Composition	Description
Gr	70% Graphite + 20% C65 + 10% PAA	Conventional graphite control
BH	70% BH + 20% C65 + 10% PAA	barley husks-based control
BH50-Si20	50% BH + 20% Si + 20% C65 + 10% PAA	BH-dominant hybrid
BH35-Si35	35% BH + 35% Si + 20% C65 + 10% PAA	Balanced BH and Si hybrid
BH20-Si50	20% BH + 50% Si + 20% C65 + 10% PAA	Si-rich hybrid
Gr20-Si50	20% Graphite + 50% Si + 20% C65 + 10% PAA	Graphite-supported Si composite
Si	70% Si + 20% C65 + 10% PAA	Pure silicon anode

7.2.2. Slurry formulation, coating and coin-cell assembly

Electrode slurries were prepared following the procedures described in Section 5.2, by dispersing the active material mixture (BH, graphite and/or Si, as defined in Section 7.2.1), carbon black (C65) and PAA binder in deionised water to give a total solid ratio of 70:20:10 by weight. The powders were mixed using planetary stirring until a homogeneous, moderately viscous slurry was obtained. The slurry was then cast onto copper foil current collectors using a doctor blade with a wet film thickness of 200 µm, followed by drying under vacuum at 80 °C for 12 h, following the protocol established in Chapter 5.

Dried electrodes were punched into 14 mm diameter disks and lightly calendared to ensure good contact between active layer and foil while maintaining comparable areal mass loadings across all anodes (≈1.0 mg cm^{-2} for the active fraction). The electrodes were transferred to an argon-filled glovebox (O_2, H_2O < 0.5 ppm) for coin-cell assembly. CR2016 half-cells were assembled using Li metal as counter electrode, Celgard 2325 microporous separators and 1.2 M $LiPF_6$ in EC:EMC (1:3 v/v) containing 15 wt% FEC and 3 wt% VC as the electrolyte.

7.2.3. Quality control and traceability

To maintain continuity with the BH series investigated in Chapters 4 and 5, all BH-containing electrodes in this chapter were prepared from the same master batch of BH-T1150-BM020 powder used previously. Commercial graphite and Si powders were taken from single production batches, and the Si powder was characterised structurally and morphologically prior to electrode fabrication (Section 7.3.1).

Slurry preparation, coating and cell assembly followed standard operating procedures identical to those used in Chapter 5, including fixed mixing times, coating thickness and drying conditions. Each batch of electrodes was labelled by both active-material composition (Gr, BH, BH50-Si20, BH35-Si35, BH20-Si50, Gr20-Si50, Si) and coating date, and coin-cell lots were grouped accordingly. This traceability ensures that performance comparisons within this chapter isolate the effect of composition and Si loading rather than uncontrolled variability in processing or materials supply.

7.3. Structural comparison

Before analysing the electrochemical data, it is useful to establish the structural baseline of the BH-T1150-BM020 host and the properties of the commercial Si powder, and then to consider how these components arrange within the composite electrodes. This section first outlines the morphology, crystallinity and size distribution of the Si powder, followed by a qualitative description of how Si is accommodated within the BH and graphite matrices and the implications for interfacial chemistry.

7.3.1. Structural baseline: BH-T1150-BM020 host and commercial Si powder

Chapter 4 established that BH-T1150-BM020 consists of a disordered hard-carbon framework containing finely dispersed silica domains. The carbon matrix displays broad (002) reflections in XRD and a D/G intensity ratio larger than unity in Raman spectroscopy, consistent with turbostratic, partially graphitised carbon with a high density of defects and edge sites. Nitrogen physisorption and t-plot analysis revealed a hierarchical pore network combining micropores and mesopores, while XPS confirmed the presence of oxygen-containing surface functionalities and Si present predominantly as SiO_2-like environments bonded to carbon. This combination of defective carbon, embedded silica and accessible porosity provides both mechanical compliance and internal free volume, making BH-T1150-BM020 a suitable scaffold for accommodating high-capacity alloying phases.

The commercial Si powder employed in this chapter was characterised prior to electrode fabrication to define its intrinsic morphology and phase composition. Low-magnification SEM imaging in Fig. 7.2a shows agglomerated, irregularly shaped particles forming a loosely packed network. Higher-magnification images combined with EDS elemental maps in Fig. 7.2b to 7.2f reveal that these agglomerates consist of densely packed Si domains coated by a thin conductive Au layer used for imaging, with only a weak, diffuse O signal. This behaviour is consistent with crystalline Si particles bearing a native oxide shell of limited thickness rather than a bulk silica phase. The absence of pronounced compositional inhomogeneity in the Si maps indicates that the powder is chemically uniform at the micrometre scale.

XRD analysis of the Si powder in Fig. 7.3a displays a series of sharp diffraction peaks at $2\theta \approx 28°$, 47°, 56°, 69° and 76°, which match well with the standard pattern of crystalline diamond-cubic Si. No additional crystalline reflections attributable to SiO_2 are observed, confirming that any oxide present is either amorphous or below the detection limit. Dynamic light scattering (DLS) measurements reported in Fig. 7.3b indicate a broad particle-size distribution concentrated between approximately 0.3 and 2 µm, with a tail extending to around 5 to 6 µm. These values are larger than the nominal primary particle size specified by the supplier, reflecting the presence of weakly bound agglomerates in suspension. Overall, the Si powder can be regarded as a highly crystalline, micron-scale material with modest surface oxidation, which is expected to deliver high specific capacity but also to undergo substantial volume change during alloying.

In combination, the BH-T1150-BM020 host and the crystalline Si powder form a complementary pair; the BH matrix provides porosity, defect sites and silica domains that can act as a mechanically compliant and chemically interactive scaffold, while the exogenous Si contributes a large reservoir of alloying capacity. The challenge for the BH/Si hybrids is to integrate these components such that Si is effectively utilised without compromising the structural integrity highlighted for BH-T1150-BM020 in earlier chapters.

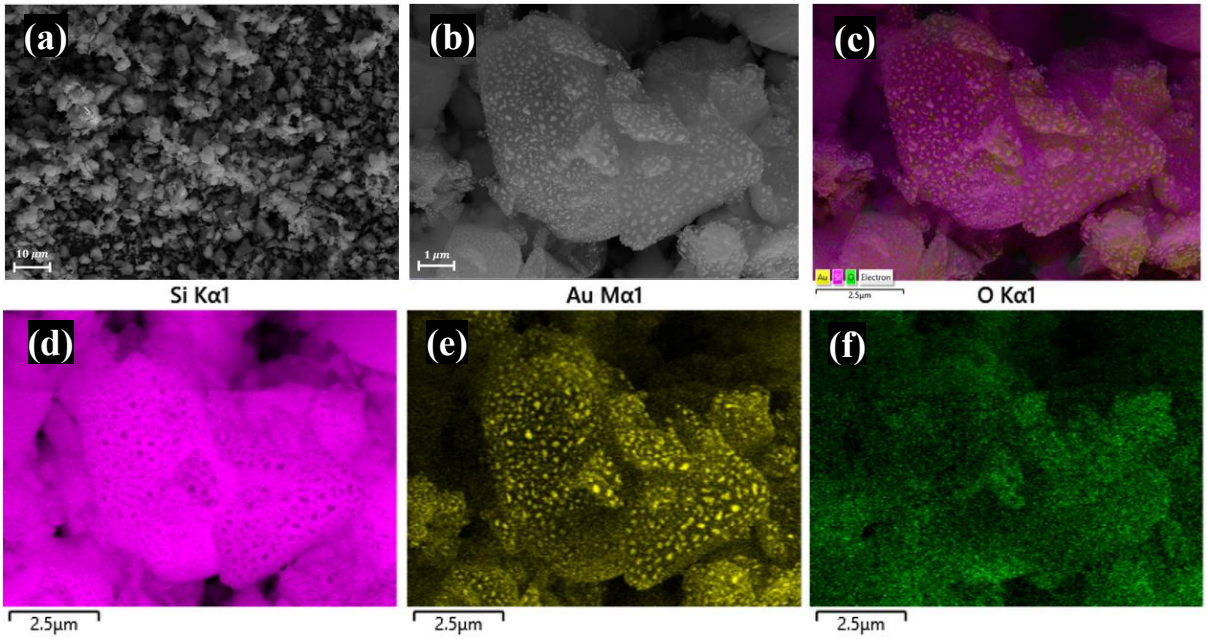

Figure 7.2. SEM and EDS characterisation of the commercial Si powder used in this chapter. (a) Low-magnification SEM image of Si powder, and (b) to (f) high-magnification SEM image and corresponding elemental maps for Si Kα₁, Au Mα₁ (sputter coating) and O Kα₁.

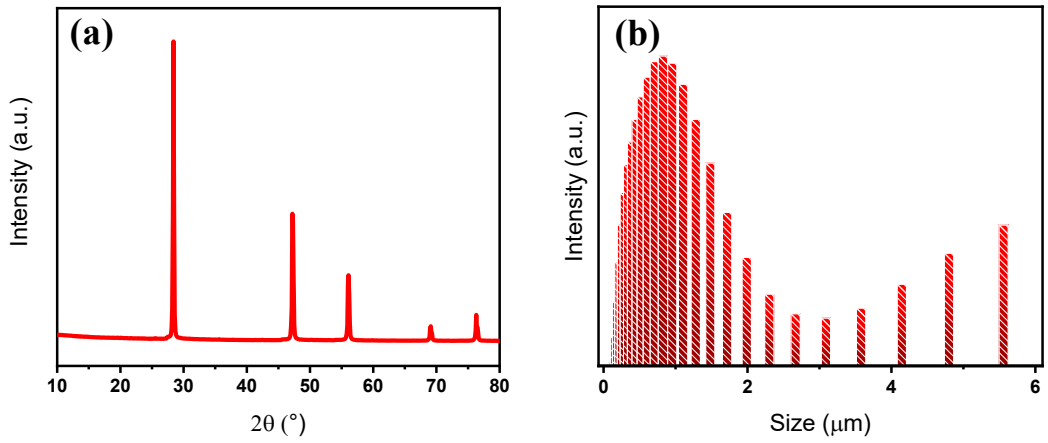

Figure 7.3. Structural and size characterisation of the commercial Si powder: (a) XRD pattern indexed to crystalline Si, showing sharp reflections characteristic of diamond-cubic Si with no

additional crystalline oxide phases; (b) particle-size distribution obtained by DLS, indicating a dominant population of sub-micrometre to few-micrometre Si agglomerates.

7.3.2. Morphology and particle architecture as a function of Si loading

The BH/Si composite anodes investigated in this chapter were designed by progressively replacing BH-T1150-BM020 with the commercial Si powder while maintaining a fixed total active-material fraction of 70 wt%. As a result, BH50-Si20, BH35-Si35 and BH20-Si50 span a transition from a BH-dominated scaffold containing isolated Si domains to a Si-rich architecture in which BH plays a secondary, buffering role. Gr20-Si50 and the Si-only electrode provide graphite-based and carbon-free comparators at the same Si loading.

In the BH50-Si20 formulation, the BH-derived carbon constitutes the majority of the solid framework. During slurry casting and drying, the porous BH particles form a continuous, irregular network, and the Si particles occupy pores and interparticle voids within this matrix. At this relatively low Si fraction, the silicon domains are expected to be predominantly isolated or form small clusters attached to the BH surfaces. The resulting architecture combines a percolated carbon skeleton for electron transport with localised Si reservoirs, leaving sufficient free volume around each Si cluster for expansion during lithiation.

Increasing the Si fraction to 35 wt% in BH35-Si35 leads to a more interconnected Si network. The higher probability of Si-Si contacts, assisted by ball milling, promotes the formation of extended Si agglomerates that remain embedded within the BH matrix rather than forming a separate continuous phase. In this configuration, BH still provides a continuous backbone and pore network, but the local volumetric fraction of Si is higher, enhancing theoretical capacity while modestly reducing the available void space for volume accommodation.

At the highest Si content in BH20-Si50, the morphology tends towards a Si-rich composite in which the silicon particles are closely packed and BH domains are interspersed between them. The pre-cycling SEM images of BH20-Si50 in Fig. 7.8a show a relatively open, porous coating, but with larger bright regions associated with Si-rich clusters embedded in the darker BH background. The BH fraction in this electrode is sufficient to maintain a continuous carbon network and to introduce mesopores, yet the reduced BH content means that the

accommodation of Si expansion relies on more localised voids and the mechanical compliance of the residual BH framework.

The Gr20-Si50 electrode, which contains the same Si fraction as BH20-Si50 but uses graphite in place of BH, exhibits a markedly different particle architecture. Before cycling, shown in Fig. 7.8c, the coating is dominated by stacked, plate-like graphite flakes, with Si particles distributed between and on top of these lamellae. This arrangement yields a denser, less porous microstructure with fewer internal voids and a more rigid backbone compared with BH-containing composites. The pure Si electrode, by contrast, consists largely of agglomerated Si particles with minimal intrinsic porosity and no continuous carbon scaffold. This morphology offers limited internal free volume and poor mechanical buffering, which is reflected in the rapid degradation of its electrochemical performance.

These architectural differences are central to the later electrochemical behaviour. BH-rich compositions provide a porous, compliant host that can distribute Si throughout the coating while preserving ion-transport pathways and electronic percolation. As the Si fraction increases, the local packing of Si becomes tighter and the capacity rises, but the risk of particle agglomeration, stress accumulation and loss of percolation also grows, particularly in the graphite-based and Si-only electrodes.

7.3.3. Interfacial chemistry and bonding considerations

The integration of exogenous Si into the BH-derived matrix creates a multi-phase Si/SiO_2/C environment in which interfacial chemistry plays a key role. Chapter 4 showed that BH-T1150-BM020 contains both C–O functionalities and silica-like Si environments, suggesting the presence of C–O–Si linkages and intimate contact between amorphous SiO_2 and the hard-carbon framework. The commercial Si powder introduces additional crystalline Si domains coated by a thin native SiO_2 layer. In the hybrids, these components are expected to form a heterogeneous network of crystalline Si cores, amorphous SiO_2 shells and BH-derived carbon and silica.

From a bonding perspective, this structure offers several potential advantages compared with a simple graphite/Si mixture. First, the presence of silica and oxygenated carbon at the BH/Si interface can promote stronger chemical adhesion between Si particles and the carbon host via

Si–O–C bridges, reducing the likelihood of interfacial debonding during repeated volume changes. Secondly, the native oxide on Si, together with the embedded SiO_2 in BH, can partially convert to inorganic Li_2O/Li_xSiO_y species upon initial lithiation. Although this process contributes to irreversible capacity loss, it also generates mechanically robust, inorganic components within the solid-electrolyte interphase that help to stabilise the Si surface during subsequent cycling.

Compared with graphite, the BH-derived carbon presents a higher density of defects, edge sites and heteroatoms, which are known to influence SEI composition and stability. The more polar BH surface is likely to favour the formation of inorganic-rich SEI layers containing LiF, Li_2CO_3 and Li_2O, while the higher specific surface area promotes rapid SEI formation during the first few cycles. In BH/Si hybrids, the SEI therefore forms not only on the external surface of the composite particles but also within the internal pore network and at Si/BH interfaces. When the BH fraction is sufficient, the mechanical compliance and porosity of the host help to accommodate this SEI without catastrophic cracking, leading to the relatively high and stable Coulombic efficiencies observed for BH50-Si20 and BH35-Si35.

In Si-rich compositions and in the graphite-supported Gr20-Si50 electrode, the interfacial chemistry is less favourable. The larger, more densely packed Si agglomerates experience greater local strain during alloying, which can fracture both the native oxide and the SEI, exposing fresh Si and driving continuous electrolyte decomposition. In the graphite-based composite, the chemically inert, low-defect graphite surface provides limited anchoring for Si and its oxide shell, promoting interfacial sliding and crack formation during cycling. This mechanistic picture is consistent with the more rapid capacity fading, increased polarisation and pronounced peak broadening observed for Gr20-Si50 and pure Si in Section 7.4.

Overall, the structural and interfacial characteristics outlined in this section provide the framework for interpreting the electrochemical trends presented later. The BH-derived host not only distributes and electronically connects the exogenous Si but also offers chemically interactive, silica-rich interfaces that can stabilise the evolving SEI. The balance between these beneficial effects and the increasing mechanical and interfacial challenges at high Si loading underpins the design window for BH/Si anodes that is discussed in Section 7.6.

7.4. Benchmarking BH/Si hybrids against BH and graphite

7.4.1. Cyclic voltammetry

The electrochemical behaviour of the different anodes was first assessed by cyclic voltammetry (CV), as shown in Fig. 7.4. Each anode exhibits distinct lithiation-delithiation signatures that reflect its dominant charge-storage mechanism and degree of reversibility.

The CV profile of the graphite anode in Fig. 7.4a displays the characteristic features of Li^+ intercalation into graphitic carbon. During the first cathodic sweep, a broad reduction peak centred at approximately 0.6 to 0.8 V vs Li^+/Li is observed, which disappears in subsequent cycles. This feature is associated with the formation of the solid electrolyte interphase (SEI) arising from reductive decomposition of the electrolyte components on the graphite surface.[4] Its absence in later cycles indicates the establishment of a passivating SEI layer that stabilises the electrode-electrolyte interface and accounts for a substantial fraction of the initial irreversible capacity loss in graphite anodes. As the potential decreases further, a sharp cathodic peak below about 0.25 V vs Li^+/Li appears, corresponding to stage-wise Li^+ intercalation into the graphite galleries and eventual formation of LiC_6. On the anodic sweep, a narrow peak at ~0.2 to 0.25 V vs Li^+/Li is recorded, associated with LiC_6 deintercalation.[4, 5] The symmetry and reproducibility of these intercalation-deintercalation peaks over the second and third cycles confirm highly reversible Li storage and low polarisation, consistent with an ordered graphitic structure and effective SEI passivation, in agreement with the graphite benchmark behaviour discussed in Chapter 6.

In contrast, the BH anode in Fig. 7.4b, corresponding to the BH-T1150-BM020 material introduced in Chapters 4 and 5, exhibits a CV response typical of disordered hard carbon. The first cathodic sweep displays a broad hump extending from ~1.0 to 0.2 V vs Li^+/Li, which is attributed to surface-controlled storage processes, including SEI formation, Li^+ adsorption at defect sites, and interactions with surface functional groups and residual silica phases.[6] A subtle shoulder around 0.4 to 0.6 V vs Li^+/Li likely reflects partial reduction of surface oxygen-containing moieties and contributions from the embedded SiO_2 domains. Below ~0.2 V vs Li^+/Li, the cathodic current increases gradually in a sloping manner, indicative of Li^+ insertion into nanopores and highly disordered carbon domains rather than stage transitions. On the anodic sweep, a broad feature between ~0.2 and 0.5 V vs Li^+/Li develops and stabilises after the first cycle, signalling improved interfacial kinetics and a more mature SEI from cycle 2 onwards, consistent with the behaviour previously reported for hard-carbon systems.[7, 8]

Introducing silicon into the BH matrix leads to a systematic evolution in CV features shown in Fig. 7.4c to 7.4e. For the BH50-Si20 hybrid in Fig. 7.4c, which contains the lowest Si fraction, the CV retains much of the broad BH-like lithiation signature, yet a new cathodic peak emerges below 0.1 V vs Li^+/Li. This low-potential peak is characteristic of alloying between Si and Li to form Li_xSi, confirming that the silicon component is electrochemically active.[9] The accompanying anodic response remains relatively broad, indicating that the BH framework continues to dominate the interfacial behaviour and provides a buffered environment for Si alloying.

As the Si content increases to 35 and 50 wt% in BH35-Si35 and BH20-Si50 in Fig. 7.4d and (e), respectively, the intensity of the sharp lithiation peak below 0.1 V vs Li^+/Li rises markedly, while the anodic scan develops pronounced features in the 0.35 to 0.55 V vs Li^+/Li range. These peaks correspond to stepwise dealloying of Li_xSi phases. At the same time, the underlying BH contribution remains evident as broad current responses between ~0.2 and 0.6 V vs Li^+/Li, indicating that both the hard-carbon host and the Si inclusions remain electrochemically active. This overlapping behaviour suggests that the BH matrix continues to modulate local volume changes and charge distribution during cycling. Notably, the cathodic and anodic peaks in BH35-Si35 are sharper and more clearly defined than in BH50-Si20, indicating improved Si utilisation while retaining sufficient BH content to maintain structural buffering and cycling stability.

The graphite/silicon composite Gr20-Si50 in Fig. 7.4f, which has the same Si content as BH20-Si50, exhibits similarly sharp alloying peaks below 0.1 V and above ~0.4 V vs Li^+/Li, but with more pronounced peak separation and asymmetry, particularly in the first cycle. The larger spacing between cathodic and anodic peaks signifies higher overpotential and poorer reaction reversibility. This behaviour suggests that graphite is less effective than the BH matrix in stabilising the Si network, consistent with its lower porosity and reduced mechanical compliance. The denser graphite structure is more susceptible to interfacial stress and SEI breakdown under repeated Si expansion and contraction, which foreshadows the inferior long-term cycling performance of Gr20-Si50 relative to the BH/Si hybrids.

Finally, the pure Si anode in Fig. 7.4g displays the most intense and narrow lithiation peak below 0.1 V vs Li^+/Li and steep dealloying peaks between approximately 0.35 and 0.55 V vs Li^+/Li, reflecting the high specific capacity of crystalline silicon. However, the rapid decrease in current intensity and the noticeable shift of these peaks over subsequent cycles indicate

extensive SEI growth, electrode cracking and Li trapping, all of which are well-known limitations of Si-based anodes.[10] Compared with this unstable baseline, the BH/Si hybrid electrodes exhibit a more gradual and stabilised electrochemical response, with BH35-Si35 in particular providing a favourable compromise between capacity, reversibility and kinetic accessibility.

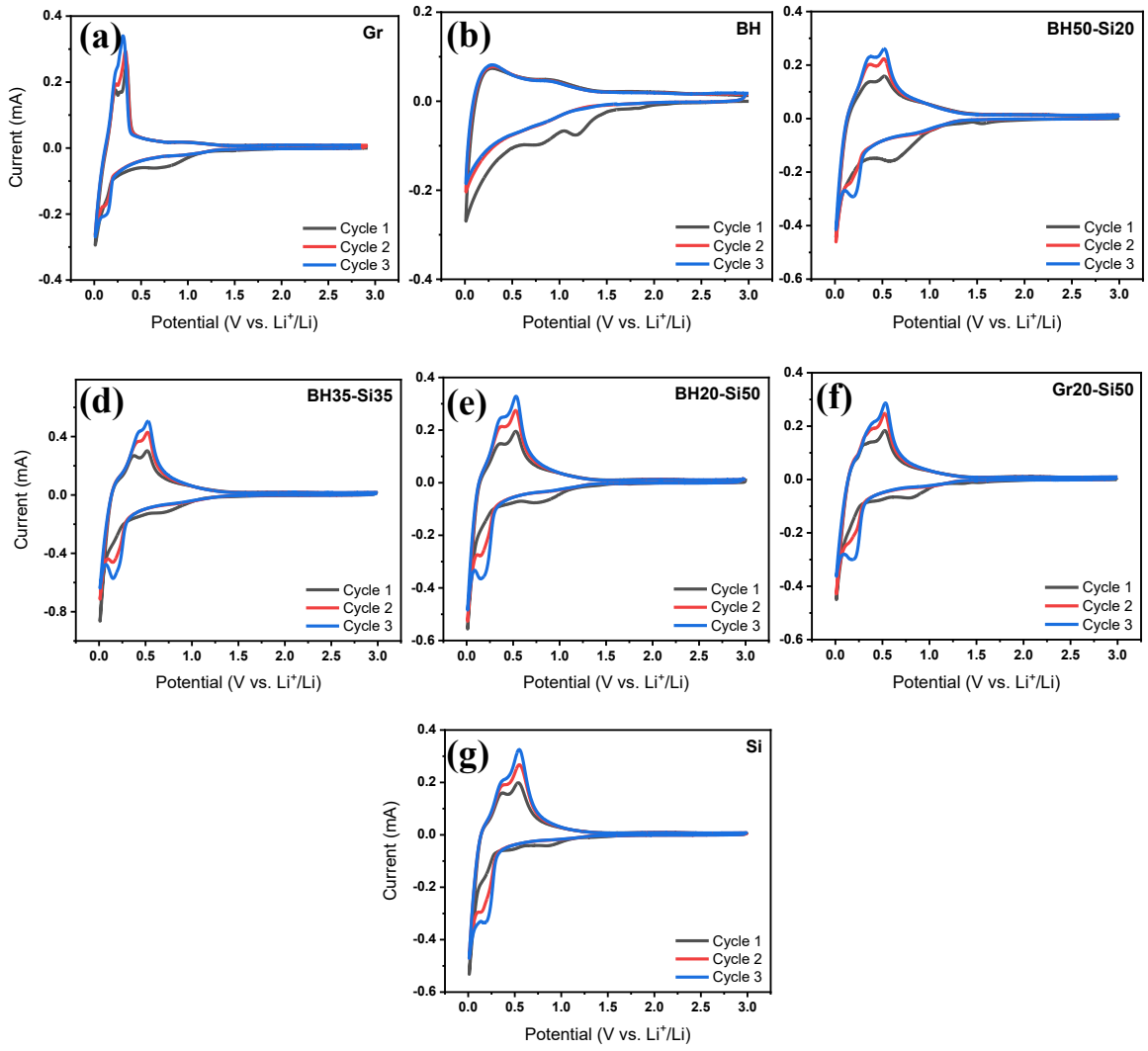

Figure 7.4. CV curves of (a) graphite labelled as Gr, (b) pure barley husk labelled as BH, (c) BH50-Si20, (d) BH35-Si35, (e) BH20-Si50, (f) Gr20-Si50, and (g) pure silicon labelled as Si anodes recorded at a scan rate of 0.2 mV s^{-1} in the voltage range of 3.0 to 0.01 V vs Li^+/Li during the first three cycles.

7.4.2. Galvanostatic voltage profiles

Galvanostatic charge-discharge profiles at C/5 for the first and third cycles are presented in Fig. 7.5. The graphite anode, labelled as Gr in Fig. 7.5a, exhibits the expected behaviour of a conventional intercalation host, with a flat lithiation plateau below 0.2 V vs Li^+/Li and a sharp delithiation plateau centred at ~0.25 V vs Li^+/Li. The small voltage hysteresis of ~0.07 V and the highly reproducible profile between the first and third cycles reflect efficient charge transfer and structurally reversible Li^+ intercalation. This is consistent with the limited irreversible capacity loss (~11 %) and an initial Coulombic efficiency (ICE) of ~89 %, in agreement with the graphite benchmark in Chapter 6.

The pure barley husk anode, labelled as BH, corresponding to BH-T1150-BM020 shown in Fig. 7.5b shows a markedly different response. The voltage profile is fully sloping, extending from 0.01 to approximately 1.0 V vs Li^+/Li without distinct plateaus. This behaviour mirrors the broad features observed in the CV response for BH and reflects Li storage dominated by surface adsorption, defect trapping and pore filling within the disordered carbon-silica framework. The relatively low ICE of ~60 % and the absence of sharp redox plateaus indicate substantial initial SEI formation and predominately capacitive storage, typical of hard-carbon-type materials discussed in Chapter 5.

Upon incorporation of exogenous Si, the BH/Si hybrids reveal a progressive evolution of the voltage profiles. The BH50-Si20 composite shown in Fig. 7.5c largely retains the sloping BH background but begins to display a weak lithiation plateau near 0.1 V vs Li^+/Li, signalling partial activation of the Si phase. As the Si fraction increases in BH35-Si35 and BH20-Si50, shown in Fig. 7.5d and 7.5e, respectively, well-defined plateaus emerge below 0.1 V vs Li^+/Li during lithiation together with broadened delithiation features between 0.35 and 0.55 V vs Li^+/Li. These signatures are characteristic of Li_xSi alloying and dealloying superimposed on the BH hard-carbon contribution. Among the hybrids, BH35-Si35 achieves a particularly balanced behaviour, combining a high ICE of ~87 % with moderate hysteresis (~0.12 V vs Li^+/Li), which suggests effective Si utilisation while maintaining the mechanical buffering and porosity of the BH host. For BH20-Si50, the further increase in Si content substantially boosts capacity but is accompanied by increased polarisation and a modest reduction in early-cycle Coulombic efficiency (~80 %), indicating higher kinetic and interfacial penalties at elevated Si loading.

The graphite/silicon composite Gr20-Si50 in Fig. 7.5f also displays pronounced lithiation-delithiation plateaus originating from the Si component; however, the associated hysteresis (~0.18 V vs Li^+/Li) is larger than in BH20-Si50. This greater overpotential, together with the sharper profile, points to more sluggish reaction kinetics and higher interfacial stress, consistent with the limited ability of the dense graphite framework to accommodate Si expansion. These observations align with the broader CV peak separation reported for Gr/Si systems and foreshadow the poorer long-term capacity retention of Gr20-Si50 compared with BH/Si composites.

Pure Si, Fig. 7.5g delivers the steepest and most well-defined alloying plateaus, reflecting its intrinsically high gravimetric capacity. However, this is achieved at the expense of stability: the ICE is only ~72 %, and the capacity declines sharply by the third cycle. The rapid loss in reversible capacity highlights extensive SEI growth, mechanical fracture and Li trapping in the unstable Si network. The overlaid profiles in Fig. 7.5h and 7.5k summarise the continuum of behaviours: Gr and BH provide stable but moderate-capacity responses at either end of the spectrum; pure Si offers very high but rapidly fading capacity; and the BH/Si hybrids, with BH35-Si35 particularly notable, deliver an intermediate regime where enhanced capacity is achieved with substantially improved reversibility and reduced hysteresis. This establishes the BH host as an effective structural and electrochemical buffer for Si, outperforming the equivalent graphite/Si formulation in early-cycle performance.

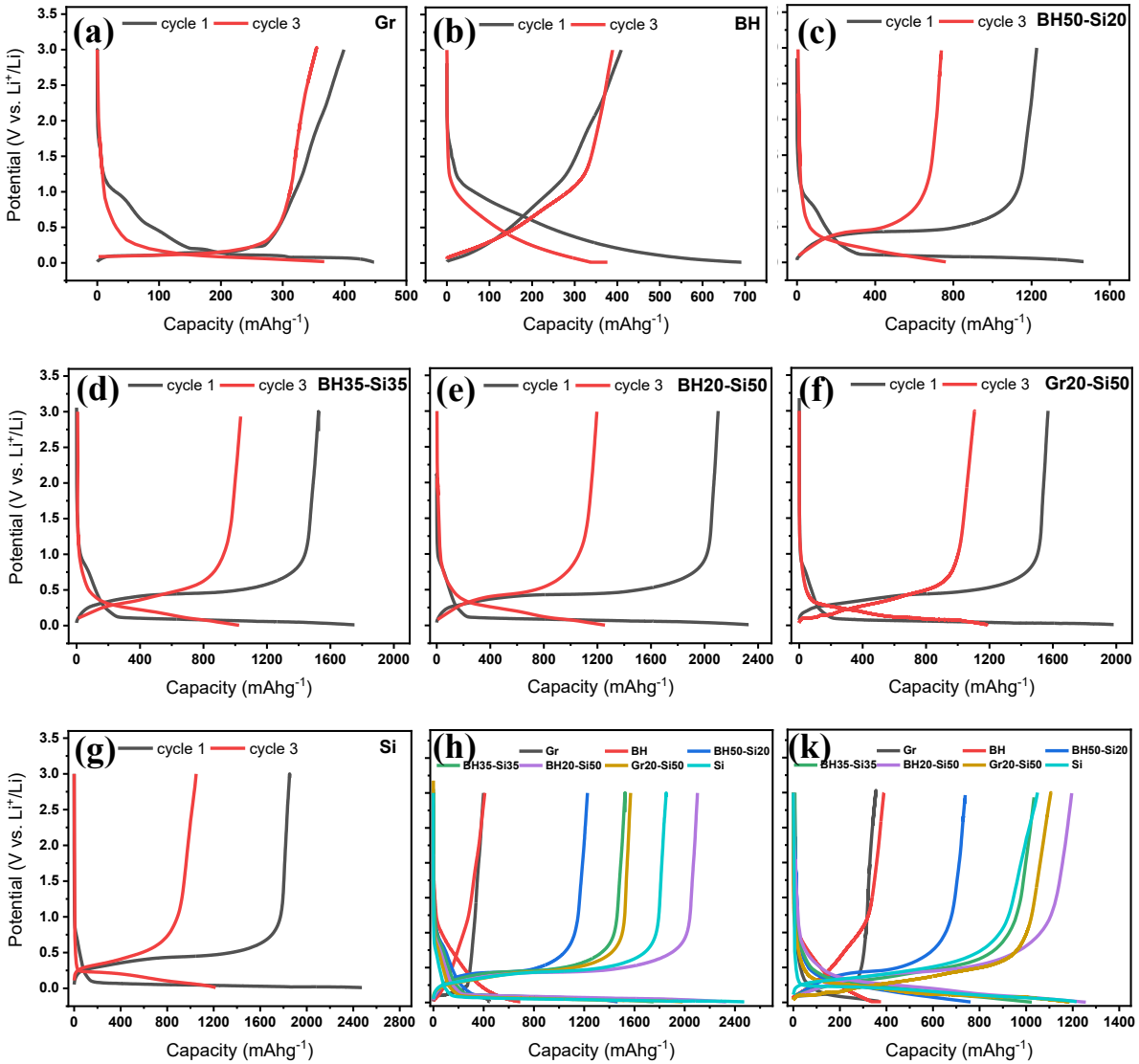

Figure 7.5. Galvanostatic charge-discharge voltage profiles of a) graphite (Gr), b) pure barley husk (BH), c) BH50-Si20, d) BH35-Si35, e) BH20-Si50, f) Gr20-Si50, and g) pure silicon (Si) anodes at a current rate of C/5, showing the 1st and 3rd cycles. h) and k) comparative overlays of all anode types in the 1st and 3rd cycles, respectively. All profiles are recorded within the voltage range of 0.01 to 3.0 V vs Li^+/Li.

7.4.3. Cycling stability, rate capability and capacity retention

Fig. 7.6 summarises the cycling stability and rate capability of the different anode formulations and reinforces the mechanistic trends inferred from the CV and voltage profiles (Sections 7.4.1 and 7.4.2). At a constant current of C/5 as shown in Fig. 7.6a, the graphite and BH electrodes deliver stable yet moderate capacities of approximately 350 and 380 mAh g^{-1}, respectively,

consistent with their structural characteristics and theoretical limits. The slightly higher capacity of BH compared with graphite reflects additional Li storage associated with defects and micro -or mesoporosity in the BH-derived hard carbon, in agreement with its sloping voltage profile and broad CV features. Both Gr and BH maintain more than 95 % of their initial capacities over 50 cycles, confirming minimal volumetric strain and a well-stabilised SEI, in line with their negligible alloying contributions.

Upon incorporation of Si, the BH/Si hybrid anodes exhibit a clear increase in deliverable capacity. After 50 cycles at C/5, BH50-Si20 reaches ~670 mAh g^{-1}, BH35-Si35 achieves ~880 mAh g^{-1} and BH20-Si50 attains ~1180 mAh g^{-1}. Despite the progressive increase in Si content, all BH/Si composites show relatively smooth capacity decay without abrupt failures, indicating that the BH matrix effectively mitigates Si volume expansion and maintains electrical connectivity. This behaviour compares favourably with several recently reported biomass-derived Si/C anodes prepared by simple mechanical blending, which commonly suffer from rapid capacity loss due to insufficient buffering of Si pulverisation.[11, 12] In direct contrast, the Gr20-Si50 composite, which contains the same Si loading as BH20-Si50, displays a noticeably faster decline in capacity (from ~960 to ~880 mAh g^{-1} over 50 cycles), indicating that graphite is less effective than BH as a mechanical and structural buffer. The performance of the pure Si electrode further highlights this limitation: although the initial capacity exceeds 2400 mAh g^{-1}, it falls below 200 mAh g^{-1} by cycle 50, evidencing severe structural degradation and unstable interfacial chemistry.

The Coulombic efficiency (CE) profiles in Fig. 7.6b provide additional insight into SEI formation and interfacial stability. All anodes reach CE values above 98 % within the first ten cycles, indicating that SEI growth becomes largely self-limiting after the initial formation period. Graphite and BH stabilise most rapidly, reflecting their relatively mild interfacial reactivity. The BH/Si hybrids display a slightly slower approach to steady-state CE, consistent with the increased surface activity and repeated volume changes associated with Si. Among the composites, BH35-Si35 stands out, achieving CE values above 99 % by approximately the 15th cycle and maintaining them thereafter, which indicates a good balance between high capacity and interfacial stability.

Rate performance data plotted in Fig. 7.6c further differentiate the anodes under dynamically varying current loads. Across all tested C-rates, BH20-Si50 delivers the highest capacities, retaining around 950 mAh g^{-1} even at 2C and recovering almost fully when the current is

returned to C/10. BH35-Si35 and BH50-Si20 follow with intermediate capacities (approximately 820 and 650 mAh g^{-1} at 1C, respectively), but all BH/Si hybrids display strong rate tolerance and excellent capacity recovery. These trends indicate robust structural integrity and relatively fast Li^+ transport within the BH-Si architecture, in agreement with the mixed hard-carbon/alloying mechanism inferred from CV and voltage profiles. Gr20-Si50, in contrast, shows reduced rate capability, particularly at high C-rates, which reflects the combination of diffusion-limited graphite intercalation and mechanically constrained Si alloying.

Long-term cycling at C/5 over 500 cycles depicted in Fig. 7.6d highlights the intrinsic stability differences more clearly. The pure Si anode loses usable capacity within only a few cycles, confirming extensive mechanical failure and continuous SEI regeneration. Graphite demonstrates excellent durability, retaining 96.6, 94.4, 90.9, 87.7 and 84.6 % of its initial capacity after 100, 200, 300, 400 and 500 cycles, respectively. The BH anode shows similarly robust behaviour, with corresponding retention values of 97.9, 96.4, 93.9, 88.0 and 80.8 %, again consistent with the mechanically stable, non-alloying nature of the BH-derived hard carbon.

For the BH/Si hybrids, increasing Si content leads to the expected trade-off between capacity and long-term retention. BH50-Si20 exhibits particularly stable cycling, maintaining 97.6, 90.3, 87.2, 82.7 and 78.1 % of its initial capacity at 100, 200, 300, 400 and 500 cycles, respectively. BH35-Si35 shows slightly lower but still strong retention of 89.0, 84.1, 79.9, 77.5 and 72.9 % at the same intervals, which is notable given its higher Si loading and increased initial capacity. BH20-Si50, with the largest Si fraction, unsurprisingly displays the most pronounced capacity fade among the BH-Si composites, yet still preserves 86.3, 80.5, 75.6, 71.3 and 65.8 % of its initial capacity up to 500 cycles. These results confirm that the BH host continues to provide effective buffering even at substantial Si contents. In sharp contrast, the Gr20-Si50 composite undergoes rapid deterioration, retaining only 67.6, 49.8, 33.2, 17.2 and finally 2.4 % of its initial capacity at the same cycle numbers. The severe decay underscores the inability of the graphite matrix to accommodate repeated Si expansion and contraction without losing structural integrity.

Taken together, these data demonstrate that BH/Si hybrid anodes combine high capacity with good rate capability and extended cycling stability. Among the formulations examined, BH35-Si35 emerges as a particularly attractive compromise, offering significantly higher capacity

than pure BH and graphite while maintaining stable Coulombic efficiency and long-term capacity retention under practically relevant cycling conditions.

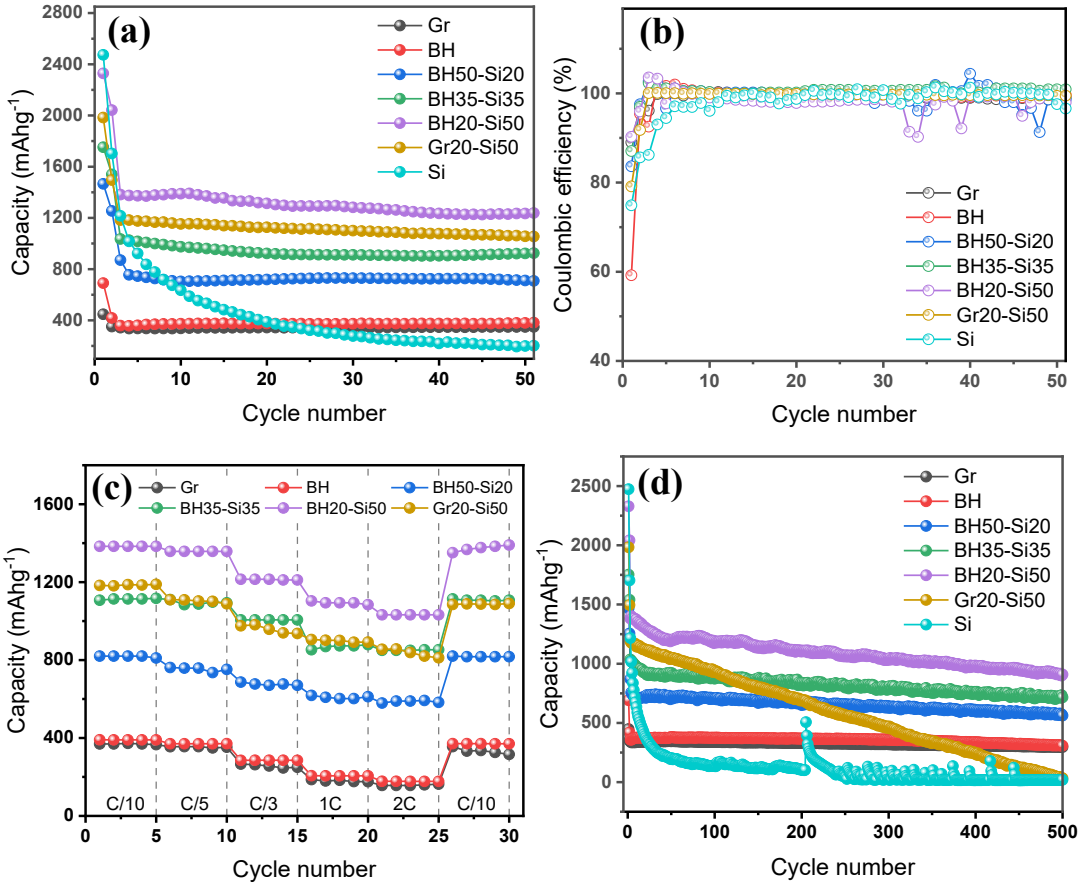

Figure 7.6. (a) Cycling performance of all anodes at a current rate of C/5 over 50 cycles, (b) Corresponding Coulombic efficiency profiles during cycling, (c) Rate capability of selected anodes evaluated across multiple current densities (C/10 to 2C) and returned to C/10, and (d) Long-term cycling performance of all anodes over 500 charge-discharge cycles.

7.4.4. Differential capacity analysis and Li-storage mechanisms

The differential capacity (dQ/dV) plots in Fig. 7.7 provide further insight into the redox mechanisms and their evolution during cycling by resolving the lithiation and delithiation processes as a function of potential. For the graphite anode depicted in Fig. 7.7a, sharp and well-defined cathodic and anodic peaks are observed at ~0.1 V and ~0.25 V vs Li^+/Li, respectively, corresponding to the reversible staging transitions between graphite and LiC_6. The peak positions and intensities remain almost unchanged up to the 50th cycle, confirming highly

reversible intercalation, limited polarisation growth and minimal structural degradation, consistent with the stable CV and galvanostatic profiles described in Sections 7.4.1 and 7.4.2.

In contrast, the BH anode in Fig. 7.7b exhibits broad and diffuse dQ/dV signatures. Cathodic activity spans a wide potential window from ~1.0 to 0.1 V vs Li^+/Li, while the corresponding anodic response extends from ~0.1 to 0.6 V vs Li^+/Li. These wide features are characteristic of pseudocapacitive and diffusion-limited Li^+ storage in disordered carbon domains and confined pores rather than discrete phase transitions. The shape of the curves remains relatively stable from the third to the fiftieth cycle, indicating that once the initial SEI is formed, the BH-derived hard-carbon framework maintains good structural and interfacial stability.

For the BH/Si hybrid anodes, the dQ/dV profiles reveal the progressive contribution of Si alloying to the overall redox behaviour. BH50-Si20 in Fig. 7.7c displays a combination of the broad BH-related background and emerging sharp peaks at ~0.05 V on lithiation and ~0.4 to 0.5 V vs Li^+/Li on delithiation, characteristic of Li_xSi alloying-dealloying reactions. These Si-related peaks increase in intensity with higher Si content in BH35-Si35 and BH20-Si50 in Fig. 7.7d and 7.7e, becoming more pronounced and better defined while still superimposed on the underlying BH contribution. The hybrid systems retain relatively stable peak positions up to the 50^{th} cycle, indicating that the alloying reactions remain accessible despite repeated volume changes. Among them, BH35-Si35 shows the least peak broadening or shift over time, signalling a favourable balance between reaction kinetics and mechanical integrity. BH20-Si50 begins to exhibit slight peak smearing and reduced sharpness by cycle 50, suggesting moderate polarisation growth associated with the higher Si loading and increased mechanical stress.

The Gr20-Si50 composite shown in Fig. 7.7f, which contains the same Si fraction as BH20-Si50 but uses graphite as the host, shows more pronounced peak distortion and broadening with cycling, especially in the anodic region. The progressive loss of peak definition indicates poorer structural accommodation of Si and increasing instability at the graphite-Si interface. These features align with the larger voltage hysteresis and faster capacity fade observed for Gr20-Si50 in Sections 7.4.2 and 7.4.3, and reinforce the conclusion that graphite is a less effective buffer for Si expansion than the BH-derived hard carbon.

The pure Si anode in Fig. 7.7g initially presents the most intense and narrow alloying peaks, with steep lithiation and delithiation features associated with multi-step Li_xSi transformations. However, these peaks decay rapidly, broaden and decrease markedly in height by the 50^{th} cycle, pointing to extensive SEI reformation, progressive loss of electrical contact and Li trapping

within fractured Si domains. This behaviour is fully consistent with the rapid capacity loss and relatively low Coulombic efficiency previously observed.

Overall, the dQ/dV analysis confirms that the BH-derived hard-carbon host plays a critical role in stabilising Si redox activity. By providing a compliant, porous matrix, BH suppresses severe peak distortion and polarisation growth that are otherwise evident in graphite-Si and pure Si electrodes. Among the BH/Si hybrids, BH35-Si35 exhibits the most stable and well-defined differential capacity signatures over 50 cycles, supporting its identification as an optimal compromise between high alloying capacity and robust structural buffering.

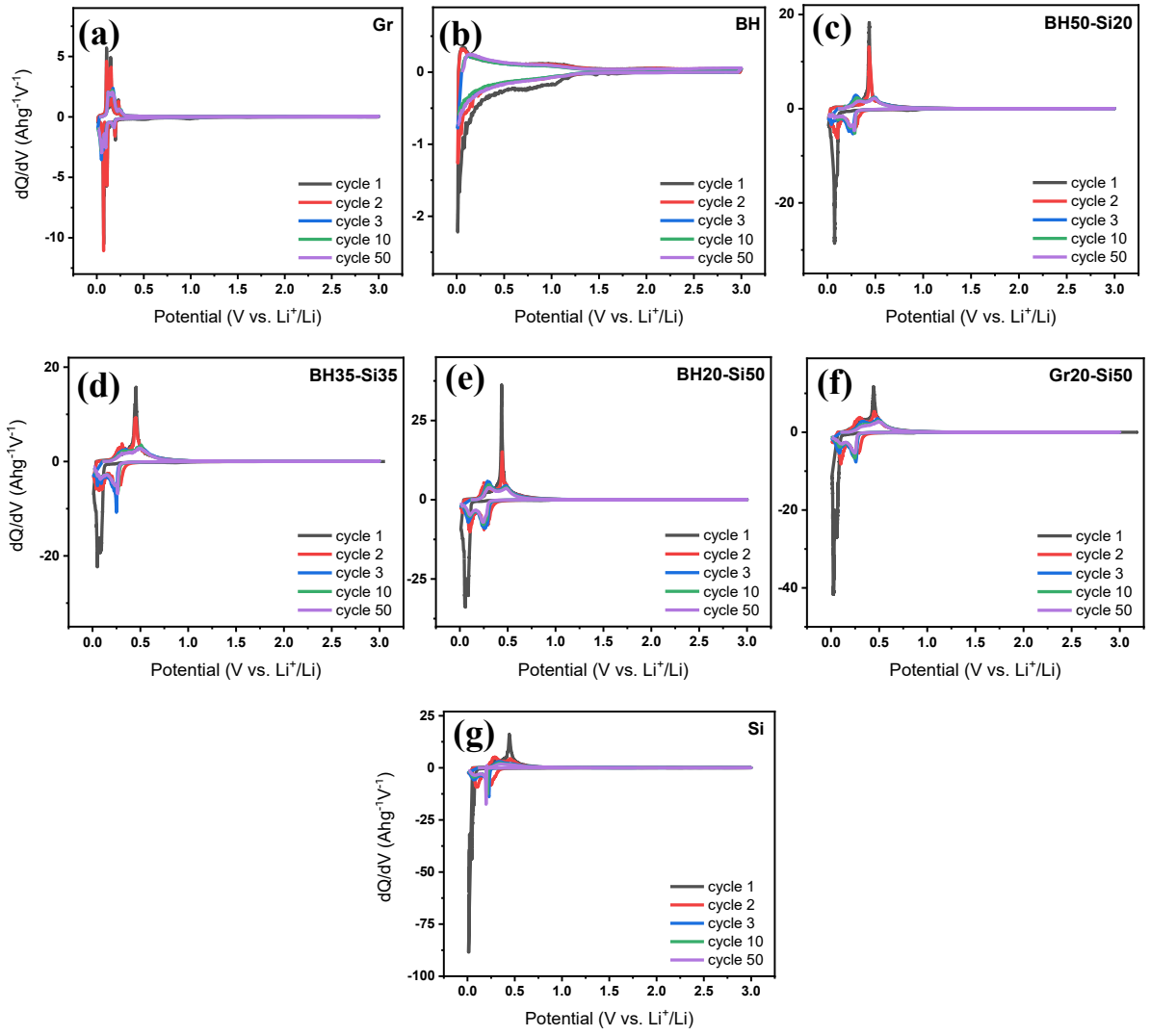

Figure 7.7. Differential capacity (dQ/dV) plots of (a) graphite, (b) barley husk, (c) BH50-Si20, (d) BH35-Si35, (e) BH20-Si50, (f) Gr20-Si50, and (g) silicon anodes recorded at a current rate of C/5 over selected cycles (1st, 2nd, 3rd, 10th, and 50th).

7.4.5. Post-mortem SEM

Post-mortem SEM analysis was carried out on BH20-Si50 and Gr20-Si50 anodes before cycling and after 100 cycles at C/5 in order to correlate the electrochemical behaviour with morphological evolution and is depicted in Fig. 7.8. Prior to cycling, both electrodes exhibit relatively homogeneous distributions of active particles within the composite coating, but with clearly different architectures. BH20-Si50 displays a highly porous, irregular network characteristic of biomass-derived carbon, into which Si particles are embedded and interconnected. In contrast, Gr20-Si50 shows smoother, plate-like graphite domains with Si particles dispersed between more compact flakes, producing a denser and less compliant microstructure.

After 100 cycles, the BH20-Si50 electrode largely preserves its porous framework. The overall morphology remains continuous, with only limited particle fragmentation and moderate surface roughening visible in local regions. The maintenance of this percolated, void-rich structure supports the notion that the BH matrix can effectively accommodate the repeated expansion and contraction of Si during alloying/dealloying, thereby sustaining electrical contact and ion-transport pathways. This observation is consistent with the relatively high capacity retention and stable differential-capacity features reported for BH20-Si50 in Sections 7.4.3 and 7.4.4.

In sharp contrast, the Gr20-Si50 electrode exhibits pronounced structural degradation after 100 cycles. Extensive cracking of the composite layer, pulverisation of active particles and a near-complete loss of the original flake-like morphology are evident. Large isolated fragments and gaps appear within the electrode, indicating loss of percolation and severe disruption of both electronic and ionic transport paths. This morphological breakdown directly correlates with the rapid capacity fading, increased hysteresis and peak broadening observed electrochemically for Gr20-Si50, and highlights the inability of the relatively rigid graphite scaffold to buffer Si volume changes. Taken together, the post-mortem SEM results provide direct visual evidence that the BH-derived carbon matrix offers a more mechanically tolerant and structurally resilient host for Si than graphite, underpinning the superior long-term cycling performance of BH/Si hybrids.

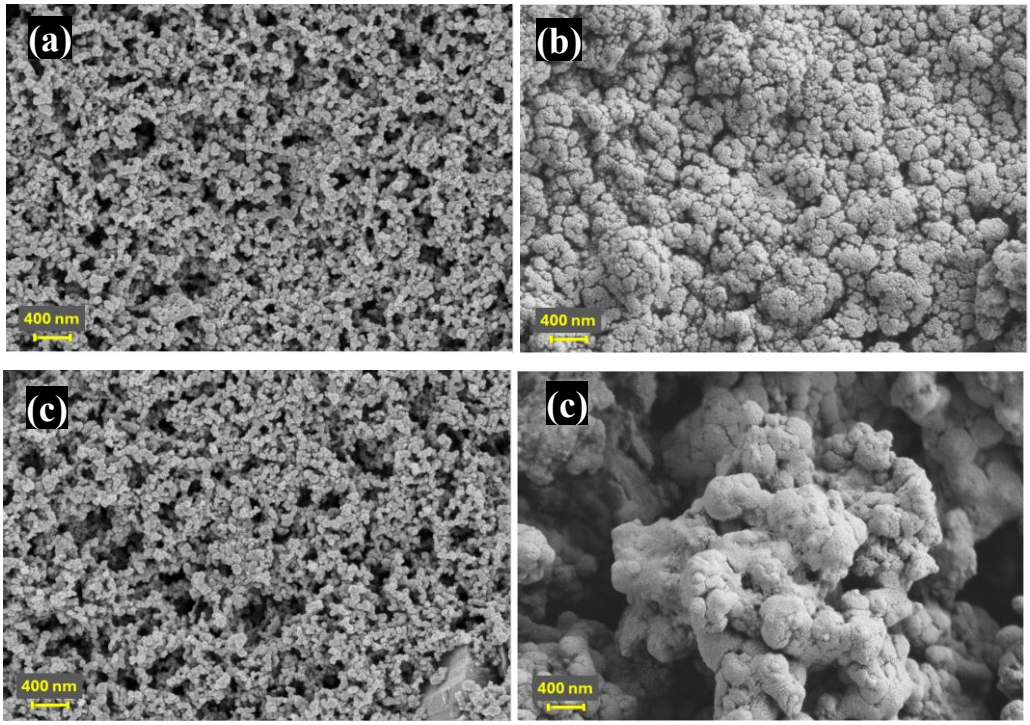

Figure 7.8. SEM images of BH20-Si50 anode (a) before cycling and (b) after 100 cycles, and Gr20-Si50 anode (c) before cycling and (d) after 100 cycles, all cycled at C/5.

7.5. Full-cell performance of BH/Si hybrids

7.5.1. NMC622 cathode baseline

To enable a meaningful assessment of BH/Si anodes under practical conditions, a well-characterised cathode baseline is required. $LiNi_{0.6}Mn_{0.2}Co_{0.2}O_2$ (NMC622) was selected as the cathode owing to its established combination of high specific capacity, structural robustness and commercial relevance. The choice of NMC622 was intended to provide a demanding and industrially relevant benchmark for evaluating the full-cell behaviour of the BH/Si anode, rather than to identify the most sustainable cathode chemistry. In the context of this thesis, the sustainability focus lies primarily in the development of a biomass-derived anode from barley husk, while the use of a commercially established cathode allows the effect of the anode design on full-cell energy density and cycling behaviour to be assessed under realistic Li-ion conditions.

The cathode performance was first examined in half-cell configuration against Li metal, and the results are summarised in Fig. 7.9. The galvanostatic profiles at C/5 for the 1st and 50th cycles as shown in Fig. 7.9a exhibit the typical response of layered oxide cathodes, with a gently sloping curve and a pronounced plateau centred around 3.8 V vs Li^+/Li associated with reversible Li^+ intercalation and deintercalation within the NMC structure. The near overlap of the 1st and 50th cycle profiles indicates limited polarisation growth and good structural stability during extended cycling. Correspondingly, the cycling data in Fig. 7.9b show a capacity retention of approximately 92 % after 50 cycles at C/5, accompanied by a Coulombic efficiency that rapidly approaches and remains close to 100 %. These features confirm fast interfacial kinetics and a largely self-limited SEI on the cathode side.

Rate capability tests in Fig. 7.9c and 7.9d further highlight the reliable kinetics of NMC622. The voltage profiles remain smooth and well defined as the current rate is increased from C/10 to 2C, and the cathode retains around 82 % of its C/10 capacity at 2C. When the current is returned to C/10, the capacity is essentially restored, demonstrating excellent structural reversibility and negligible irreversible damage under the applied rate protocol.

Overall, the half-cell results establish NMC622 as a stable, high-performing cathode with suitable rate response and cycling retention for pairing with high-capacity anodes. This behaviour provides a robust reference for subsequent full-cell tests with BH20-Si50 and underpins the interpretation of anode-limited performance in Section 7.5.2.

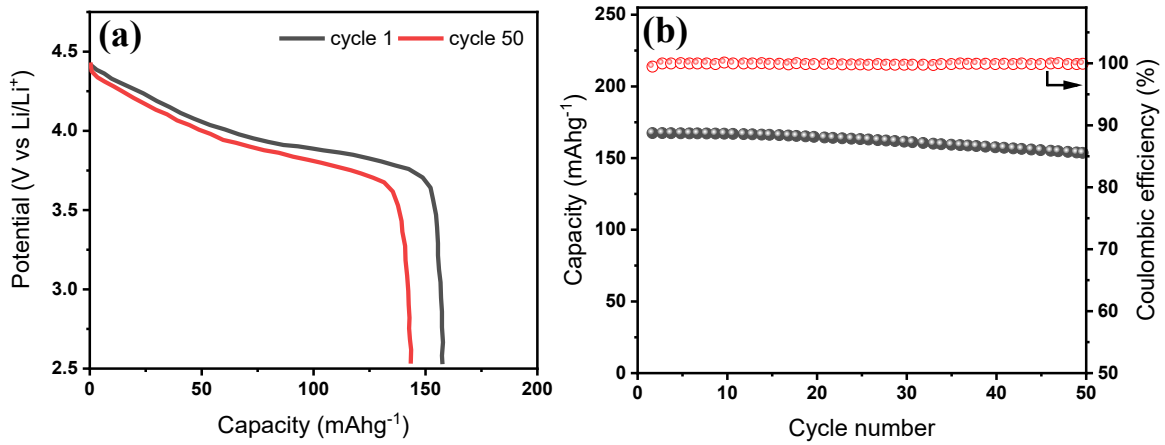

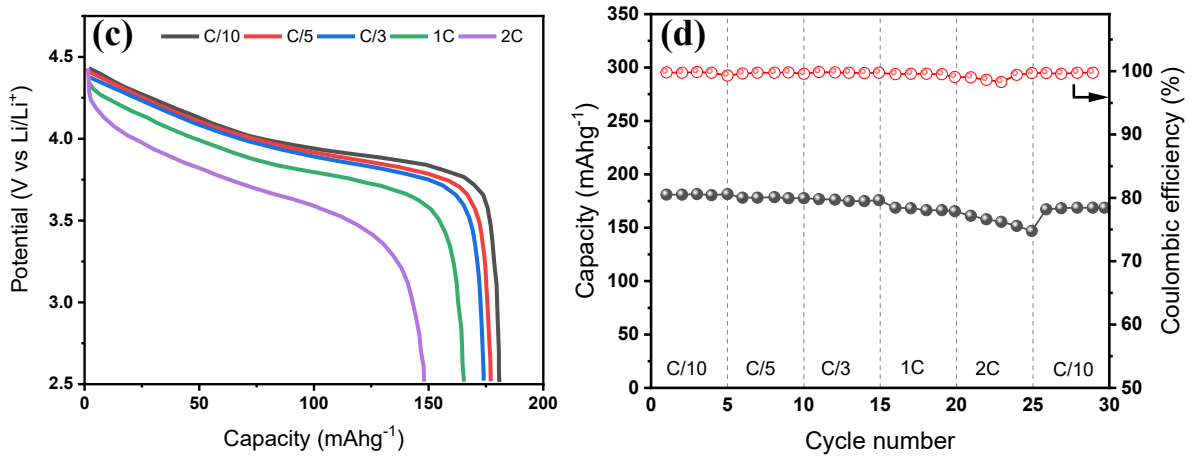

Figure 7.9. Electrochemical performance of NMC622 in half-cell configuration; (a) Voltage profiles at 1st and 50th cycles at C/5 current, (b) Cycling stability and Coulombic efficiency at C/5 current, (c) Voltage profiles at various rates from C/10 to 2C, and (d) Rate capability and capacity recovery.

7.5.2. BH20-Si50 // NMC622 full-cell performance

The practical applicability of the BH20-Si50 composite anode was evaluated in full cells paired with the NMC622 cathode. Representative charge-discharge profiles for the 1st and 100th cycles at C/5 are shown in Fig. 7.10a. The cell exhibits a predominantly sloping voltage response with a distinct discharge plateau near 3.6 V, characteristic of layered oxide cathodes operating against a mixed hard-carbon/alloying anode. A gradual increase in polarisation is observed between the 1st and 100th cycles, indicating modest resistance growth and progressive interfacial evolution on one or both electrodes, but without significant distortion of the overall profile.

The cycling performance at C/5 is summarised in Fig. 7.10b. Based on the cathode mass, the full cell delivers an initial discharge capacity of 165 mAh g^{-1} with a high initial Coulombic efficiency of 98.3 %. After 100 cycles, the discharge capacity remains at 147 mAh g^{-1}, corresponding to a capacity retention of 89 %, while the Coulombic efficiency stabilises at approximately 99.5 %. These data demonstrate efficient utilisation of both electrodes, limited ongoing side reactions and effective SEI passivation over prolonged cycling, in line with the stable behaviour of the individual NMC622 and BH20-Si50 half-cells.

Fig. 7.10c and 7.10d present the rate performance of the BH20-Si50 // NMC622 full cell. The voltage profiles remain well defined as the current is increased from C/10 to 2C, although increased polarisation and shortened plateaus are evident at higher rates. The cell retains close to 160 mAh g^{-1} up to 1C, corresponding to a rate capability of about 90 % relative to C/10, and shows good capacity recovery when the current is returned to C/10, indicating that no significant irreversible structural damage occurs during high-rate cycling. At 2C, the capacity decreases to 113 mAh g^{-1} (approximately 63 % of the C/10 value), reflecting increasing kinetic limitations and interfacial polarisation across the electrodes and electrolyte under more demanding conditions.

Based on the combined mass of active materials and electrolyte, the gravimetric energy density of the full cell is estimated to be 385, 373, 361, 344 and 245 Wh kg^{-1} at C/10, C/5, C/3, 1C and 2C, respectively. These values compare favourably with typical graphite//NMC systems and can be attributed to the enhanced anode-side capacity provided by the Si incorporated within the BH-derived carbon matrix. The BH host affords mechanical buffering and maintains electrical connectivity around the Si domains, mitigating particle disintegration and preserving reversible capacity during extended cycling. Overall, the full-cell data confirm that BH20-Si50 is electrochemically compatible with high-voltage NMC622 cathodes and demonstrate its feasibility as a high-energy-density anode in practical Li-ion full-cell architectures.

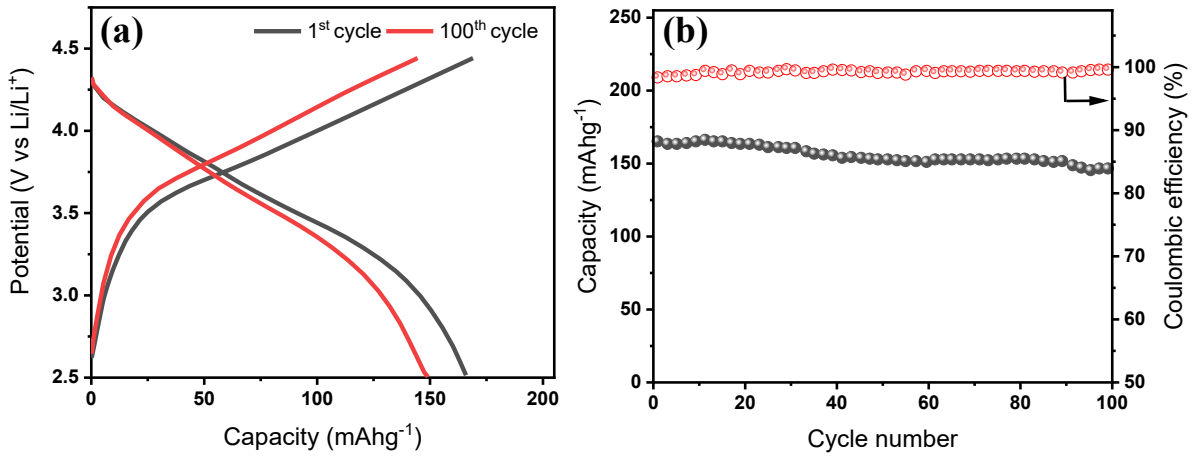

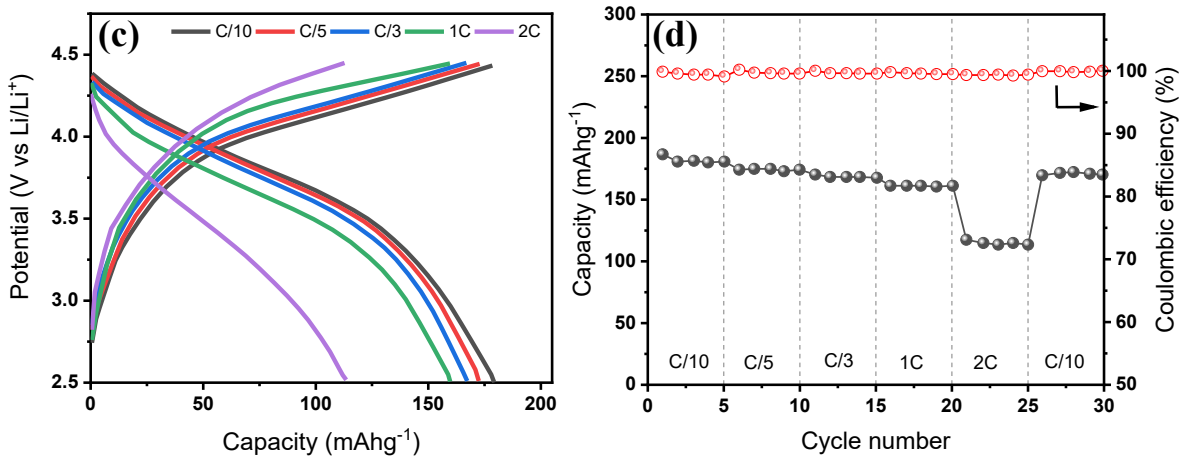

Figure 7.10. Electrochemical performance of the BH20-Si50 // NMC622 full cell. (a) Charge-discharge voltage profiles at the 1st and 100th cycles, (b) cycling stability and Coulombic efficiency over 100 cycles at C/5, (c) Voltage profiles at varying current densities from C/10 to 2C, and (d) Rate capability and capacity recovery.

7.6. Design window for Si incorporation in BH-derived anodes

The results above show that introducing exogenous Si into the BH-T1150-BM020 host produces a family of Si/SiO_2/C hybrids that span a wide range of capacities, efficiencies and stabilities. Increasing Si content systematically boosts gravimetric capacity, but also modifies ICE, rate performance and long-term retention through changes in SEI formation, alloying behaviour and mechanical stress. This section integrates the half-cell, full-cell and post-mortem data to outline a practical design window for Si loading in BH-derived anodes and to position the BH/Si hybrids relative to both the pure BH benchmark and a standard graphite anode.

7.6.1. Trade-off between Si content, ICE and reversible capacity

The half-cell data in Sections 7.4.1 to 7.4.4 reveal a clear capacity-efficiency trade-off as the Si fraction in the BH matrix is increased. At one extreme, pure BH (BH-T1150-BM020) behaves as a typical hard-carbon-type anode, with a moderate initial capacity (~380 mAh g^{-1} at C/5) and relatively low ICE (~60 %), limited mainly by SEI formation and the partial irreversibility of reactions involving the embedded SiO_2 domains. The graphite anode, by

contrast, delivers a slightly lower capacity (~350 mAh g^{-1}) but a much higher ICE (~89 %), due to its well-defined intercalation mechanism and the formation of a thin, stable SEI.

Incorporating Si into the BH host substantially increases reversible capacity, but the initial efficiency reflects a balance between additional alloying capacity and extra irreversible processes. The Si-rich hybrid BH20-Si50 achieves the highest reversible capacity in the series (~1180 mAh g^{-1} after 50 cycles at C/5), supported by strong alloying peaks and pronounced plateaus in both the voltage and dQ/dV profiles. However, its ICE is reduced to around 80 %, reflecting larger irreversible Li loss during the first cycle, associated with extensive SEI growth on the enlarged surface area and the formation of Li_2O/Li-silicate phases at partially oxidised Si sites.

The more balanced hybrids, BH35-Si35 and BH50-Si20, occupy intermediate positions. BH35-Si35 combines a high reversible capacity (~880 mAh g^{-1} at C/5) with an ICE of ~87 %, approaching that of graphite while more than doubling its capacity. BH50-Si20 offers a smaller capacity gain (~670 mAh g^{-1}) but retains particularly strong capacity retention over 500 cycles, reflecting a more conservative Si loading and a BH-dominant microstructure. In all cases, the BH matrix reduces the severity of the ICE penalty relative to pure Si (ICE ~72 %), by distributing Si within a porous carbon network, lowering local current density and stabilising SEI formation.

The long-term cycling data highlight how this initial trade-off propagates over time. Capacity retention over 500 cycles decreases systematically from BH50-Si20 to BH35-Si35 to BH20-Si50, mirroring the increasing Si fraction and associated mechanical strain. BH50-Si20 approaches the retention of pure BH, BH35-Si35 sustains ~70 to 75 % of its initial capacity, and BH20-Si50 remains above ~65 %, still far superior to the graphite-supported Gr20-Si50 and pure Si electrodes, which lose most of their capacity. These trends define a practical design envelope: Si contents around 20 to 35 wt% in the composite (BH50-Si20 and BH35-Si35) yield a favourable compromise between elevated capacity, acceptable ICE and robust long-term stability, whereas higher Si fractions move the system towards maximum capacity at the expense of cycle life.

7.6.2. Balancing performance

Rate-performance measurements in Section 7.4.3, combined with the impedance and diffusion analysis framework established for BH-T1150-BM020 in Chapter 5, provide guidance on how Si loading affects kinetic accessibility. Pure graphite is known to operate via a diffusion-limited intercalation mechanism, which is reflected in its modest rate capability and small but noticeable capacity loss at high C-rates. The optimised BH-T1150-BM020 anode, by contrast, benefits from a more open, disordered structure; EIS in Chapter 5 showed low charge-transfer resistance and the highest apparent Li^+ diffusion coefficient among the BH series, which supports its superior rate retention.

The BH/Si hybrids inherit the favourable transport characteristics of the BH host while introducing additional alloying kinetics from the Si component. At moderate Si loadings (BH50-Si20 and BH35-Si35), the rate capability remains excellent: both electrodes retain a large fraction of their C/10 capacity at 1C and show nearly full capacity recovery when returned to C/10. The smooth voltage profiles and relatively stable dQ/dV peaks over cycling indicate that the BH framework provides continuous ion and electron pathways and prevents severe contact loss around Si particles. In this Si range, any increase in interfacial resistance or diffusion path length introduced by alloying is effectively offset by the high surface area and mesoporous network of the BH matrix, which promotes rapid Li^+ access.

For BH20-Si50, the higher Si fraction further raises capacity and, remarkably, this electrode still maintains ~950 mAh g^{-1} at 2C, indicating that the composite remains kinetically accessible even under aggressive rates. Nevertheless, the larger polarisation observed in its voltage profiles, together with slight peak smearing in dQ/dV by the 50th cycle, suggests growing contributions from charge-transfer and diffusion limitations as cycling progresses. In design terms, this behaviour marks the upper end of the practical Si window for applications where high-rate operation is important. Above this level, one would expect the combined effects of thicker SEI, increased alloying overpotential and longer diffusion pathways through the evolving Si/SEI microstructure to erode rate capability and accelerate capacity fade.

A useful contrast is provided by the Gr20-Si50 composite. Despite having the same Si content as BH20-Si50, it exhibits noticeably poorer rate tolerance and much faster capacity decay. The voltage, dQ/dV and SEM analyses indicate that the layered graphite scaffold is less able to accommodate Si expansion, leading to crack formation, loss of electrical percolation and progressive impedance growth. In kinetic terms, this means that the nominally high-capacity

Si fraction becomes increasingly inaccessible at high current densities. The BH/Si hybrids, in particular BH35-Si35, therefore occupy a region of composition space where alloying capacity is significantly enhanced while the underlying transport properties remain close to those of the optimised BH host.

7.6.3. Positioning BH/Si hybrids relative to BH-T1150-BM020 and graphite

Chapters 5 and 6 established BH-T1150-BM020 and a commercial graphite anode as two complementary baselines: graphite providing high ICE, low hysteresis and industrially proven stability, and BH-T1150-BM020 offering higher capacity and excellent rate performance derived from a tunable biomass precursor. The BH/Si hybrids developed in this chapter can now be positioned between and beyond these baselines in a combined capacity-stability-complexity space.

Relative to pure BH, adding Si increases processing complexity only modestly, as it relies on mixing pre-optimised BH-T1150-BM020 with commercial Si rather than introducing new synthetic steps. The payoff is substantial: even the BH50-Si20 composition provides a significant capacity uplift while preserving BH-like cycling stability over hundreds of cycles. BH35-Si35 further extends this advantage, delivering more than double the capacity of graphite and BH at comparable C-rates, with ICE and long-term retention that remain compatible with practical device requirements. From the perspective of Chapter 5, where BH-T1150-BM020 emerged as the optimum within the BH-only parameter space, BH35-Si35 can be seen as the next “tier” of performance when Si is incorporated while still maintaining the favourable characteristics of the BH host.

BH20-Si50 occupies a more aggressive design point. It offers the highest gravimetric capacity and the strongest rate capability among the BH-Si hybrids, and supports full-cell energy densities up to ~385 Wh kg^{-1} at C/10 when paired with NMC622. However, it also shows the largest capacity fade within the BH-Si family and more pronounced polarisation growth, reflecting the increasing difficulty of mechanically and electrochemically stabilising a Si-rich network. In applications where peak energy density is prioritised over extreme cycle life, BH20-Si50 represents a viable high-capacity option; where extended durability is critical, BH35-Si35 or even BH50-Si20 may be more appropriate choices.

Compared with graphite, all BH/Si hybrids deliver substantially higher capacities and full-cell energy densities, while maintaining acceptable ICE and Coulombic efficiency after formation. Graphite still provides the narrowest voltage hysteresis and the most straightforward intercalation mechanism, but its inability to buffer large Si volume changes is evident from the rapid degradation of Gr20-Si50. The BH-derived host, by contrast, combines structural compliance, mesoporosity and a mixed storage mechanism that is inherently more compatible with alloying-type additives.

In summary, the combined structural, electrochemical and full-cell results identify a practical design window for Si incorporation into BH-derived anodes. Si fractions of roughly 20 to 35 wt% in the BH/Si composite maximise the benefits of alloying while keeping ICE, rate performance and long-term stability within acceptable bounds. Within this window, BH35-Si35 stands out as a particularly well-balanced formulation, providing a strong basis for further optimisation and scaling of BH-derived Si/SiO_2/C hybrids as next-generation anodes for high-energy Li-ion batteries.

7.7. Conclusion

This chapter explored the incorporation of commercial silicon into an optimised barley-husk-derived silica-carbon host to create high-capacity BH/Si hybrid anodes. Using a common electrode formulation and test protocol, the hybrids were benchmarked against both pure BH-T1150-BM020 and commercial graphite, combining structural characterisation with half-cell and full-cell electrochemical evaluation.

Structural analysis showed that the BH host provides a disordered hard-carbon framework with embedded silica and a hierarchical pore network, whereas the Si additive consists of crystalline particles coated by a thin native SiO_2 layer. Within the hybrids, these components form a heterogeneous Si/SiO_2/C architecture in which Si agglomerates are distributed throughout the BH matrix. The presence of silica-rich interfaces and oxygenated carbon at the BH-Si boundary is expected to promote stronger interfacial adhesion and to contribute inorganic species to the SEI during initial lithiation, partially mitigating the mechanical and chemical instability typically observed in Si-only electrodes.

Electrochemical measurements revealed a clear composition-dependent trade-off between reversible capacity, ICE and long-term stability. Relative to pure BH and graphite, all BH/Si hybrids delivered substantially higher capacities, with BH35-Si35 and BH20-Si50 in particular surpassing 800 to 1100 mAh g^{-1} at C/5 while maintaining acceptable ICE values. Increasing Si content led to progressively larger irreversible losses on the first cycle and to enhanced capacity fade on extended cycling, but the BH host significantly moderated these penalties compared with a graphite-supported Si composite and with pure Si. Rate capability tests further showed that moderate Si loadings could be accommodated without severe kinetic penalties, with BH35-Si35 retaining strong capacity even at 1 to 2C and exhibiting nearly full recovery on returning to C/10.

Full-cell tests pairing the Si-rich BH20-Si50 anode with an NMC622 cathode demonstrated that the benefits observed in half-cells translate into substantial energy-density gains at device level. Specific energies approaching ~385 Wh kg^{-1} at C/10 were achieved under realistic negative-to-positive capacity balancing, significantly exceeding those attainable with graphite-based configurations under comparable conditions. Although the high Si fraction in BH20-Si50 incurs faster capacity fade, the comparison highlights the potential of BH-derived Si/SiO_2/C hybrids to deliver high energy densities within industrially relevant electrode architectures.

Taken together, the results identify a practical Si loading window of approximately 20 to 35 wt% in BH-based composites, within which alloying contributions can be exploited while preserving BH-like rate performance, ICE and cycling stability. Within this window, BH35-Si35 emerges as a particularly well-balanced formulation, offering more than double the capacity of graphite with robust long-term retention and only modest increases in processing complexity. These findings provide a clear pathway for the further optimisation of biomass-derived Si/SiO_2/C anodes, including future work on surface engineering, prelithiation strategies and electrode-level design to unlock the full potential of silicon while retaining the sustainability advantages of biomass carbon.

7.8. References

[1] A. Fereydooni, C. Yue, Y. Chao. *Small* 2024,20,2307275.

[2] A. V. Baskar, G. Singh, A.M. Ruban, J.M. Davidraj, R. Bahadur, P. Sooriyakumar, P. Kumar, A. Karakoti, J. Yi, A. Vinu. *Adv Funct Mater* 2023,33,2208349.

[3] Z. Gao, Y. Zhang, N. Song, X. Li. *Mater Res Lett* 2017,5,69–88.

[4] S.J. An, J. Li, C. Daniel, D. Mohanty, S. Nagpure, D.L. Wood. *Carbon N Y* 2016,105,52–76.

[5] J. Collins, G. Gourdin, M. Foster, D. Qu. *Carbon N Y* 2015,92,193–244.

[6] Z. Yang, Y. Du, G. Hou, Y. Ouyang, F. Ding, F. Yuan. *Electrochim Acta* 2020,329,135141.

[7] W. Wu, M. Wang, J. Wang, C. Wang, Y. Deng. *ACS Appl Energy Mater* 2020,3,3884–3892.

[8] C. Yue, A. Fereydooni, P. Nakhanivej, M.B. Murria, M. Liu, Y. Zeng, Z. Wei, Q. Fu, X. Zhao, M.J. Loveridge, Y. Chao. *RSC Sustainability* 2025,3,2915.

[9] J. Tu, Y. Yuan, P. Zhan, H. Jiao, X. Wang, H. Zhu, S. Jiao. *Journal of Physical Chemistry C* 2014,118,7357–7362.

[10] J. Rohrer, K. Albe. *Journal of Physical Chemistry C* 2013,117,18796–18803.

[11] F. Dou, L. Shi, G. Chen, D. Zhang. *Electrochemical Energy Reviews* 2019,2,149–198.

[12] P. Molaiyan, G.S. Dos Reis, D. Karuppiah, C.M. Subramaniyam, F. García-Alvarado, U. Lassi. *Batteries* 2023,9,116.

8. Optimising barley-husk-derived hard carbon for Sodium-ion battery anodes

8.1. Introduction

8.1.1. Motivation and Na-ion context

The rapid growth of renewable electricity generation and decentralised energy systems has intensified interest in electrochemical storage technologies that are not limited by the cost and geographical concentration of lithium. Sodium-ion batteries (NIBs) have emerged as a promising complementary technology for large-scale and cost-sensitive applications, owing to the natural abundance, low cost and widespread distribution of sodium-containing resources. At the cell level, Na-ion systems can offer acceptable energy densities for stationary storage and selected mobility sectors, provided that suitable electrode materials are identified which can accommodate the larger Na-ion while maintaining long-term cyclability and competitive efficiency.[1]

On the anode side, graphite is unsuitable for most Na-ion systems under conventional electrolytes, so attention has shifted towards disordered carbons.[2–4] As discussed in Section 2.7, hard carbon with its turbostratic stacking, enlarged interlayer spacing and hierarchical porosity is now regarded as the state-of-the-art anode for NIBs, combining adsorption, interlayer insertion and pore-filling processes to deliver competitive reversible capacities at low operating potentials.

Alongside performance, the sustainability and cost of hard-carbon production are increasingly important (Section 2.6). Biomass-derived carbons offer a route to valorise agricultural residues into functional electrodes.[5–7] Within this context, barley husk is particularly attractive owing to its abundance, low economic value and intrinsic content of both carbon and silica. Chapters 4 and 5 have shown that controlled carbonisation and ball milling of barley husk yield hard carbons with tunable interlayer spacing, defect density and porosity, which already deliver competitive performance in Li-ion half-cells.

These Li-based studies provide a well-defined structural and electrochemical baseline, but the suitability of the same barley-husk-derived carbons for Na-ion storage cannot be assumed a priori. The larger ionic radius and different solvation behaviour of Na^+, together with its distinct thermodynamics of insertion into disordered carbon, alter the relative importance of interlayer

spacing, pore architecture and surface chemistry. For example, the interlayer distance required to host Na^+ is generally larger than that needed for Li^+, and the balance between defect-mediated adsorption and low-potential pore filling may shift under Na operation. In addition, NIBs are often more sensitive to irreversible consumption of Na^+ during solid-electrolyte interphase formation, which places different constraints on surface area and pore accessibility than in the Li-ion case.

Against this background, the present chapter investigates the Na-ion storage behaviour of barley-husk-derived hard carbon as a function of carbonisation temperature at a fixed, pre-optimised milling duration. By focusing on a temperature series that is structurally characterised and electrochemically benchmarked in Li-ion cells, this chapter aims to clarify how processing-induced changes in turbostratic ordering, porosity and surface area influence capacity, initial Coulombic efficiency, cycling stability, rate performance and Na^+ transport. This Na-ion study not only assesses the viability of barley husk as a sustainable precursor for hard carbon anodes in NIBs, but also provides insight into how a single biomass-derived carbon platform can be tuned to serve both Li- and Na-based chemistries.

8.1.2. Textural characterisation of the Na batch

To establish the textural state of the barley-husk-derived hard carbons used in Na-ion half-cells, N_2 adsorption-desorption measurements at 77 K were carried out on the BH-T####-BM020 series, where the milling duration was fixed at 20 min and the carbonisation temperature was varied between 550 and 1150 °C. The measurements were performed following the same degassing and analysis protocol described in Chapter 4 (Section 4.3.1), with BET specific surface areas extracted using the Rouquerol criteria and mesopore-size distributions obtained from the desorption branch via the BJH formalism. The resulting isotherms, pore-size distributions and BET surface areas are summarised in Fig. 8.1.

All samples display mesoporous-carbon isotherms with gradual low-pressure uptake and open hysteresis at higher P/P_0. The overall adsorbed volume and hysteresis amplitude increase strongly from 550 to 750 °C and then decrease at higher temperatures, mirroring the evolution of BET surface area from 14.1 to 108.2 $m^2\ g^{-1}$ and back to 40.0 to 36.3 $m^2\ g^{-1}$ (Fig. 8.1c).

The BJH pore-size distributions derived from the desorption branches reveal that all samples contain a broad mesopore population extending over a few to several nanometres, consistent with the formation of slit-type pores and inter-aggregate voids during pyrolysis and milling. The intensity of this mesopore band is highest for BH-T750-BM020, in line with its large BET surface area, while BH-T950-BM020 and BH-T1150-BM020 display weaker, but still appreciable, mesopore signals. The BH-T550-BM020 sample shows only a shallow distribution, indicating that incomplete devolatilisation and a more polymeric carbon matrix at this temperature limit the development of accessible mesoporosity. Taken together with the Li-based milling study at 1150 °C in Chapter 4, which showed that BH-T1150-BM020 has a BET surface area of 37.93 $m^2 g^{-1}$ and a stable mesopore envelope centred in the 2 to 5 nm range, the present Na batch data confirm that the intermediate-temperature sample (750 °C) is texturally the most open, whereas the highest-temperature carbons are more compact despite their higher degree of structural ordering.

These trends can be rationalised in the context of the structural evolution described earlier. At 550 °C, the carbon matrix retains a significant fraction of non-aromatic and heteroatom-containing moieties, as indicated by the Raman and XRD analyses in Chapter 4, which restricts pore opening and leaves a low external surface area. Increasing the temperature to 750 °C drives off volatiles and promotes aromatisation without yet fully collapsing the developing pore network, resulting in a highly porous, high-surface-area hard carbon. Further heating to 950 and 1150 °C tightens the turbostratic stacking, reduces defect density and promotes structural densification, which narrows or closes smaller pores and reduces the accessible surface area, even though the carbon becomes more ordered at the bonding scale.

From the perspective of Na-ion storage, this textural landscape has several implications. The very high surface area of BH-T750-BM020 is expected to enhance electrolyte access and shorten Na^+ diffusion paths, which can be beneficial for rate performance, but it also increases the area available for solid-electrolyte interphase formation and irreversible Na consumption, with a likely penalty in initial Coulombic efficiency. In contrast, the low-surface-area BH-T550-BM020 may suppress SEI growth but offers limited mesopore volume and poorer connectivity to internal storage sites. The intermediate surface areas and mesopore contents of BH-T950-BM020 and BH-T1150-BM020 represent a compromise between kinetic accessibility and parasitic surface reactions, and are expected to support more balanced Na storage behaviour. The following sections

examine how these textural differences, superimposed on the temperature-dependent changes in interlayer spacing and aromatic ordering established in Chapters 4 and 5, translate into the observed Na-ion electrochemical response.

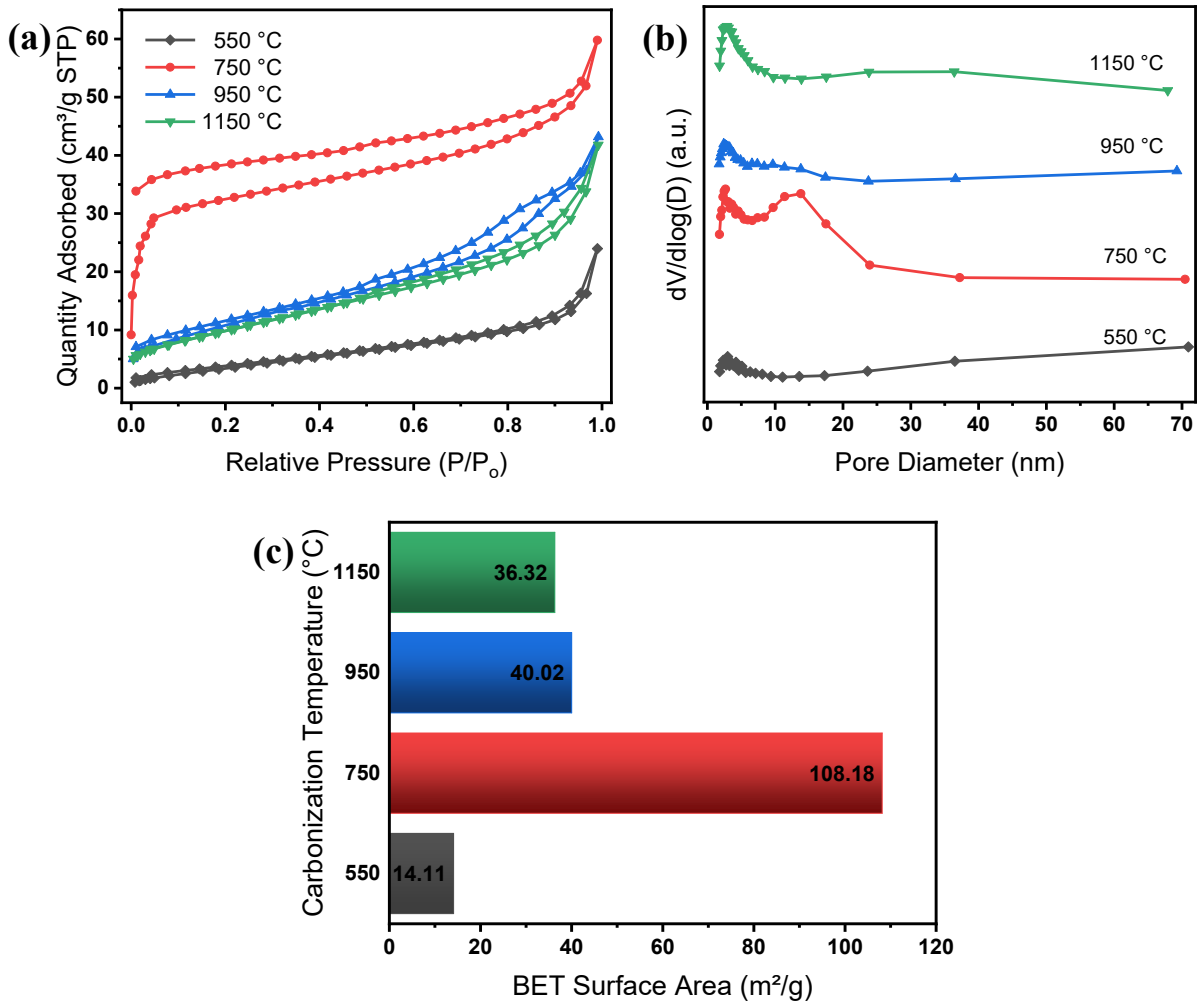

Figure 8.1. N_2 adsorption-desorption isotherms at 77 K for BH-T####-BM020 carbons carbonised at 550, 750, 950 and 1150 °C, showing (a) adsorption-desorption behaviour, (b) BJH pore-size distributions and (c) BET surface area as a function of carbonisation temperature.

8.2. Electrochemical performance in Na half-cells

8.2.1. Scope, sample set and testing protocol

All Na-ion measurements in this chapter were performed on CR2016 half-cells prepared under a common electrode architecture, electrolyte and testing schedule, so that differences in performance can be attributed directly to the carbonisation temperature of the barley-husk-derived hard carbon. The active materials are the four BH powders carbonised at 550, 750, 950 and 1150 °C and subsequently milled for 20 min, denoted BH-T0550-BM020, BH-T0750-BM020, BH-T0950-BM020 and BH-T1150-BM020, respectively. These labels are used consistently throughout Section 8.2 and link the Na half-cell dataset to the structural and textural descriptors established in Chapters 4 and 5 and in Fig. 8.1.

Electrode preparation for the Na-ion study followed the slurry formulation and coating protocol described in Section 5.2.1. In brief, the working anodes were fabricated from aqueous slurries containing 70 wt% BH-T####-BM020 active material, 20 wt% carbon black (C65) and 10 wt% polyacrylic acid (PAA) binder, cast onto aluminium foil current collectors and dried under vacuum. The electrodes were then punched into 14 mm disks, yielding an active-material loading of approximately 1.0 mg cm^{-2}, consistent with the Li-ion study in terms of electrode composition and loading, in order to minimise architectural contributions to performance trends. The anode compositions and sample labels used throughout this chapter are summarised in Fig. 8.2.

Coin cells were assembled in an argon-filled glovebox (O_2, H_2O < 0.5 ppm) using the BH-based electrodes as working anodes, metallic sodium as the counter electrode, and a microporous polyolefin separator (Celgard 2500). The electrolyte was 1 M $NaPF_6$ in diglyme (100 vol% diglyme), an ether-based sodium salt solution chosen for its favourable wetting of porous carbons and its ability to form a stable SEI on hard carbon surfaces. All electrochemical tests were conducted at room temperature.

Unless stated otherwise, galvanostatic cycling and voltage profiling were carried out in the potential window 0.01 to 2.5 V vs Na^+/Na, using a C-rate protocol analogous to that employed for Li-ion cells in Chapter 5. Formation comprised three cycles at C/20 to stabilise the SEI and to establish the initial Coulombic efficiency. Cycling stability was then assessed at C/5 for 200 cycles, with Coulombic efficiency recorded each cycle. Rate performance was evaluated using a stepped

sequence of C/10 → C/5 → C/3 → 1C → C/10, with five cycles at each rate; capacities at each step, together with the final C/10 recovery, were used to quantify rate capability and reversibility. The C-rate is defined relative to a theoretical capacity of 300 mAh g^{-1} for hard carbon and 170 mAh g^{-1} for the silica component, reflecting their expected Na-storage limits; given the ~14 wt% silica content determined by TGA in Chapter 4, this corresponds to an overall composite theoretical capacity of 281.8 mAh g^{-1} for these anodes. The applied current densities are reported explicitly in mA g^{-1} (per total active mass) where relevant.

Cyclic voltammetry was performed between 0.01 and 2.5 V vs Na^+/Na at a scan rate of 0.2 mV s^{-1}, to facilitate direct comparison of redox features between Li^+ and Na^+ operation. Electrochemical impedance spectroscopy (EIS) measurements were acquired after the 1st and 50th galvanostatic cycles using a 5 to 10 mV perturbation over the 100 to 0.01 Hz frequency range, following the protocol in Chapter 5. Spectra were fitted using the same equivalent circuit as in the Li-ion study to extract the solution resistance (R_s), charge-transfer resistance (R_{ct}) and Warburg coefficient (σ); the apparent Na^+ diffusion coefficient (D_{Na^+}) was then calculated from the low-frequency Z' vs $\omega^{-0.5}$ relation using the same expression as Eq. (5.2) in Chapter 5, with Li^+ replaced by Na^+. The extracted parameters for BH-T0550-BM020, BH-T0750-BM020, BH-T0950-BM020 and BH-T1150-BM020 are compiled in Table 8.1 and form the basis for the discussion in Section 8.2.6.

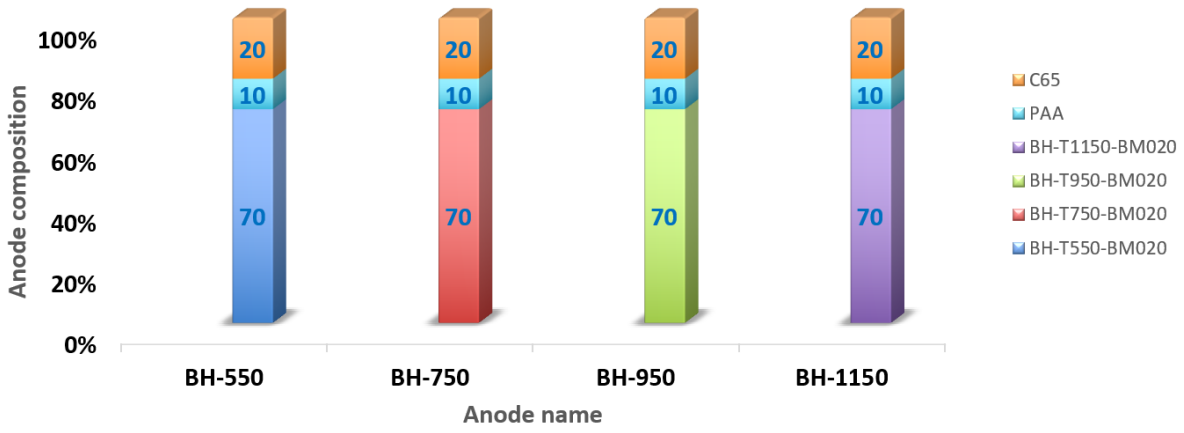

Figure 8.2. Electrode compositions and labeling of anodes investigated in this chapter.

8.2.2. Cyclic voltammetry as a function of carbonisation temperature

The Na-ion storage behaviour of the barley-husk-derived hard carbons was first probed by cyclic voltammetry (CV) between 0.01 and 2.5 V vs Na^+/Na at 0.2 mV s^{-1}. Fig. 8.3 shows the first three CV cycles for BH-T0550-BM020, BH-T0750-BM020, BH-T0950-BM020 and BH-T1150-BM020. In all cases the initial scan exhibits a large cathodic feature at low potential, followed by a smaller anodic counterpart on the return sweep, while subsequent cycles display reduced irreversible currents and progressively overlapping profiles, signalling the establishment of a more stable Na-storage response after the formation stage.

For all four temperatures, the first cathodic scan from open-circuit potential down to 0.01 V is dominated by a sharp current spike just above 0.01 V, reaching peak currents of approximately −0.10 mA for BH-T0550-BM020, −0.20 to −0.22 mA for BH-T0750-BM020 and BH-T0950-BM020, and around −0.10 mA for BH-T1150-BM020. This intense low-voltage reduction in the first cycle is attributed mainly to the reductive decomposition of the $NaPF_6$-diglyme electrolyte and the formation of a solid-electrolyte interphase on the hard carbon surface, together with the filling of the most accessible nanopores. The corresponding anodic scan shows a relatively sharp oxidation feature slightly above 0.01 V, with a magnitude that is substantially smaller than the first-cycle cathodic peak and which stabilises in the second and third cycles. The incomplete reversibility of this low-potential peak between the first cathodic and anodic sweeps reflects the largely irreversible nature of SEI formation and the trapping of Na^+ in deep or poorly connected sites during the initial sodiation.

Beyond the immediate vicinity of 0.01 V, each sample exhibits broader cathodic and anodic currents extending roughly from 0.1 to about 1.0 V, superimposed on a quasi-rectangular background. These features are commonly ascribed to Na^+ adsorption at defect and edge sites, redox activity associated with residual functional groups, and reversible Na storage in more weakly confined domains within the disordered carbon matrix. The gradual decrease of these currents from the first to the third cycle suggests that part of the high-potential response is also related to the consumption of electrolyte and the stabilisation of surface chemistry, while the remaining current in cycles 2 and 3 is associated with reversible Na pore/interlayer filling.

Clear differences emerge when the CV responses are compared across the carbonisation temperatures. The BH-T0550-BM020 electrode, which has the lowest BET surface area and the

least developed aromatic and turbostratic order, shows relatively small peak currents and a noticeable evolution of the curve shape between the first and third cycles. The broad cathodic response above 0.1 V remains comparatively featureless, indicative of a predominance of disordered, defect-rich storage sites and a lack of well-defined low-potential insertion domains. In contrast, BH-T0750-BM020, which combines a highly porous texture with intermediate structural ordering, exhibits the largest first-cycle cathodic peak and the highest overall current density across the potential window. This behaviour is consistent with its high surface area (108.18 $m^2 g^{-1}$), which provides abundant sites for SEI formation and Na adsorption, enhancing both irreversible and reversible charge transfer. The second and third cycles for BH-T0750-BM020 nearly overlap, indicating rapid stabilisation once the initial surface reactions are complete.

For BH-T0950-BM020 and BH-T1150-BM020, the CV profiles display intermediate peak magnitudes and more reproducible shapes from cycle to cycle. The reduction of high-potential current relative to BH-T0750-BM020 reflects the lower surface area and mesopore content of these higher-temperature carbons, which restricts the number of exposed defect sites and external surface available for Na^+ adsorption and SEI growth. At the same time, the sharper low-potential redox response and improved overlap of the second and third cycles suggest that Na storage becomes increasingly dominated by more defined interlayer and nanopore domains within the harder, more aromatised carbon matrix. This trend echoes the Li-ion CV behaviour reported in Chapter 5 in Section 5.3 for the same BH-T####-BM020 series, where higher carbonisation temperatures also promoted more stable and reproducible low-voltage features associated with pore/interlayer filling, although the absolute potential positions and relative contributions differ between Li^+ and Na^+ because of their distinct insertion thermodynamics.

Overall, the CV data indicate that increasing carbonisation temperature from 550 to 1150 °C shifts the Na-storage mechanism from predominantly defect- and surface-controlled uptake, with significant irreversible charge, towards a regime where reversible low-potential processes in more ordered hard-carbon domains play a larger role. The particularly large first-cycle cathodic current of BH-T0750-BM020 highlights the trade-off introduced by its very high surface area: enhanced kinetics and strong redox response are accompanied by extensive electrolyte decomposition and Na loss. These mechanistic tendencies foreshadow the trends in initial Coulombic efficiency, cycling stability and rate performance discussed in Sections 8.2.3 and 8.2.4.

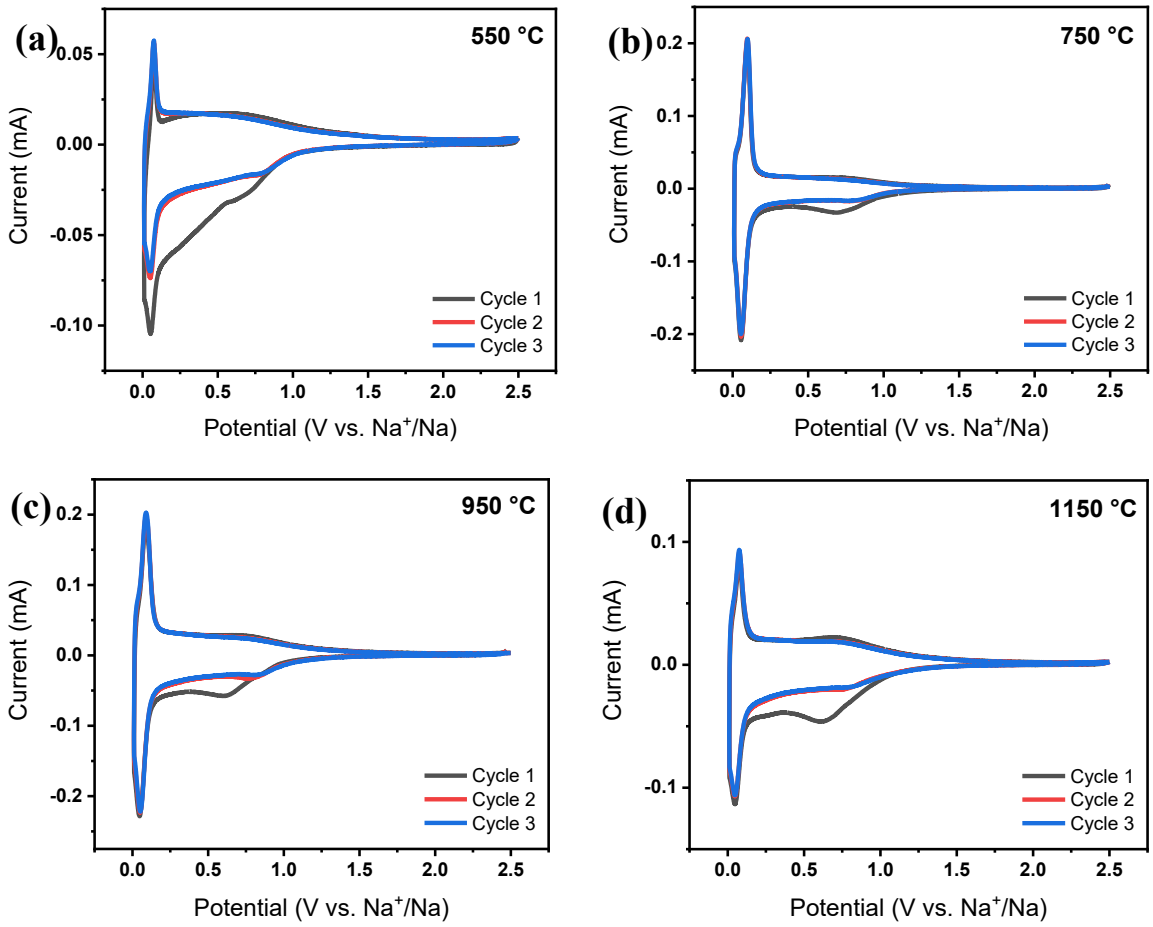

Figure 8.3. Cyclic voltammograms of BH-T####-BM020 anodes in Na half-cells over the first three cycles at 0.2 mV s^{-1} between 0.01 and 2.5 V vs Na^+/Na, comparing the effect of carbonisation temperature (550, 750, 950 and 1150 °C).

8.2.3. Galvanostatic voltage profiles

The galvanostatic charge-discharge profiles of BH-T550-BM020, BH-T750-BM020, BH-T950-BM020 and BH-T1150-BM020 over the first five cycles at the formation rate shown in Fig. 8.4 and exhibit the typical two-stage behaviour of hard carbons in Na-ion systems, combining a sloping region at intermediate potentials with a lower-voltage segment closer to 0 V vs Na^+/Na. In all cases, the first sodiation curve shows a pronounced irreversible capacity extending from the open-circuit potential down to approximately 0.1 to 0.2 V, consistent with electrolyte reduction, SEI formation and Na uptake at high-energy defect and surface sites, in agreement with the

cathodic features identified in the CVs in Fig. 8.3. Subsequent desodiation traces recover only a fraction of this charge on the first cycle, but the degree of overlap between sodiation and desodiation improves markedly from cycle 2 to 5 as the SEI stabilises and the electrochemically active sites approach steady utilisation.

For BH-T550-BM020, the voltage profile is dominated by a continuous slope from about 1.5 V down to the lower cut-off, with only a very short and poorly developed low-voltage segment. This behaviour indicates that Na storage occurs mainly via adsorption at defects, edges and disordered surface sites rather than through efficient nanopore or interlayer filling. The large voltage hysteresis between charge and discharge in the first cycle, together with the limited growth of a distinct low-potential plateau upon cycling, reflects the highly disordered microstructure at 550 °C, where Chapter 4 showed a broad (002) reflection, large d_{002} and short L_c, combined with relatively low BET surface area (14.1 $m^2\ g^{-1}$). These structural features promote extensive irreversible reactions during SEI formation but do not provide well-defined graphitic domains for reversible Na pore/interlayer filling, which is consistent with the relatively low reversible capacity and modest first-cycle overlap seen in Fig. 8.4.

In contrast, the BH-T750-BM020 anode delivers the highest reversible capacity and displays the clearest separation between the sloping and plateau-like regions. Its first sodiation curve extends to the largest capacity in Fig. 8.4, and already by the second cycle a more pronounced low-voltage segment below ~0.1 V develops, indicative of Na filling in nanopores and enlarged interlayer galleries. The corresponding desodiation traces show relatively small hysteresis and good overlap from cycle 2 onwards, pointing to efficient and largely reversible occupation of these sites. This electrochemical behaviour can be linked directly to the textural properties in Fig. 8.1, where BH-T750-BM020 exhibits the highest BET surface area (108 $m^2\ g^{-1}$) and significant mesopore volume. Together with the large d_{002} and high defect density identified in Chapter 4, this combination provides abundant adsorption sites and accessible pore networks while still maintaining sufficient structural coherence for Na storage in turbostratic domains. The result is a strong contribution from both the sloping and plateau regions, giving a high reversible capacity.

Moving to higher temperatures, BH-T950-BM020 and BH-T1150-BM020 show intermediate behaviour. Their first-cycle profiles retain a noticeable sloping region, but the relative share of the low-voltage segment becomes larger than in BH-T550-BM020 yet less extended than in BH-T750-

BM020. The plateau in these samples is somewhat shorter and slightly more tilted, suggesting that Na pore/interlayer filling is increasingly limited by the shrinking d_{002} and growing crystallite size reported in Chapter 4. The narrower hysteresis between discharge and charge compared with BH-T550-BM020 reflects improved electronic connectivity and reduced defect density at higher carbonisation temperature, but the reduced gallery spacing likely imposes steric constraints on Na pore/interlayer filling, so that the total reversible capacity does not reach that of the 750 °C sample.

These qualitative trends in voltage shape are mirrored in the initial Coulombic efficiencies extracted from the first-cycle charge and discharge capacities. As summarised in Fig. 8.5c, the ICE values are 51.1 % for BH-T550-BM020, 73.5 % for BH-T750-BM020, 65.3 % for BH-T950-BM020 and 68.1 % for BH-T1150-BM020. The non-monotonic dependence on carbonisation temperature contrasts with the monotonic increase observed in Li half-cells, where ICE rose steadily from 48.6 % to 59.2 % as temperature increased from 550 to 1150 °C. In the Na system, the highest ICE at 750 °C indicates that, although this sample possesses the largest surface area and therefore the greatest absolute SEI charge, it also delivers the largest reversible capacity after formation. The net effect is a favourable ratio of reversible to irreversible Na uptake, yielding a higher ICE than in both more disordered (550 °C) and more graphitised (950 to 1150 °C) carbons. For BH-T550-BM020, the combination of highly defective carbon and relatively low surface area translates into extensive trapping of Na in deep defect states and a thick, heterogeneous SEI, giving a low ICE and poor first-cycle overlap. At 950 to 1150 °C, the more ordered stacking and smaller d_{002} reduce the fraction of Na that can be reversibly stored at low potentials, so that even though SEI formation is more controlled, the ICE does not exceed that of the 750 °C sample.

Overall, the Na voltage profiles and associated ICE trends reinforce the processing-structure-performance links established in Chapters 4 and 5. The 750 °C carbon, which combines enlarged interlayer spacing, high porosity and a still highly defective but continuous sp^2 network, emerges as the most effective compromise for Na storage, maximising reversible capacity and first-cycle efficiency. In contrast, very low and very high carbonisation temperatures bias the storage mechanism towards predominantly defect-controlled adsorption (550 °C) or constrained interlayer insertion (950 to 1150 °C), both of which limit reversible Na uptake and degrade the initial utilisation of the active material.

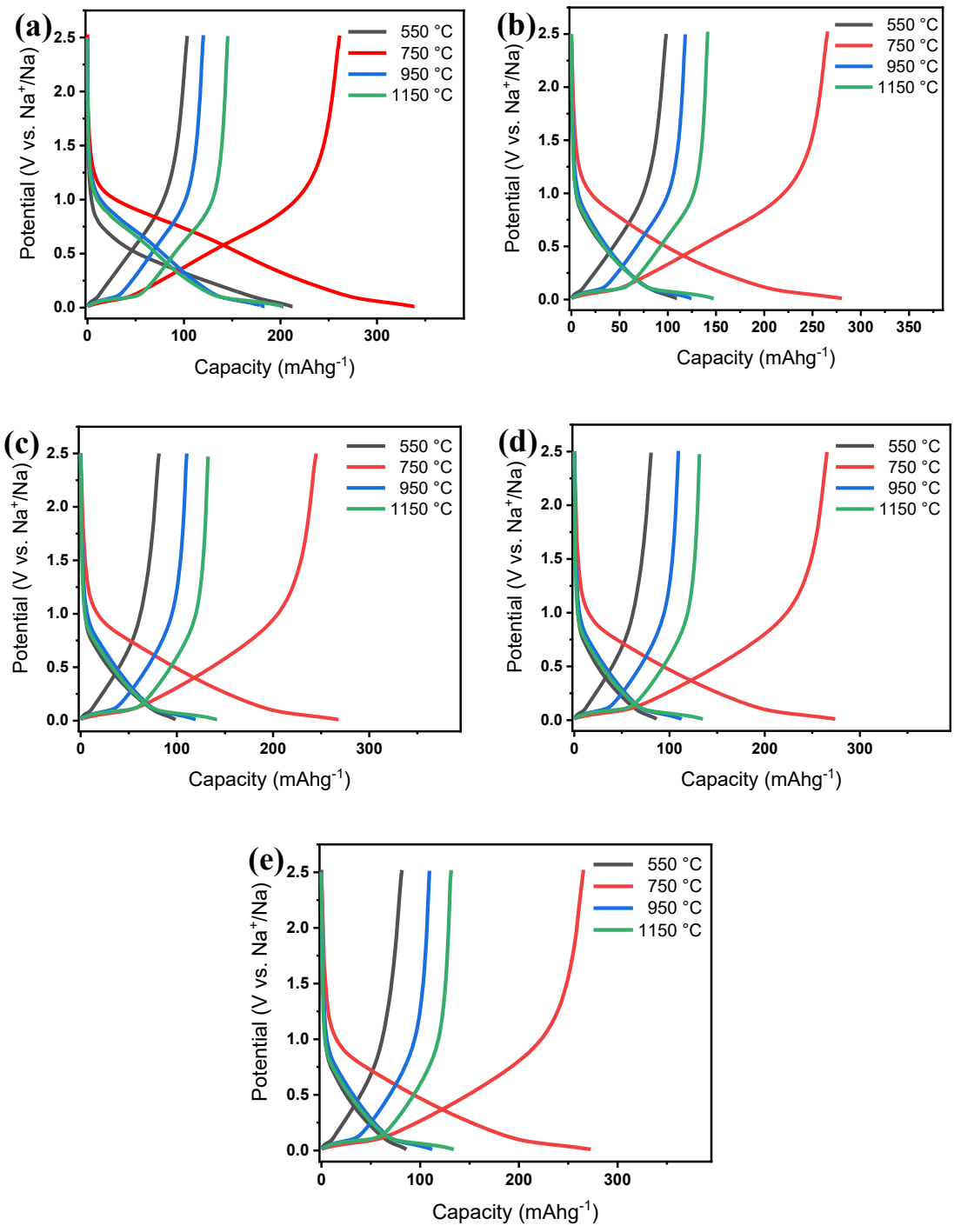

Figure 8.4. Galvanostatic charge-discharge voltage profiles of BH-T550-BM020, BH-T750-BM020, BH-T950-BM020 and BH-T1150-BM020 at their (a) 1st, (b) 2nd, (c) 3rd, (d) 4th, and (e) 5th cycle under a C/5 current.

8.2.4. Cycling stability and rate capability

The long-term cycling behaviour of the BH-T####-BM020 anodes at C/5 and their Coulombic efficiencies are shown in Fig. 8.5a and 8.5b, together with the ICE in Fig. 8.5c and the rate capability over a stepped C-rate sequence in Fig. 8.5d. After the initial formation cycles, all electrodes exhibit comparatively stable capacities over 200 cycles, with clear differences in both absolute capacity and retention that reflect the interplay between carbonisation temperature, texture and Na-storage mechanism.

At the baseline rate, BH-T750-BM020 delivers by far the highest reversible capacity. After the initial drop between cycles 1 and 5, the capacity stabilises at around 260 mAh g^{-1} and remains in the range 250 to 260 mAh g^{-1} up to the 200th cycle, corresponding to a capacity retention of approximately 95 to 100 % relative to the fifth cycle in Fig. 8.5a. In contrast, BH-T550-BM020 exhibits a much lower reversible capacity, settling near 80 to 90 mAh g^{-1} after formation and maintaining this level with only a slight upward drift over extended cycling. The higher-temperature carbons, BH-T950-BM020 and BH-T1150-BM020, show intermediate capacities of roughly 90 to 110 mAh g^{-1} and 130 to 140 mAh g^{-1}, respectively, with a modest gradual increase over the 200 cycles, suggestive of progressive activation of internal storage sites as the electrolyte penetrates deeper pores and the SEI becomes more uniform. Overall, the capacity ranking at C/5 is in line with the voltage-profile analysis in Section 8.2.3.

The evolution of Coulombic efficiency further clarifies the stability of Na storage in these electrodes as shown in Fig. 8.5b. For all four temperatures, the Coulombic efficiency increases sharply from the first to the second cycle and exceeds 95 % by the third cycle. Thereafter, the efficiency approaches or slightly surpasses 99 % and remains close to this level up to 200 cycles, indicating that parasitic reactions are substantially suppressed once the SEI has formed. BH-T750-BM020 reaches high efficiencies particularly rapidly, consistent with its relatively high ICE of 73.5 % and large reversible capacity. BH-T550-BM020, with the lowest ICE of 51.1 %, requires a slightly longer stabilisation period and displays marginally more scatter in the early cycles, reflecting its more defective microstructure and less homogeneous SEI. The higher-temperature samples, BH-T950-BM020 and BH-T1150-BM020, converge to steady-state efficiencies that are comparable to or marginally higher than that of BH-T750-BM020, which is consistent with their

more ordered carbon frameworks and lower surface areas that reduce the extent of continuous electrolyte decomposition.

The ICE summarised in Fig. 8.5c emphasise the non-monotonic dependence of first-cycle reversibility on carbonisation temperature. As noted above, BH-T750-BM020 exhibits the highest ICE (73.5 %), with BH-T1150-BM020 and BH-T950-BM020 following at 68.1 % and 65.3 %, respectively, and BH-T550-BM020 lagging at 51.1 %. This behaviour differs from the Li-ion case, where ICE increased monotonically with temperature, and can be rationalised by considering the combined effects of texture and stacking. The 750 °C carbon combines the largest surface area and mesopore volume with still enlarged d-spacing and high defect density, providing both extensive adsorption sites and accessible nanopores for Na storage. Although the high surface area increases the absolute amount of SEI formed, the associated gain in reversible capacity more than compensates, yielding a high ICE. At 550 °C, the poorly developed porosity and highly disordered bonding environment lead to substantial Na trapping in deep defect states and an inhomogeneous SEI, which severely depress ICE. At 950 to 1150 °C, the more ordered turbostratic structure and smaller d_{002} reduce irreversible reactions but also limit the number of sites that can reversibly host Na, so that the ICE does not surpass that of the 750 °C carbon.

The rate performance of the four electrodes, probed by stepping the current from C/10 to C/5, C/3 and 1C and then returning to C/10, is presented in Fig. 8.5d. BH-T750-BM020 again displays the highest rate capability, delivering approximately 270 to 280 mAh g^{-1} at C/10, around 260 to 270 mAh g^{-1} at C/5, 240 to 250 mAh g^{-1} at C/3 and still about 220 to 230 mAh g^{-1} at 1C. When the rate is reduced back to C/10, the capacity recovers to nearly its initial value, indicating that most of the capacity loss at high rate is kinetic rather than due to irreversible degradation. BH-T1150-BM020 sustains capacities of roughly 140 to 150, 135 to 140, 125 to 130 and 115 to 120 mAh g^{-1} at C/10, C/5, C/3 and 1C, respectively, with similarly good recovery on the final C/10 step. The lower-rate sensitivity of this sample is consistent with its more compact but electronically well-connected structure, where transport limitations are mitigated by improved electronic conductivity, even though the total number of Na-accessible sites is lower than in BH-T750-BM020.

The BH-T950-BM020 and BH-T550-BM020 electrodes exhibit the lowest rate performance. Their capacities decrease from roughly 100 and 90 mAh g^{-1} at C/10 to about 80 to 90 and 70 to 80 mAh g^{-1} at 1C, respectively, with only partial recovery on returning to C/10. For BH-T550-BM020, this

behaviour reflects the combination of poorly developed porosity, which restricts electrolyte access and Na transport, and a highly disordered carbon network that introduces tortuous ion pathways. For BH-T950-BM020, the reduced d_{002} and intermediate surface area likely constrain Na pore/interlayer filling, so that higher currents accentuate diffusion limitations and underutilisation of active domains.

Taken together, the cycling and rate data confirm that carbonisation at 750 °C and 1150 °C yields the most attractive combinations of reversible capacity, stability and rate capability for Na storage in barley-husk-derived hard carbon, albeit for different reasons. The 750 °C material benefits from high porosity and enlarged interlayer spacing, which maximise capacity and confer strong rate tolerance, while the 1150 °C material leverages a more ordered turbostratic structure to deliver moderate capacities with excellent stability and reasonable rate performance. The extremes of the temperature range, 550 °C and 950 °C, are penalised either by excessive disorder and limited porosity (550 °C) or by over-contracted stacking that hinders Na insertion (950 °C). These findings reinforce the importance of balancing surface area, pore structure and stacking order when optimising biomass-derived hard carbons for Na-ion applications.

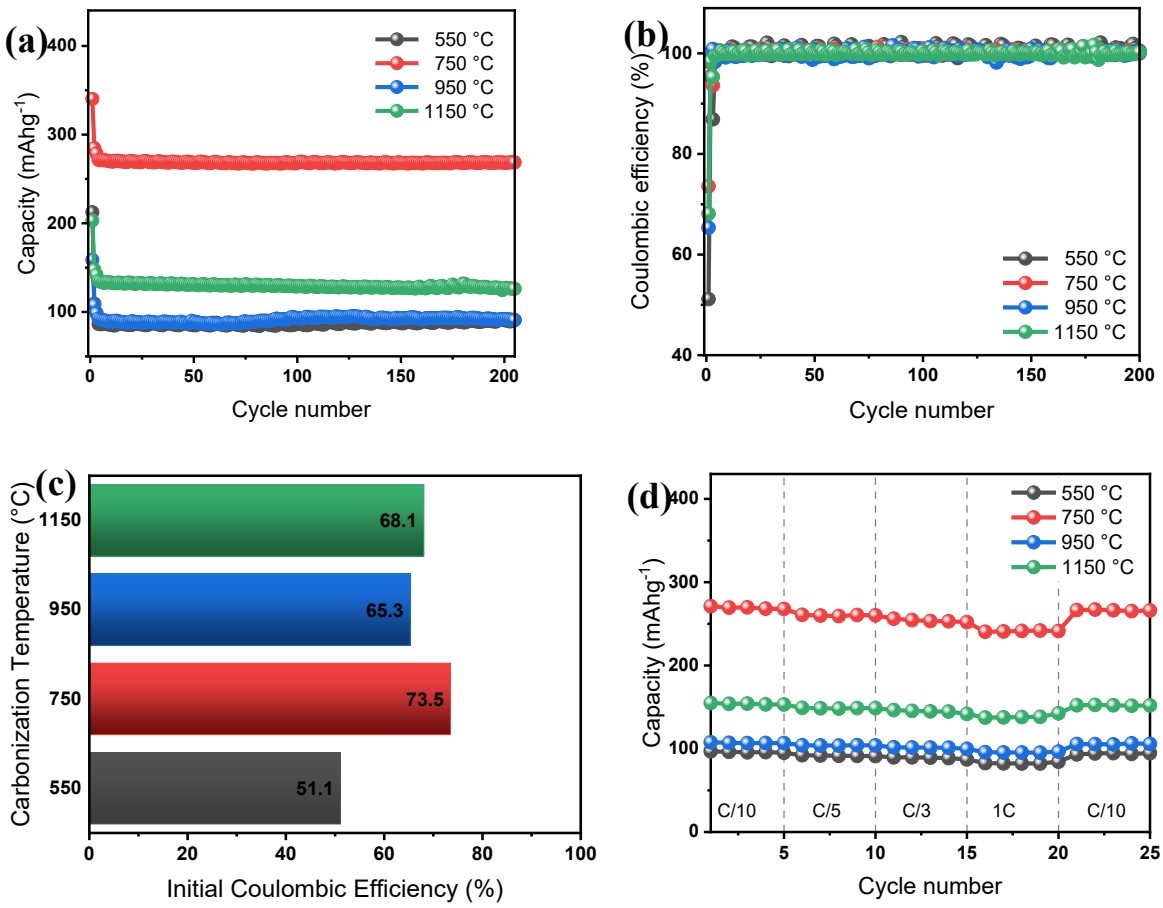

Figure 8.5. Electrochemical performance of BH-T####-BM020 anodes in Na half-cells: (a) cycling performance at C/5 over 200 cycles, (b) corresponding Coulombic efficiency, (c) initial Coulombic efficiency (ICE) as a function of carbonisation temperature and (d) rate capability over a stepped C/10 → C/5 → C/3 → 1C → C/10 sequence.

8.2.5. Differential capacity analysis and Na-storage mechanisms

Further insight into the Na-storage processes in the BH-T####-BM020 electrodes was obtained by differential capacity analysis. Fig. 8.6 presents dQ/dV profiles for cycles 1, 2, 3, 10 and 50 between 0.01 and 2.5 V vs Na^+/Na for the four carbonisation temperatures. For each sample the first cycle shows more intense and less resolved features, while subsequent cycles converge to nearly overlapping curves, indicating the progressive stabilisation of the SEI and the underlying Na-storage mechanisms.

In all four electrodes the most prominent features appear at low potentials, close to 0 V vs Na^+/Na. On the cathodic side, a sharp negative peak is observed below ~0.05 V in the first cycle, particularly pronounced for BH-T750-BM020 and BH-T1150-BM020, reflecting a combination of electrolyte reduction, SEI formation and initial Na filling of the most accessible nanopores and interlayer domains. The corresponding anodic peak, slightly shifted to higher potential, is much smaller in the first cycle, which confirms the largely irreversible character of the initial reduction processes. From the second cycle onwards, the magnitude of the low-potential cathodic peak decreases and the associated anodic peak becomes more symmetric and reproducible, consistent with the completion of SEI formation and the emergence of a predominantly reversible low-voltage process attributed to Na insertion/extraction in confined domains such as enlarged interlayer spaces and closed pores that become electrochemically accessible.

At higher potentials, broad cathodic and anodic features extend from approximately 0.1 to 0.8 to 1.0 V. These bands are most clearly developed in BH-T750-BM020 and BH-T1150-BM020 and are weaker and less defined in BH-T550-BM020 and BH-T950-BM020. They are assigned to Na^+ adsorption/desorption on defect sites, edges and surface functional groups, together with redox activity in more weakly confined carbon regions. The broadness and modest potential shift of these features with cycling indicate a distribution of adsorption energies and local environments typical of disordered hard carbons. The gradual reduction in intensity of the high-potential bands between cycles 1 and 10, followed by near-complete overlap between cycles 10 and 50, suggests that a fraction of the initially accessible sites becomes irreversibly passivated during SEI maturation, whereas the remaining population supports reversible adsorption-based storage with stable energetics.

Comparing the four temperatures reveals how carbonisation governs the balance between adsorption-dominated and pore/interlayer-dominated storage. For BH-T550-BM020 the dQ/dV response is dominated by relatively broad, low-amplitude features across the 0.1 to 1.0 V window and a comparatively muted low-potential peak, even after formation. This pattern reflects a microstructure in which Na storage is mainly controlled by heterogeneous defect and surface sites in a highly disordered carbon, with only a limited contribution from well-defined nanopores or enlarged interlayer galleries, consistent with the sloping voltage profiles and low capacities discussed in Section 8.2.3. In BH-T750-BM020 both the low-potential peak and the intermediate-

potential band are intense and well developed, and retain high amplitude up to the 50th cycle. This indicates a strong contribution from reversible Na filling of nanopores and interlayer domains, superimposed on a substantial population of adsorption sites; together these processes underpin the high reversible capacity and rate performance of this sample.

For BH-T950-BM020 and BH-T1150-BM020, the dQ/dV curves show relatively sharp low-potential peaks but reduced intensity in the 0.1 to 0.8 V region compared with BH-T750-BM020. The sharpening of the low-voltage peaks with increasing temperature suggests that Na pore/interlayer filling becomes more localised in better-defined turbostratic domains as d_{002} contracts and stacking order increases. At the same time, the loss of area under the intermediate-potential bands indicates a reduction in the density of accessible defect and surface sites, in line with the decreasing BET surface area and defect content at high carbonisation temperature. The net result is a more "intercalation-like" profile with lower total capacity, congruent with the moderate reversible capacities and good Coulombic efficiencies observed for BH-T950-BM020 and BH-T1150-BM020.

When compared qualitatively with the Li-ion dQ/dV signatures reported in Chapter 5 for the same temperature series, several similarities and distinctions emerge. In both chemistries the higher-temperature carbons exhibit sharper low-potential peaks and reduced high-potential contributions, reflecting the common structural evolution toward more ordered turbostratic carbon. However, in the Na system the optimum balance between the low-potential and sloping regions is shifted towards the intermediate temperature of 750 °C, where enlarged interlayer spacing and high porosity enable extensive pore filling and Na pore/interlayer filling without excessively suppressing adsorption-based storage. The 1150 °C carbon, which was close to optimal for Li storage, shows a comparatively weaker low-potential contribution in Na, consistent with the more stringent steric requirements of Na^+ pore/interlayer filling. Overall, the differential capacity analysis confirms that Na storage in barley-husk-derived hard carbon involves a combination of defect-mediated adsorption at intermediate potentials and pore/interlayer filling at low potentials, with the relative weight of these processes finely tuned by carbonisation temperature and the resulting microstructure.

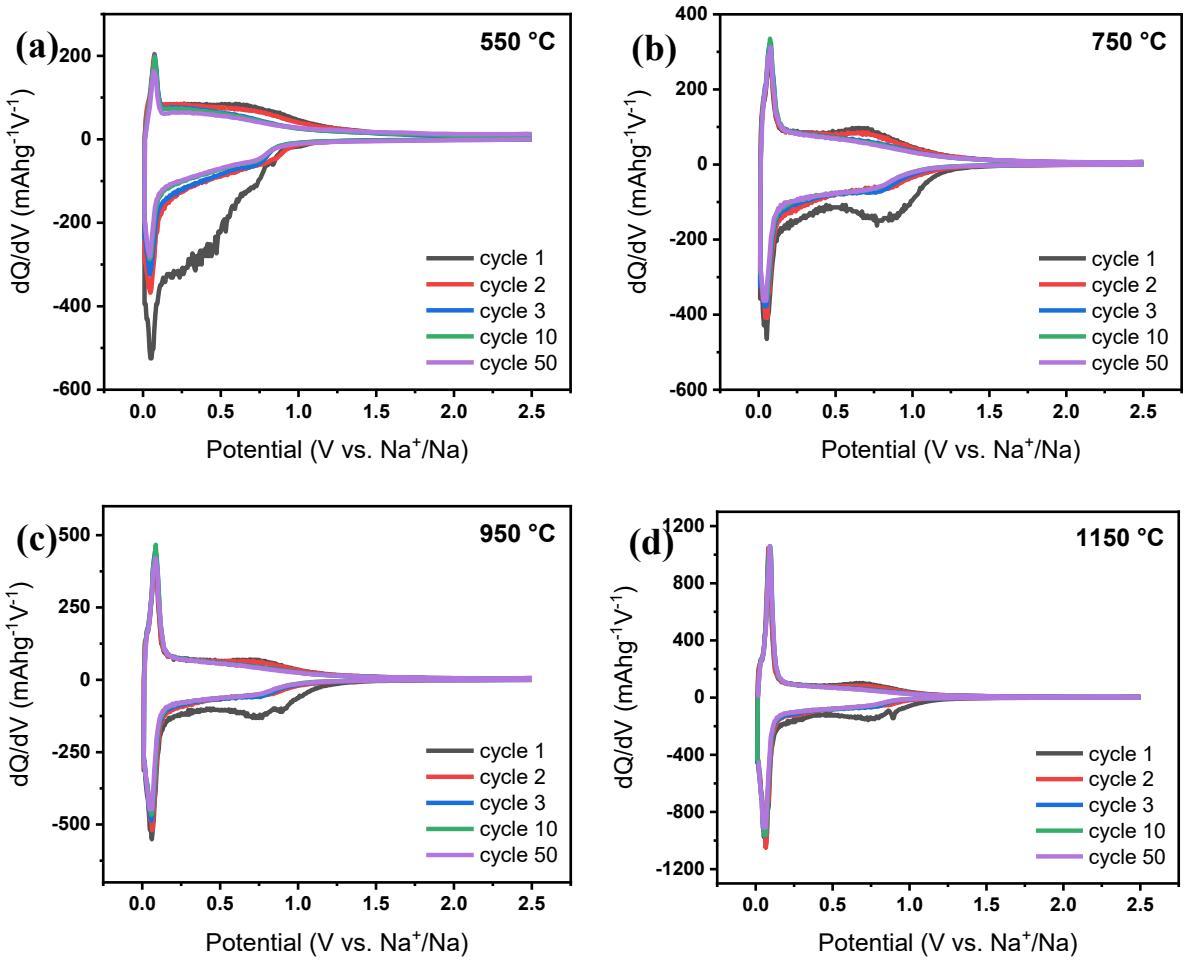

Figure 8.6. Differential capacity (dQ/dV) profiles for BH-T####-BM020 anodes at 550, 750, 950 and 1150 °C over cycles 1, 2, 3, 10 and 50 between 0.01 and 2.5 V vs Na^+/Na, highlighting the evolution of low-potential plateau features and higher-potential sloping contributions.

8.2.6. Electrochemical impedance analysis and Na^+ diffusion

Electrochemical impedance spectroscopy (EIS) was employed to probe the charge-transfer and diffusion properties of the BH-T####-BM020 electrodes during Na-ion storage. Nyquist plots and corresponding Z' vs. $\omega^{-0.5}$ relations after the 1st and 50th cycles are shown in Fig. 8.7, and the fitted parameters are summarised in Table 8.1. Spectra were fitted using the same Randles-type circuit model shown in Fig. 5.5, comprising a solution resistance R_s in series with two parallel R–CPE elements (assigned to the SEI and charge-transfer processes, respectively) and a Warburg

diffusion element to describe Na^+ transport at low frequencies. As in Chapter 5, the low-frequency Warburg region was analysed by fitting the linear part of the Z' versus $\omega^{-0.5}$ plot according to Eq. (5.1), where the intercept corresponds to the real impedance at the end of the semicircle and the slope yields the Warburg coefficient σ. The apparent Na^+ diffusion coefficient, D_{Na^+}, was then calculated using the same expression as Eq. (5.2), with the Li^+ concentration term replaced by the Na^+ concentration in the electrode. The resulting σ and D_{Na^+} values for BH-T0550-BM020, BH-T0750-BM020, BH-T0950-BM020 and BH-T1150-BM020 are listed in Table 8.1.

The Nyquist plots after the first cycle in Fig. 8.7a display a high-frequency intercept on the real axis corresponding to R_s, followed by a depressed semicircle attributed to the combined SEI and charge-transfer contributions, and a low-frequency inclined line associated with diffusion-controlled Na^+ transport. The extracted R_s values decrease with increasing carbonisation temperature from 15.60 Ω for BH-T0550-BM020 to 11.17 Ω for BH-T1150-BM020, with the lowest value (7.70 Ω) obtained for BH-T0750-BM020 (Table 8.1). This trend reflects a combination of electrolyte resistance and contact resistance within the composite electrode, and indicates that the more porous and/or better-connected carbons (750 to 1150 °C) offer improved ionic and electronic pathways compared with the highly disordered 550 °C material.

A more pronounced dependence on temperature is seen in the charge-transfer resistance R_{ct}. After the first cycle, R_{ct} is 47.39 Ω for BH-T0550-BM020, drops to 23.70 Ω for BH-T0750-BM020, and then increases again to 43.16 and 36.22 Ω for BH-T0950-BM020 and BH-T1150-BM020, respectively. The lowest R_{ct} at 750 °C indicates that this carbon provides the most favourable Na^+ transfer kinetics across the electrolyte/SEI/hard-carbon interface, consistent with its high surface area and extensive pore network, which enhance electrolyte wetting and increase the density of active sites. The higher R_{ct} values for BH-T0550-BM020 and BH-T0950-BM020 point to sluggish interfacial kinetics, in the former case due to a highly defective, poorly percolated carbon matrix and limited mesoporosity, and in the latter case due to a more compact structure with reduced accessible surface and smaller interlayer spacing. BH-T1150-BM020 exhibits intermediate behaviour, combining lower disorder and good electronic conductivity with a somewhat constrained Na-accessible microstructure.

Upon extended cycling, both R_s and R_{ct} decrease for all samples as shown in Fig. 8.7b and reported in Table 8.1. After 50 cycles, R_s falls to 13.36, 5.66, 11.79 and 9.59 Ω for BH-T0550-BM020, BH-

T0750-BM020, BH-T0950-BM020 and BH-T1150-BM020, respectively, while R_{ct} decreases to 39.15, 19.53, 35.22 and 29.40 Ω. The reduction of R_{ct} with cycling is commonly associated with consolidation and homogenisation of the SEI layer and progressive wetting of internal pores, which reduce interfacial impedance. The 3D Nyquist representation in Fig. 8.7e, comparing BH-T0750-BM020 and BH-T1150-BM020, highlights this effect: in both electrodes the semicircle contracts from the first to the fiftieth cycle, with BH-T0750-BM020 consistently exhibiting the smallest radius. The fact that R_{ct} remains lowest for BH-T0750-BM020 after 50 cycles corroborates its superior long-term kinetics, in line with its high-rate capability and stable capacity retention.

The Warburg coefficient σ, obtained from the linear fits of Z' versus $\omega^{-0.5}$ and shown in Fig. 8.7c and 8.7d, exhibits a similar dependence on carbonisation temperature. After the first cycle σ is highest for BH-T0550-BM020 (39.04 Ω $s^{-1/2}$) and BH-T0950-BM020 (35.49 Ω $s^{-1/2}$), and lower for BH-T1150-BM020 (25.57 Ω $s^{-1/2}$) and especially BH-T0750-BM020 (19.06 Ω $s^{-1/2}$). Because σ is inversely related to the diffusion coefficient, these values translate into D_{Na^+} of 2.32 × 10^{-11}, 9.75 × 10^{-11}, 2.81 × 10^{-11} and 5.42 × 10^{-11} cm^2 s^{-1} for BH-T0550-BM020, BH-T0750-BM020, BH-T0950-BM020 and BH-T1150-BM020, respectively. After 50 cycles, σ decreases for all samples, reaching 30.86, 15.58, 28.05 and 23.38 Ω $s^{-1/2}$, and D_{Na^+} increases correspondingly to 3.72 × 10^{-11}, 1.46 × 10^{-10}, 4.50 × 10^{-11} and 6.48 × 10^{-11} cm^2 s^{-1}. The approximately twofold enhancement of D_{Na^+} from the first to the fiftieth cycle indicates that Na^+ transport within the hard carbon becomes progressively facilitated, again consistent with SEI stabilisation and gradual activation of pore and interlayer domains.

Across both cycles, BH-T0750-BM020 exhibits the highest Na^+ diffusion coefficients and the lowest σ, whereas BH-T0550-BM020 and BH-T0950-BM020 show the poorest diffusion characteristics. This behaviour can be rationalised by considering the combined effects of stacking and texture: at 750 °C, the enlarged interlayer spacing, high mesoporosity and continuous, though still defective, sp^2 network provide short diffusion pathways and a large number of accessible channels for Na^+ transport. At 550 °C, the poorly developed pore structure and highly disordered framework introduce tortuous and partially blocked pathways, while at 950 °C the contraction of d_{002} and partial collapse of pores restrict Na^+ mobility despite the improved electronic conductivity. At 1150 °C, the tighter stacking further limits diffusion, but the relatively low σ and moderate

D_{Na^+} values show that transport is still acceptable, which is consistent with the reasonable rate performance of this electrode.

When compared with the Li-ion results for the same carbonisation series, the Na^+ diffusion coefficients are one to two orders of magnitude lower (10^{-11} to 10^{-10} cm^2 s^{-1} for Na^+ versus 10^{-8} to 10^{-7} cm^2 s^{-1} for Li^+), reflecting the larger ionic radius of Na^+, its different solvation shell in diglyme and the more stringent steric requirements for pore/interlayer filling. Nevertheless, the qualitative trends with carbonisation temperature are similar in both chemistries: intermediate-to-high temperatures that balance sufficient interlayer spacing with improved structural coherence yield the most favourable combination of low R_{ct} and high diffusion coefficients. In the Na system, this optimum is shifted towards the 750 °C sample, whereas in the Li system the 1150 °C carbon was closer to optimal. This divergence underscores the need to tailor biomass-derived hard carbons specifically for the targeted charge carrier, rather than assuming that a processing window optimised for Li-ion operation will automatically transfer to Na-ion cells.

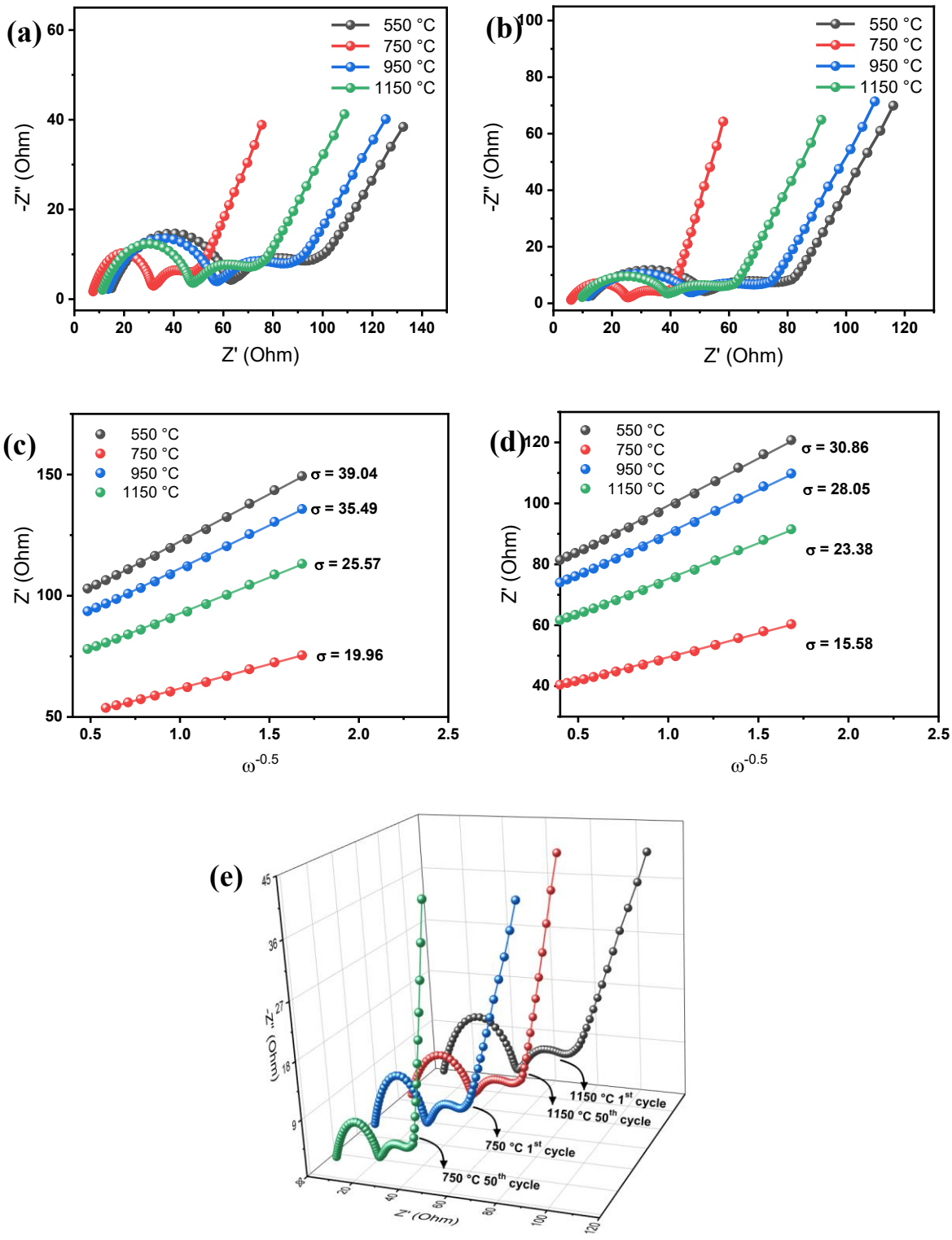

Figure 8.7. Electrochemical impedance spectra of BH-T####-BM020 anodes in Na half-cells after (a) the 1st cycle and (b) the 50th cycle. Corresponding Z′ vs $\omega^{-0.5}$ plots with linear fits after (c) the 1st cycle and (d) the 50th cycle used to obtain the Warburg coefficient σ. (e) The 3D overlay

compares the evolution of the spectra for BH-T750-BM020 and BH-T1150-BM020 at their 1st and 50th cycles.

Table 8.1. EIS-derived parameters for BH-T####-BM020 anodes in Na half-cells after the 1st and 50th cycles.

Temp. (° C)	1st cycle				50th cycle			
	$R_s(\Omega)$	$R_{ct}(\Omega)$	$\sigma(\Omega\, s^{-0.5})$	$D_{Na^+}(cm^2 s^{-1})$	$R_s(\Omega)$	$R_{ct}(\Omega)$	$\sigma(\Omega\, s^{-0.5})$	$D_{Na^+}(cm^2 s^{-1})$
550	15.60	47.39	39.04	2.324×10^{-11}	13.36	39.15	30.86	3.719×10^{-11}
750	7.70	23.70	19.06	9.748×10^{-11}	5.66	19.53	15.58	1.459×10^{-10}
950	13.87	43.16	35.49	2.812×10^{-11}	11.79	35.22	28.05	4.501×10^{-11}
1150	11.17	36.22	25.57	5.417×10^{-11}	9.59	29.40	23.38	6.479×10^{-11}

8.3. Comparative discussion: Na vs Li storage in BH-derived anodes

8.3.1. Processing-structure-performance links under Na vs Li operation

The comparative analysis of Li- and Na-ion operation in the barley-husk-derived hard carbons highlights both shared processing trends and clear differences in the location of the optimum carbonisation window. In Li half-cells, higher carbonisation temperature was consistently beneficial: BH-T1150-BM020 delivered the highest reversible capacity, the best rate performance and the lowest interfacial and diffusion-related resistances, with ICE increasing monotonically from 48.6 % at 550 °C to 59.2 % at 1150 °C. In Na half-cells, by contrast, the performance metrics show a non-monotonic dependence on temperature. BH-T750-BM020 provides the highest reversible capacity at C/5 (~260 mAh g^{-1}), the most favourable capacity retention, the highest initial Coulombic efficiency (73.5 %) and the largest Na^+ diffusion coefficient (1.46×10^{-10} cm^2

s^{-1} after 50 cycles), whereas both lower and higher temperatures lead to reduced Na storage and/or less efficient utilisation of the active material.

These differences can be traced back to how Li^+ and Na^+ weight the same structural descriptors. Increasing carbonisation temperature reduces d_{002}, increases L_c and promotes growth of larger sp^2 domains, while simultaneously decreasing defect density and accessible surface area. For Li^+, whose smaller ionic radius permits pore/interlayer filling, the contraction of d_{002} and increase in structural order at 1150 °C do not significantly impede access to interlayer domains, but do improve electronic conductivity and reduce parasitic surface reactions, resulting in higher capacity and ICE. For Na^+, which requires larger interlayer distances and experiences stronger steric constraints, the same contraction of d_{002} progressively restricts the population of galleries that can accommodate Na^+, so that the highest-temperature carbons no longer provide sufficient low-potential storage sites despite their favourable conductivity and moderate surface areas.

At 750 °C, the barley-husk carbon matrix retains enlarged interlayer spacing and a high defect content, while the N_2-sorption data indicate a pronounced maximum in BET surface area (108.2 $m^2\ g^{-1}$) and mesopore volume. This combination creates a microstructure in which Na storage is distributed between abundant adsorption sites at intermediate potentials and extensive nanopore/interlayer domains at low potentials, as reflected in the intense dQ/dV features across both potential regions and the large reversible capacity. Under Li operation, however, the same high surface area and defect density promote excessive SEI formation and trapping in deep sites, so that BH-T750-BM020 is outperformed by the more aromatised and compact BH-T1150-BM020. In this sense, the 750 °C carbon is over-textured for Li but ideally textured for Na.

The impedance results reinforce this picture. In Li half-cells the apparent diffusion coefficient increased steadily with carbonisation temperature, reaching ~10^{-7} $cm^2\ s^{-1}$ at 1150 °C, whereas in Na half-cells the maximum D_{Na^+} (~10^{-10} $cm^2\ s^{-1}$) is achieved at 750 °C, with both lower and higher temperatures displaying slower transport. This contrast arises because Li^+ benefits primarily from improved electronic connectivity and reduced disorder at high temperature, whereas Na^+ additionally requires sufficiently open pathways through pores and interlayer gaps. Once these pathways are constricted at 950 to 1150 °C, the gain in electronic transport is outweighed by the loss of Na-accessible channels.

8.3.2. Design implications for dual-chemistry BH-based anodes

The divergent optima identified for Li and Na storage have important implications for the design of barley-husk-derived hard carbons as platform anodes. From a single-chemistry perspective, the guidelines are clear: for Li-ion cells, carbonisation near 1150 °C combined with moderate milling yields the most favourable combination of high reversible capacity, elevated ICE, strong rate performance and fast Li^+ transport. For Na-ion cells, processing around 750 °C at the same milling time produces a microstructure that maximises reversible capacity and ICE while maintaining excellent rate capability and Na^+ diffusivity.

For applications that seek to explore both Li and Na chemistries on a common biomass platform, there is no single carbonisation temperature that simultaneously optimises all metrics for both ions. Instead, different processing windows offer different compromises. Carbons prepared at 750 °C deliver outstanding Na performance and still provide competitive Li capacities (~250 mAh g^{-1} at C/5), albeit with higher hysteresis and lower ICE than the 1150 °C material. Materials carbonised at 1150 °C, conversely, maximise Li performance while offering moderate Na capacities (~130 to 140 mAh g^{-1} at C/5) with very good stability and acceptable kinetics. For dual-chemistry demonstrators, these two processing points could therefore be used deliberately to bracket the Li-optimised and Na-optimised regimes, or combined (for example, via blending or graded electrodes) to engineer intermediate behaviour.

More broadly, the comparative analysis positions barley-husk-derived hard carbon favourably among biomass-based anodes for NIBs. The Na capacities and ICE values achieved at 750 °C are within the range reported for optimised hard carbons from other lignocellulosic precursors, while the ability to shift performance towards Li- or Na-preferential behaviour simply by adjusting carbonisation temperature highlights an intrinsic tunability that is attractive for sustainable electrode design. The fact that the same waste-derived precursor can be processed into distinct, chemistry-specific hard carbons reduces the need for multiple feedstocks and simplifies integration into future recycling and circular-economy frameworks.

8.4. Conclusion

This chapter has examined Na-ion storage in barley-husk-derived hard carbon as a function of carbonisation temperature at fixed milling time, building on the structural and Li-ion electrochemical baseline established in earlier chapters. N_2 adsorption-desorption measurements confirmed that the Na batch exhibits a pronounced maximum in BET surface area and mesoporosity at 750 °C, superimposed on the temperature-driven evolution of interlayer spacing, crystallite size and defect content previously identified by Raman and XRD. These textural and structural differences translate directly into distinct Na-storage behaviours when the materials are evaluated as anodes in $NaPF_6$-diglyme half-cells.

Electrochemical characterisation revealed that BH-T750-BM020 outperforms the other temperatures in Na-ion operation, delivering the highest reversible capacity (~260 mAh g^{-1} at C/5), the best capacity retention over 200 cycles, the highest initial Coulombic efficiency (73.5 %) and the strongest rate capability. In contrast, BH-T550-BM020 suffers from low capacity and ICE due to excessive disorder and poorly developed porosity, while BH-T950-BM020 and BH-T1150-BM020 provide moderate capacities and high efficiencies consistent with more ordered, but more constrained, turbostratic structures. The differential capacity analysis demonstrated that Na storage combines defect-mediated adsorption at intermediate potentials with pore and interlayer filling at low potentials, with the balance of these contributions tuned by carbonisation temperature. The EIS further showed that Na^+ diffusion coefficients are maximised at 750 °C and decrease at both lower and higher temperatures, reflecting the need to combine open transport pathways with sufficient structural coherence.

By comparing these Na-ion results with the Li-ion behaviour of the same barley-husk carbons, the chapter has clarified how Li^+ and Na^+ respond differently to identical processing-induced structural changes. Li operation is favoured by the highest-temperature, more ordered carbons, whereas Na operation is optimised at intermediate temperature where interlayer spacing and porosity remain large. This divergence underscores the central thesis of the work: barley husk constitutes a versatile, sustainable precursor whose carbonisation conditions can be tuned to engineer hard carbons tailored either for Li-ion or for Na-ion storage. In this way, the barley-husk platform offers a realistic route towards dual-chemistry negative electrodes based on a single, low-cost biomass

feedstock, supporting the development of both high-energy Li-ion and resource-abundant NIB technologies.

8.5. References

[1] A. Fereydooni, C. Yue, Y. Chao. *Small* 2024,20,2307275.

[2] V.L. Chevrier, G. Ceder. *J Electrochem Soc* 2011,158,A1011.

[3] P. Molaiyan, G.S. Dos Reis, D. Karuppiah, C.M. Subramaniyam, F. García-Alvarado, U. Lassi. *Batteries* 2023,9,116.

[4] M. Saavedra, L. Simonin, C. Matei, C. Vaulot, S. Perez, C. Dupont. *Fuel Processing Technology* 2022,231,107223.

[5] A. V. Baskar, G. Singh, A.M. Ruban, J.M. Davidraj, R. Bahadur, P. Sooriyakumar, P. Kumar, A. Karakoti, J. Yi, A. Vinu. *Adv Funct Mater* 2023,33,2208349.

[6] Z. Gao, Y. Zhang, N. Song, X. Li. *Mater Res Lett* 2017,5,69–88.

[7] Y. Zhu, M. Chen, Q. Li, C. Yuan, C. Wang. *Carbon N Y* 2018,129,695–701.

9. General conclusions and outlook

9.1. Overview of the thesis

This thesis examines barley husk as a multifunctional biomass precursor for silica/carbon composite anodes in lithium-ion and sodium-ion batteries. The study couples controlled processing (hard carbon and silica/carbon composites) with structural/textural and electrochemical characterisation, and then tests selected formulations in Si-enriched hybrids and full-cell configurations. Chapters 2 to 8 addressed a sequence of research questions spanning anode mechanisms, biomass-derived carbon design, comparative benchmarking against graphite, and the translation of barley husk-derived anodes from Li-ion to Na-ion chemistries.

9.2. Cross-cutting discussion: processing-structure-performance

A key result is the quantitative relationship established between processing parameters and the structural descriptors governing ion storage in the barley husk-derived anodes. Carbonisation temperature primarily controls the carbon framework: increasing 450 to 1150 °C drives aromatisation, reduces d_{002}, increases L_C, and sharpens the (002) reflection, while retaining a turbostratic, non-graphitising character. These structural changes were accompanied by a non-monotonic evolution of texture and surface area, with an optimum mesoporous development at intermediate temperatures.

Ball milling was found to act mainly on the accessible texture and particle morphology rather than on the underlying carbon structure. Short-to-moderate milling increased surface area and mesopore connectivity, improving electrolyte wettability and shortening ion-transport paths, whereas excessive milling led to diminishing returns and potential agglomeration. Together, temperature and milling define a processing window in which the barley husk-derived silica/carbon composite attains a balanced combination of structural order, residual interlayer spacing and accessible porosity.

These structural and textural descriptors translate directly into electrochemical behaviour in Li-ion cells. Higher carbonisation temperatures improved initial Coulombic efficiency, low-rate capacity and rate capability, with the BH-T1150-BM020 formulation identified as an optimum that maximises reversible capacity while maintaining hard-carbon-like stability and kinetics. Impedance analysis and diffusion-coefficient estimates revealed that this optimisation arises from reduced charge-transfer resistance and more efficient Li^+ transport within the active material, consistent with a more ordered yet still accessible turbostratic framework.

When benchmarked against commercial graphite, the optimised barley husk-derived composite delivered higher reversible capacity and comparable or slightly better rate performance, at the expense of a lower ICE and a more sloping voltage profile. This comparison confirms that a biomass-derived silica/carbon composite can match or exceed the performance of conventional graphitic anodes in Li half-cells while offering clear sustainability advantages and a different balance of energy and voltage characteristics.

Incorporating silicon into the barley husk-derived host altered this balance by introducing high-capacity alloying contributions. The BH/Si hybrids demonstrated that the barley husk carbon/silica framework can accommodate moderate Si loadings while maintaining mechanical integrity and reasonable Coulombic efficiency. A practical window of approximately 20 to 35 wt% Si was identified, within which capacities above 800 mAh g^{-1} were achieved with acceptable cycling stability and rate performance. Outside this window, high Si content led to rapid capacity fade despite the buffering effect of the BH host. Full-cell tests with NMC622 cathodes confirmed that Si-rich BH/Si composites can deliver substantially higher specific energy than graphite-based cells under realistic balancing, albeit with accelerated degradation that will require further mitigation.

Extending the optimised barley husk-derived hard carbon to sodium-ion cells provided additional insight into the ion storage mechanisms. The same structural hierarchy that benefited Li storage also governed Na storage, but Na^+ insertion shifted the balance towards adsorption-controlled processes and pore filling, with a more pronounced plateau at low potentials. The Na results revealed both parallels and differences compared with Li, emphasising the dual role of interlayer spacing and closed porosity in governing plateau capacity, and confirmed that barley husk-derived hard carbon is a viable anode for SIBs within the performance range of other biomass-derived hard carbons.

9.3. Original contributions

The main original contributions of this thesis are:

- Development of a processing-structure map for barley husk-derived silica/carbon composites. A systematic carbonisation and ball-milling study established how temperature and milling duration control interlayer spacing, crystallite thickness, defect density and pore structure in barley husk-derived materials, supported by Raman, XRD and N_2 physisorption analysis.
- Identification of an optimised barley husk-derived anode for Li-ion batteries. BH-T1150-BM020 was identified as a balanced formulation that combines high reversible capacity, improved initial Coulombic efficiency, strong rate capability and robust cycling stability, with its performance quantitatively linked to structural descriptors and kinetic parameters such as R_{ct} and $D_{Li}+$.
- Benchmarking of barley husk-derived anodes against commercial graphite under identical conditions. A like-for-like comparison in CR2016 half-cells demonstrated that the optimised barley husk-derived composite can match or surpass the performance of graphite in terms of capacity and rate capability, while revealing trade-offs in ICE and voltage profile that are relevant for practical cell design.
- Design and evaluation of silicon-enriched BH/Si hybrid anodes. A family of BH/Si composites spanning BH-dominated to Si-rich compositions was synthesised and characterised. The study identified a practical Si loading window and showed that the barley husk host mitigates some of the typical mechanical and interfacial instabilities of Si anodes, enabling high capacities in both half- and full-cell configurations.
- Demonstration of barley husk-derived hard carbon as a dual-chemistry anode for Li-ion and Na-ion batteries. The optimised barley husk-derived hard carbon was evaluated as an anode for sodium-ion batteries, and its Na^+ storage behaviour was compared directly with its Li^+ behaviour. The work clarified how processing-induced structural features influence ion storage in both chemistries and positioned the material within the broader family of biomass-derived hard carbons.

9.4. Limitations and critical reflection

Three limitations are particularly relevant for interpreting the present results. First, the electrochemical evaluation was largely conducted in coin-type half-cells with Li or Na metal counter electrodes. While this configuration is standard for mechanistic studies, it does not capture all aspects of performance in large-format commercial cells, including electrode thickness effects, stack pressure and long-term electrolyte degradation. Full-cell experiments were restricted to a subset of BH/Si composites paired with NMC622, and further validation in a broader range of practical configurations would be valuable.

Second, although the influence of carbonisation temperature, ball milling and silicon content was investigated systematically, other parameters such as binder chemistry, electrode calendering and electrolyte formulation were kept fixed once a suitable baseline was established. Alternative binders or electrolyte additives might further improve Coulombic efficiency and long-term stability, particularly for Si-rich composites, but exploring these variables in depth was beyond the scope of this thesis.

Third, the study relied on ex situ structural and interfacial characterisation at selected states of charge and cycle numbers. In situ or operando techniques such as XRD, X-ray tomography or spectroelectrochemistry could provide more direct evidence of phase evolution, SEI dynamics and mechanical degradation during cycling. Such methods are experimentally demanding, especially for heterogeneous biomass-derived composites, but would complement and refine the conclusions reached here.

9.5. Future work

The results presented in this thesis open several avenues for future work. From a materials-design perspective, the barley husk-derived silica/carbon framework could be further tailored through controlled activation, templating or heteroatom doping to adjust pore structure and electronic properties while maintaining mechanical robustness. Optimising the distribution and morphology

of silicon within the BH host, for example through nanoscale Si deposition or pre-oxidation strategies, may allow higher Si loadings without compromising stability.

At the electrode and cell levels, there is scope for exploring alternative binder systems, electrolyte formulations and prelithiation methods to mitigate the low ICE inherent to high-surface-area carbons and Si-containing composites. In particular, combinations of inorganic-rich SEI-forming additives, sacrificial salts and mechanical prelithiation techniques could be evaluated to reduce irreversible capacity losses while preserving safety.

For sodium-ion batteries, further work is needed to refine the balance between interlayer spacing, closed porosity and surface area in barley husk-derived hard carbons, and to examine their performance in full cells with sodium layered oxide or Prussian blue analogue cathodes. Comparative studies across different biomass feedstocks with similar processing protocols would help to disentangle the roles of precursor chemistry and morphology.

Finally, techno-economic and life-cycle assessments would strengthen the case for these anodes by quantifying cost, energy demand and environmental impact relative to graphite and synthetic carbons. Such analyses, combined with continued materials optimisation, could support the case for integrating biomass-derived $Si/SiO_2/C$ anodes into future lithium- and sodium-ion battery technologies.